



HAL
open science

Transformation optics: Application for antennas and microwave devices

Jianjia Yi

► **To cite this version:**

Jianjia Yi. Transformation optics: Application for antennas and microwave devices. Electromagnetism. Université Paris Saclay (COmUE), 2015. English. NNT : 2015SACLS027 . tel-01297057

HAL Id: tel-01297057

<https://theses.hal.science/tel-01297057>

Submitted on 2 Apr 2016

HAL is a multi-disciplinary open access archive for the deposit and dissemination of scientific research documents, whether they are published or not. The documents may come from teaching and research institutions in France or abroad, or from public or private research centers.

L'archive ouverte pluridisciplinaire **HAL**, est destinée au dépôt et à la diffusion de documents scientifiques de niveau recherche, publiés ou non, émanant des établissements d'enseignement et de recherche français ou étrangers, des laboratoires publics ou privés.

NNT : 2015SACLS027

THESE DE DOCTORAT
DE L'UNIVERSITE PARIS-SACLAY,
préparée à l'Université Paris Sud

ÉCOLE DOCTORALE N°575
Electrical, optical, bio-physics and engineering

Spécialité de doctorat : Physique

Par

M. Jianjia Yi

TRANSFORMATION OPTICS: APPLICATION FOR ANTENNAS AND
MICROWAVE DEVICES

Thèse présentée et soutenue à Orsay, le 12 Octobre 2015 :

Composition du Jury :

M. X. Bégaud	Professeur, TELECOM ParisTech	Président
M. S. Guenneau	Directeur de Recherche, Institut Fresnel	Rapporteur
M. R. Sauleau	Professeur, IETR	Rapporteur
M. G.-P. Piau	Senior Expert, Airbus Group Innovations	Examineur
M. A. de Lustrac	Professeur, IEF	Directeur de thèse
M. S. N. Burokur	Maître de Conférences/HDR, IEF	Co-directeur de thèse
M. P.-H. Tichit	Docteur, Institut Pascal	Invité



SUMMARY (IN FRENCH)

Fin 2006 apparaissait dans la revue Science la première cape d'invisibilité électromagnétique. Réalisée par l'équipe de D. R. Smith à l'université de Duke aux Etats-Unis et conçue théoriquement par J. B. Pendry ce nouveau dispositif électromagnétique éveilla l'intérêt de la communauté scientifique. Quelques mois auparavant c'était une innovante et fascinante technique mathématique qui avait été dévoilée sous le nom « optique de transformation » ou plus communément « transformation d'espace ». Cet outil extrêmement puissant, basé sur la réinterprétation des équations de Maxwell, offre un énorme potentiel pour la conception de dispositifs aux propriétés extraordinaires. De plus, le couplage avec l'ingénierie des résonateurs à métamatériaux permet la réalisation des milieux générés par ces transformations. En effet, des recherches récentes ont établi la possibilité de fabriquer des structures dans les domaines micro-ondes et optique, permettant de contrôler la lumière d'une manière inconcevable avec les matériaux naturels.

A partir d'éléments sub-longueur d'onde que sont les résonateurs à métamatériaux, il est possible d'obtenir les distributions spatiales bien spécifiques de la permittivité ϵ et de la perméabilité μ , offrant ainsi le potentiel pour guider et contrôler le flux de l'énergie par une ingénierie d'espace. Ces métamatériaux ont ouvert la porte à de nombreuses applications qui, jusque-là, avaient été considérées comme impossibles. Ceux-ci permettent en effet de s'abstraire des réponses électromagnétiques des matériaux naturels ainsi que de leur composition chimique, grâce au contrôle de la forme et des dimensions de leurs cellules unités, ces dernières pouvant être vues comme des atomes artificiels homogènes puisque leurs dimensions sont beaucoup plus petites que la longueur d'onde.

L'apparition de la méthode de la transformation d'espace en 2006 a donc apporté une nouvelle vision sur les fondations de l'optique. Analogue à la relativité générale où temps et espace ne font plus qu'un et sont modifiés par l'énergie et la masse, la transformation d'espace montre qu'il

Summary (In French)

est possible de déformer l'espace à volonté afin d'imposer la trajectoire des rayons lumineux. Cette ingénierie d'espace fournit un contrôle du flux lumineux jusqu'à une précision nanométrique. Ainsi, la relativité générale trouve une application dans de nouveaux systèmes optiques basés sur la transformation d'espace où la lumière est guidée par les métamatériaux d'une manière contrôlée et prédéfinie. Ce point de vue n'est pas totalement nouveau puisque déjà dans les années 1920 W. Gordon avait pu remarquer que des milieux isotropes en mouvement pouvaient apparaître comme une géométrie d'espace-temps pour le champ électromagnétique.

L'objectif de cette thèse est donc de comprendre la théorie de l'optique de transformation et d'appliquer ce concept pour concevoir de nouveaux systèmes électromagnétiques liés aux antennes. J'expose dans un premier temps le principe de l'optique de transformation ainsi que les bases et concepts mathématiques nécessaires à l'utilisation d'un tel outil. Dans cette thèse, je me consacre donc au concept de l'optique de transformation qui permet de contrôler le trajet des ondes électromagnétiques à volonté en appliquant une variation spatiale judicieusement définie dans les paramètres constitutifs. Il est exploré pour concevoir des nouveaux types d'antennes et de dispositifs dans le domaine des micro-ondes.

Deux méthodes sont utilisées pour concevoir les dispositifs : la transformée de coordonnées et la transformation spatiale. La transformation de coordonnées est faite en redéfinissant les paramètres électromagnétiques. Suivant cette approche, les équations de Maxwell sont écrites de telle façon qu'elles sont invariantes dans les transformations. En fait les transformations de coordonnées fournissent les tenseurs de perméabilité et permittivité appropriés dus à l'invariance des équations de Maxwell dans ces transformations, ce qui rend possible le contrôle de la lumière à toute échelle, du macroscopique jusqu'au microscopique. En créant les distributions de permittivité et perméabilité, l'espace peut être déformé à volonté, rendant ainsi possible par exemple la création de trajectoire "fantaisistes" avec des indices pouvant être négatifs.

Il en résulte ainsi la conception de deux systèmes électromagnétiques proposés dans cette thèse ;

un dispositif d'illusion et un adaptateur de guide d'ondes. Le dispositif d'illusion capable de modifier l'apparence d'une émission électromagnétique et de la délocaliser, est validé par le biais de simulations numériques. En effet, en comprimant l'espace contenant un élément rayonnant, nous montrons qu'il est capable de modifier son diagramme de rayonnement et aussi de faire en sorte que la source d'émission apparaisse à l'extérieur de cet espace. Nous décrivons la transformation de l'espace métrique et le calcul des paramètres du matériau. Des modèles continus et discrets avec les valeurs des paramètres électromagnétiques calculés sont proposés. Une réduction des paramètres électromagnétiques suivant une polarisation bien fixe pour la source est également proposée afin de penser à une possible fabrication du dispositif en utilisant des valeurs réalisables de la permittivité et la perméabilité de métamatériaux existants.

Nous concevons par la suite un adaptateur entre deux guides d'ondes de sections différentes. Après une étude de plusieurs techniques de transformation différentes, nous en proposons une basée sur un système de double adaptateur afin d'assurer une transmission entre deux guides avec un rapport de 11,4 entre les sections. Les milieux provenant de cette méthode présentent une perméabilité et une permittivité anisotrope. Cependant, nous montrons qu'une transformation de type 'inverse proportionnelle' conduit à la conception d'un système adaptateur à partir d'un matériau avec les paramètres du matériau physiquement réalisables. Les paramètres complexes sont simplifiés et discrétisés pour une réalisation du dispositif. Le prototype fabriqué à partir de résonateurs à métamatériaux électriques et magnétiques de cet adaptateur de guide d'ondes est ensuite présenté. Une validation du concept est réalisée en comparant les distributions de champs simulé et mesuré.

Dans une seconde partie, la transformation spatiale basée sur l'équation de Laplace et quasi-conforme est étudiée pour concevoir des lentilles large bande pour les applications antennaires. Cette méthode de conception fait appel à un ensemble de conditions aux limites qui définissent l'effet du dispositif, tout en limitant la transformation à l'intérieur du matériau. En particulier, les angles entre les lignes de coordonnées sont quasiment conservés et il y a une anisotropie limitée

des coordonnées « carrées », autrement dit, elles sont toujours sensiblement carrées, plutôt que rectangulaires. Contrairement à la transformation de coordonnées, cette technique permet au module conforme des deux domaines d'être différent que dans une certaine mesure, ce qui constitue une caractéristique cruciale pour une conception fonctionnant sur une large bande de fréquence et donc à partir de matériaux non résonants. Pour une transformation en deux dimensions, cela conduit à la prescription d'un matériau d'anisotropie très limitée qui peut être bien approximée par une réponse diélectrique uniquement.

Cette transformation spatiale quasi-conforme est donc utilisée pour concevoir deux lentilles ; une lentille de focalisation capable de restaurer les émissions en phase d'un réseau conforme d'éléments rayonnants et une lentille à dépointage qui permet de dévier la direction du faisceau rayonné d'une antenne. La lentille de focalisation est appliquée à un réseau d'éléments rayonnants conformé sur une surface cylindrique. Elle permet de compenser les déphasages introduits par la localisation des éléments sur la surface cylindrique et ainsi annuler l'effet de défocalisation pour produire une émission en phase. La deuxième lentille est conçue pour produire un dépointage de faisceau à partir d'une source avec un rayonnement dans la direction normale au plan de la source. Ces deux lentilles sont réalisées à partir d'un matériau isotrope tout-diélectrique grâce à la technologie d'impression en trois dimensions (3D). Les prototypes permettent de valider expérimentalement la fonctionnalité des lentilles sur une large bande de fréquence.

Les travaux présentés dans cette thèse montrent donc toute la richesse du concept de l'optique de transformation pour concevoir de nouveaux systèmes électromagnétiques.

ACKNOWLEDGEMENTS

As is often the case of overseas students, I have found the experience during my thesis fascinating but full of challenges at the same time. Today when I finish this thesis and retrospect, I find that all the challenges came together with rewards. During these three years, I appreciate and honor all the people that have participated in my life and offered help generously. I would like to spend my ink on the words of gratitude for them.

I would like to begin with thanking my thesis supervisor, Prof. André de Lustrac. Prof. De Lustrac welcomed me into his group when I was at the crossroad of working or continuing my academic career. The subject of the thesis he offered to me is brand new and interesting to me. He has shown me nothing but patience and encouragement even at the lows of my research work.

I want to send my appreciation to my co-supervisor Prof. Shah Nawaz Burokur for his guidance. From project modelling to experimental setups, even on the manuscript of scientific papers, his generous tutoring has permeated into all the details in my work. He also helped me out of difficulties in personal life, such as accommodation problems and so on. He has made my work and life here in Paris filled of warmth and fun.

I would like to give my great thanks to Dr. Paul-Henri Tichit. My thesis started by continuing the coordinate transformation based designs of Dr. Tichit's thesis. Dr. Tichit has taught me everything he could give on this subject. As to a freshman in face of transformation optics, the knowledge he imparted to me make the rudiments of the subject much easier to me.

In addition I need also express my gratitude to the opportunity for discourse and collaboration with many colleagues. Dr. Anotole Lupu, Dr. Aloyse Degiron and Dr. Tatiana Teperik all have offered me help in physic problems and give me instructions and ideas. I also thank Dr. G.P. Piau from AIRBUS Innovation Works for his scientific support along this thesis, and

Acknowledgements

particularly in the technical realization of several prototypes.

Moreover, I also want to thank my colleagues, Alexandre Sellier, Natalia Dubrovina, Quynh Le Van, Simon Marcellin, Anna Niang, Yulong Fan, Eleana Bochkova and Badreddine Ratni for their concern and accompany.

Finally, I would like to sincerely thank my parents who have brought me up and encourage me to see the rest of the world. They have given me everything supported me unconditionally but asked nothing in return.

My fiends TY Ding, Y Wang, YL Zhu, YK Pei, YY Wang, C Wang have spare their time with me during the three years. Their friendship has lightened up the life far from home.

I hope the name I missed here can accept my appreciation. Thank you for all your helps.

I acknowledge the French Ministry of Higher Education and Research for the financial support.

In the end, I would like to say that spending three years of my best age at University Paris-sud is an indelible memory which I will always remember and never regret.

CONTENTS

SUMMARY IN FRENCH	i
ACKNOWLEDGEMENTS	v
LIST OF TABLES	xi
LIST OF FIGURES	xiii
LIST OF ABBREVIATIONS AND ACRONYMES	xxvii
GENERAL INTRODUCTION.....	1
1 TRANSFORMATION OPTICS: DEFINITION AND RELATED TOOLS.....	3
1.1 STATE OF ART ON METAMATERIALS AND METAMATERIAL-BASED DEVICES	3
1.2 TRANSFORMATION OPTICS.....	10
1.2.1 <i>Coordinate transformations</i>	12
1.2.2 <i>Space transformation based on Laplace's equation</i>	18
1.3 NUMERICAL CALCULATION SOFTWARES	25
1.3.1 <i>Mathematica</i>	25
1.3.2 <i>COMSOL Multiphysics</i>	26
1.3.3 <i>ANSYS HFSS</i>	27
1.4 EXPERIMENTAL SETUPS	29
1.4.1 <i>Near-field measurement setup</i>	29
1.4.2 <i>Far-field measurement setup</i>	30
1.5 VALIDATION TECHNOLOGY	31
1.5.1 <i>Electric LC (ELC) resonators</i>	32
1.5.2 <i>Split ring resonator (SRR)</i>	33
1.5.3 <i>All-dielectric material</i>	34
1.6 CONCLUSION.....	35
2 ILLUSION OPTICS: OPTICALLY TRANSFORMING THE NATURE AND THE	

LOCATION OF ELECTROMAGNETIC EMISSIONS.....	41
2.1 INTRODUCTION	42
2.2 SPATIAL COORDINATE TRANSFORMATION FORMULATION.....	45
2.2.1 <i>The concept of the sinusoidal transformation.....</i>	<i>46</i>
2.2.2 <i>The concept of the linear transformation.....</i>	<i>50</i>
2.2.3 <i>Comparison between sinusoidal and linear transformations</i>	<i>53</i>
2.3 NUMERICAL SIMULATIONS AND RESULTS	54
2.3.1 <i>Parametric study of q.....</i>	<i>54</i>
2.3.2 <i>Parametric study of the position of the real source.....</i>	<i>56</i>
2.3.3 <i>Parametric study of the dimensions of the shell</i>	<i>58</i>
2.4 LAYERED MATERIAL DESIGN	59
2.5 CONCLUSION	63
3 WAVEGUIDE TAPER.....	65
3.1 INTRODUCTION.....	66
3.2 SPATIAL COORDINATE TRANSFORMATION FORMULATION.....	69
3.2.1 <i>Cosinusoidal transformation</i>	<i>70</i>
3.2.2 <i>Parabolic transformation</i>	<i>71</i>
3.2.3 <i>Logarithmic transformation.....</i>	<i>73</i>
3.2.4 <i>Reciprocal transformation.....</i>	<i>74</i>
3.3 TWO TAPERS AND TWO ADAPTERS SYSTEM.....	75
3.3.1 <i>Parametric study on the two adapters</i>	<i>79</i>
3.3.2 <i>2D discrete model</i>	<i>81</i>
3.3.3 <i>Parameter reduction.....</i>	<i>82</i>
3.4 EXPERIMENTAL VALIDATION USING ELC AND SPLIT RINGS RESONATOR.....	83
3.5 CONCLUSION	87
4 RESTORING IN-PHASE EMISSIONS FROM NON-PLANAR RADIATING	

ELEMENTS USING WAVE-MATTER INTERACTION.....	91
4.1 INTRODUCTION	92
4.2 DESIGN OF THE DIRECTIVITY ENHANCEMENT LENS.....	94
4.2.1 <i>Concept and analytical design</i>	94
4.3 DIMENSION STUDY OF THE LENS.....	100
4.3.1 <i>Parametric study of the thickness of the lens</i>	100
4.3.2 <i>Parametric study of the radius of the sector:</i>	102
4.4 2D DISCRETIZATION AND FULL-WAVE SIMULATIONS	103
4.5 DIELECTRIC MATERIAL ANALYSE AND 3D PROTOTYPE PROPOSAL	108
4.6 FULL-WAVE SIMULATIONS ON 3D DISCRETE MODEL.....	109
4.7 CONFORMAL LENS FABRICATION AND EXPERIMENTAL CHARACTERIZATION	112
4.8 CONCLUSIONS	115
5 COHERENT BEAM CONTROL WITH A TRANSFORMATION OPTICS BASED	
LENS.....	117
5.1 DESIGNS OF THE BEAM STEERING LENS AND 2D ANALYSIS.....	118
5.1.1 <i>Beam steering lens design 1</i>	118
5.1.2 <i>Beam steering lens design 2</i>	129
5.2 DISCRETIZATION OF THE LENS DESIGN 1	133
5.3 EXPERIMENTAL VALIDATION USING ELECTRIC LC RESONATORS	135
5.4 EXPERIMENTAL VALIDATION USING ALL-DIELECTRIC MATERIAL.....	143
5.5 CONCLUSION	149
CONCLUSION	151
BIBLIOGRAPHY	153
LIST OF PUBLICATIONS	165

LIST OF TABLES

TABLE 1-I: $H_u, H_v,$ AND H_w EXPRESSIONS IN DIFFERENT COORDINATE SYSTEMS.....	15
TABLE 1-II: EXPRESSIONS OF ROTATION MATRIX \mathbf{R} IN DIFFERENT COORDINATE SYSTEMS.....	16
TABLE 2-I: DISCRETIZATION OF THE PARAMETERS FOR THE LAYERED MATERIAL SHELL.	61
TABLE 3-I: COMPONENTS VALUES OF $\overset{=}{\theta}$ TENSOR FOR THE TRANSFORMATION OF TWO TAPER PARTS.....	77

LIST OF FIGURES

FIGURE 1-1: (A) METAMATERIAL IMPLEMENTATION-CLOAKING DEVICE [1]. (B) A MODEL OF 3D METAMATERIAL [2].	4
FIGURE 1-2: EFFECTIVE MEDIUM PARAMETER DIAGRAM SHOWING THE FOUR QUADRANTS OF MATERIAL PARAMETERS ϵ AND μ	6
FIGURE 1-3: (LEFT) COMPARISON OF REFRACTION OF AN INCIDENT RAY PROPAGATING INTO A POSITIVE AND NEGATIVE INDEX MATERIAL (RIGHT) [7].	6
FIGURE 1-4: (A) GEOMETRICAL INTERPRETATION OF THE EMISSION OF A SOURCE INSIDE A SLAB OF A LOW INDEX METAMATERIAL (NOT NEGATIVE). (B) CONSTRUCTION IN THE RECIPROCAL SPACE. (C) SCHEMATIC REPRESENTATION OF THE STRUCTURE [9].	7
FIGURE 1-5: METAMATERIAL LINER GEOMETRY, PROPERTIES AND INCORPORATION INTO A RECTANGULAR HORN ANTENNA [10].	8
FIGURE 1-6: CONFIGURATION OF (A) THE QUARTER-WAVE MONOPOLE ANTENNA AND (B) THE SAME MONOPOLE WITH ULTRATHIN FLEXIBLE ANISOTROPIC MM COATING [11], AND (C) THE SIMULATED VSWR OF THE MODELS.	9
FIGURE 1-7: DIAGRAMS SHOWING (A) ACTUAL PICTURE OF A LENS DISK, (B) BLOW-UP ILLUSTRATING UNIT-CELL ARRAY, (C) FURTHER BLOWN UP SINGLE UNIT CELL WITH SRR AND WIRE ELEMENTS [12].	10
FIGURE 1-8: ILLUSTRATION OF THE EMBEDDED COORDINATE TRANSFORMATION FOR $\alpha = \pi/5$ [81].	17
FIGURE 1-9: DISTRIBUTION OF THE ELECTRIC FIELD COMPONENT NORMAL TO THE PLANE OF PROPAGATION FOR $\alpha = \pi/2$ WITH (A) $\Gamma = 0.02$ AND (B) $\Gamma = 0.3$ [82].	18
FIGURE 1-10: THE SCHEME OF CONSTRUCTING AN ARBITRARY CLOAK [82].	19
FIGURE 1-11: MATERIAL PARAMETERS (A) ϵ_{zz} , (B) μ_{xx} , (C) μ_{xy} AND (D) μ_{yy} . ELECTRIC FIELD DISTRIBUTION FOR INCIDENT WAVE (E) HORIZONTALLY (F) 45° [82].	21

FIGURE 1-12: DEPICTION OF THE QUASI-CONFORMAL MAPPING USING INTERMEDIATE TRANSFORMATIONS [79]. LINES OF CONSTANT x AND y , (VIRTUAL DOMAIN COORDINATES), ARE SHOWN IN EACH DOMAIN. THE THICK BLACK LINE REPRESENTS A PEC BOUNDARY IN EACH DOMAIN. 23

FIGURE 1-13: INTERFACE OF COMSOL MULTIPHYSICS. 26

FIGURE 1-14: SKETCH OF SIMULATION SETUP OF ANTENNAS. 27

FIGURE 1-15: SKETCH OF SIMULATION SETUP OF UNIT CELLS. 28

FIGURE 1-16: NEAR FIELD SCANNING EXPERIMENTAL SETUP. 30

FIGURE 1-17: FAR FIELD SCANNING EXPERIMENTAL SETUP. 31

FIGURE 1-18: ELECTRIC-LC RESONATOR [97]. (A) A TYPICAL ELC RESONATOR IS COMPOSED OF A CENTER CAPACITIVE GAP CONNECTED TO TWO INDUCTIVE LOOPS. (B) AN EQUIVALENT CIRCUIT OF THE RESONATOR CONSTITUTES AN LC RESONATOR (THE RESISTANCE IS NEGLECTED HERE). 32

FIGURE 1-19: SKETCH OF SIMULATION SETUP OF ELC RESONATORS. 33

FIGURE 1-20: SPLIT RING RESONATOR [98]. A TYPICAL SRR IS COMPOSED OF TWO RINGS WITH GAPS FACING THE OPPOSITE DIRECTIONS AND ITS EQUIVALENT CIRCUIT OF THE RESONATOR CONSTITUTES AN LC RESONATOR. 34

FIGURE 1-21: PHOTOGRAPH OF OBJET EDEN260VS 3D PRINTER AND ITS PRODUCT. 35

FIGURE 2-1: DIAGRAMMATIC SKETCH OF THE FUNCTION OF THE DELOCALIZATION DEVICE. . 41

FIGURE 2-2: SIMULATED ELECTRIC FIELD DISTRIBUTIONS OF (A)-(C) THE OPTICAL TRANSFORMATION OF AN OBJECT INTO ANOTHER OBJECT [28], (D)-(F) THE SHRINKING DEVICE OF AN ARBITRARY OBJECT USING METAMATERIALS [114], AND (G)-(I) THE GHOST ILLUSION DEVICE USING METAMATERIALS IN WAVE DYNAMICS [115]. 43

FIGURE 2-3: PRINCIPLE OF THE TRANSFORMATION: A DETECTOR WILL OBSERVE THE ELECTROMAGNETIC RADIATION COMING FROM ANOTHER DIRECTION WHILE THE REAL

SOURCE IS PLACED IN THE MATERIAL SHELL [117]. 45

FIGURE 2-4: A NEGATIVE REFRACTIVE INDEX MEDIUM BENDS LIGHT TO A NEGATIVE ANGLE WITH THE SURFACE NORMAL [50]. 46

FIGURE 2-5: PRINCIPLE OF THE SINUSOIDAL TRANSFORMATION: AN OBSERVER OUTSIDE THE REGION SHELL THINK THAT THE RADIATION COME FROM ANOTHER DIRECTION AND THAT THE EMITTING ANTENNA IS VERY LARGE. THE TRANSFORMATION USED TO CREATE SUCH DEVICE IS ACHIEVED WITH A SINUSOIDAL TRANSFORMATION. D REPRESENTS THE DISTANCE BETWEEN THE SOURCE AND THE IMAGE, WHILE R IS THE RADIUS OF THE DEVICE [117]. 47

FIGURE 2-6: REPRESENTATION OF THE COMPONENTS OF THE PERMITTIVITY AND PERMEABILITY TENSOR WITH THE SINUSOIDAL TRANSFORMATION WITH $B = 61.2$. THE RADIUS OF THE MATERIAL IS CHOSEN TO BE $R = 4.5$ CM [117]. 50

FIGURE 2-7: THE TRANSFORMATION USED TO CREATE SUCH DEVICE IS ACHIEVED WITH TWO STEPS OF LINEAR TRANSFORMATIONS [129]. 51

FIGURE 2-8: VARIATION OF THE MATERIAL PARAMETER TENSOR COMPONENTS Ψ_{RR} , $\Psi_{\theta\theta}$ AND Ψ_{ZZ} WITH $Q = 4.5$ IN THE LINEAR TRANSFORMATION. THE RADIUS OF THE COMPRESSION ZONE IS CONSIDERED TO BE $R_1 = 2$ CM, WHILE THE RADIUS OF THE WHOLE MATERIAL SHELL R_2 EQUALS TO 5 CM. 53

FIGURE 2-9: ELECTRIC FIELD (E_z) DISTRIBUTION OF A POINT SOURCE PLACED AT THE POSITION $(x, y) = (1.9$ CM, 0 CM) IN THE MATERIAL DEFINED BY THE LINEAR TRANSFORMATION. (A) NO TRANSFORMATION IS APPLIED. (B) TRANSFORMATION WITH $Q = 4.5$. (C) TRANSFORMATION WITH $Q = 6$. (D) TRANSFORMATION WITH $Q = 7.5$ 55

FIGURE 2-10: ELECTRIC FIELD (E_z) DISTRIBUTION IN THE CASE OF A LINEAR TRANSFORMATION WITH $Q = 4.5$ FOR A SOURCE PLACED AT DIFFERENT POSITION. (A) $R' = R_A$. (B) $R' = R_B$. (C) $R' = R_C$ 56

FIGURE 2-11: ELECTRIC FIELD DISTRIBUTION IN THE CASE OF A LINEAR TRANSFORMATION WITH

$Q = 4.5$ FOR A SOURCE PLACED AT DIFFERENT POSITION IN THE COMPRESSION ZONE. (A) $R_A = 0.4$ CM. (B) $R_A = 0.7$ CM. (C) $R_A = 1.5$ CM. (D) $R_A = 2.5$ CM. (E) $R_A = 3.5$ CM. (F) $R_A = 4.5$ CM. 57

FIGURE 2-12: ELECTRIC FIELD (E_z) DISTRIBUTION OF A POINT SOURCE PLACED AT THE POSITION $(x, y) = (1.9 \text{ CM}, 0 \text{ CM})$ IN THE MATERIAL DEFINED BY THE LINEAR TRANSFORMATION, AND THE VALUE $R_1/R_2 = 2/5$. (A) TRANSFORMATION WITH $R_2 = 5$ CM. (B) TRANSFORMATION WITH $R_2 = 7.5$ CM. (C) TRANSFORMATION WITH $R_2 = 10$ CM. 58

FIGURE 2-13: ELECTRIC FIELD (E_z) DISTRIBUTION OF A POINT SOURCE PLACED AT THE POSITION $(x, y) = (1.9 \text{ CM}, 0 \text{ CM})$ IN THE MATERIAL DEFINED BY THE LINEAR TRANSFORMATION, AND THE VALUE $R_2 = 5$ CM. (A) TRANSFORMATION WITH $R_1 = 2$ CM. (B) TRANSFORMATION WITH $R_1 = 3$ CM. (C) TRANSFORMATION WITH $R_1 = 4$ CM. 59

FIGURE 2-14: REPRESENTATION OF THE LINEAR TRANSFORMATION AND THE LAYERED MATERIAL FOR A POSSIBLE PHYSICAL REALIZATION. THE MATERIAL IS DISCRETIZED INTO SEVEN ZONES. 60

FIGURE 2-15: MAGNETIC FIELD DISTRIBUTION FOR TM WAVE POLARIZATION AT 10 GHz. (A) SOURCE IN FREE SPACE. (B) SOURCE IN THE CONTINUOUS TRANSFORMED MATERIAL SHELL. (C) SOURCE IN THE DISCRETIZED MATERIAL SHELL. 61

FIGURE 2-16: DIRECTIVE RADIATION PATTERN AT 5 GHz WHEN A HIGHER Q IS APPLIED. 62

FIGURE 2-17: HIGH LOSS IN THE NEGATIVE INDEX DETERIORATES THE DELOCALIZATION. 63

FIGURE 3-1: SKETCH DIAGRAM OF THE WAVEGUIDE TAPERING FUNCTIONALITY. 65

FIGURE 3-2: TRANSFORMED TAPER (GREEN LINES) BETWEEN TWO WAVEGUIDES (BLACK LINES) WITH DIFFERENT CROSS SECTIONS. (A) LINEAR, (B) PARABOLIC, AND (C) EXPONENTIAL TRANSFORMATION FORMULATIONS [66]. 67

FIGURE 3-3: REPRESENTATION OF COMPONENTS OF THE PERMITTIVITY AND PERMEABILITY TENSORS $\overset{=}{\theta}$ FOR THE THREE TRANSFORMATIONS WITH $A = 10$ CM, $B = 2$ CM AND $L = 5$ CM.

.....	68
FIGURE 3-4: SKETCH DIAGRAM OF FOUR KINDS OF TRANSFORMATION. (A) COSINUSOIDAL, (B) PARABOLIC, (C) LOGARITHMIC AND (D) RECIPROCAL TRANSFORMATION.	70
FIGURE 3-5: REPRESENTATION OF COMPONENTS OF THE PERMITTIVITY AND PERMEABILITY TENSORS Θ FOR THE COSINUSOIDAL TRANSFORMATION.	71
FIGURE 3-6: (A) REAL PART OF ELECTRIC FIELD AND (B) NORM OF ELECTRIC FIELD DISTRIBUTION FOR THE COSINUSOIDAL TRANSFORMATION.	71
FIGURE 3-7: REPRESENTATION OF COMPONENTS OF THE PERMITTIVITY AND PERMEABILITY TENSORS Θ FOR THE PARABOLIC TRANSFORMATION.	72
FIGURE 3-8: (A) REAL PART OF ELECTRIC FIELD AND (B) NORM OF ELECTRIC FIELD DISTRIBUTION FOR THE PARABOLIC TRANSFORMATION.	72
FIGURE 3-9: REPRESENTATION OF COMPONENTS OF THE PERMITTIVITY AND PERMEABILITY TENSORS Θ FOR THE LOGARITHMIC TRANSFORMATION.	73
FIGURE 3-10: (A) REAL PART OF ELECTRIC FIELD AND (B) NORM OF ELECTRIC FIELD DISTRIBUTION FOR THE LOGARITHM TRANSFORMATION.	74
FIGURE 3-11: REPRESENTATION OF COMPONENTS OF THE PERMITTIVITY AND PERMEABILITY TENSORS Θ FOR THE RECIPROCAL TRANSFORMATION.	75
FIGURE 3-12: (A) REAL PART OF ELECTRIC FIELD AND (B) NORM OF ELECTRIC FIELD DISTRIBUTION FOR THE RECIPROCAL TRANSFORMATION.	75
FIGURE 3-13: SKETCH OF TWO TRANSFORMED TAPERS (ORANGE ZONES) AND TWO ADAPTERS (YELLOW ZONES) DEVICE BETWEEN TWO WAVEGUIDES (RED ZONES) WITH DIFFERENT CROSS SECTIONS.	76
FIGURE 3-14: VARIATION OF THE MATERIAL PARAMETER TENSOR COMPONENTS Ψ_{xx} , Ψ_{xy} , Ψ_{yy} AND Ψ_{zz} OF TWO DIFFERENT TAPER PARTS. THE DIMENSION VARIABLES ARE $A = 28.5$ CM, $B_1 = 10.5$ CM, $B_2 = 2.5$ CM, $L_1 = 7.5$ CM, $L_2 = L_4 = 4.5$ CM AND $L_3 = 6$ CM.	78
FIGURE 3-15: (A) REAL PART OF ELECTRIC FIELD AND (B) NORM OF ELECTRIC FIELD	

DISTRIBUTION FOR THE TWO TAPERS AND TWO ADAPTERS SYSTEM. 79

FIGURE 3-16: PARAMETRIC STUDY ON THE STARTING INDEX OF THE FIRST ADAPTER N_1 80

FIGURE 3-17: PARAMETRIC STUDY ON THE STARTING INDEX OF THE SECOND ADAPTER N_2 80

FIGURE 3-18: (A) REAL PART OF ELECTRIC FIELD AND (B) NORM OF ELECTRIC FIELD DISTRIBUTION FOR 2D DISCRETE TWO TAPERS AND TWO ADAPTERS SYSTEM..... 81

FIGURE 3-19: (A) SKETCH OF THE PRINCIPLE OF THE PARAMETER REDUCTION. (B) PERMITTIVITY AND PERMEABILITY DISTRIBUTION IN THE EIGENVECTOR COORDINATE SYSTEM. (C) PERMITTIVITY AND PERMEABILITY DISTRIBUTION AFTER PARAMETER REDUCTION IN THE EIGENVECTOR COORDINATE SYSTEM. THE SOURCE IS SOMETIMES SATURATED AND THE WHITE REGION IN THE FIGURE CORRESPONDS TO PARAMETERS OUTSIDE THE COLOR SCALE. 82

FIGURE 3-20: (A) TYPICAL ELC UNIT CELL STRUCTURE AND THE EXTRACTED PERMITTIVITY AND PERMEABILITY CHARACTERISTICS OF SUCH ELC RESONATOR ($P_x = 5$ MM, $A = 4.5$ MM, $T = 0.2$ MM, $D = 0.5$ MM, $w = 3$ MM). (B) TYPICAL SPLIT RINGS UNIT CELL STRUCTURE AND THE EXTRACTED PERMITTIVITY AND PERMEABILITY CHARACTERISTICS OF SUCH SPLIT RINGS RESONATOR ($P_x = 5$ MM, $B = 4$ MM, $B_1 = 1.8$ MM, $G_1 = 0.4$ MM, $G_2 = 0.3$ MM). 84

FIGURE 3-21: (A) 3D DISCRETE MODEL DESIGN AND (B) THE FABRICATED PROTOTYPE..... 85

FIGURE 3-22: NUMERICALLY CALCULATED REAL PART OF ELECTRIC FIELD DISTRIBUTION OF (A) 2.5 CM SOURCE AND (B) TAPERING SYSTEM. MEASURED ELECTRIC FIELD DISTRIBUTION OF (C) 2.5 CM SOURCE AND (D) TAPERING SYSTEM. THE WAVELENGTH IS 3.75 CM AND THE SIZE LENGTH OF THE UNIT CELLS IS 5 MM. 86

FIGURE 4-1: DIAGRAMMATIC SKETCH OF THE FUNCTION OF THE CONFORMAL LENS AND THE PHOTOGRAPH OF THE FABRICATED PROTOTYPE. 91

FIGURE 4-2: COORDINATE SYSTEMS FOR LENS DESIGNS FOR 2-D DIPOLE ARRAYS ON A CONDUCTING GROUND PLANE [121]. (A) (x, y, z) SYSTEM FOR A LINEAR ARRAY OF

SOURCES. (B) (X', Y', Z') SYSTEM FOR A CYLINDRICAL ARRAY OF SOURCES. (C) REAL PART OF ELECTRIC FIELD OF CYLINDRICAL ARRAY WITH A CARPET-CLOAK LENS. (D) THE SAME ARRAY WITHOUT LENS. 93

FIGURE 4-3: ILLUSTRATION SHOWING THE SPACE MAPPING FROM THE VIRTUAL SPACE TO THE PHYSICAL SPACE..... 95

FIGURE 4-4: PERMITTIVITY DISTRIBUTION (A) ϵ_{xx} , (B) ϵ_{xy} , (C) ϵ_{yy} , (D) ϵ_{zz} 97

FIGURE 4-5: REAL PART OF ELECTRIC FIELD DISTRIBUTION FOR THREE DIFFERENT CONFIGURATION OF THE DIPOLE ARRAY AT 10 GHZ. (A) IDEAL RECTILINEAR ARRAY SHOWING PLANAR WAVEFRONTS AND A DIRECTIVE EMISSION. (B) CONFORMAL ARRAY WITH THE LENS ASSIGNED BY ALL THE FOUR PARAMETERS RESTORING THE EMISSION ALMOST IDENTICAL WITH THE PLANAR ARRAY. (C) CONFORMAL ARRAY WITH THE LENS ASSIGNED BY ISOTROPIC MATERIAL RESTORING THE EMISSION WITH HIGHER SIDE LOBES. 98

FIGURE 4-6: 2D FAR FIELD RADIATION PATTERN AT 10 GHZ FOR THREE DIFFERENT CONFIGURATIONS..... 98

FIGURE 4-7: REAL PART OF ELECTRIC FIELD DISTRIBUTION FOR THREE DIFFERENT CONFIGURATION OF THE DIPOLE ARRAY AT 10 GHZ. (A) IDEAL RECTILINEAR ARRAY SHOWING PLANAR WAVEFRONTS AND A DIRECTIVE EMISSION. (B) CONFORMAL ARRAY SHOWING CYLINDRICAL WAVEFRONTS AND DIFFUSION. (C) CONFORMAL ARRAY IN PRESENCE OF THE CALCULATED LENS (WITH CONTINUOUS PARAMETER PROFILE) RESTORING THE IN-PHASE EMISSIONS. 99

FIGURE 4-8: PERMITTIVITY (ϵ_{zz}) DISTRIBUTION OF DIFFERENT THICKNESS OF THE LENS, (A) $D = 6$ CM. (B) $D = 4$ CM. (C) $D = 2$ CM..... 100

FIGURE 4-9: REAL PART OF ELECTRIC FIELD DISTRIBUTION EMITTED FROM THE CONTINUOUS LENS. (A) $D = 2$ CM. (B) $D = 4$ CM. (C) $D = 6$ CM. ELECTRIC FIELD NORM DISTRIBUTION

List of Figures

EMITTED FROM THE LENS. (D) $D = 2$ CM. (E) $D = 4$ CM. (F) $D = 6$ CM.	101
FIGURE 4-10: PERMITTIVITY DISTRIBUTION OF DIFFERENT RADIUS. (A) $R = 22.5$ CM. (B) $R = 27.5$ CM. (C) $R = 32.5$ CM.	102
FIGURE 4-11: REAL PART OF ELECTRIC FIELD DISTRIBUTION EMITTED FROM THE CONTINUOUS LENS. (A) $R = 22.5$ CM. (B) $R = 27.5$ CM. (C) $D = 32.5$ CM. ELECTRIC FIELD NORM DISTRIBUTION EMITTED FROM THE LENS. (D) $R = 22.5$ CM. (E) $R = 27.5$ CM. (F) $R = 32.5$ CM.	103
FIGURE 4-12: DESIGN OF 2D DISCRETE MODEL COMPOSED OF 92 CUBIC CELLS.	104
FIGURE 4-13 REAL PART OF ELECTRIC FIELD AND ELECTRIC FIELD NORM DISTRIBUTION EMITTED FROM THE LENS.	105
FIGURE 4-14: 2D FAR FIELD RADIATION PATTERN AT 10 GHZ FOR THREE DIFFERENT CONFIGURATIONS.	105
FIGURE 4-15: REAL PART OF ELECTRIC FIELD DISTRIBUTION FOR THREE DIFFERENT CONFIGURATION OF THE DIPOLE ARRAY AT 8 GHZ AND 12 GHZ. (A) AND (B) IDEAL RECTILINEAR ARRAY SHOWING PLANAR WAVEFRONTS AND A DIRECTIVE EMISSION. (C) AND (D) CONFORMAL ARRAY SHOWING CYLINDRICAL WAVEFRONTS AND DEFOCUSING PHENOMENON. (E) AND (F) REAL PART OF ELECTRIC FIELD, (G) AND (H) ELECTRIC FIELD NORM OF CONFORMAL ARRAY IN PRESENCE OF THE CALCULATED LENS (WITH DISCRETE PARAMETER PROFILE) RESTORING THE IN-PHASE EMISSIONS.	106
FIGURE 4-16: 2D FAR FIELD RADIATION PATTERN FOR THREE DIFFERENT CONFIGURATIONS. (A) 8GHZ. (B) 12GHZ.	107
FIGURE 4-17: EFFECTIVE PERMITTIVITY OF THE CELL COMPOSED OF AIR HOLE IN A DIELECTRIC HOST MEDIUM. A PARAMETRIC ANALYSIS IS PERFORMED TO EXTRACT THE EFFECTIVE PERMITTIVITY VALUE ACCORDING TO THE RADIUS R_A OF THE AIR HOLE WITH RESPECT TO A CUBIC CELL OF PERIOD P (P CHANGES ACCORDING TO THE REGIONS OF THE DISCRETE LENS).	108

FIGURE 4-18: DESIGN OF THE 3D DISCRETE LENS COMPOSED OF FIVE REGIONS. 109

FIGURE 4-19: THE CONFORMAL MICROSTRIP PATCH ARRAY. (A) RESONANCE AT 8 GHZ. (B) RESONANCE AT 10 GHZ. (C) RESONANCE AT 12 GHZ. (D) THE RETURN LOSS OF THE THREE MICROSTRIP PATCH ARRAYS..... 110

FIGURE 4-20: 3D SIMULATED RADIATION PATTERNS AT 10 GHZ. (A) PLANAR ARRAY WITH A DIRECTIVITY OF 15.3 DB. (B) CONFORMAL ARRAY WITHOUT LENS WITH A DIRECTIVITY OF 12.3 DB. (C) CONFORMAL ARRAY IN PRESENCE OF LENS WITH A DIRECTIVITY OF 15.7 DB. THE COLOR SCALE IS IN DB. 111

FIGURE 4-21: SIMULATED RADIATION PATTERNS IN THE FOCUSING PLANE (X-Y PLANE). (A) 8 GHZ. (B) 10 GHZ. (C) 12 GHZ. THE CONFORMAL ARRAY PRESENTS A DISTORTED DIAGRAM WITH A LOWER RADIATION LEVEL THAN THE PLANAR ARRAY. THE LENS ABOVE THE CONFORMAL ARRAY ALLOWS RESTORING THE IN-PHASE EMISSION TO CREATE A RADIATION PATTERN WITH A CLEAR DIRECTIVE MAIN BEAM, SIMILAR TO A PLANAR ARRAY. 111

FIGURE 4-22: PHOTOGRAPHY OF THE FABRICATED PROTOTYPE. 112

FIGURE 4-23: MEASURED S11 DISTRIBUTION AT (A) 8 GHZ, (B) 10 GHZ AND (C) 12 GHZ, WHERE THE BLUE CURVES REPRESENT THE S11 OF THE PATCH ARRAY AND THE RED CURVES REPRESENT THE S11 OF THE PATCH AND LENS SYSTEM. 112

FIGURE 4-24: REAL PART OF ELECTRIC FIELD DISTRIBUTION AT 10 GHZ. (A) PLANAR ARRAY. (B) CONFORMAL ARRAY. (C) CONFORMAL ARRAY IN PRESENCE OF LENS. THE DEFOCUSING INTRODUCED BY THE CONFORMAL ARRAY IS CORRECTED THROUGH THE USE OF THE LENS. 113

FIGURE 4-25: MEASURED REAL PART OF ELECTRIC FIELD DISTRIBUTION FOR THE CONFORMAL ARRAY IN PRESENCE OF LENS. (A) AT 8 GHZ. (B) AT 12 GHZ. 114

FIGURE 4-26: MEASURED RADIATION PATTERNS IN THE FOCUSING PLANE (X-Y PLANE). (A) 8 GHZ. (B) 10 GHZ. (C) 12 GHZ. THE CONFORMAL ARRAY PRESENTS A DISTORTED DIAGRAM

WITH A LOWER RADIATION LEVEL THAN THE PLANAR ARRAY. THE LENS ABOVE THE CONFORMAL ARRAY ALLOWS RESTORING THE IN-PHASE EMISSION TO CREATE A RADIATION PATTERN WITH A CLEAR DIRECTIVE MAIN BEAM, SIMILAR TO A PLANAR ARRAY. 115

FIGURE 5-1: DIAGRAMMATIC SKETCH OF THE FUNCTION OF THE BEAM STEERING LENS. 117

FIGURE 5-2: ILLUSTRATION OF CONFORMAL MAPPING FROM THE VIRTUAL SPACE TO THE PHYSICAL SPACE FOR DESIGN 1 OF THE BEAM STEERING LENS. 119

FIGURE 5-3: ANISOTROPIC MATERIAL PARAMETER VALUES FOR DESIGN 1 OF THE BEAM STEERING LENS, (A) ψ_{xx} AND ψ_{zz} , (B) ψ_{xy} , (C) ψ_{yy} 121

FIGURE 5-4: (A) ELECTRIC FIELD AND (B) NORM OF THE ELECTRIC FIELD DISTRIBUTION AT 10 GHZ ILLUSTRATING THE PROPAGATION OF THE RADIATED BEAM OF A LINEAR SOURCE IN AIR-FILLED INITIAL VIRTUAL SPACE. (C) ELECTRIC FIELD AMPLITUDE AND (D) NORM AT 10 GHZ ILLUSTRATING THE PROPAGATION OF THE RADIATED BEAM OF A LINEAR SOURCE THROUGH AND OUT OF THE LENS WHEN $H = 0.5$ M. A 45° BEAM DEFLECTION IS OBSERVED IN THE DESIGN. 122

FIGURE 5-5 MATERIAL PARAMETER VALUES FOR DESIGN 1 OF THE BEAM STEERING LENS. (A) $H = 0.2$ M. (B) $H = 0.8$ M. 123

FIGURE 5-6: REAL PART OF ELECTRIC FIELD AND NORM OF THE ELECTRIC FIELD DISTRIBUTION AT 10 GHZ ILLUSTRATING THE PROPAGATION OF THE RADIATED BEAM OF A LINEAR SOURCE IN AIR-FILLED INITIAL VIRTUAL SPACE [(A), (B), (E) AND (F)] AND OF SOURCE-LENS SYSTEM [(C), (D), (G) AND (H)]. (A) – (D) $H = 0.2$ M. (E) – (H) $H = 0.8$ M. 124

FIGURE 5-7: (A) REAL PART OF ELECTRIC FIELD AMPLITUDE AND (B) NORM AT 10 GHZ ILLUSTRATING THE PROPAGATION OF THE RADIATED BEAM OF A LINEAR SOURCE THROUGH AND OUT OF THE LENS ASSIGNED BY SIMPLIFIED PARAMETERS. 125

FIGURE 5-8: (A) AND (C) REAL PART OF ELECTRIC FIELD AND (B) AND (D) NORM OF THE ELECTRIC FIELD DISTRIBUTION AT 10 GHZ ILLUSTRATING THE PROPAGATION OF THE

List of Figures

RADIATED BEAM OF A LINEAR SOURCE THROUGH AND OUT OF THE LENS ASSIGNED BY SIMPLIFIED PARAMETERS. (A) AND (B) $H = 0.2$ M. (C) AND (D) $H = 0.8$ M. 126

FIGURE 5-9: NORMALIZED ANTENNA RADIATION PATTERNS SHOWING THE BEAM STEERING PERFORMANCES OF THE LENS DESIGNS WITH DIFFERENT HEIGHT H 127

FIGURE 5-10: BEAM SPLITTING DEVICE. (A) REAL PART OF ELECTRIC FIELD DISTRIBUTION AT 10 GHZ ILLUSTRATING THE TRANSMISSION OF FOUR SPLITTED BEAMS. (B) NORM OF THE ELECTRIC FIELD. 127

FIGURE 5-11: PARAMETRIC STUDY PERFORMED ON THE SIZE OF THE LENS. WHEN REDUCING THE DIMENSIONS OF THE LENS, THE BEAM DEFLECTION IS NOT MODIFIED. 128

FIGURE 5-12: FREQUENCY STUDY PERFORMED ON THE LENS. WHEN CHANGING THE OPERATING FREQUENCY, THE BEAM DEFLECTION IS NOT MODIFIED. 129

FIGURE 5-13: ILLUSTRATION OF CONFORMAL MAPPING FROM THE VIRTUAL SPACE TO THE PHYSICAL SPACE FOR DESIGN 2 OF THE BEAM STEERING LENS. 129

FIGURE 5-14: MATERIAL PARAMETER VALUES FOR DESIGN 2 OF THE BEAM STEERING LENS. 130

FIGURE 5-15: (A) REAL PART OF ELECTRIC FIELD AND (B) NORM OF THE ELECTRIC FIELD DISTRIBUTION AT 10 GHZ ILLUSTRATING THE PROPAGATION OF THE RADIATED BEAM OF A LINEAR SOURCE THROUGH AND OUT OF THE LENS DESIGN 2 ASSIGNED BY ANISOTROPIC PARAMETERS. 131

FIGURE 5-16: (A) REAL PART OF ELECTRIC FIELD AND (B) NORM OF THE ELECTRIC FIELD DISTRIBUTION AT 10 GHZ ILLUSTRATING THE PROPAGATION OF THE RADIATED BEAM OF A LINEAR SOURCE THROUGH AND OUT OF THE LENS DESIGN 2 ASSIGNED BY SIMPLIFIED PARAMETERS. 132

FIGURE 5-17: NORMALIZED ANTENNA RADIATION PATTERNS SHOWING THE BEAM STEERING PERFORMANCES OF LENS DESIGN 2 ASSIGNED BY ANISOTROPIC MATERIAL AND ISOTROPIC MATERIAL. 133

FIGURE 5-18: DISCRETIZATION OF THE PROPOSED LENS DESIGN 1. THE PERMITTIVITY (ϵ_{zz})

DISTRIBUTION VARIES FROM 1 TO 4. 134

FIGURE 5-19: (A) REAL PART OF ELECTRIC FIELD AND (B) NORM OF THE ELECTRIC FIELD DISTRIBUTION AT 10 GHZ ILLUSTRATING THE PROPAGATION OF THE RADIATED BEAM OF A LINEAR SOURCE THROUGH AND OUT OF THE DISCRETE LENS ASSIGNED BY SIMPLIFIED PARAMETERS..... 135

FIGURE 5-20: (A) PHOTOGRAPHY OF THE METAMATERIAL BASED FABRICATED PROTOTYPE. (B) TOP VIEW OF ONE METAMATERIAL LAYER COMPOSED OF ELC RESONATORS. 136

FIGURE 5-21: (A) ARRAY OF EQUALLY FED MICROSTRIP PATCH ANTENNA USED AS WAVE LAUNCHER FOR THE LENS AT 10 GHZ. (B) RETURN LOSS OF THE PATCH ARRAY ANTENNA. 137

FIGURE 5-22: (A) TYPICAL ELC UNIT CELL STRUCTURE. (B) RESONANCE OF A PARAMETERIZED UNIT CELL WITH $P_x = P_y = 5$ MM, $B = 4.4$ MM, $C = 2$ MM, $D = 0.2$ MM, AND $G = 1$ MM. (C) THE EXTRACTED PERMITTIVITY AND PERMEABILITY CHARACTERISTICS OF SUCH ELC RESONATOR. (D) INFLUENCE OF DIFFERENT GEOMETRICAL PARAMETERS ON THE EXTRACTED PERMITTIVITY. THE FIXED PARAMETERS FOR ALL SWEEPS ARE: $P_x = P_y = 5$ MM AND $D = 0.2$ MM. WHEN G IS MADE VARIABLE, $B = 4.8$ MM AND $C = 3$ MM, WHEN C IS MADE VARIABLE, $B = 4.8$ MM AND $G = 0.5$ MM AND WHEN B IS MADE VARIABLE, $C = 3$ MM AND $G = 0.3$ MM..... 138

FIGURE 5-23: SIMULATED 3D RADIATION PATTERNS IN LINEAR SCALE. (A) LINEAR ARRAY OF PATCH ELEMENTS AT 10 GHZ. (B) LENS ANTENNA SYSTEM AT 10 GHZ. THE INFLUENCE OF THE LENS IS TWOFOLD; FIRSTLY TO ENHANCE THE DIRECTIVITY OF THE PATCH ARRAY SOURCE AND SECONDLY, TO STEER THE RADIATED BEAM..... 139

FIGURE 5-24: MEASURED S11 DISTRIBUTION AT 10 GHZ, WHERE THE BLUE CURVE REPRESENTS THE S11 OF THE PATCH ARRAY AND THE RED CURVE REPRESENTS THE S11 OF THE PATCH AND METAMATERIAL LENS SYSTEM..... 140

FIGURE 5-25: SIMULATED AND MEASURED FAR-FIELD RADIATION PATTERNS IN THE

DEFLECTION LANE (X-Y PLANE) AT (A) 9.3 GHz, (B) 10 GHz AND (C) 10.7 GHz. 141

FIGURE 5-26: MEASURED REAL PART OF ELECTRIC NEAR-FIELD DISTRIBUTIONS AT (A) 9.3 GHz, (B) 10 GHz AND (C) 10.7 GHz. A DEFLECTION OF THE BEAM FROM THE NORMAL DIRECTION IS OBSERVED. 142

FIGURE 5-27: MEASURED REAL PART OF ELECTRIC NEAR-FIELD DISTRIBUTIONS AT (A) 9 GHz, (B) 11 GHz. NO DEFLECTION IS OBSERVED. 142

FIGURE 5-28: FREQUENCY STUDY ON BEAM STEERING ANGLE VARIATION. 143

FIGURE 5-29: BEAM STEERING LENS REALIZATION. (A) CALCULATED DISCRETE LENS WITH 170 VALUES OF ϵ_{zz} VARYING FROM 1 TO 2.8. (B) PHOTOGRAPHY OF THE FABRICATED ALL-DIELECTRIC LENS PROTOTYPE, WHERE $W = 8.5$ CM, $H = 5$ CM, $T = 2.5$ CM AND $P = 5$ MM. (C) ARRAY OF EQUALLY FED MICROSTRIP PATCH ANTENNAS USED AS WAVE LAUNCHER FOR THE LENS. 144

FIGURE 5-30: RETURN LOSS OF THE ARRAY OF EQUALLY FED MICROSTRIP PATCH ANTENNA USED AS WAVE LAUNCHER FOR THE LENS AT 8 GHz, 10 GHz AND 12 GHz. 145

FIGURE 5-31: (A)-(C) 2D SIMULATED ELECTRIC FIELD DISTRIBUTION AT 8 GHz, 10 GHz AND 12 GHz, WHERE AN ARRAY OF DIPOLES IS USED AS EXCITATION FEED FOR THE LENS WITH DISCRETE PARAMETER PROFILE. A DIRECTIVE BEAM SHOWING PLANAR WAVEFRONTS ORIENTED IN AN OFF-NORMAL DIRECTION IS OBSERVED. (D)-(F) NORM OF THE ELECTRIC FIELD SHOWING VERY GOOD IMPEDANCE MATCHING BETWEEN THE ARRAY-LENS SYSTEM AND FREE SPACE. 146

FIGURE 5-32: SIMULATED 3D RADIATION PATTERNS IN LINEAR SCALE. (A) LINEAR ARRAY OF PATCH ELEMENTS AT 10 GHz. (B) LENS ANTENNA SYSTEM AT 8 GHz. (C) LENS ANTENNA SYSTEM AT 10 GHz. (D) LENS ANTENNA SYSTEM AT 12 GHz. THE INFLUENCE OF THE LENS IS TWOFOLD; FIRSTLY TO ENHANCE THE DIRECTIVITY OF THE PATCH ARRAY SOURCE AND SECONDLY, TO STEER THE RADIATED BEAM. 147

FIGURE 5-33: MEASURED S11 DISTRIBUTION AT (A) 8 GHz, (B) 10 GHz AND (C) 12 GHz,

WHERE THE BLUE CURVES REPRESENT THE S_{11} OF THE PATCH ARRAY AND THE RED CURVES REPRESENT THE S_{11} OF THE PATCH AND LENS SYSTEM..... 148

FIGURE 5-34: MEASURED REAL PART OF ELECTRIC NEAR-FIELD DISTRIBUTION AT (A) 8 GHz, (B) 10 GHz AND (C) 12 GHz, WHERE AN ARRAY OF PATCH RADIATORS IS USED AS EXCITATION FEED FOR THE LENS. A DIRECTIVE BEAM SHOWING PLANAR WAVEFRONTS ORIENTED IN AN OFF-NORMAL DIRECTION IS OBSERVED..... 148

FIGURE 5-35: COMPARISON OF THE NORMALIZED SIMULATED AND MEASURED RADIATION PATTERNS IN THE FOCUSING PLANE (X-Y PLANE). (A) 8 GHz. (B) 10 GHz. (C) 12 GHz... 149

LIST OF ABBREVIATIONS AND ACRONYMS

2D	Two-dimensional
3D	Three-dimensional
TO	Transformation Optics
QCTO	Quasi-conformal Transformation Optics
TE	Transverse Electric
TM	Transverse Magnetic
TEM	Transverse Electromagnetic
MM	Metamaterial
ELC	Electric LC
SRR	Split Ring Resonator
PDE	Partial Differential Equation
FEM	Finite Element Method
HFSS	High Frequency Structural Simulator

GENERAL INTRODUCTION

Transformation optics, as a powerful designing tool based on space transformation, opens up many further ways to control electromagnetic (EM) waves, which can be employed to design applications based on engineered materials like metamaterials and dielectrics. This thesis aims to apply the transformation optics concept for microwave devices designs. Following the previous works done in the framework of Paul-Henri Tichit's thesis in CRIME group at IEF, my thesis works started by continuing with the design concepts based on classical coordinate transformations. Then I focused on the transformation based on Laplace's equation, and two lens antennas are designed by this concept. My thesis is financially supported by the French Ministry of Higher Education and Research. Fabrication and measurements have been made with the help of the AIRBUS Group Innovations.

In the first chapter, the state of art of metamaterials is discussed firstly. The principle of metamaterials is presented, and several antenna applications based on metamaterials are introduced. Then the design concept – transformation optics is introduced. Coordinate transformation as the most well-known methodology is presented firstly. An example of a beam bending is studied helping for a better understanding. Then transformations based on Laplace's equation, including solutions with only Dirichlet boundary conditions, conformal mapping and

quasi-conformal transformation optics, are introduced. The definition of the material properties for these three kinds of transformations are provided by PDE solvers from Comsol Multiphysics numerical simulation software. The numerical calculation softwares, near field and far field experimental setups we use for the thesis are presented. For the realistic validation (simulated and experimental) of the designs, electric and magnetic metamaterial resonators and dielectric materials engineering are also presented.

The manuscript is then decomposed into two parts. Part I consists of two chapters related to two microwave device designs based on coordinate transformations. In Chapter 2, an illusion device which is able to change the radiation pattern and location of a source is presented. Numerical calculations are performed and a discrete model is proposed. Chapter 3 introduces a scheme to taper the electric field from a wide waveguide into an output waveguide that is 11.4 times smaller than the input. We develop the method and show how to reduce the parameters' value and also the number of the parameters needed for the design. A prototype is fabricated by resonant metamaterials and is experimentally validated by near-field measurements.

In Part II, two designs of transformations based on Laplace's equation are presented in two different chapters. Such type of transformations allows realizations from materials with dielectric-only response and thus broadband operations. In Chapter 4, a functional lens which restores in-phase emissions from a non-planar array of radiators over a broad frequency range is proposed. An all-dielectric prototype is realized by 3D printing and validated experimentally by near-field and far-field measurements. The radiation emitted by the conformal lens antenna system is consistent with that of a planar array of radiators. In Chapter 5, the design procedure of a lens antenna, which steers the radiated beam of an array of similarly fed patch antennas, is presented. Two prototypes are fabricated for this device, one by using electric LC metamaterial resonators and the other by all-dielectric 3D printing. The dielectric prototype allows validating the beam steering functionality over a broad frequency range spanning from 8 to 12 GHz.

Finally, we conclude on the two different design concepts and validation technologies.

1 TRANSFORMATION OPTICS: DEFINITION AND RELATED TOOLS

1.1 State of art on metamaterials and metamaterial-based devices

The burgeoning field of metamaterials has attracted a great deal of interest over the past years. With roots in the foundations of optics and electromagnetics, researchers have heavily explored much of the underlying physics in what is now called metamaterials for over a century. Electromagnetic metamaterials which are artificially structured materials composed of periodic arrays of typically resonant and sub-wavelength metallic structures whose electric or magnetic response provide the freedom to design dielectric or magnetic properties that might not exist in conventional materials. The realized dielectric or magnetic properties can be engineered by changing the geometrical parameters of the constituent structure of a metamaterial. The convergence of numerical tools, fabrication technologies and a need for additional flexibility from optical devices across the spectrum has led to the discovery of novel optical phenomena. Metamaterials for the moment has covered a large quantity of topics with a rich history of

scientific exploration. A metamaterial is most acknowledged as a microstructured material that is patterned in order to achieve a desired interaction with some wave-type phenomena, and usually it's either acoustic or electromagnetic. Electromagnetic metamaterials, which are the emphasis of this dissertation, include a number of useful techniques, which have been extensively studied such as frequency selective surfaces, artificial dielectrics and electromagnetic bandgap materials.

The recent surge in interest in metamaterials, however, has been fueled by experimental and theoretical demonstrations of physical phenomena—resulting from this patterning—which mimic materials that are not available in nature. Figure 1-1(a) shows the most well-known metamaterial implementation-cloaking at microwave frequencies [1]. And Figure 1-1(b) shows a model of 3D metamaterial presented by the U.S. Department of Energy's Ames Laboratory [2].

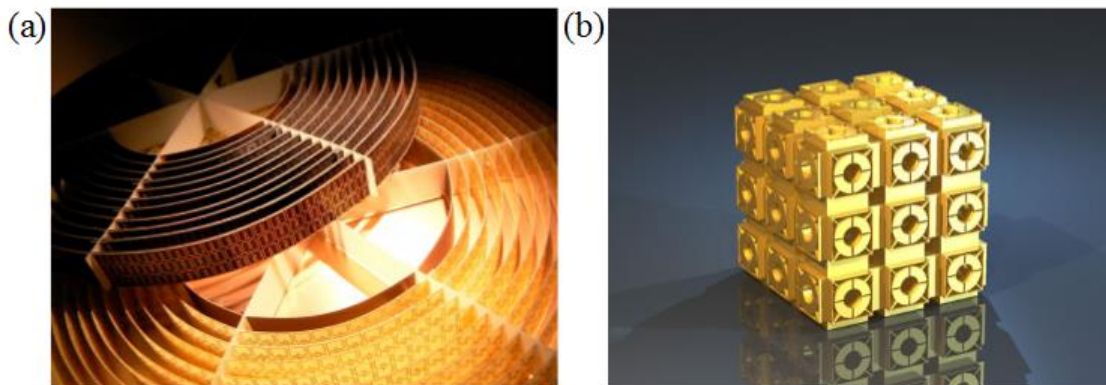


Figure 1-1: (a) metamaterial implementation-cloaking device [1]. (b) A model of 3D metamaterial [2].

The principle of metamaterials relies on sub-wavelength structures engineering. By this engineering the metamaterial has the functionality as electric and magnetic particles that behave in the same fashion as atoms and molecules of continuous media. It is found out that for metamaterials with certain particle structures, such as resonant objects [3, 4] or cut wires [5, 6], the effective ϵ and μ of the equivalent medium can achieve both positive and negative values across certain frequency bands. Although the concept of negative ϵ has been accepted and

understood for a long time, negative permeability is a less familiar phenomenon typically not found generally in natural materials, except for ferrite materials.

In naturally occurring materials with positive index of refraction, solutions of the Maxwell Equations yield propagating electromagnetic waves in which the phase and energy velocities are in the same direction. To explain why this is true, imagine a uniform plane wave propagating in an unbounded medium so that no boundary conditions are applied to the wave. Taking the direction of propagation of this plane wave with angular frequency ω to be in the $+z$ direction, we can express the electric and magnetic fields as

$$E(z, t) = E_0 e^{j(\omega t - kz)} \hat{x} \quad (1-1)$$

$$H(z, t) = \frac{E_0}{\eta} e^{j(\omega t - kz)} \hat{y} \quad (1-2)$$

where the spatial wave number $k = k_r + jk_i$ is in general complex, with k_i contributing to attenuation along the direction of propagation. The power flow in such a medium is given by the time averaged Poynting vector

$$S = \frac{1}{2} \text{Re}(E \times H^*) = \frac{1}{2} \text{Re}\left(\frac{k_z E_x^2}{\omega \mu}\right) \hat{z} \quad (1-3)$$

As presented in Figure 1-2, in most natural materials, ϵ and μ are positive, and this forces k_z to assume a continuum of real values. Thus, \mathbf{S} maintains a non-zero value, and energy is free to propagate in the $+z$ direction.

Not classically considered is the case when both $\mu_r < 0$ and $\epsilon_r < 0$. When both ϵ and μ are simultaneously negative, the material will have a refractive index $n < 0$. The wave number

$k_z = \frac{\omega}{c} \sqrt{\mu_r \epsilon_r}$ becomes negative, while the power flow \mathbf{S} flows in the $+z$ direction. Thus, the

power flow becomes anti-parallel with the phase velocity, and because of this property, negative index materials are referred to as “left-handed” materials since a simultaneously negative ϵ and μ makes the vector triplet $[\mathbf{k}, \mathbf{E}, \mathbf{H}]$ left handed. ‘Left-Handed’ materials are so-called because

the wave vector is antiparallel to the Poynting vector—seemingly violating the right-hand rule.

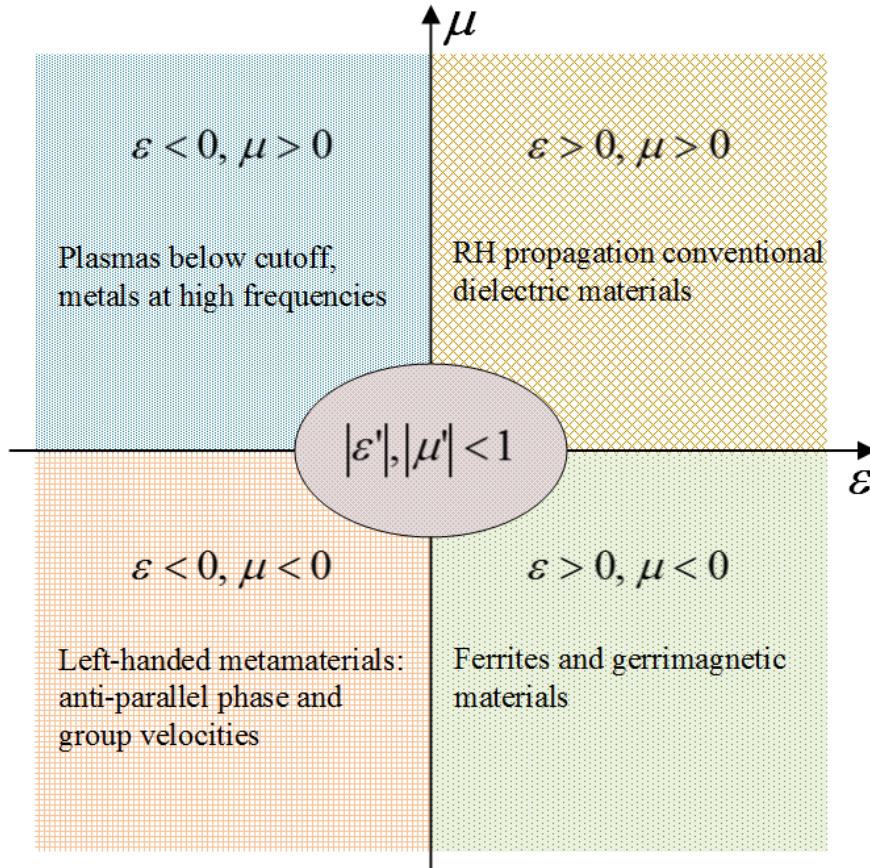


Figure 1-2: Effective medium parameter diagram showing the four quadrants of material parameters ϵ and μ .

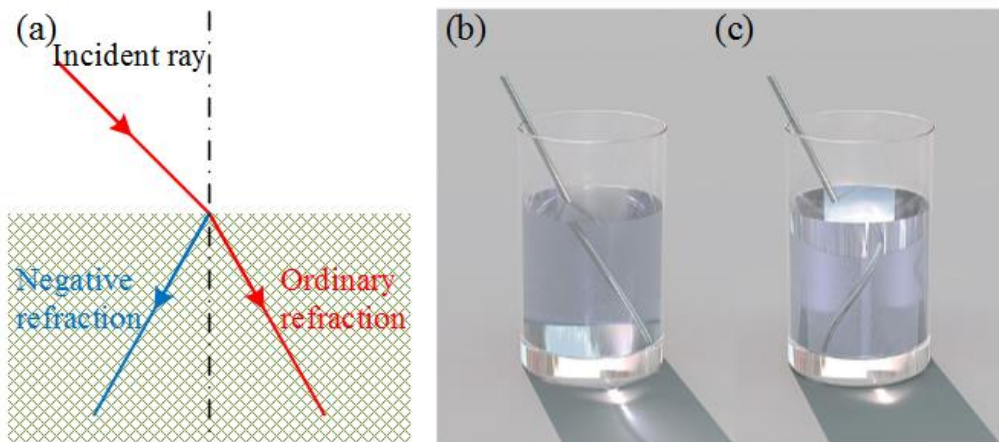


Figure 1-3: (left) Comparison of refraction of an incident ray propagating into a positive and negative index material (right) [7].

Figure 1-3 shows the difference when an incident ray propagates into a positive index and a negative index. In a positive index medium, waves with a larger wave-vector than in the free space are evanescent: rather than oscillating in free space, they decay exponentially. In a negative index medium, however, the amplitudes of these evanescent waves grow exponentially—allowing for the transmission of information about features on a much finer scale than is available using conventional optical elements.

A further significant advantage of the manual patterning of a material is that it can be made to be inhomogeneous—the properties of the material can change as a function of position. This allows for the curving of light ray trajectories throughout the bulk of a material and can lead to a significantly increased phase space in which to design optical devices.

Lots of applications based on metamaterials have been proposed since J. Pendry introduced Split Ring Resonators (SRR) and wire structures to realize respectively negative permeability and permittivity medium (ref). Then they were used to create the first negative index material [8]. In my thesis, metamaterials are implemented in microwave device applications, designed by transformation optics. So here we present several metamaterial applications that we consider interesting for the thesis and for the antenna domain.

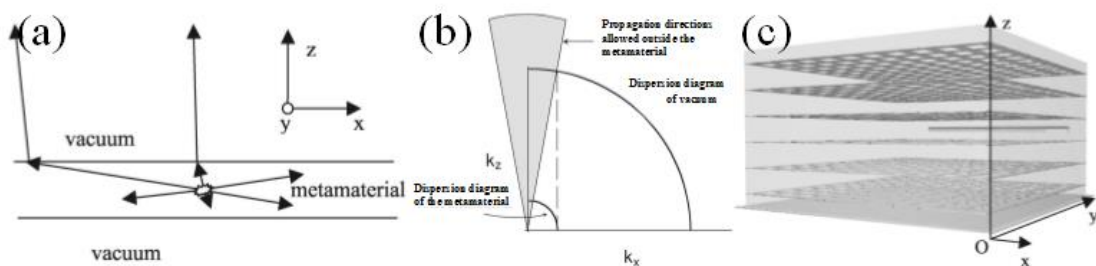


Figure 1-4: (a) geometrical interpretation of the emission of a source inside a slab of a low index metamaterial (not negative). (b) Construction in the reciprocal space. (c) Schematic representation of the structure [9].

In Figure 1-4, a low index metamaterial for directive emission is introduced [9]. This material has an index lower than 1. It's shown that the specific properties of this metallic composite

material can strongly modify the emission of an embedded source. In this application, under proper conditions the energy radiated by a source embedded in a slab of metamaterial will be concentrated in a narrow cone in the surrounding media.

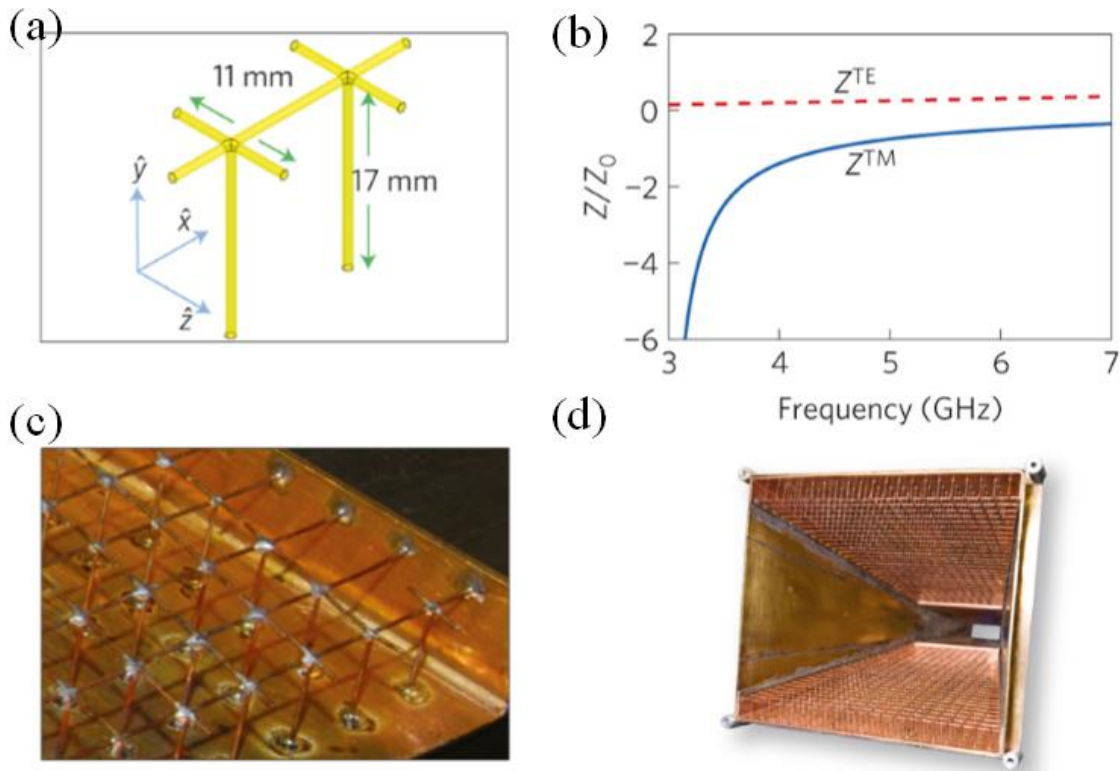


Figure 1-5: Metamaterial liner geometry, properties and incorporation into a rectangular horn antenna [10].

In Figure 1-5, D. Werner together with colleagues from the Pennsylvania State University and Lockheed Martin Commercial Space Systems have succeeded enabling specific device performance over usable bandwidths by employing dispersion engineering of metamaterial properties [10]. In particular, they have designed metamaterials that considerably improve performances of conventional horn antennas over greater than an octave bandwidth with negligible loss and advance the state of the art in the process.

A new type of compact flexible anisotropic metamaterial (MM) coating is proposed in Figure

1-6, which greatly enhances the impedance bandwidth of a quarter-wave monopole to over an octave [11]. The MM coating has a high effective permittivity for the tensor component oriented along the direction of the monopole. By properly choosing the radius and tensor parameter of the MM coating, another resonance at a higher frequency can be efficiently excited without affecting the fundamental mode of the monopole. Additionally, the similar current distributions on the monopole at both resonances make stable radiation patterns possible over the entire band.

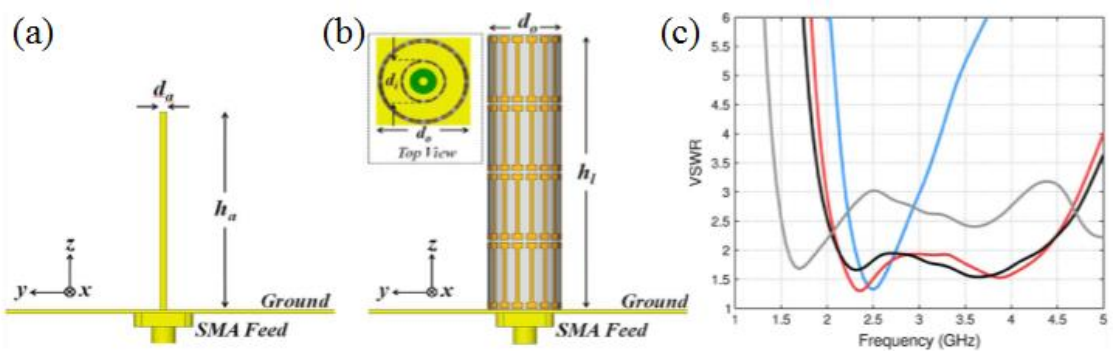


Figure 1-6: Configuration of (a) the quarter-wave monopole antenna and (b) the same monopole with ultrathin flexible anisotropic MM coating [11], and (c) the simulated VSWR of the models.

T. Driscoll and colleagues have presented a radial gradient-index lens with an index of refraction ranging from -2.67 (edge) to -0.97 (center), shown in Figure 1-6. They showed that the lens can produce field intensities at the focus that are greater than that of the incident plane wave.

A biplanar gradient lens with negative gradient is constructed which can produce field intensities at the focus that are greater than that of the incident plane wave. by T. Driscoll *et al.* [12] as shown in Figure 1-7.

In the CRIME group at IEF, other studies related to metamaterial surfaces for Fabry-Perot type directive antennas and lenses are conducted [13-18].

These applications are either based on the antenna impedance matching or the dispersion of the MMs. In my thesis, we focus on the application of metamaterials for transformation optics

designs. The concept of transformation optics (TO) will be discussed in the next section.

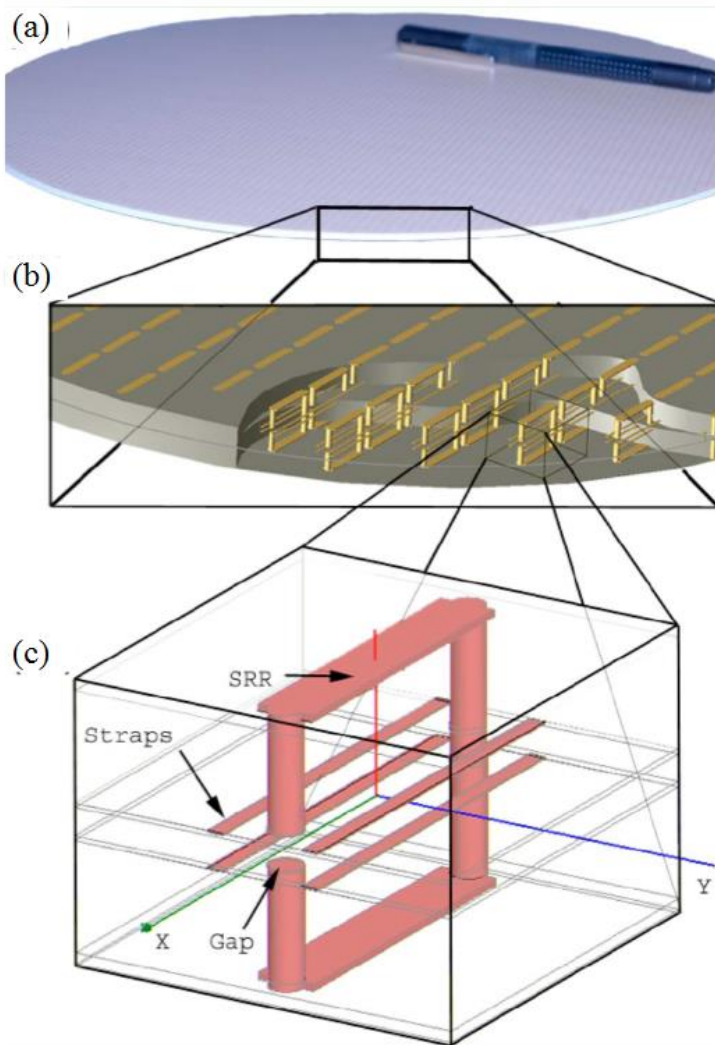


Figure 1-7: Diagrams showing (a) actual picture of a lens disk, (b) blow-up illustrating unit-cell array, (c) further blown up single unit cell with SRR and wire elements [12].

1.2 Transformation optics

Transformation optics (TO) is one of the most powerful conceptual techniques for the design of devices which leverage complex materials. TO enables to alter the field distribution by choosing material parameters which cause light to ‘behave’ as if it was in a transformed set of coordinates [18, 19] and novel applications have been explored rapidly and quantitatively, including:

- **optical cloaking [1][20-26]**
- **optical illusion devices [27-31]**
- **optical lenses [32-37]**
- **optical black holes [38, 39]**
- **optical wormholes [40, 41]**
- **transformation plasmonics [42]**
- **electromagnetic wave concentrators [43-45]**
- **rotators [46, 47]**
- **perfect imaging devices [48-52]**
- **super-scatters and super-absorbers [53-58]**
- **beam shifters and splitters [59]**
- **polarization controllers [60, 61]**
- **electromagnetic cavities [62-64]**
- **special waveguides [65-69]**
- **light source transforming devices [70-74]**
- **carpet cloaking [75-79], etc..**

In order to provide the reader with the background information necessary to understand the rest of the dissertation, this section would be a full introduction to different kinds of transformations. Transformation optics relies on what is termed the ‘form-invariance’ of Maxwell’s equations [80], which means that transformation optics provide a method to modify the field by changing the variables in the Maxwell’s equations. This chapter begins with a derivation of this property beginning with the familiar form of Maxwell’s equations. And then it is followed by a description of the consistent manner in which transformation optical calculations may be performed for arbitrary geometries. Transformations based on Laplace’s equations will also be introduced. Some applications will act as examples to help understanding the principles.

1.2.1 Coordinate transformations

In this section, the transformation from Cartesian coordinates to other orthogonal coordinate systems is introduced by the statement of the media equations. Several applications of such coordinate transformations will also be introduced later. We start from the Maxwell's equations to explain the principles and then focus to write out the material parameters in a very explicit way for future studies by means of numerical finite element methods. Coordinate transformation is achieved by redefining the constituent material parameters. The Maxwell's equations are written such that the differential form of the equations is invariant under coordinate transforms:

$$\begin{aligned}\nabla \times H &= \varepsilon \frac{\partial E}{\partial t} + J, \\ \nabla \times E &= -\mu \frac{\partial H}{\partial t}, \\ \nabla \cdot \varepsilon E &= \rho, \\ \nabla \cdot \mu H &= 0.\end{aligned}\tag{1-4}$$

These equations are rewritten in covariant notation in Cartesian coordinates. The invariance form is completely a property of the differential equations. The covariant notation is used for compactness.

$$\begin{aligned}\varepsilon^{ijk} \partial_j H_k &= \varepsilon^{ij} \frac{\partial E_j}{\partial t} + J^i \\ \varepsilon^{ijk} \partial_j E_k &= -\mu^{ij} \frac{\partial H_j}{\partial t} \\ \partial_i \varepsilon^{ij} E_j &= \rho, \\ \partial_i \mu^{ij} H_j &= 0.\end{aligned}\tag{1-5}$$

i, j and k are the indices that take value from 1 to 3. We note that a particular coordinate is identified by x^i , for example (x, y, z) . And ∂_i is short for $\partial / \partial x^i$. The completely anti-symmetric Levi-Cevita tensor is expressed by ε^{ijk} .

We consider that the properties of these equations are under a coordinate transform between x and x^i , which is the transformed coordinate (x', y', z') . E and H are transformed as

$$\begin{aligned} E_{i'} &= A_i^{i'} E_i \\ E_i &= A_i^{i'} E_{i'} \end{aligned} \quad (1-6)$$

where $A_i^{i'}$ is the Jacobian matrix and is given by

$$A_i^{i'} = \frac{\partial x^{i'}}{\partial x^i} \quad (1-7)$$

So after several steps of derivations and simplifications, the transformed equations can be written as:

$$\begin{aligned} \varepsilon^{i'j'k'} \partial_{j'} H_{k'} &= \frac{A_i^{i'} A_j^{j'}}{|A|} \varepsilon^{ij} \frac{\partial E_{j'}}{\partial t} + \frac{A_i^{i'}}{|A|} J^i \\ \varepsilon^{i'j'k'} \partial_{j'} E_{k'} &= - \frac{A_i^{i'} A_j^{j'}}{|A|} \mu^{ij} \frac{\partial H_{j'}}{\partial t} \\ \partial_{i'} \frac{A_i^{i'} A_j^{j'}}{|A|} \varepsilon^{ij} E_{j'} &= \frac{\rho}{|A|}, \\ \partial_{i'} \frac{A_i^{i'} A_j^{j'}}{|A|} \mu^{ij} H_{j'} &= 0. \end{aligned} \quad (1-8)$$

When we compare the Maxwell's equation before and after a coordinate transformation, we can find that there exist some transformation rules of the material parameters, current and charge that will make the transformed equations to be in the identical form of the equations before transformation. With a proper choice of materials and sources, one can arrive at an identical set of equations to those which are found under an arbitrary coordinate transformation. In another word, if we choose a certain material whose properties are as below:

$$\begin{aligned} \varepsilon^{i'j'} &= \frac{A_i^{i'} A_j^{j'}}{|A|} \varepsilon^{ij} \\ \mu^{i'j'} &= \frac{A_i^{i'} A_j^{j'}}{|A|} \mu^{ij} \\ J^{i'} &= \frac{A_i^{i'}}{|A|} J^i \\ \rho' &= \frac{\rho}{|A|} \end{aligned} \quad (1-9)$$

Then the transformed Maxwell's equations can be rewritten as

$$\begin{aligned}
 \varepsilon^{i'j'k'} \partial_{j'} H_{k'} &= \varepsilon^{i'j'} \frac{\partial E_{j'}}{\partial t} + J^{i'} & (1-10) \\
 \varepsilon^{i'j'k'} \partial_{j'} E_{k'} &= -\mu^{i'j'} \frac{\partial H_{j'}}{\partial t} \\
 \partial_{i'} \varepsilon^{i'j'} E_{j'} &= \rho', \\
 \partial_{i'} \mu^{i'j'} H_{j'} &= 0.
 \end{aligned}$$

Now we continue with the transformation between two Cartesian coordinate systems.

$$\begin{aligned}
 \varepsilon_c^{i'j'} &= A_i^{i'} A_j^{j'} \varepsilon_c^{ij} / \det(A_i^{i'}) & (1-11) \\
 \mu_c^{i'j'} &= A_i^{i'} A_j^{j'} \mu_c^{ij} / \det(A_i^{i'})
 \end{aligned}$$

where ε_c^{ij} and μ_c^{ij} are the components of the permittivity and permeability tensors in the original Cartesian coordinate. $\varepsilon_c^{i'j'}$ and $\mu_c^{i'j'}$ are the components of the permittivity and permeability tensors of the transformed media in the new Cartesian coordinate. The subscript C stands for Cartesian coordinate system. And the subscript O in the following equations stands for other orthogonal coordinate systems.

For the transformation between any two kinds of orthogonal coordinate systems, such as between cylindrical coordinate system and spherical coordinate system and etc., we define the original coordinate system as (u, v, w) and the transformed coordinate system as (u', v', w') , to distinguish with the typical Cartesian coordinate expression (x, y, z) . The mapping $(u, v, w) \Leftrightarrow (u', v', w')$ can be written as

$$\begin{cases} u' = u'(u, v, w) \\ v' = v'(u, v, w) \\ w' = w'(u, v, w) \end{cases} \quad (1-12)$$

The transformation media equations in the orthogonal coordinate can be expressed as

$$\begin{aligned}
 \varepsilon_0^{k'l'} &= T_k^{k'} T_l^{l'} \varepsilon_0^{kl} / \det(T_k^{k'}) & (1-13) \\
 \mu_0^{k'l'} &= T_k^{k'} T_l^{l'} \mu_0^{kl} / \det(T_k^{k'})
 \end{aligned}$$

with $T_k^{k'} = (h_{u^{k'}} \partial u^{k'}) / (h_{u^k} \partial u^k)$. h_{u^k} is defined in the line element expression in the orthogonal coordinate in the original space. In Cartesian coordinate, the line element is the original space is

$ds^2 = dx^2 + dy^2 + dz^2$. While in the orthogonal coordinate in the original space, the line element is

$$\begin{aligned} ds^2 &= h_u(u, v, w)^2 du^2 + h_v(u, v, w)^2 dv^2 + h_w(u, v, w)^2 dw^2 \\ &= h_u^2 du^2 + h_v^2 dv^2 + h_w^2 dw^2 \end{aligned} \quad (1-14)$$

For different coordinate systems, of course, h_u , h_v , and h_w have different expressions. For Cartesian coordinate (x, y, z) , cylindrical coordinate (ρ, φ, z) and spherical coordinate (r, θ, ϕ) these expressions are presented in Table 1-I.

Table 1-I: $h_u, h_v,$ and h_w expressions in different coordinate systems.

Cartesian coordinate	Cylindrical coordinate	Spherical coordinate
$ds^2 = dx^2 + dy^2 + dz^2$	$ds^2 = d\rho^2 + \rho^2 d\varphi^2 + dz^2$	$ds^2 = dr^2 + r^2 d\theta^2 + r^2 \sin^2 \theta d\phi^2$
$\begin{cases} h_u = 1 \\ h_v = 1 \\ h_w = 1 \end{cases}$	$\begin{cases} h_u = 1 \\ h_v = \rho \\ h_w = 1 \end{cases}$	$\begin{cases} h_u = 1 \\ h_v = r \\ h_w = r \sin \theta \end{cases}$

So the Jacobian transformation matrix in the orthogonal coordinate is

$$T = \begin{bmatrix} \frac{h_u}{h_u} \frac{\partial u'}{\partial u} & \frac{h_u}{h_v} \frac{\partial u'}{\partial v} & \frac{h_u}{h_w} \frac{\partial u'}{\partial w} \\ \frac{h_v}{h_u} \frac{\partial v'}{\partial u} & \frac{h_v}{h_v} \frac{\partial v'}{\partial v} & \frac{h_v}{h_w} \frac{\partial v'}{\partial w} \\ \frac{h_w}{h_u} \frac{\partial w'}{\partial u} & \frac{h_w}{h_v} \frac{\partial w'}{\partial v} & \frac{h_w}{h_w} \frac{\partial w'}{\partial w} \end{bmatrix} \quad (1-15)$$

For example, if the transformation takes place between two cylindrical coordinate systems $(\rho, \varphi, z) \Leftrightarrow (\rho', \varphi', z')$, the Jacobian transformation matrix will take the form:

$$T = \begin{bmatrix} \frac{\partial \rho'}{\partial \rho} & \frac{1}{\rho} \frac{\partial \rho'}{\partial \varphi} & \frac{\partial \rho'}{\partial z} \\ \rho' \frac{\partial \varphi'}{\partial \rho} & \frac{\rho'}{\rho} \frac{\partial \varphi'}{\partial \varphi} & \rho' \frac{\partial \varphi'}{\partial z} \\ \frac{\partial z'}{\partial \rho} & \frac{1}{\rho} \frac{\partial z'}{\partial \varphi} & \frac{\partial z'}{\partial z} \end{bmatrix} \quad (1-16)$$

Normally, the parameters we obtain above will be assigned to the transformed media as

properties and simulated by the numerical finite element methods, for instance the COMSOL Multiphysics finite element-based electromagnetics solver. So the required parameters should be expressed in the form of (x', y', z') .

$$\begin{aligned}\epsilon_c^{i'j'} &= R\epsilon_0^{k'l}R^T / \det(R) \\ \mu_c^{i'j'} &= R\mu_0^{k'l}R^T / \det(R)\end{aligned}\tag{1-17}$$

where the rotation matrix R is given as

$$R = \begin{bmatrix} \frac{1}{h_{u'}} \frac{\partial x'}{\partial u'} & \frac{1}{h_{v'}} \frac{\partial x'}{\partial v'} & \frac{1}{h_{w'}} \frac{\partial x'}{\partial w'} \\ \frac{1}{h_{u'}} \frac{\partial y'}{\partial u'} & \frac{1}{h_{v'}} \frac{\partial y'}{\partial v'} & \frac{1}{h_{w'}} \frac{\partial y'}{\partial w'} \\ \frac{1}{h_{u'}} \frac{\partial z'}{\partial u'} & \frac{1}{h_{v'}} \frac{\partial z'}{\partial v'} & \frac{1}{h_{w'}} \frac{\partial z'}{\partial w'} \end{bmatrix}\tag{1-18}$$

In cylindrical and spherical coordinate systems, the expressions of matrix R are presented in Table 1-II.

Table 1-II: Expressions of rotation matrix R in different coordinate systems.

Cylindrical coordinate	Spherical coordinate
$R = \begin{bmatrix} \cos \phi' & -\sin \phi' & 0 \\ \sin \phi' & \cos \phi' & 0 \\ 0 & 0 & 1 \end{bmatrix}$	$R = \begin{bmatrix} \sin \theta' \cos \phi' & -\cos \theta' \cos \phi' & -\sin \phi' \\ \sin \theta' \sin \phi' & -\cos \theta' \sin \phi' & \cos \phi' \\ \cos \theta' & \sin \theta' & 0 \end{bmatrix}$

Coordinate transformation has been applied to design plenty of devices. In my thesis, there are two projects based on coordinate transformation that will be presented. In the following, we take an example for discovering how this concept works in designs. In 2008, D. R. Smith proposed a device which can bend the beam by certain angle [81]. This beam bending device is based on coordinate transformation. The sketch of the principle for the device is presented in Figure 1-8. The formulation of this transformation is also presented in the figure. The variable k is a scale factor and α is the angle of the bend.

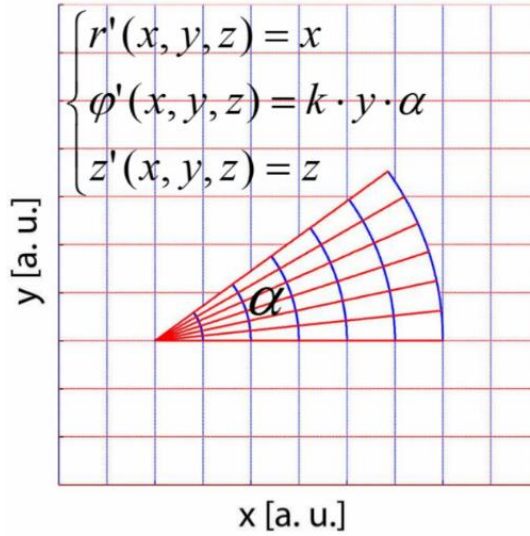


Figure 1-8: Illustration of the embedded coordinate transformation for $\alpha = \pi/5$ [81].

As we can see from the formulation, the transformation is between an original Cartesian coordinate and a transformed cylindrical coordinate. To be more in details, the x -axis is transformed to the radial distance r' , and the y -axis is transformed to a scaled azimuth axis. Following the recipe we have discussed above, one obtains the permittivity and permeability tensors of the beam bend expressed in cylindrical coordinate system

$$\varepsilon^{i'j'} = \mu^{i'j'} = \begin{bmatrix} \gamma / r & & \\ & r / \gamma & \\ & & \gamma / r \end{bmatrix} \quad (1-19)$$

with $\gamma = 1 / (k \cdot \alpha)$. Note that r' was substituted by r for possible simulations in Comsol.

The polarization of the electric field was chosen to lie in the z -direction normal to the $(x-y)$ plane of the wave propagation. The frequency considered in the simulations was 8.5 GHz. However it should be noted that the transformation-optical approach is valid for any arbitrary frequency. The dark grey lines represent the direction of the power flow. Figure 1-9 shows the spatial distribution of the electric field (color map) in the example of a $\pi/2$ -bend. In Figure 1-9(a) the material properties were calculated for $\gamma = 0.02$ whereas in Figure 1-9(b) the tensors were obtained for $\gamma = 0.3$. As can be seen from Figure 1-9, each material realization bends the incoming light by $\alpha = \pi/2$.

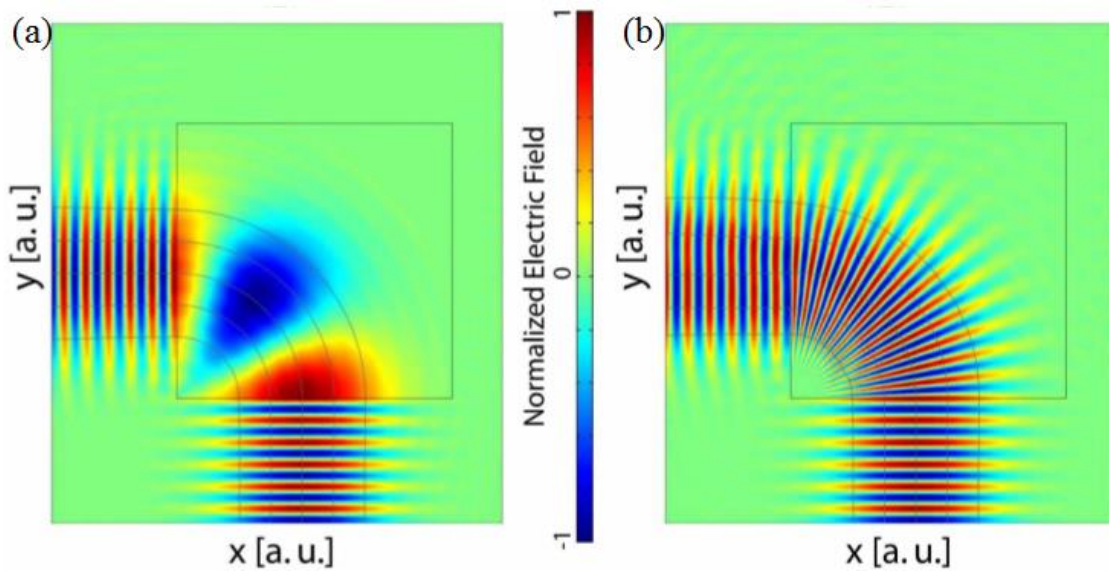


Figure 1-9: Distribution of the electric field component normal to the plane of propagation for $\alpha = \pi/2$ with (a) $\gamma = 0.02$ and (b) $\gamma = 0.3$ [82].

1.2.2 Space transformation based on Laplace's equation

The specific coordinate transformation is used in turn to determine the distribution of constitutive parameters which is discussed in the last section. These determined parameters are assigned to some TO device to obtain functional physical field distributions. However, the field distribution within the volume of the device is of no consequence in most instances: only the fields on the boundaries of the device are relevant, since the function of most optical devices is to relate a set of output fields on one port or aperture to a set of input fields on another port or aperture. From the TO point of view, device functionality is determined by the properties of the coordinate transformation at the boundaries of the domain. Since there is an infinite number of transformations that have identical behaviour on the boundary, there is considerable freedom to find a transformation that is close to optimal in the sense that it maximizes a desired quantity, such as isotropy.

1.2.2.1 Transformations based on Laplace's equation with Dirichlet boundary conditions

As we have mentioned in Eq. 1-11, the permittivity ε' and permeability μ' in the transformed space can be expressed as $\varepsilon' = \mu' = \eta' = A\eta A^T / \det(A)$. A is the Jacobian transformation tensor, which characterizes the geometrical variations between the original space Ω and the transformed space Ω' . The determination of the matrix A is the crucial point for designing transformation mediums. A can be obtained from the mapping point to point defined by coordinated transformation formulations. A can also be obtained from the mapping between two domains by specifying proper boundary conditions.

Here we take an arbitrary shaped cloak as example to introduce the transformation based on Laplace's equation with only Dirichlet boundary conditions [82, 83] [101].

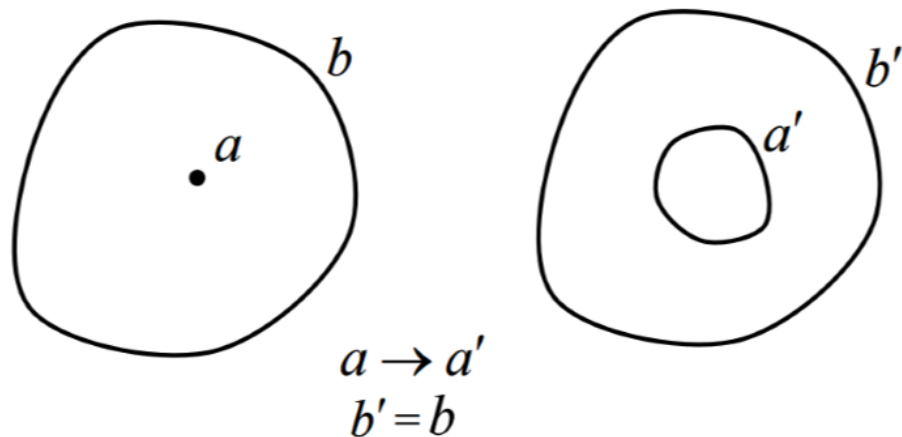


Figure 1-10: The scheme of constructing an arbitrary cloak [82].

Figure 1-10 shows the scheme for constructing an arbitrary shaped cloak. Suppose an original region enclosed by the outer boundary represented by b , and inside of this region, we define a point denoted by a . An arbitrary cloak can be constructed by enlarging the point a to the inner boundary a' , while keeping the outer boundary of the region fixed ($b = b'$). This condition can

be expressed by $U'(a) = a'$ and $U'(b) = b'$, where the operator is the new coordinates for a given point during the transformation. Now the problem is how to determine the deformation field $\partial U' / \partial x$ within the cloak layer enclosed by the inner and outer boundaries and for a specific transformation. The commonly used operator U' for designing a cloak is a linear transformation [21, 85-102]. For example, the radial displacement of a spherical cloak is assumed to be a linear relation $r' = (b'-a')r/b'+a'$. However, for an arbitrary cloak, it is very difficult to express analytically the boundaries a' and b' , the calculation of deformation field is usually very complicated.

To ensure a cloak without reflections, the internal deformation field of the cloak layer must be continuous and wave impedance must be constant along the structure. The deformation tensor is calculated by the partial derivative of displacement with respect to the original coordinate, so the displacement fields must be smooth enough. It is known that the Laplace's equations with Dirichlet boundary conditions will always give rise to harmonic solutions [91]. This suggests that the displacement field inside of the cloak layer can be calculated by solving Laplace's equations $\Delta U' = 0$ with the boundary conditions $U'(a) = a'$ and $U'(b) = b'$. In order to eliminate the singular solution of the Laplace's equations, we can use the inverse form of the Laplace's equations as

$$\left(\frac{\partial^2}{\partial x_1'^2} + \frac{\partial^2}{\partial x_2'^2} + \frac{\partial^2}{\partial x_3'^2} \right) U_i = 0, \quad i = 1,2,3 \quad (1-20)$$

where U_i denotes the original coordinates in the original space.

After solving this equation by a PDE solver provided by the commercial software such as COMSOL Multiphysics, we are able to obtain $\partial x_j / \partial x'_i$, which means we can obtain the matrix A^{-1} . Then A can be calculated and so does the permittivity and permeability.

A two-dimensional arbitrary cloak is then proposed and verified numerically as presented in Figure 1-11. This concept of transformation provides generally complex parameters. Often these parameters are too high to achieve. But from the field distribution, the cloaking device performs

a good functionality.

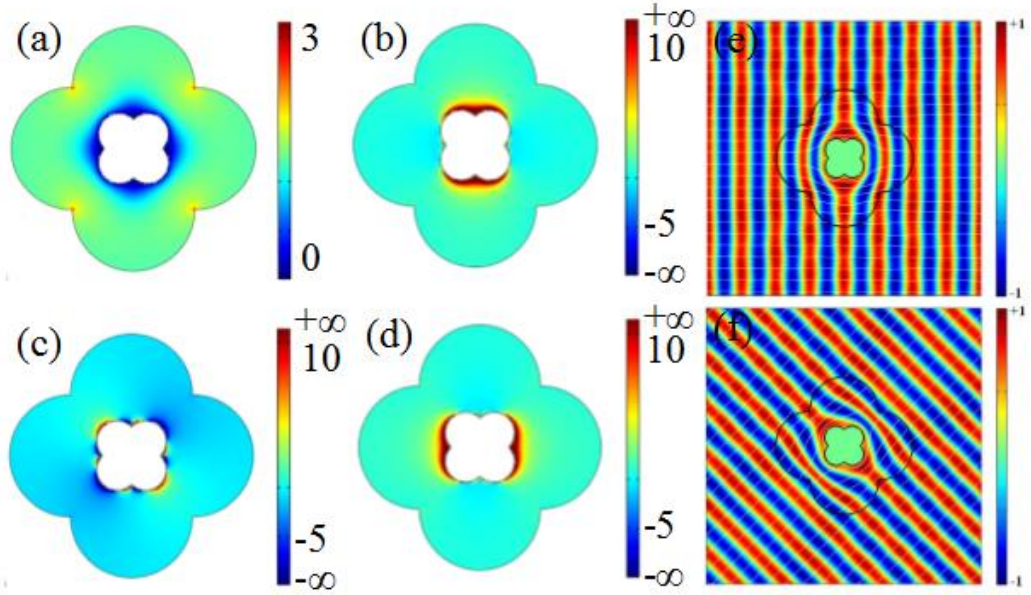


Figure 1-11: Material parameters (a) ϵ_{zz} , (b) μ_{kx} , (c) μ_{ky} and (d) μ_{by} . Electric field distribution for incident wave (e) horizontally (f) 45° [82].

1.2.2.2 Conformal mapping

An invertible mapping is called conformal mapping if it preserves angles. We start discussing the conformal mapping by a review of the 2D mapping between (x, y) and (x', y') systems of the form $X' = [x'(x, y), y'(x, y)]$. The tensors can be written as:

$$\begin{bmatrix} x'^2_x + x'^2_y & x'_x y'_x + x'_y y'_y & 0 \\ x'_x y'_x + x'_y y'_y & y'^2_x + y'^2_y & 0 \\ 0 & 0 & 1 \end{bmatrix} \quad (1-21)$$

Ideally, the constitutive tensors have only diagonal components, this implies that

$x'_x y'_x = -x'_y y'_y$. Since $\epsilon_{xx} \neq \epsilon_{yy}$, we can find that

$$\begin{aligned} x'_x &= y'_y \\ x'_y &= -y'_x \end{aligned} \quad (1-22)$$

And these equations are the well-known Cauchy-Riemann equations that define conformal maps.

Now we can find out that the coordinates X' satisfy the vector form of Laplace's equation

$$\nabla^2_{X'} = 0 \quad (1-23)$$

This leads to the simple material parameters, permittivity and permeability that are given below:

$$\varepsilon = \mu = \begin{bmatrix} 1 & 0 & 0 \\ 0 & 1 & 0 \\ 0 & 0 & |A|^{-1} \end{bmatrix} \quad (1-24)$$

TO media that are of the form of Equation I-24 are often described as “isotropic” and “dielectric-only”. The full transformation could be obtained with an isotropic dielectric if the electric field is polarized to be parallel to the z -axis, (TM^z polarization). It seems to be a challenge to find conformal mappings analytically while explicitly solving the Cauchy-Riemann differential equations, for example, the analysis of mapping between $z = x + iy$ and $z' = x' + iy'$ is very complex. However, the limitations of conformal maps arise when we truncate our transformation domain. That is, once boundary conditions are applied to the governing differential equations, it is not always possible to achieve conformal modules M , the aspect ratio of the differential rectangle corresponding to a set of orthogonal coordinates, equal to unity, and hence the Cauchy-Riemann equations do not apply universally to all geometries.

1.2.2.3 Quasi-conformal transformation optics (QCTO)

As we discussed previously, much of the power of the TO is determined by the transformation at the boundary of the domain. For instance, we might require that our transformation does not introduce reflections or change the direction of a wave entering or exiting our transformed domain. These conditions introduce additional restrictions to our transformation. The most straightforward way to satisfy these conditions is to stipulate that the coordinates are the same as free space on the boundary of our transformed domain, for instance Dirichlet boundary conditions.

This extra constraint severely limits the scope of conformally-equivalent domains. Specifically,

let's take the mapping between two quadrilateral domains for instance. Once the sides of the quadrilateral domain have been specified, the region can only be mapped to another quadrilateral that shares the same conformal module. If the domain is rectangular, then M is the aspect ratio of the entire domain. Another concern relates to the boundary conditions directly. While Dirichlet boundaries are ideal for most purposes, they may be incompatible with our requirement of orthogonality at all points in the mapped domain. If we simultaneously specify $x'(x)$ and M at the boundary, the problem becomes over-determined and we are not guaranteed that the mapping will be orthogonal at the boundary [92]. Instead, we require a combination of Dirichlet and Neumann boundaries to simultaneously fix the geometry of the transformed domain and maintain orthogonality on the boundary.

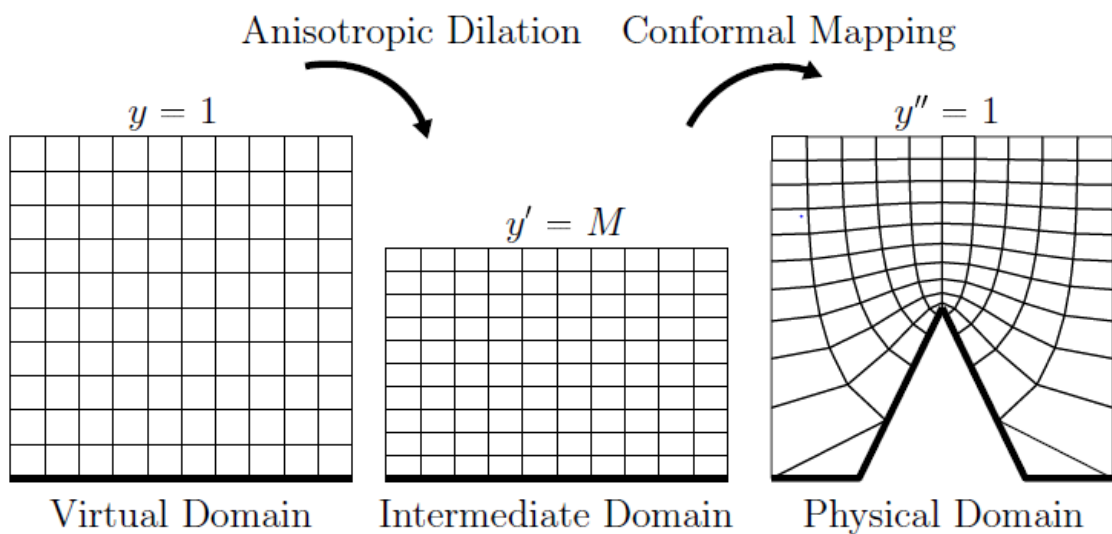


Figure 1-12: Depiction of the quasi-conformal mapping using intermediate transformations [79]. Lines of constant x and y , (virtual domain coordinates), are shown in each domain. The thick black line represents a PEC boundary in each domain.

We now start to discuss the mapping between two domains that don't share the same conformal module. As presented in Figure 1-12, the physical domain is a rectangle domain with a hump on the bottom boundary whose conformal module is M . We intend to map this physical domain to

the rectangle virtual domain whose conformal module is 1 on the left of the figure.

To compensate for the mismatch in conformal modules, we first map our virtual domain to an intermediate domain having the same conformal module as the physical domain. And the Jacobian matrix of the conformal transformation A_c is assumed to be obtained. The simplest way to do this is with a uniform dilation of the form $y' = My$. We can then conformally map this intermediate domain onto the physical domain with a conformal transformation.

The combined dilation and conformal mapping produce material tensors of the form:

$$\frac{AA^T}{|A|} = \text{Diag}[M^{-1}, M, (M|A_c|)^{-1}] \quad (1-25)$$

The conformal module provides an immediate measure of the anisotropy of the TO medium, as well as its required magnetic response, since $M = \sqrt{\mu_x/\mu_y}$. We have

$$\begin{aligned} Mx'_x &= y'_y \\ Mx'_y &= -y'_x \end{aligned} \quad (1-26)$$

The inverse form of this equation is

$$\begin{aligned} Mx_x &= My_y \\ My_{x'} &= -x_{y'} \end{aligned} \quad (1-27)$$

We find that we recover the Laplacian vector for the inverse problem:

$$\nabla^2 x = 0 \quad (1-28)$$

The following steps are the same as we have discussed previously in the part of the transformation based on Laplace's equation with Dirichlet boundary conditions.

We see that the cost of the quasi conformal (QC) map is immediately clear: the in-plane material tensors elements are no longer equal to each other. However, it is generally the case that small deformations of space create small perturbations to the conformal module of the physical domain. Li and Pendry [80] suggested that the "small" anisotropy can be ignored in this case. The geometric average of these quantities is simply

$$n = \sqrt{\epsilon_z} = (M|A_c|)^{-1/2} \quad \text{(1-29)}$$

Since the virtual and physical domains are no longer of the same size, the resulting distributions of material parameters are only approximately correct, and will introduce a number of aberrations. Despite its limitations, the QC method has found many applications. QC method may be applied to flatten conventional dielectric lens-antennas and parabolic reflector-antennas without significant loss in performances [92-94]. The quasi-isotropic properties can then further be implemented by all-dielectric devices, which benefits a wide frequency band of operation.

1.3 Numerical calculation softwares

In this section, I present the different softwares used as tools to design transformation optics devices.

1.3.1 Mathematica

Wolfram Mathematica is a computational software program used in many scientific, engineering, mathematical and computing fields, based on symbolic mathematics. In my thesis, Wolfram Mathematica is mainly used as a tool for parameter calculations of coordinate transformation designs. By coding the formulation of the coordinate transformation designs, Mathematica can provide the simplified formulations of the tensors, such as ϵ , μ . Applying a polarization of the field or other techniques, Mathematica can complete the parameter reduction. After assigning values to the variables, a parameter distribution or even discretization can be achieved.

1.3.2 COMSOL Multiphysics

COMSOL Multiphysics® is a general-purpose software platform, based on advanced numerical methods, for modeling and simulating physics-based problems. In the thesis, COMSOL is used for 2-D near field and far field calculations. In COMSOL, continuous formulations can be assigned to material properties. This is very convenient for transformation optic designs.

Figure 1-13 shows an example of coordinate transformation design in COMSOL. In the area of the transformed object, continuous permittivity and permeability are defined by formulations. Models of feeding sources, such as surface current and wave ports, can be assigned for full wave simulations.

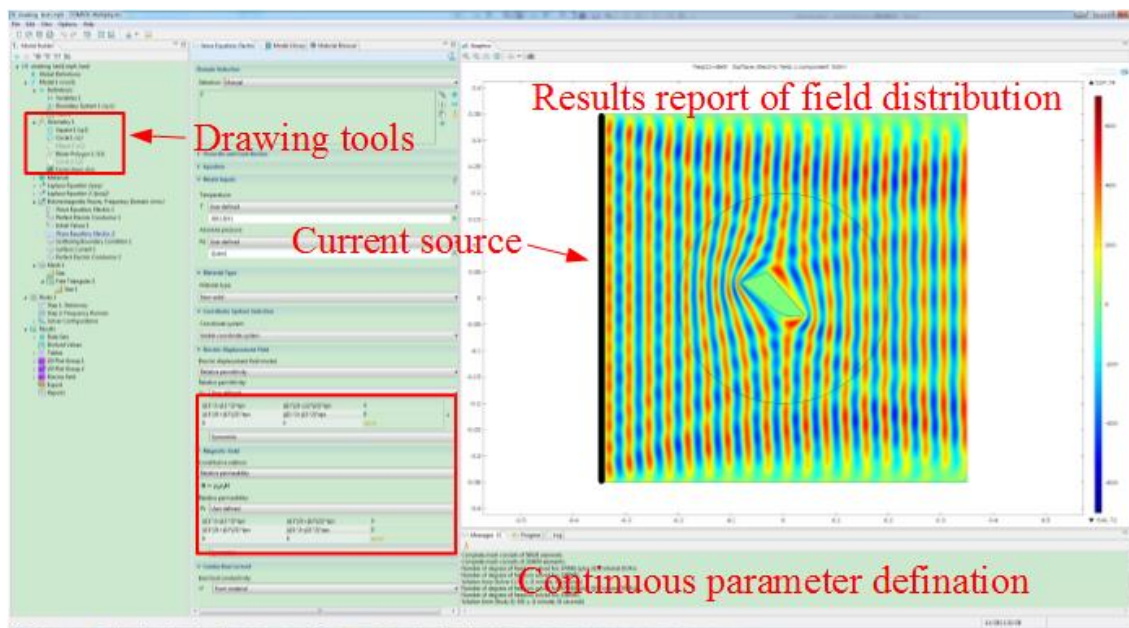


Figure 1-13: Interface of COMSOL Multiphysics.

In addition to conventional physics-based user interfaces, COMSOL Multiphysics also allows for entering coupled systems of partial differential equations (PDEs). The PDEs can be entered directly or using the so-called weak form. The PDE solver can be used for the calculation of the space transformations. The designs using the method of transformation based on Laplace’s equation can be calculated by the PDE solvers. Then the parameters from this calculation can be

assigned as the material properties of the transformed zone.

1.3.3 ANSYS HFSS

ANSYS HFSS software is a commercial software for simulating 3-D full-wave electromagnetic devices. It is one of several industrial tools used for antenna design, and the design of complex RF electronic circuit elements including filters, transmission lines, and packaging.

In HFSS, with the help of the drawing tools we are able to simulate a 3-D model that is quite similar to a realistic model. In my thesis, the first utilization of HFSS is to design antennas that can feed the lenses we proposed by transformation optics. Then together with the sources, 3-D models of the lens-antennas can be simulated as in real case.

As show by the example in Figure 1-14, the patch antenna is feed by a circular waveport and conformed on to cylindrical surface. The dielectric material of the lens is assigned the same properties of the material for fabrication. Air holes of different radius made in the lens as in 2-D designs.

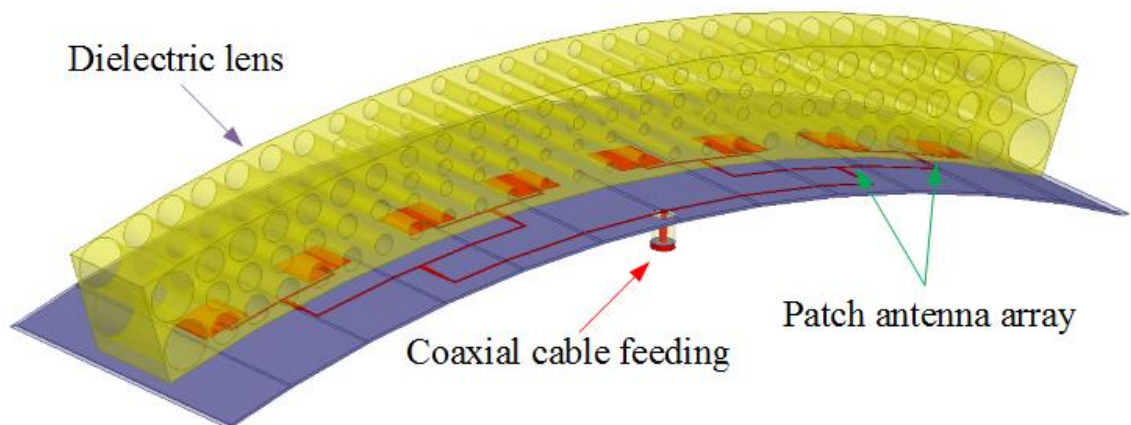


Figure 1-14: Sketch of simulation setup of antennas.

In Figure 1-15, the second utilization of HFSS is presented. The cell of a unit resonator is simulated in a cubic cell. Perfect electric and magnetic (or Master/Slave) boundary conditions are assigned to simulate an infinite array of cells. Floquet ports are used to launch transverse

electric and magnetic polarized waves. In this figure, a unit cell of air hole in a cubic dielectric material is simulated. The effective parameters (ϵ and μ) can be extracted from the calculations of the S -parameters.

To calculate the effective parameters of the resonators shown Figure 1-15, a homogenization procedure is briefly described in the following part of this section. The homogenization procedure is based on the use the coefficients of transmittance and reflectance obtained by simulations and measures. Parameters such as the index n and the impedance Z can be calculated depending on the transmission and reflection from the following equations [21]:

$$Z = \pm \sqrt{\frac{(1 + r^2) - t^2}{(1 - r^2) - t^2}} \quad (1-30)$$

$$\cos(nkd) = \frac{1}{2t} [1 - (r^2 - t^2)] \quad (1-31)$$

Thus, we can reduce parameters such as the effective permittivity and the effective permeability

$$\epsilon_{eff} = \frac{n}{Z} \text{ and } \mu_{eff} = nZ .$$

Two causal conditions for passive media must, however, be followed:

$$\text{Re}(Z) \geq 0 \text{ and } \text{Im}(Z) \geq 0$$

(1-32)

Indeed, this method involves reversing the coefficients of reflection and transmitting a uniform metamaterial sample.

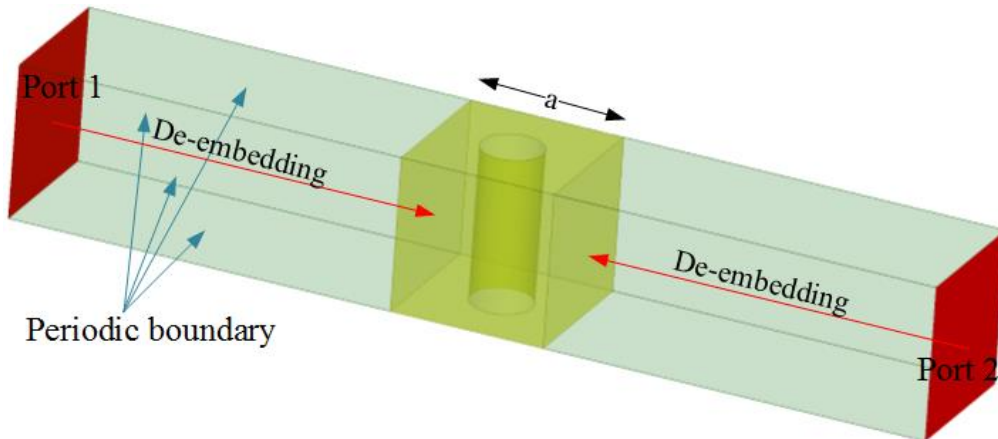


Figure 1-15: Sketch of simulation setup of unit cells.

Since the 1970s, Nicholson and Ross [95] were interested in this method. Smith and colleagues retraced the method by applying it successfully to basic bricks metamaterials and adding conditions branches selection conditions when multifaceted functions such as the argument of a complex number [96]. Note that the index of a medium is set over the entire frequency band in which material is excited by a single electromagnetic mode. However defining an impedance requires continuity of material or less, the assumption of long wavelength compared to the size of the heterogeneities of so that diffraction phenomena are negligible.

1.4 Experimental setups

Two experimental setups have been used during my thesis to validate the proposed concepts from fabricated prototypes. One is based on near-field measurements in order to be able to show the wavefronts and the other one is based on far-field measurements to show antennas radiation patterns.

1.4.1 Near-field measurement setup

A first experimental system aiming to scan the electric near-field microwave radiation is used. The electric field is scanned by a field-sensing monopole probe connected to one port of a vector network analyser by a coaxial cable. The probe is mounted on two orthogonal linear computer-controlled translation stages as presented in Figure 1-16, so that the probe can be moved within the radiation region of the system under test.

By stepping the field sensor in small increments and recording the field amplitude and phase at every step, a full 2D spatial field map of the microwave near-field pattern is obtained either in free-space or in parallel-plate TEM waveguide configuration. The total scanning area can cover a surface area of 400 x 400 mm². Microwave absorbers are applied around the measurement

stage in order to suppress undesired scattered radiations.

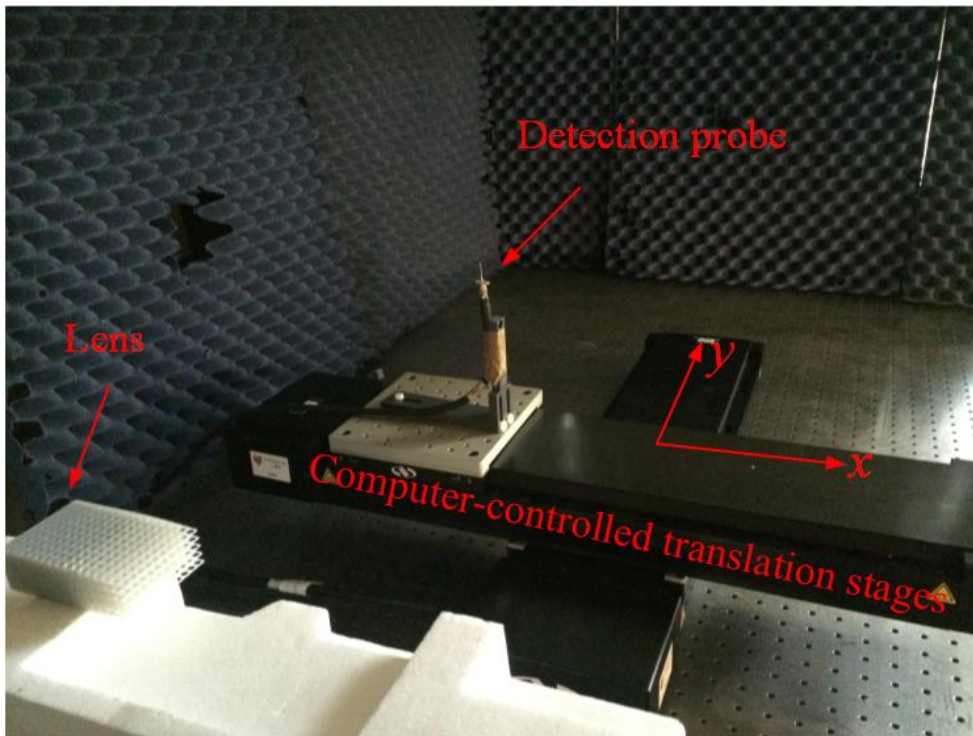


Figure 1-16: Near field scanning experimental setup.

1.4.2 Far-field measurement setup

The second experiment system consists of measuring the far-field radiation patterns of the antenna in an anechoic chamber. Figure 1-17 shows the far-field measurement system.

In such an emission-reception setup, the fabricated transformation based device is excited by a designed source which can be in the form of a patch antenna or patch array or even monopole or dipole. A dual-polarized wideband horn antenna is used as the receiver to measure the radiated power level of the emitter. The measurements are done for computer-controlled elevation angle varying from -90° to $+90^\circ$. The microwave source is a vector network analyser (Agilent 8722 ES) that we also use for detection. The feeding port is connected to the metamaterial antenna by means of a coaxial cable, and the detecting port is connected to the horn antenna also by means of a coaxial cable.

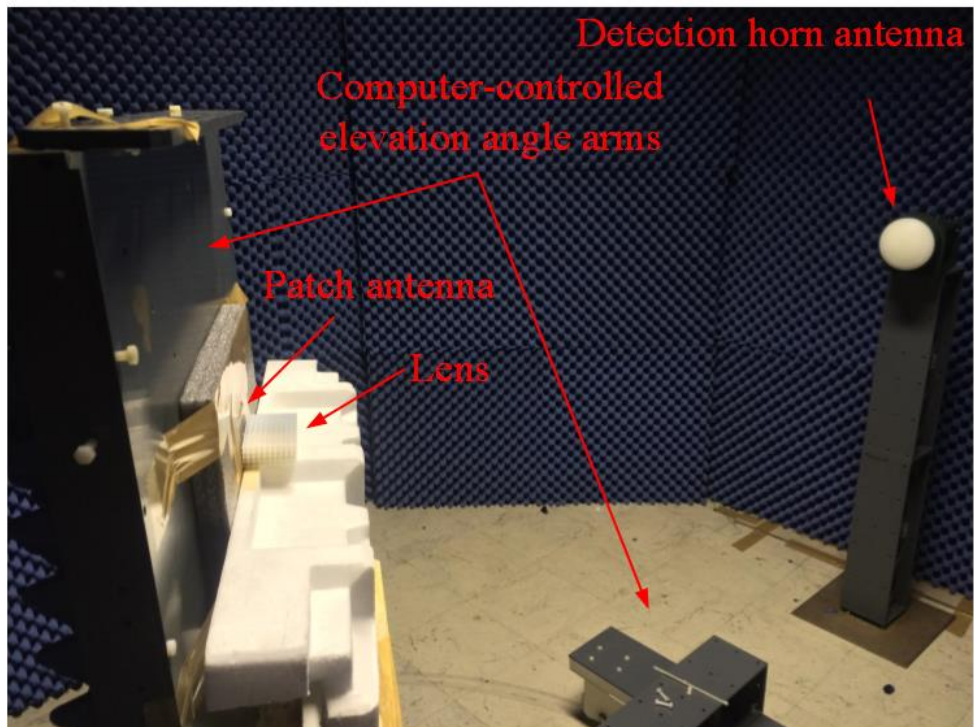


Figure 1-17: Far field scanning experimental setup.

1.5 Validation technology

In the previous sections, we have introduced the transformation optics concept and the softwares used for the numerical calculations and also the types of measurements performed. In my thesis, the implementation of microwave devices designed by transformation optics concept requires the realization of permittivity and permeability materials or cells. We implement both resonant metamaterial resonators and all dielectric materials. The metamaterial resonators will provide a wide range of permittivity or permeability values ranging from negative to positive. High permittivity values around 15 can also be produced. But they will suffer from the narrow frequency band limitation. These resonators are normally fabricated by printed circuit board technology.

On the contrary, the all-dielectric materials can only provide a limit range of positive permittivity values larger than 1. But the advantage is the wide frequency band and an easy

adaptation to THz and optics domain. The all-dielectric prototypes presented in this thesis are fabricated by 3D printing and therefore we are able to realize air holes with extremely small radius.

In the following parts, I present the metamaterial and dielectric cells used to produce permittivity and permeability values requires in my proposed designs.

1.5.1 Electric LC (ELC) resonators

An electromagnetic metamaterial is a man-made composite material comprising a periodic array of subwavelength inclusions. Typically, a single metallic metamaterial inclusion can be considered as an LC resonant circuit with its inductance and capacitance influenced by its shape and dimensions.

The ELC resonator is presented and illustrated in Figure 1-18(a). This resonator consists of an inductive loop connected to a capacitive element. Only the capacitive element formed by the central gap couples strongly with the field electrical (Figure 1-18(b)) to produce an electric response.

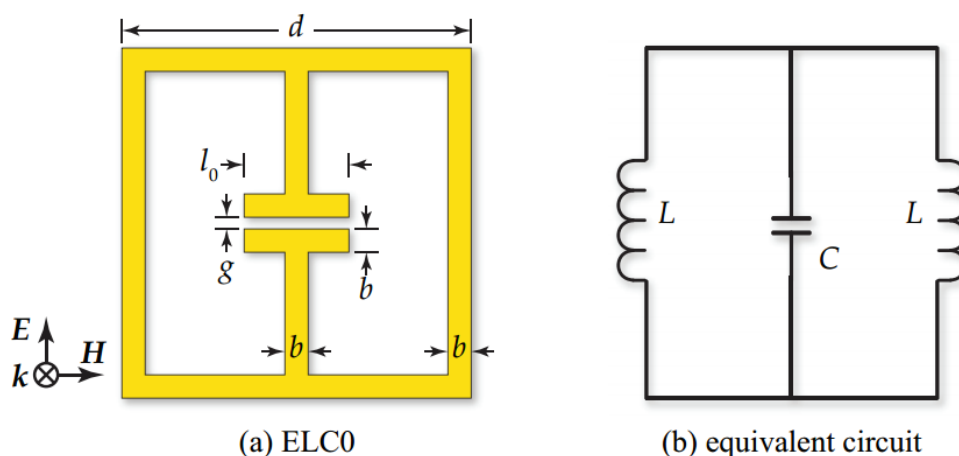


Figure 1-18: Electric-LC resonator [97]. (a) A typical ELC resonator is composed of a center capacitive gap connected to two inductive loops. (b) An equivalent circuit of the resonator constitutes an LC resonator (the resistance is neglected here).

To examine the performance of the ELC resonator, the electromagnetic properties of the structure are analysed numerically by applying the appropriate periodic conditions on a unit cell.

The simulation environment of a resonator is given in Figure 1-19.

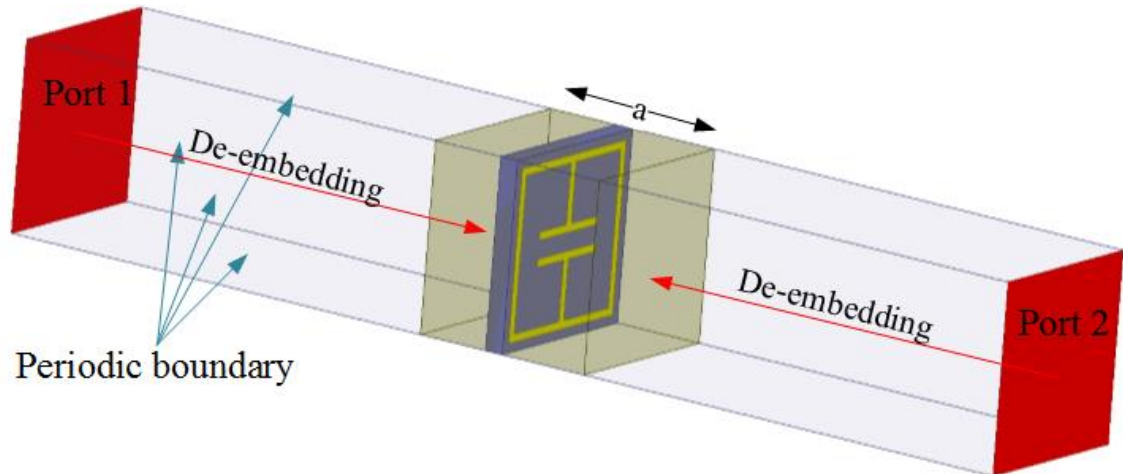


Figure 1-19: Sketch of simulation setup of ELC resonators.

Two Floquet ports are used along the direction of propagation. These ports are placed at a sufficiently large distance so that the incident wave is planar at the surface of the resonators. A de-embedding allows to cancel phase delay due to the distance travelled by the wave in vacuum from the exciting ports.

1.5.2 Split ring resonator (SRR)

Split ring resonators (SRRs) consist of a pair of subwavelength concentric metallic rings, etched on a dielectric substrate, with gaps on opposite sides. We use the SRR structure for its ability to present a magnetic resonance and hence the possibility of producing negative permeability values.

The electromagnetic properties of SRRs have been analysed in lots of works [98] and [99]. A SRR behaves as an *LC* resonator that can be excited by an external magnetic flux, exhibiting a strong diamagnetism above their first resonance. SRRs can also exhibit cross-polarization

effects (magneto-electric coupling) [99] so that excitation by a properly polarized time-varying external electric field is also possible. Figure 1-20 shows the basic topology of the SRR, as well as the equivalent-circuit model proposed in [98].

The numerical analysis of the SRR resonator is similar to the simulation we have introduced for the ELC resonators. The only difference is the polarization of the incident wave is according to the one shown in Figure 1-20.

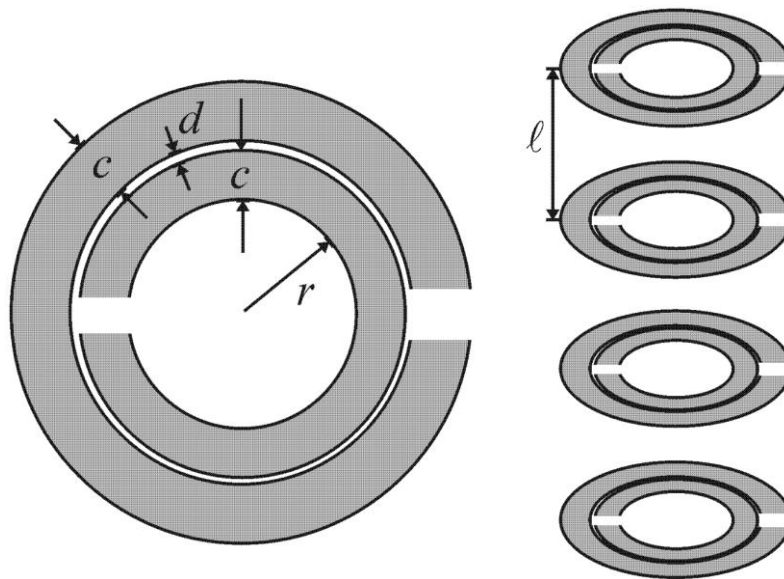


Figure 1-20: Split ring resonator [98]. A typical SRR is composed of two rings with gaps facing the opposite directions and its equivalent circuit of the resonator constitutes an LC resonator.

1.5.3 All-dielectric material

To realize the transformation designs, positive permittivity values above 1 can be realized from non-resonant cells to benefit a broad frequency range. Air holes in a dielectric host medium of relative permittivity $\epsilon_h = 2.8$ is therefore considered in my thesis. Suppose that air and the dielectric are mixed together, the effective parameter can be calculated by:

$$\varepsilon_o = \varepsilon_a f_a + \varepsilon_h f_h \quad (1-33)$$

where $\varepsilon_a = 1$ is the relative permittivity of air and f_a and f_h are the volume fraction of the air holes and the host material, respectively. By adjusting the volume fraction of the air holes in the dielectric host medium, the effective permittivity of the cell can then be engineered.



Figure 1-21: Photograph of Objet Eden260VS 3D printer and its product.

The air holes in a dielectric medium are fabricated by 3D polyjet printing from the Objet Eden260VS printer shown in Figure 1-21. The Objet Eden260VS professional 3D printer works with 15 materials to deliver outstanding precision and productivity [100]. The printer can build models up to $255 \times 252 \times 200$ mm. The 3D printing is based on the polyjet technology consisting in jetting layers of curable liquid photopolymer onto a build tray. During the printing process, the air holes are filled with a gel-like material that is easily removed with water. The material we use as photopolymer for the fabrication has a permittivity $f_h = 2.8$.

1.6 Conclusion

In this chapter, the principle of metamaterials is presented, and several antenna applications

based on metamaterials are introduced at first. Then the design concept – transformation optics - is introduced. Then coordinate transformation and transformations based on Laplace’s equation, including transformation with only Dirichlet boundary conditions, conformal mapping and quasi-conformal transformation optics, are introduced. The numerical calculation softwares, near field and far field experimental setups we use for the thesis are presented. For the realistic validation (simulated and experimental) of the designs, electric and magnetic metamaterial resonators and dielectric materials engineering are also presented. All the design concepts, numerical calculation tools, validation technologies and experimental setups will be used for the designs of the microwave devices we propose in the thesis.

PART I

*DESIGNS OF MICROWAVE DEVICES BASED
ON COORDINATE TRANSFORMATION*

The interests in invariance of Maxwell equations to coordinate transformations have been revived in 2006 when U. Leonhardt [21] and J. B. Pendry et al. [101] showed how the paths of electromagnetic waves travelling within a material can be controlled at will by applying a judiciously defined spatial variation in the constitutive parameters. The concept of coordinate transformation electromagnetics, presented in the introduction chapter, appears to be a convenient tool to design devices or components with special properties difficult to obtain with naturally occurring materials and has been successfully utilized to experimentally validate the emblematic electromagnetic cloak [79][102]. Other conceptual and functional electromagnetic devices have then proposed using this method. To name a few, field concentrators [79], beam bends and expanders [44][56][60][103], waveguide tapers [104] and field rotators [67] have been designed. For microwave antenna applications, focusing lens antennas have been theoretically designed [28][105]. The performances of an omnidirectional retroreflector [106] based on the transmutation of singularities and a Luneberg lens [107] have been experimentally demonstrated. Furthermore, techniques of source transformation [35][71][74,75][108-111], where source distribution is included in the transformed space, have offered new opportunities for the design of active devices. In this Part I, we will discuss two devices that have been designed based on coordinate transformation optics in the framework of this thesis. One of the two has been fabricated by making use of resonant metamaterials, typically electric-LC (ELC) resonators, introduced by Schurig *et al.* for its electric resonance [97].

Part I consists of three chapters, where two designs of microwave devices are introduced in Chapter 2 and Chapter 3 respectively. The concepts of these two designs are both based on coordinate transformation optics. In Chapter 2, we introduce a coordinate transformation optics approach to delocalize sources inside a metamaterial assigned shell to appear outside the shell. The design we propose consists in a novel radiating device that can change the position of an apparent emitting source. By applying radial transformations that compress space, and then that match it to the surrounding environment, we show how a source placed in the core region can be apparently displaced at a distance outside the second matching region corresponding to a

space folding. Moreover, the radiation pattern of the virtual source can be changed and we show that an omnidirectional radiation can be changed into a directive one. We describe transformation of the metric space and the calculation of the material parameters. In Chapter 3, following the transformation optics approach still, we design a taper between two waveguides of different cross sections. Three different transformation techniques are presented so as to achieve a low-reflection taper between the two waveguides. The media obtained from these three methods presents complex anisotropic permittivity and permeability. The taper is finally designed with two compression parts and two matching parts. This structure allows us to succeed in the tapering function with a factor of 11 between the two different cross sections of the waveguides. However we show that using a reciprocal transformation leads to the design of a taper from a material with physically achievable material parameters. The complex parameters are simplified and discretized for a physical realization. The fabricated prototype of this waveguide taper is then presented. Full wave simulations are performed at different frequencies to validate the proposed two devices. The tapering function is also further verified by experimental demonstrations showing the scanned near field of the device.

2 ILLUSION OPTICS: OPTICALLY TRANSFORMING THE NATURE AND THE LOCATION OF ELECTROMAGNETIC EMISSIONS

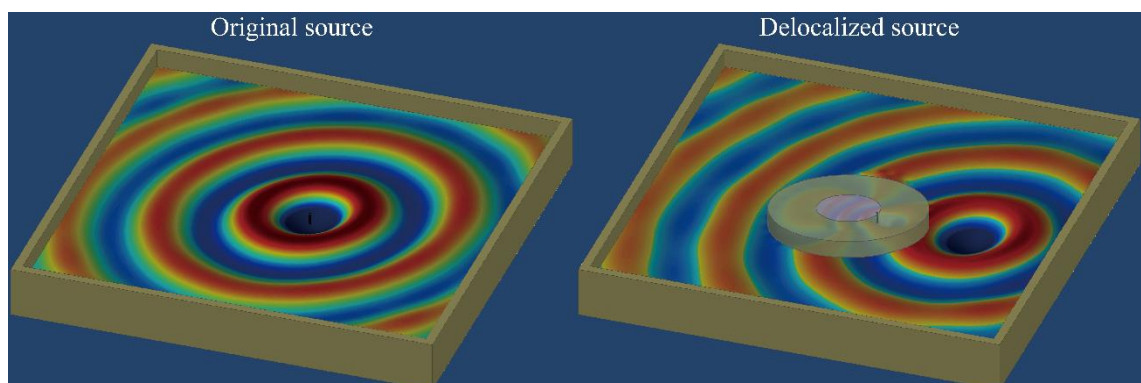


Figure 2-1: Diagrammatic sketch of the function of the Delocalization device.

Complex electromagnetic structures can be designed by using the powerful concept of

transformation electromagnetics as it has been introduced previously [128]. In this chapter, we define a spatial coordinate transformation that shows the possibility of designing a device capable of producing an illusion on an antenna radiation pattern as shown in Figure 2-1. Indeed, by compressing the space containing a radiating element, we show that it is able to change the radiation pattern and to make the radiation location appear outside the latter space. Both continuous and discretized models with calculated electromagnetic parameter values are presented. A reduction of the electromagnetic material parameters is also proposed for a possible physical fabrication of the device with achievable values of permittivity and permeability that can be obtained from existing well-known metamaterials. Following that, the design of the proposed antenna using a layered metamaterial is presented. Full wave numerical simulations using Finite Element Method (FEM) are performed to demonstrate the performances of such a device.

2.1 Introduction

As well known to all, transformation electromagnetics concept has motivated a series of studies on illusion optics devices [28, 29] [112-115], which can create optical illusions. For example, an object can be made to appear like another one by transforming the scattered light outside a virtual boundary into that of the object chosen for the illusion [28]. A shrinking device able to transform an object virtually into another one of smaller size with different material parameters has further been experimentally demonstrated [114]. A “ghost” illusion device, which is capable of creating multiple virtual ghost images of the original object’s position has also been realized and validated [115]. These three designs are illustrated in Figure 2-2.

Figure 2-2(a)-(c) show the concept of the optical transformation of an object into another object. This transformation is capable of transforming the electric field distribution diffracted by a metallic spoon into another distribution. This transformed field is distributed as if the plane

wave is diffracted by a metallic cup instead of a spoon. However this design requires a perfect electric conductor surface or boundary conditions. The creation of the illusion is achieved by firstly cancelling the original object and then creating another object, not by delocalizing the position or transforming the shape of the object.

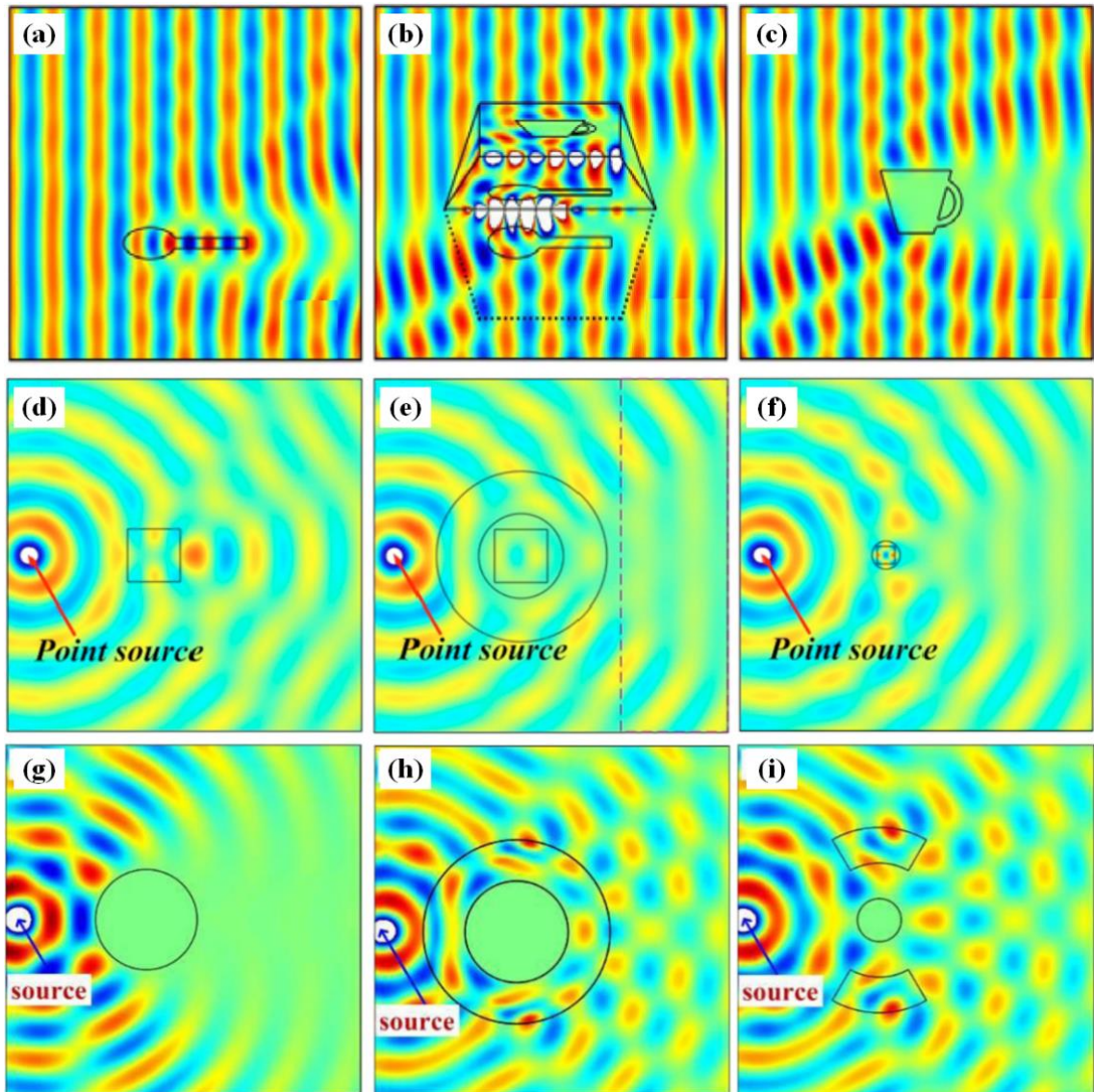


Figure 2-2: Simulated electric field distributions of (a)-(c) the optical transformation of an object into another object [28], (d)-(f) the shrinking device of an arbitrary object using metamaterials [114], and (g)-(i) the ghost illusion device using metamaterials in wave dynamics [115].

Figure 2-2(d)-(f) represent the electric field distribution of the shrinking device of an arbitrary object using metamaterials. The idea of this transformation is to shrink the inner boundary of the device into a circle with a smaller radius. This design is similar to the concept of the cloaking device. The object inside this shrinking device is covered instead of shrinking indeed.

Figure 2-2(g)-(i) represent the field distribution of a point source transmitting through a ghost illusion device using metamaterials in wave dynamics. This annular shape device will transform the dielectric object into a smaller one, and meanwhile create two dielectric ‘ghosts’ on two sides of the object. This transformation consists two steps. The first step is a shrinking device. The concept of this step is more less the same as the shrinking device we presented in the previous paragraph. The two dielectric ghosts are created by increasing the permittivity value at the region of the ‘ghost’. Actually these ghosts don't really come from the transformation. One can also fabricate this device by just implanting the shrinking device in two dielectric blocks.

Here we bring up a real challenge of creating the illusion only by applying a coordinate transformation. The question we ask ourselves is whether we can delocalize the emission of radiating element contained in a material shell such that we have the impression that the emission appears like coming from a virtual source at another location? With such manipulation, we will therefore be able to generate an electromagnetic radiation from a location where no radiator is physically present. In this chapter, we use transformation electromagnetics to change the appearance of a source and virtually delocalize the emission outside its core material shell. Such an illusion device can be potentially used to fool radar detectors. We will show how from a coordinate transformation that compresses space and then expands it, it is not only possible to transform the electromagnetic radiation of a small antenna into one equivalent to that of a large one, but also to change its spatial location. We discuss the space parameters generated from our study and validate the concept through numerical simulations. We propose a structure in transverse magnetic (TM) polarization with simplified reduced parameters. Finally a layered structure of the metamaterial is presented in order to make a first step towards the physical

realization process of this illusion device.

2.2 Spatial coordinate transformation formulation

The basic idea of our concept is to virtually modify the spatial location of a radiating electromagnetic source outside the material shell in which it is placed. An observer will then have the impression the emitter is elsewhere instead of its real physical location, as illustrated in Figure 2-3.

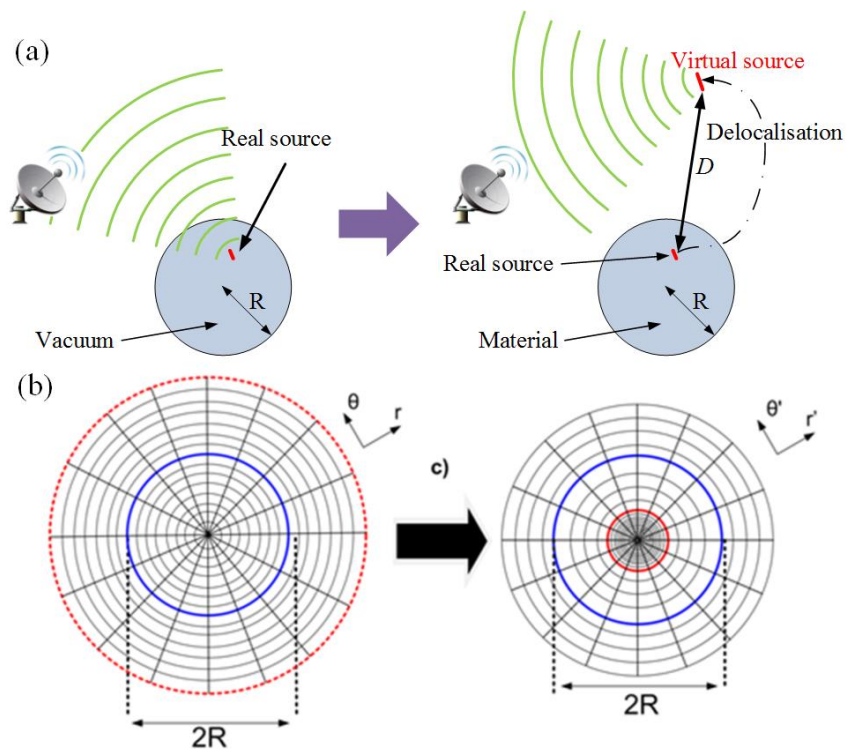


Figure 2-3: Principle of the transformation: A detector will observe the electromagnetic radiation coming from another direction while the real source is placed in the material shell [117].

An analogy can be found in the study addressed in [50] with a perfect lens, where it has been shown that a source (green point) placed in a slab with refractive index $n=-1$ creates two focusing points outside the slab in Figure 2-4. In transformation electromagnetic, the perfect

lens can be viewed as a medium where space is totally suppressed and folded outside. Such manipulation has been referred to as embedded transformation [61]. Other cases of perfect lenses having a cylindrical geometry have been utilized as magnifying devices through linear transformations [51][116]. For the proposed delocalization of electromagnetic radiation, different transformation methods can be applied. For example, a radial transformation using a sinusoidal function is firstly presented. Such transformation has been introduced in our recent work [117].

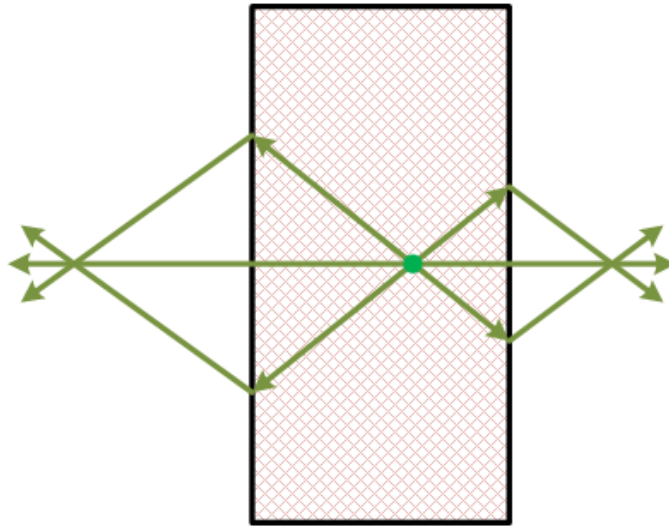


Figure 2-4: A negative refractive index medium bends light to a negative angle with the surface normal [50].

2.2.1 The concept of the sinusoidal transformation

The concept of the sinusoidal transformation is presented in Figure 2-5. Such transformation consists in stretching a part of the space contained in a radius outside the shell and compressing it in the radius $r = R$ of the material, as illustrated in Figure 2-3. In Figure 2-3(a), an observer detects the source at the location of the long red line. But this source is a virtual source created by the illusion. The real source is located at the short red line inside the material shell, shown in blue. The properties of the material in the shell are related to the sinusoidal transformation

presented in Figure 2-3(b). By doing continuous transformation, a part of a space is folded near the boundaries of the material shell. This continuous transformation (not embedded) is represented in Figure 2-3(c) where the material shell is represented in blue line, which has not been transformed to assure perfect space metric matching at the boundary of the shell.

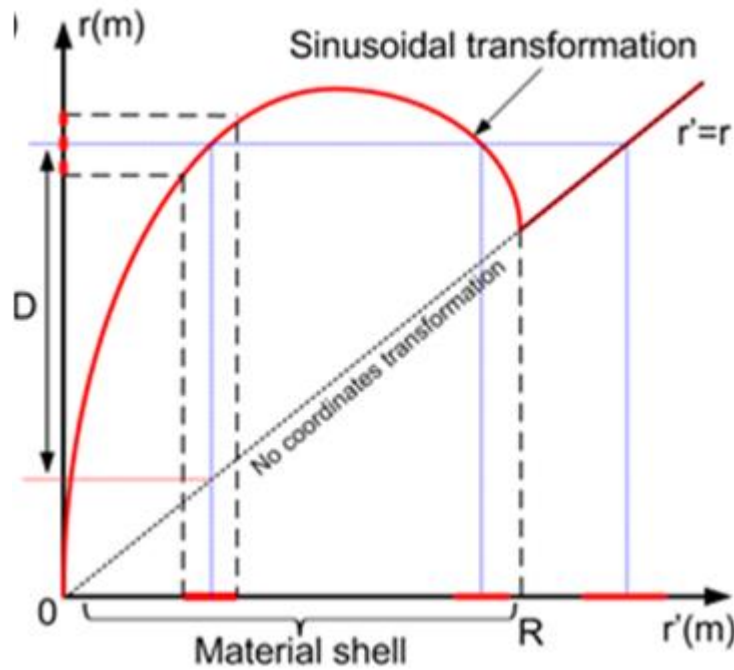


Figure 2-5: Principle of the sinusoidal transformation: An observer outside the region shell think that the radiation come from another direction and that the emitting antenna is very large. The transformation used to create such device is achieved with a sinusoidal transformation. D represents the distance between the source and the image, while R is the radius of the device [117].

The angular part of the transformation is not changed and we assume a z -independence of the transformation for possible parameter reduction. Thus, any source placed at a certain distance in material will have 3 images source as represented with the projection on the r' axis and at different positions.

We consider (r, θ, z) to be the coordinates in the initial fictitious cylindrical space and (r', θ', z') to be the coordinates in the final real physical transformed space. In the transformation, we

assume θ and z independence. Mathematically this transformation is expressed as:

$$\begin{cases} r' = f(r) \\ \theta' = \theta \\ z' = z \end{cases} \quad (2-1)$$

where $f(r)$ corresponds to a perfect radial transformation and takes the form $f(r) = (\arcsin(r/A))/B$. In order to calculate the parameters we need to determine the Jacobian matrix **(2-2)** in the cylindrical coordinates:

$$\overline{\overline{J}}_{cyl} = \begin{pmatrix} \frac{\partial r'}{\partial r} & \frac{\partial r'}{\partial \theta} & \frac{\partial r'}{\partial z} \\ \frac{\partial \theta'}{\partial r} & \frac{\partial \theta'}{\partial \theta} & \frac{\partial \theta'}{\partial z} \\ \frac{\partial z'}{\partial r} & \frac{\partial z'}{\partial \theta} & \frac{\partial z'}{\partial z} \end{pmatrix} = \begin{pmatrix} \frac{\partial f(r)}{\partial r} & 0 & 0 \\ 0 & 1 & 0 \\ 0 & 0 & 1 \end{pmatrix} \quad (2-2)$$

This Jacobian matrix does not take into account the equivalence with the Cartesian coordinates which allows to create the material. We therefore need to introduce the component of the metric tensors into the final Jacobian matrix J , given by:

$$\overline{J} = \begin{pmatrix} \frac{\partial f(r)}{\partial r} & 0 & 0 \\ 0 & \frac{r'}{r} & 0 \\ 0 & 0 & 1 \end{pmatrix} \quad (2-3)$$

The permittivity and permeability tensors ψ are then calculated as $\overline{\overline{\psi}} = \frac{JJ^T}{\det(J)}$. The results

of such calculation are given by **(1-4)** in the cylindrical base:

$$\begin{cases} \psi_{rr} = \frac{r}{r'} \frac{\partial f(r)}{\partial r} \\ \psi_{\theta\theta} = \frac{r}{r'} \frac{\partial f(r)}{\partial r} \\ \psi_{zz} = \frac{r}{r'} \frac{\partial f(r)}{\partial r} \end{cases} \quad (2-4)$$

This final components in the Cartesian coordinates are given by the expression **(2-5)** and are

calculated using passage matrix into the 2 different coordinate system:

$$\square \varepsilon = \begin{bmatrix} \psi_{xx} & \psi_{xy} & \\ \psi_{yx} & \psi_{yy} & \\ & & \psi_{zz} \end{bmatrix} \varepsilon_0 \quad \square \mu = \begin{bmatrix} \psi_{xx} & \psi_{xy} & \\ \psi_{yx} & \psi_{yy} & \\ & & \psi_{zz} \end{bmatrix} \mu_0 \quad (2-5)$$

As we can see here, this sinusoidal transformation is mainly between the r axis and r' axis in cylindrical coordinate systems. This delocalization function is achieved by one step of transformation. The field is firstly compressed when the sinusoidal function is increasing, then it is extended when the function is decreasing, and finally it is matched when the curve of the function cross the line $r = r'$ at the point $r' = R$. The transformation used to achieved our material engineering device is defined as $g(r') = A \sin(Br')$ where $A = R/\sin(BR)$. This condition assures the perfect impedance matching outside between the air and the material and keeps the blue line of the Figure 2-3(c) unchanged. The value of variable B is considered *equal to* 61.2 in order to delocalize the source outside the shell.

The value of the permeability and permittivity components are very strong at the maximum point of $g(r')$ when $r'=R_0$ and we have plotted in the Figure 2-6 the components in a fixed interval. We can remark that there two zones: a red one which corresponds to the core zone with positive values creating the stretching and the delocalisation of the space and a blue one which corresponds to negatives values and to the space folding and a matching zone for the impedance matching. This second zone corresponds to a space where the propagation of the waves are backward and opposite to the core and the air area.

If we take a closer look at the distribution of the permittivity, it is obvious that all the four parameters have both positive and negative values. This is not surprising, since the transformation has two regions. One region is the compression region and the other region is the extension region. These two parts are opposite. Negative values can be possibly achieved. But the extremum values of ε_{zz} , -11 and 53, are almost impossible to realize.

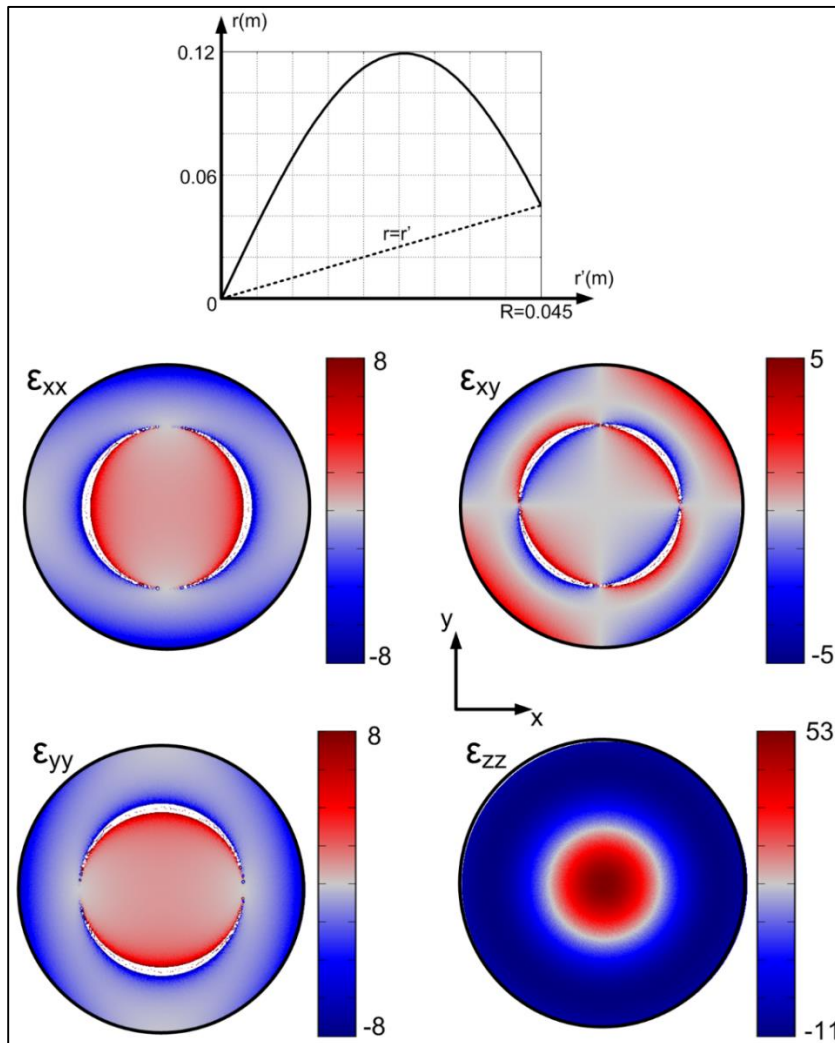


Figure 2-6: Representation of the components of the permittivity and permeability tensor with the sinusoidal transformation with $B = 61.2$. The radius of the material is chosen to be $R = 4.5$ cm [117].

2.2.2 The concept of the linear transformation

However in such sinusoidal transformation, the material parameters values can be very high and even after the parameter reduction process, they can be still difficult to achieve with common metamaterial structures. So we have to search for another transformation; one which can provide reasonable material parameter values and less complex permittivity distribution. In fact,

many kinds of transformations can create this folding and extension concept. As long as the function increases with a differential coefficient larger than 1, then decreases with a differential coefficient smaller than -1, and finally matches at the boundary of the shell, it will create this illusion. At last, we propose another transformation which is linear. This linear transformation is simple to calculate and the material properties can be possibly achieved. The principle of the proposed transformation is depicted in Figure 2-7. The space is first compressed by a linear transformation with a slope larger than 1 and then extended by another linear transformation whose slope is negative.

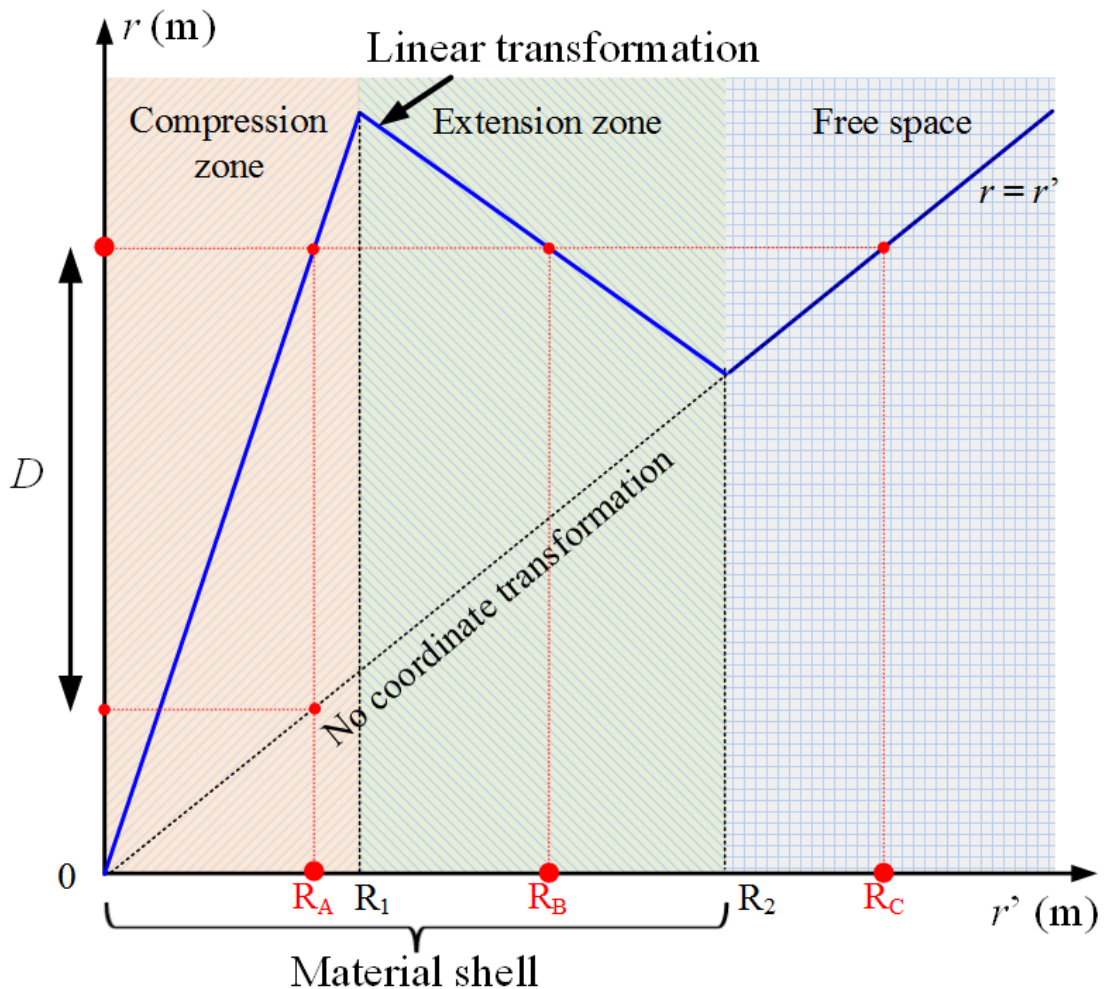


Figure 2-7: The transformation used to create such device is achieved with two steps of linear transformations [129].

In this transformation, a part of the space is folded near the boundaries of the material shell. Such folding of space corresponds to the zone between $r = R_1$ and $r = R_2$, presenting a negative derivative on the transformation in Figure 2-7 and corresponding also to the use of negative material parameters. The space transformation is decomposed into two linear parts: a first part where the value of r increases linearly, corresponding to a space compression (derivative > 1) and a second part where r decreases linearly (derivative < 1) where the space is extended in order to assure a perfect impedance matching with vacuum. Any source placed at a certain distance in the material shell will produce three images at different positions as represented by the projections R_A , R_B and R_C on the r' axis.

Here in the transformation, the function $f(r)$ of Equation (1-1) is given as:

$$f(r) = \begin{cases} r/q & (0 < r < R_1 * q) \\ (a * r) + b & (R_1 * q < r < R_2) \end{cases} \quad (2-6)$$

With variables $q > 1$, $a = \frac{R_2 - R_1}{R_2 - R_1 * q}$ and $b = \frac{(1 - q)R_2 * R_1}{R_2 - R_1 * q}$. This transformation consists in

two steps. In the domain where $0 < r < R_1 * q$, the field is compressed and in the domain $R_1 * q < r < R_2$, the field is released to match at the boundary. Even though this transformation is not continuous, it provides much simpler material properties.

The transformation used to achieve the engineered material device is defined as:

$$r = g(r') = \begin{cases} q * r' & (0 < r' < R_1) \\ (r' - b)/a & (R_1 < r' < R_2) \end{cases} \quad (2-7)$$

This condition assures a perfect impedance matching between the material and vacuum and leaves the boundary at $r = R_2$ unchanged. The radius R_2 of the whole material shell is considered here to be equal to 5cm and the radius R_1 of the compression zone is taken as 2cm. The ratio q in the compression zone is chosen to be 4.5 which can lead to a maximum delocalization

distance $D = 0.07$ m at r maximum (or $r' = R_1$).

$$D = (q - 1)r \quad (2-8)$$

Figure 2-8 shows the variation in the permittivity tensor components in the transformed space. As before, the three components of the permittivity take values varying from negative to positive. The extremum values depend on the value of q . If we increase q , the real source in the shell will be delocalize to a further location. But meanwhile, the maximum positive value and the minimum negative value will increase. For this reason, we have choose $q = 4.5$, so that the maximum positive value 20 is possible to achieve.

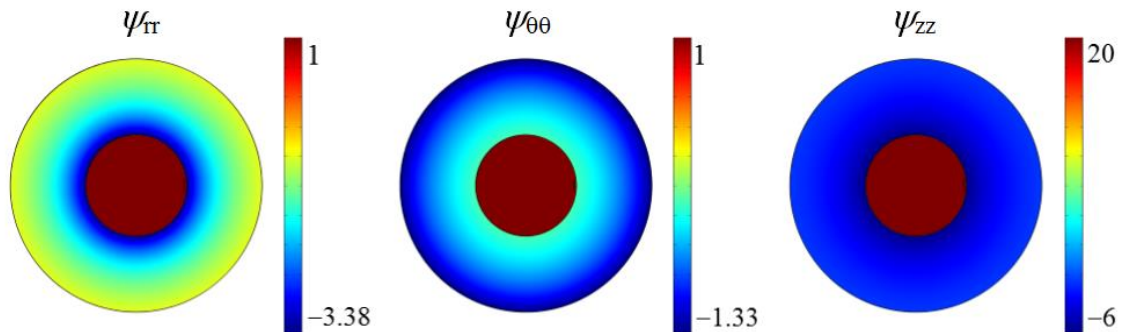


Figure 2-8: Variation of the material parameter tensor components ψ_{rr} , $\psi_{\theta\theta}$ and ψ_{zz} with $q = 4.5$ in the linear transformation. The radius of the compression zone is considered to be $R_1 = 2$ cm, while the radius of the whole material shell R_2 equals to 5 cm.

2.2.3 Comparison between sinusoidal and linear transformations

Actually, there could exist many kinds of transformation which can create this delocalization. In this thesis, we only take two of them as examples. The sinusoidal transformation can achieve this functionality by only one step, while the linear transformation consists in two steps. The distribution of the permittivity and permeability of the sinusoidal transformation is continuous in most cases and there are singular points in some parts. The distribution of the permittivity and permeability of the linear transformation is separated into two parts due to the two steps of

transformation. One part is purely positive and constant, the other part is negative. The parameter values given by the linear transformation are achievable because they are relatively moderate. The positive part can be fabricated with certain kind of dielectric material, such as ceramics whose permittivity can achieve high values at room temperature. The negative part can be realized by resonant metamaterials.

2.3 NUMERICAL SIMULATIONS AND RESULTS

In this section, FEM based numerical simulations with Comsol Multiphysics [118] are used to design and characterize the proposed illusion device at microwave frequencies (300 MHz-300 GHz). The validation of the material is performed in a two-dimensional configuration in a transverse magnetic (TM_z) mode. Continuity and matching conditions are respectively applied to the internal and external boundaries. The line current source of length $l = 5$ mm along the z -axis is placed at an offset distance $d = 1.9$ cm from the centre. The frequency is 5 GHz, with a wavelength of 6 cm. The source is an electric dipole with a length of 5 mm.

2.3.1 Parametric study of q

The corresponding calculated z -component of the electric field (E_z) is depicted in Figure 2-9. The radiation emitted by the source in free space is illustrated in Figure 2-9(a). An isotropic antenna diagram is obtained due to the small width of the source compared to the operating wavelength. In Figure 2-9(b), the material shell defined for the linear transformation with $q = 4.5$ as represented by the parameters calculated in Figure 2-8, is applied around the source. Such a configuration leads to two virtual sources; one appearing in the zone between R_1 and R_2 and another one outside R_2 at $r = 8.55$ cm, with therefore a delocalization distance $D = 6.65$ cm. Using $q = 6$ and the appropriate electromagnetic parameters leads to a virtual source outside R_2

at $r = 11.4$ cm and a delocalization distance $D = 9.5$ cm, as shown in Figure 2-9(c). When $q = 7.5$, this transformation created a virtual source outside the material shell at $r = 14.25$ cm and a delocalization distance $D = 12.35$ cm, as shown in Figure 2-9(d).

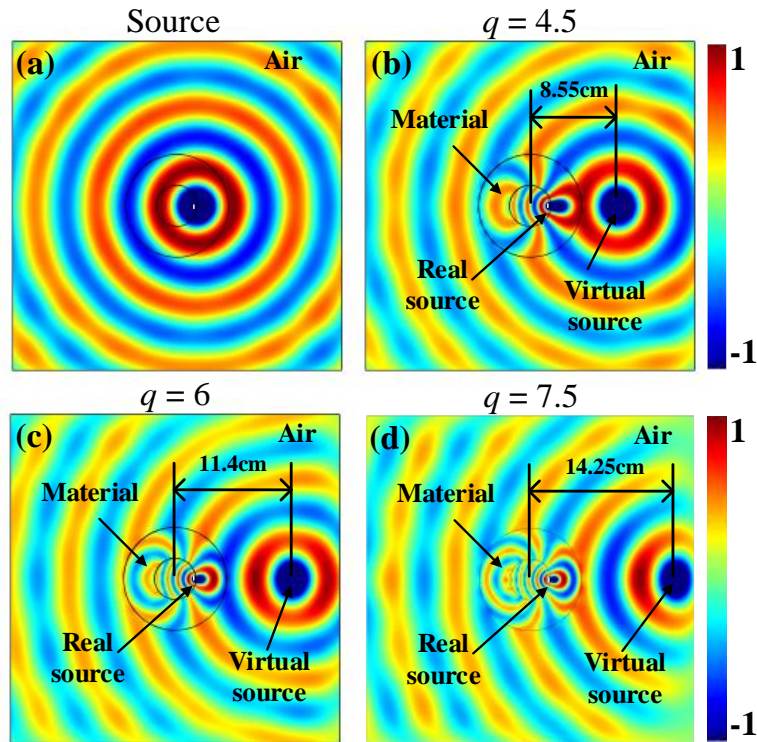


Figure 2-9: Electric field (E_z) distribution of a point source placed at the position $(x, y) = (1.9$ cm, 0 cm) in the material defined by the linear transformation. (a) No transformation is applied. (b) Transformation with $q = 4.5$. (c) Transformation with $q = 6$. (d) Transformation with $q = 7.5$.

As addressed in [119], surface waves supported by the negative electromagnetic parameters propagate on the material shell and the delocalized virtual source is created by the interference of the surface waves since there is no space for the evanescent field to decay exponentially. The absence of space is due to the fact that the negative index medium cancels optically some of the surrounding positive index material. This phenomenon is similar to what occurs in a perfect lens from a negative index slab.

In fact, the location of the virtual source $r = dq$ where d is the distance between the real source

and the center of the material, as presented in Figure 2-7. If the position of the real source d is fixed, $d = 1.9$ cm in our case, the location of the virtual source is a proportional function of q . And then the distance D between the real source and the virtual source is $D = d(q-1)$. In another word, if we increase the value of q , the virtual source will appear at a further place from the real source. Here we conclude that when the virtual source is fixed, by changing the value of q , we can control the position of the virtual source as we wish. Based on this result, we start to wonder what if we fix the value of q , and place the real source at different positions considering that we are limited by the size of the material. This question will be discussed in the next section.

2.3.2 Parametric study of the position of the real source

The two virtual sources observed in Figure 2-9(b) and (c) are in good agreement with the schematic of Figure 2-7(b) where it is obvious that three emissions points (the real and the two virtual sources) are present. They are defined by the projection of the source on the r axis directly on the r' axis; there are 2 intersections with the linear transformation curve and one intersection with the curve $r = r'$.

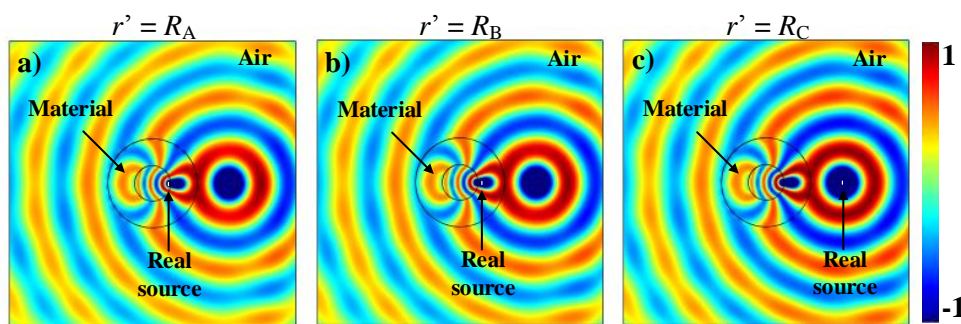


Figure 2-10: Electric field (E_z) distribution in the case of a linear transformation with $q = 4.5$ for a source placed at different position. (a) $r' = R_A$. (b) $r' = R_B$. (c) $r' = R_C$.

As shown in Figure 2-10, it is very clear that when we place the source at different positions, similar electric field distributions can be observed. These three positions referred as R_A , R_B and

R_C (Figure 2-7(b)), should correspond to the following relation: $q * R_A = (a * R_B) + b = R_C$

Even when the real source is placed in the compression zone, the virtual emission can be observed either in the material shell or in vacuum, as illustrated in Figure 2-3.

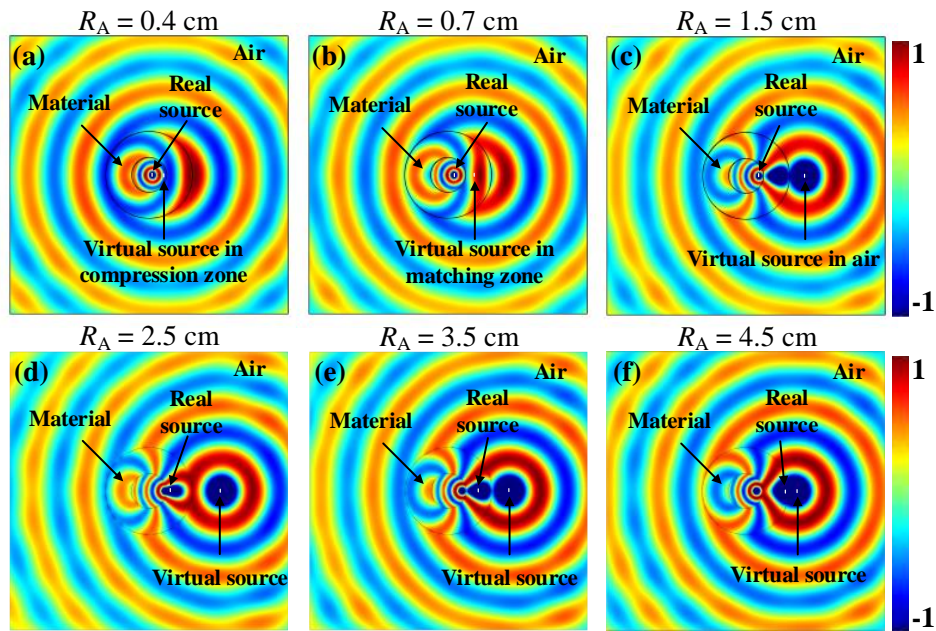


Figure 2-11: Electric field distribution in the case of a linear transformation with $q = 4.5$ for a source placed at different position in the compression zone. (a) $R_A = 0.4$ cm. (b) $R_A = 0.7$ cm. (c) $R_A = 1.5$ cm. (d) $R_A = 2.5$ cm. (e) $R_A = 3.5$ cm. (f) $R_A = 4.5$ cm.

When the source is placed in the region $0 \leq r \leq R_1/q$ as in Figure 2-11(a), the virtual emission will be located in the compression zone. However the real source placed in the region $R_1/q \leq r \leq R_2/q$ produces a virtual emission in the matching zone (Figure 2-11(b)). Finally, when the source is placed in the region $R_2/q \leq r \leq R_2$ as in Figure 2-11(c), the virtual emission is produced in vacuum outside the material shell.

In Figure 2-11(d) – (f), we continue another study of the positions of the real source in the extension region. When the real source moves further from the centre of the material shell, the position of the virtual source moves back closer to the centre of the shell. This can be explained by the principle of this linear transformation as shown in Figure 2-7 in the extension zone.

2.3.3 Parametric study of the dimensions of the shell

In this study, we fix the scale factor $q = 4.5$. The position of the real source will always be at the same location as we mentioned just before. First we make a parametric study on the dimensions R_1 and R_2 of the shell, while keeping the ratio R_1/R_2 always equals to $2/5$.

The results are presented in Figure 2-12. We increase the dimension R_2 of the shell from 5 cm to 10 cm, and as shown in the figure, the distribution of the electric field E_z inside the shell is scaled. But the distribution of the electric field outside the shell remains the same. No matter how large the shell is, the virtual source always appears at $r = 8.55$ cm. Of course this is only true in the situation that the real source remains at the same location and in the compression region. So, we can conclude that as long as the ratio of the thickness of the two regions remains the same, the location of the virtual source doesn't depend on the dimension of the shell.

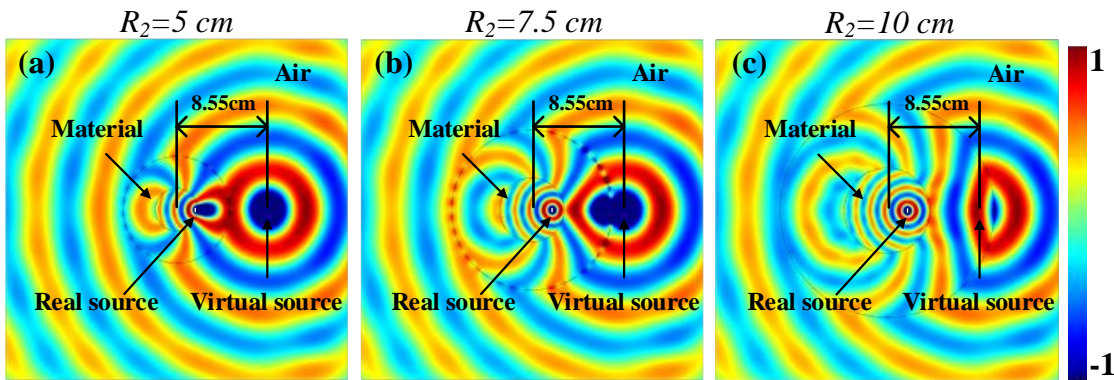


Figure 2-12: Electric field (E_z) distribution of a point source placed at the position $(x, y) = (1.9 \text{ cm}, 0 \text{ cm})$ in the material defined by the linear transformation, and the value $R_1/R_2 = 2/5$. (a) Transformation with $R_2 = 5$ cm. (b) Transformation with $R_2 = 7.5$ cm. (c) Transformation with $R_2 = 10$ cm.

What if we change this ratio? We carry on this study by fixing $R_2 = 5$ cm, and varying the value of R_1 . The outer boundary of the material shell remains the same, and the radius of the compression region increases from 2 cm to 4 cm. We can observe in Figure 2-13 that the same

phenomenon as in the last parametric study appears. The distribution of the electric field inside the shell is scaled. But the distribution of the electric field outside the shell remains the same. So we can also conclude that in the case of the real source remaining at the same location and in the compression region, the location of the virtual source does not depend on the dimension of the shell.

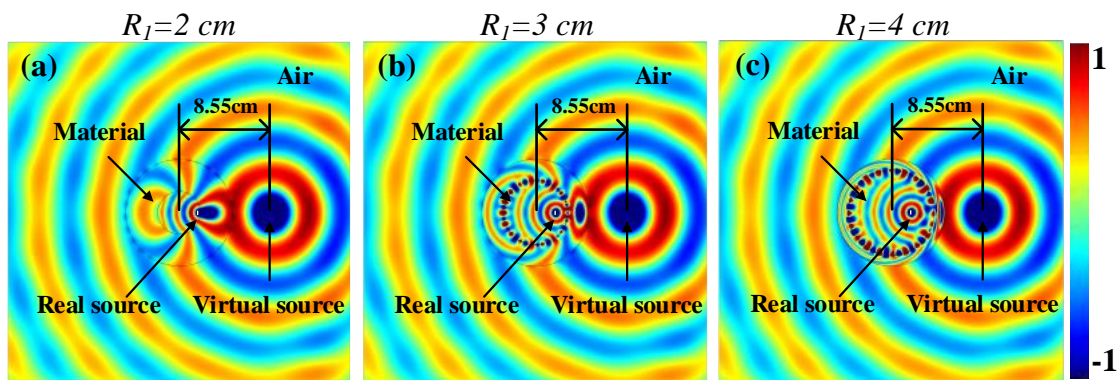


Figure 2-13: Electric field (E_z) distribution of a point source placed at the position $(x, y) = (1.9 \text{ cm}, 0 \text{ cm})$ in the material defined by the linear transformation, and the value $R_2 = 5 \text{ cm}$. (a) Transformation with $R_1 = 2 \text{ cm}$. (b) Transformation with $R_1 = 3 \text{ cm}$. (c) Transformation with $R_1 = 4 \text{ cm}$.

2.4 LAYERED MATERIAL DESIGN

The simulations in the previous section have shown the possibility of achieving a delocalization of electromagnetic radiation. A possible realization is considered at a frequency of 10 GHz. In order to realize the material described in Figure 2-8, the shell is discretized into seven zones; one zone in the central region with radius $R_1 = 2 \text{ cm}$, where space is compressed and six others for the matching zone corresponding to negative permittivity and permeability values.

If we consider a metamaterial unit cell with dimension 5 mm at the operating frequency of 10 GHz, four cells will then be used in the first zone and one cell only is needed in each of the other six zones. Choosing a polarization along z for the magnetic field direction, we are able to

deal only with three effective parameters, which are μ_{zz} , ϵ_{rr} and $\epsilon_{\theta\theta}$. The discretized zones are illustrated in Figure 2-14(a) and (b).

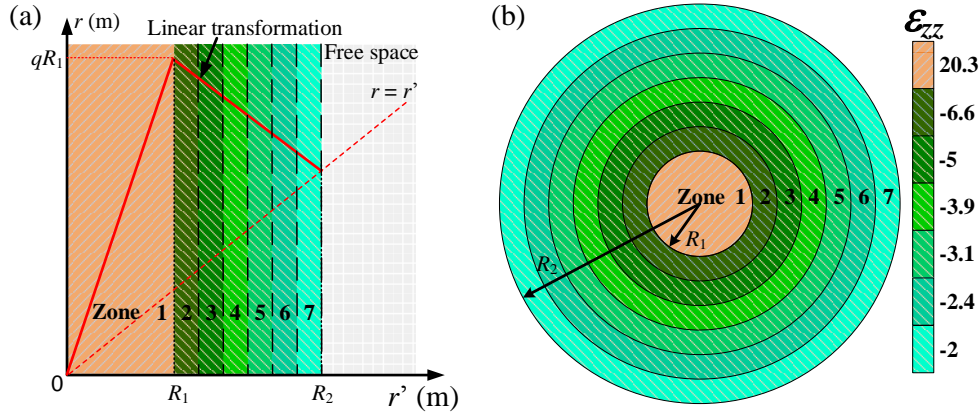


Figure 2-14: Representation of the linear transformation and the layered material for a possible physical realization. The material is discretized into seven zones.

The thickness of the layers in the matching zone are set to $d = 5$ mm in order to design the metamaterial cells and this model will later be tested under the frequency 10 GHz with the wavelength of 3 cm. Using a compression ration $q = 4.5$ at such frequency, it will be possible to show the change in nature of the electromagnetic radiation. We assume the value in the centre of each zone to be the value of the whole zone. The material parameter values, namely μ_{zz} , ϵ_{rr} and $\epsilon_{\theta\theta}$, are summarized in Table 2-I.

Split Ring Resonators (SRRs) [120], known to produce a magnetic resonance where the permeability ranges from negative to positive values, can be efficiently used to produce the μ_{zz} values. Cut wires [121] or electric-LC (ELC) [97] resonators are good candidates to produce the ϵ_{rr} and $\epsilon_{\theta\theta}$ values as we have introduced in Chapter 1. As stated in the introduction chapter, metamaterial resonators such as SRRs, ELCs and cut wires can be considered to produce the desired material parameters. The previous achievements using these metamaterial resonators suggest that the material parameters can be realized through the use of metamaterial structures and that the proposed device is feasible.

Table 2-I: Discretization of the parameters for the layered material shell.

Zone	μ_{zz}	ϵ_{rr}	$\epsilon_{\theta\theta}$
1	20.3	1	1
2	-6.6	-2.2	-0.3
3	-5	-1.7	-0.4
4	-3.9	-1.3	-0.5
5	-3.1	-1	-0.6
6	-2.4	-0.8	-0.7
7	-2	-0.7	-0.9

Full wave simulations are performed with the layered material having electromagnetic parameters of Table I and the performances of the device are presented in Figure 2-15.

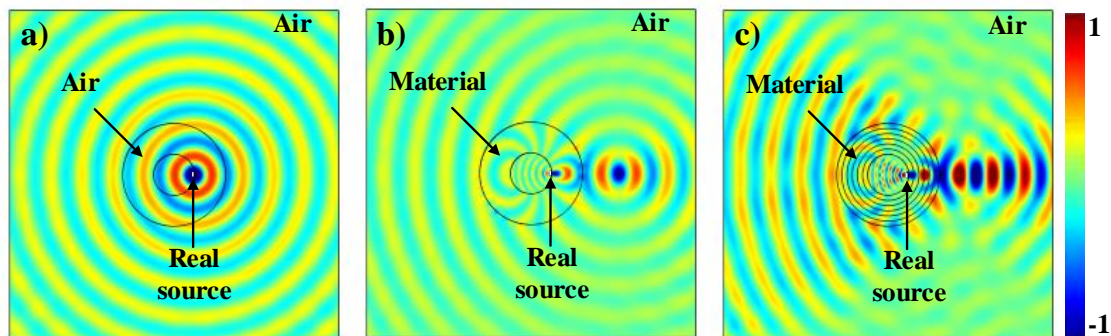


Figure 2-15: Magnetic field distribution for TM wave polarization at 10 GHz. (a) Source in free space. (b) Source in the continuous transformed material shell. (c) Source in the discretized material shell.

To verify the wide band device, we perform this study at 10 GHz, where the wavelength is 3 mm while the thickness of each layer is 5 mm. The radiation emitted at 10 GHz by the current line source in free space is presented in Figure 2-15(a). The observed field distribution is isotropic as previously shown at 5 GHz in Figure 2-9(a). Figure 2-15(b) and (c) show the field distribution when the source is placed at 1.9 cm from the centre in respectively the continuous

material shell and the discretized shell. Even if the reconstruction of the wavefronts is not perfect due to the discontinuity of the discretized material, the field distributions are in good qualitative agreement with the simulation performed using the continuous material parameters.

We can clearly observe that the radiation pattern of the source in the transformed material is directive. This is due to the compression of the space in which the source is placed. A higher q at 5 GHz leads to similar change in radiation pattern as shown in Figure 2-16.

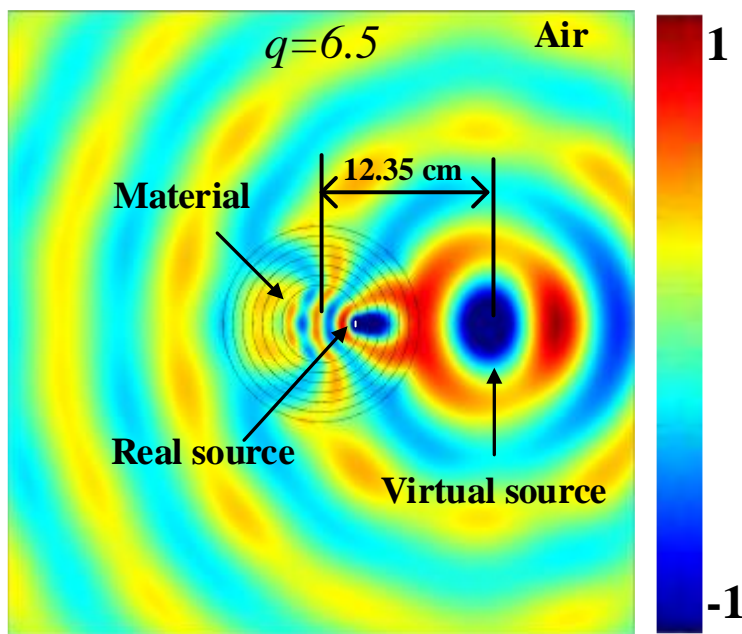


Figure 2-16: Directive radiation pattern at 5 GHz when a higher q is applied.

Finally, we should mention that the use of metamaterials implies the presence of losses due to their resonant nature. Since a negative index medium is needed in the device to amplify evanescent waves so as to obtain an image as clear as the source, the device will be very sensitive to losses. High losses in the negative index medium will definitely deteriorate the image formed and no delocalization will be observed, presented in Figure 2-17.

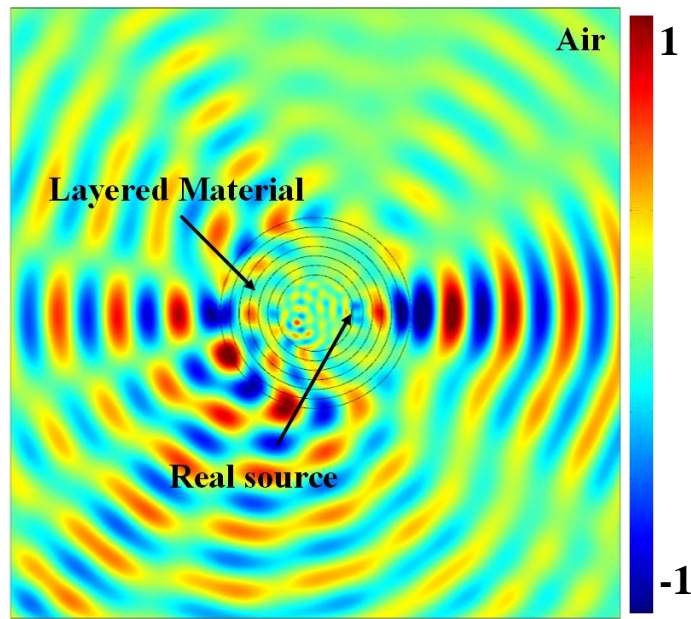


Figure 2-17: High loss in the negative index deteriorates the delocalization.

2.5 CONCLUSION

In this chapter, we have introduced a delocalization device designed using two kinds of coordinate transformations. The device can create an image of the real source in the radiated field by folding the space. A sinusoidal transformation is first applied. This transformation can achieve the illusion functionality by only one step of transformation, but the parameters values are too high to achieve. Then a linear transformation has been used to design the material that is able of producing a virtual emission outside the latter material with achievable values of the metamaterial parameters. When the real source remains at the same location and in the compression region, the location of the virtual source doesn't depend on the dimension of the shell. If the real source in the compression zone is close to the boundary or just inside the extension zone, two other images will be created. Here we try to place the real source in the compressing region inside the core shell, in order to create a ghost target outside the shell to protect the real source from radar detectors or other potential usage. For a practical fabrication of the device with common metamaterial structures, a layered material has also been proposed

and tested at 10 GHz. But this discretization is still not perfect and must be optimized. It has been shown that the material shell creates the illusion that an electromagnetic radiation comes from outside the shell while the real source is placed in the latter. But for the moment, due to the complex permittivity and permeability distributions, it is still difficult for us to achieve simultaneously the three material parameters of the device.

3 WAVEGUIDE TAPER

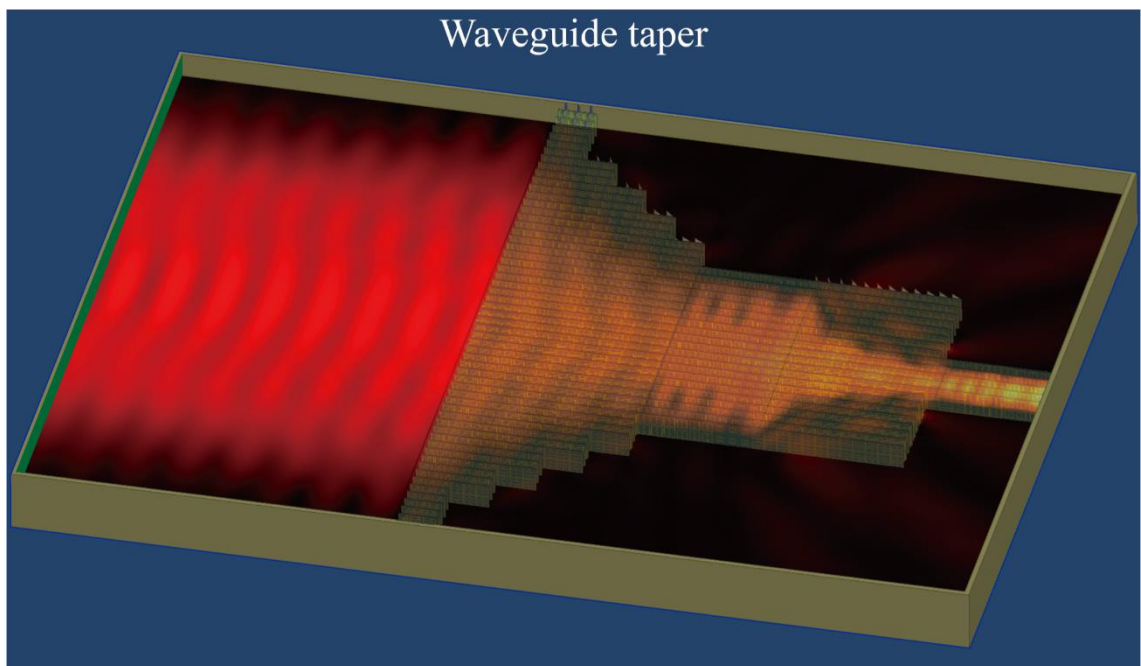


Figure 3-1: Sketch diagram of the waveguide tapering functionality.

In this chapter, we propose a scheme to taper the electric field from a wide waveguide into an output waveguide that is 11.4 time smaller than the input one, as presented in Figure 3-1. In closed rectangular waveguides, due to the cut-off frequency of the output waveguide, the taper can also perform as a mode selector. A complex parameter tensor is simplified first by eigenvalues and then reduced by assuming certain polarization and dispersion for potential

experimental realization. The taper is designed and fabricated by common metamaterial resonators. Very good tapering and transmission are achieved in 2-D full wave simulations for both continuous and discrete models. Experiments in the microwave frequency range demonstrate reasonable performances.

3.1 Introduction.

Tapering devices have been discussed in a previous research work of our group. A tapering device between two waveguides that are 5 times different in width have been proposed in 2010 by P.-H. Tichit. Since this first proposition, it has drawn interests from many researchers all around the world. Plenty of designs have been explored on this subject. But none of these designs made a significant breakthrough, nor experimental validation realized.

Basically there are two main reasons that limit the development of this subject. The first reason is that the value of the permittivity and permeability relies on the difference of the width of the two waveguide. The larger this difference is, the higher permittivity and permeability value one can obtain. When the input waveguide is 4 or 5 times wider than the output waveguide, the parameters can reach about 25, which is already the maximum value for metamaterial resonators to realize. The second reason is the complex material properties. In most cases, there exist four parameters to realize. This is also a big challenge to overcome.

But in this thesis, these two problems are solved. In the model I proposed, the width for the input waveguide is 11.4 times of the width of the output waveguide. We manage to achieve this huge difference by achievable permittivity and permeability. Moreover, by several successive steps of parameter reduction, we simplify the four parameters into two. And a prototype is fabricated and experimentally verified.

In P.-H. Tichit's work, three different kinds of transformation were introduced: linear, parabolic and exponential [67]. The sketches and formulations of these three kinds of transformation are

presented in Figure 3-2.

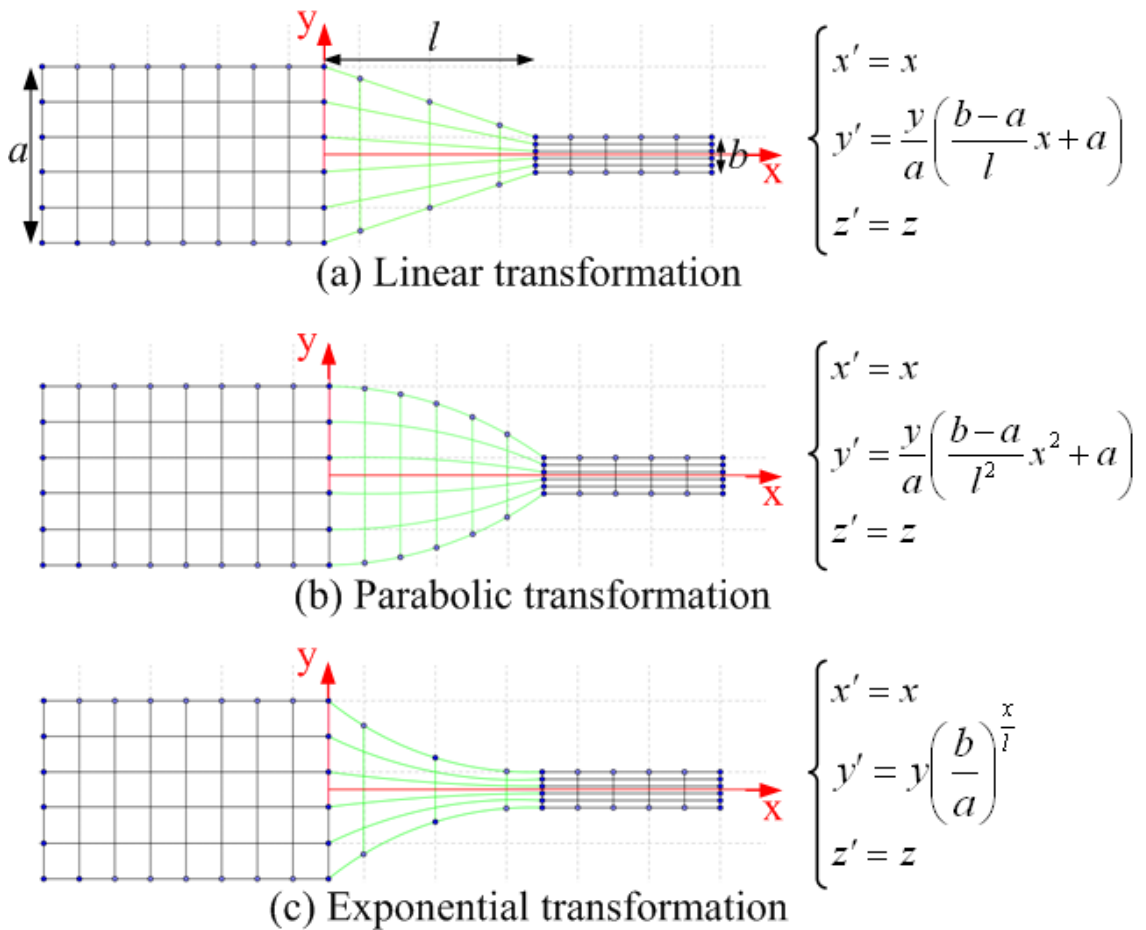


Figure 3-2: Transformed taper (green lines) between two waveguides (black lines) with different cross sections. (a) Linear, (b) parabolic, and (c) exponential transformation formulations [66].

Each waveguide is represented by black lines in its respective space given in Cartesian coordinates. The aim is to connect each horizontal lines of each space to assure full transmission of electromagnetic waves. Thus in geometric approximation, each ray of light in the first waveguide is guided into the second one by green lines representing the taper. For the first formulation, we assume a linear transformation by connecting both spaces with straight lines as shown in Figure 3-2(a). The second formulation uses a parabolic transformation to achieve the connection (Figure 3-2(b)). For the third one, an exponential transformation is defined as shown

in Figure 3-2(c). In all three cases, the geometrical properties of the schematic design under analysis remain unchanged. The width of the input and output waveguides is respectively noted a and b , and the length of the taper in all three cases is taken to be l . Mathematical expressions defining each formulation of the transformation approaches are given in Figure 3-2. x' , y' and z' are the coordinates in the transformed (new) space and x , y and z are those in the initial space. As it can be observed from the mathematical expressions, the different formulations depend on the geometric parameters (a , b , l).

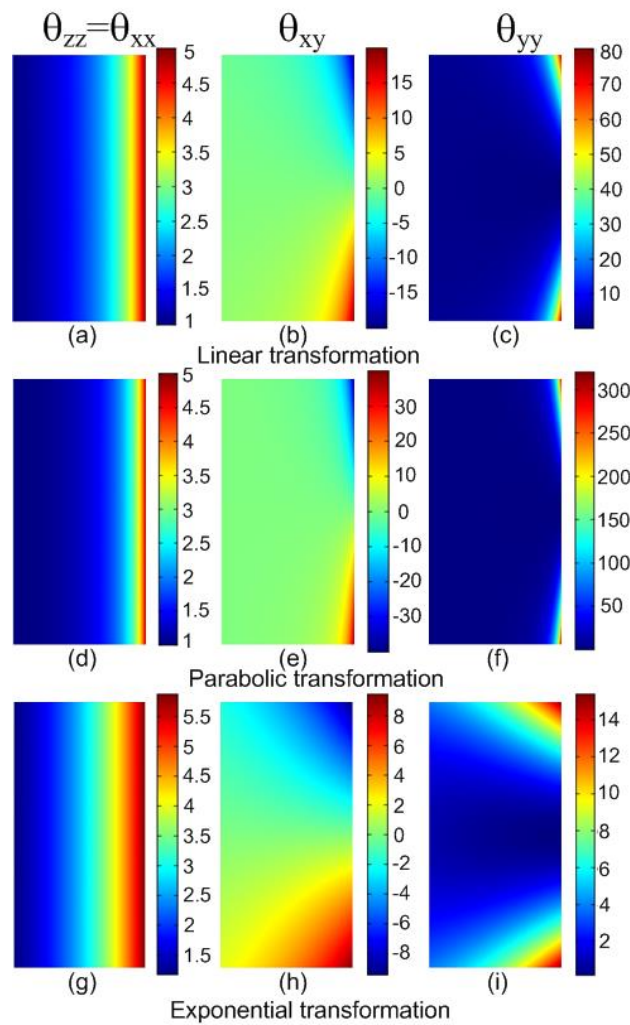


Figure 3-3: Representation of components of the permittivity and permeability tensors $\bar{\theta}$ for the three transformations with $a = 10$ cm, $b = 2$ cm and $l = 5$ cm.

The waveguides widths are chosen to be $a = 10$ cm and $b = 2$ cm with respectively 1.5 GHz and 7.5 GHz cut-off frequencies. Length of the taper is chosen as $l = 5$ cm allowing to generate the entire spatial dependence of the material parameters $\theta_{xx}(x')$, $\theta_{zz}(x')$, $\theta_{xy}(x',y')$ and $\theta_{yy}(x',y')$ as shown in Figure 3-3. Values of permittivities and permeabilities presented in Figure 3-3 account for the control of the electromagnetic field in the taper and the conservation of the propagating modes from waveguide 1 to waveguide 2. Although quasi-similar spatial distribution profile can be observed for the three different formulations, parameters values are completely different. For linear and parabolic transformations, values of θ_{yy} are too high to be physically achievable with existing metamaterials. However, it is clear that the exponential transformation leads to values more easily achievable with metamaterials.

In Tichit's study, the size difference between the input and output waveguides is only 5 times, which is limited by the unachievable large parameter values. My contribution in this field is to develop this tapering device by increasing the size difference between the input and output waveguide to 11.4 times. My final goal is to realize a prototype for an experimental demonstration of the tapering device.

3.2 Spatial coordinate transformation formulation

In order to study the performance of different kinds of coordinate transformations and the material properties they provide, we introduce four other types of transformations. These are: cosinusoidal, parabolic, logarithmic and reciprocal transformations. We compare their permittivity and permeability distributions and the electric field distributions in the device respectively. For all the models of the four new transformations in this chapter, the width of the input waveguide is set to $a = 28.5$ cm and the width of the output waveguide is set to $b_2 = 2.5$ cm. The length of the taper l is fixed to 18 cm. The following designs will be tested at 8 GHz in simulations.

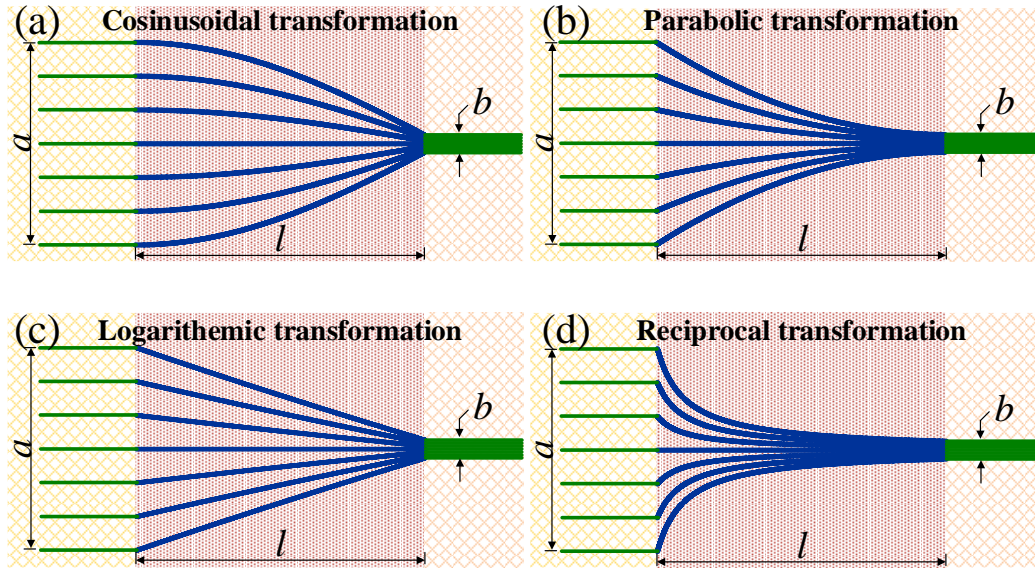


Figure 3-4: Sketch diagram of four kinds of transformation. (a) cosinusoidal, (b) parabolic, (c) logarithmic and (d) reciprocal transformation.

3.2.1 Cosinusoidal transformation

Firstly a cosinusoidal transformation is introduced. At the beginning of the taper, when $y = a/2$, the cosinusoidal function starts from its maximum, while at the end of the taper, the function stops at its minimum. The formulation of the transformation approach is presented in the Equation below:

$$\begin{cases} x' = x \\ y' = y \cos(kx) \\ z' = z \end{cases} \quad (3-1)$$

where $k = \arccos(b/a)/l$.

Figure 3-5 shows the permittivity and permeability distributions of this transformation. For ψ_{xx} and ψ_{zz} , the range of values is achievable. But the negative value -152 for ψ_{xy} and the positive value 2026 for ψ_{yy} are impossible to realize.

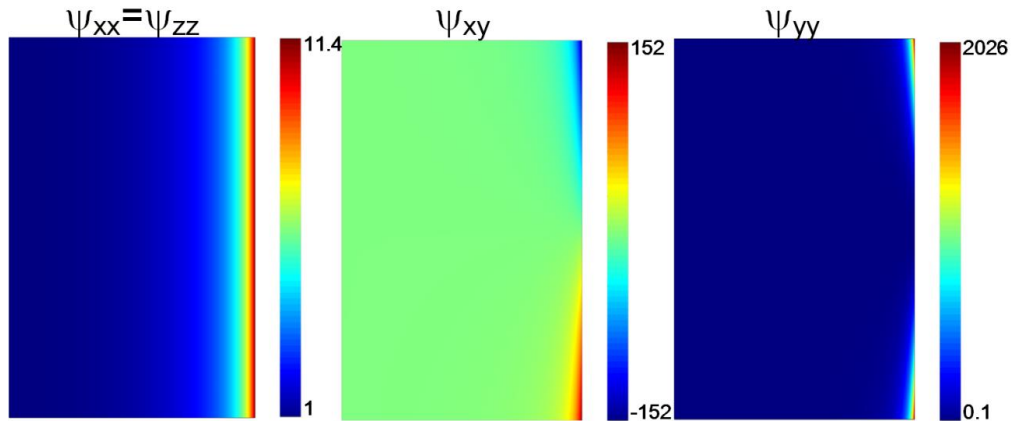


Figure 3-5: Representation of components of the permittivity and permeability tensors θ for the cosinusoidal transformation.

The corresponding electric field amplitude and norm are presented in Figure 3-6. The wavefronts show a clear curve of a cosinusoidal function. But in the output waveguide, the field is very weak. In other words, the transmission is quite low.

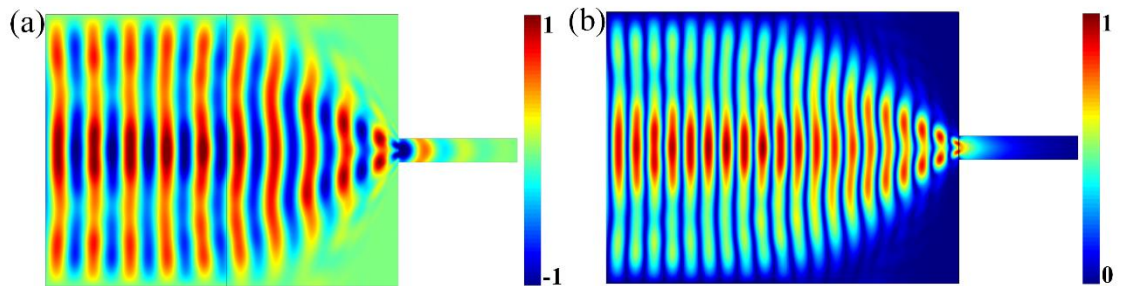


Figure 3-6: (a) Real part of electric field and (b) norm of electric field distribution for the cosinusoidal transformation.

3.2.2 Parabolic transformation

The parabolic function introduced in this section is a concave upward function. The minimum of this function appears at the end of the taper when $y = b_l/2$. The formulation of the transformation approach is presented in the Equation (3-2):

$$(3-2)$$

where $m = \frac{a-b}{a^2}$ and $n = \frac{b}{a}$.

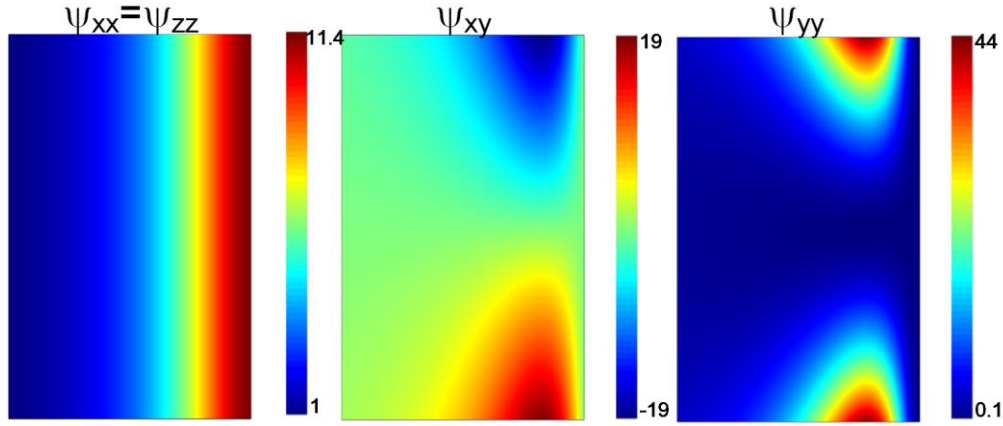


Figure 3-7: Representation of components of the permittivity and permeability tensors θ for the parabolic transformation.

Figure 3-7 shows the permittivity and permeability distributions of this transformation. For ψ_{xx} and ψ_{zz} , the range of values is achievable. But the negative value -19 for ψ_{xy} remains unrealizable.

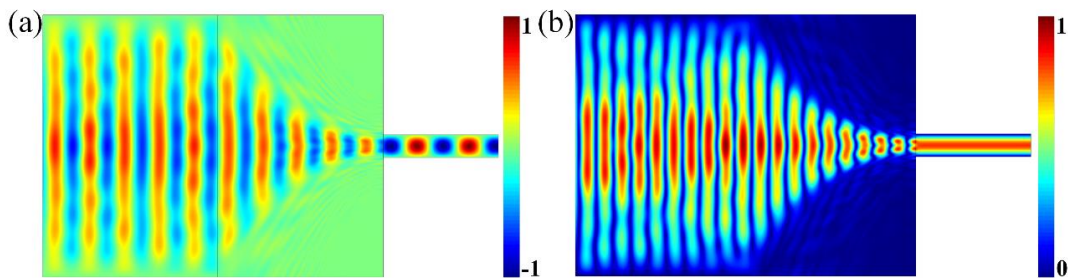


Figure 3-8: (a) Real part of electric field and (b) norm of electric field distribution for the parabolic transformation.

The electric field and norm of electric field for such configuration are presented in Figure 3-8 respectively. The wavefronts show a clear curve of a parabolic function. In the output waveguide, the field is stronger than the one in the cosinusoidal transformation, but a reflection can be observed from the norm of electric field in Figure 3-8(b).

3.2.3 Logarithmic transformation

We continue our study on the logarithmic transformation. The logarithm function has a negative coefficient. So the function decreases from $a/2$ when $x = 0$ to $b/2$ when $x = l$. The formulation of the transformation approach is presented in the Equation (3-3):

$$\begin{cases} x' = x \\ y' = \frac{2y}{a} \left(\frac{a}{2} - \ln(mx + 1) \right) \\ z' = z \end{cases} \quad (3-3)$$

where $m = \frac{e^{\frac{a-b}{2}} - 1}{l}$.

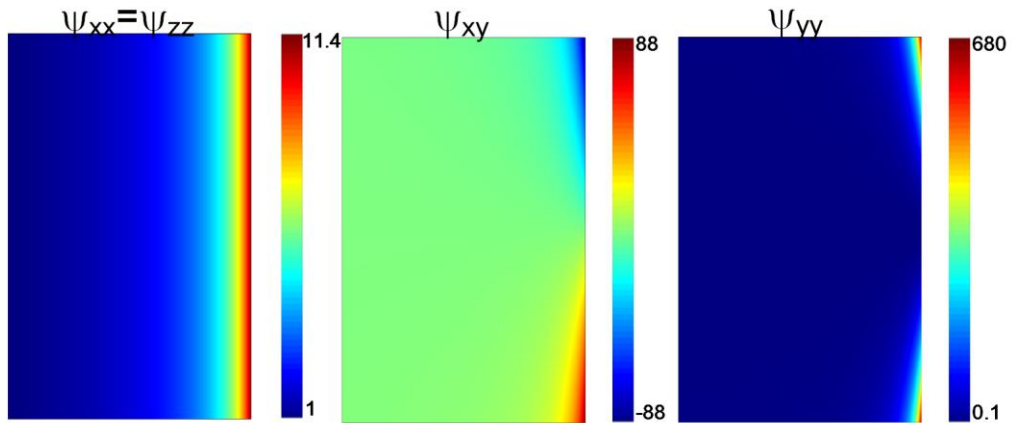


Figure 3-9: Representation of components of the permittivity and permeability tensors θ for the logarithmic transformation.

The permittivity and permeability distributions of this logarithmic transformation are presented in Figure 3-9. For ψ_{xx} and ψ_{zz} , the range of values is achievable. But the negative value -88 for ψ_{xy} and the positive value 680 for ψ_{yy} are impossible to realize.

Then we check the field distribution. Figure 3-10 presents the electric field and norm of electric field distributions. The wavefronts show a clear curve of a logarithmic function. In the output waveguide, the field is stronger than the one in the cosinusoidal transformation and almost similar to the one in the parabolic transformation.

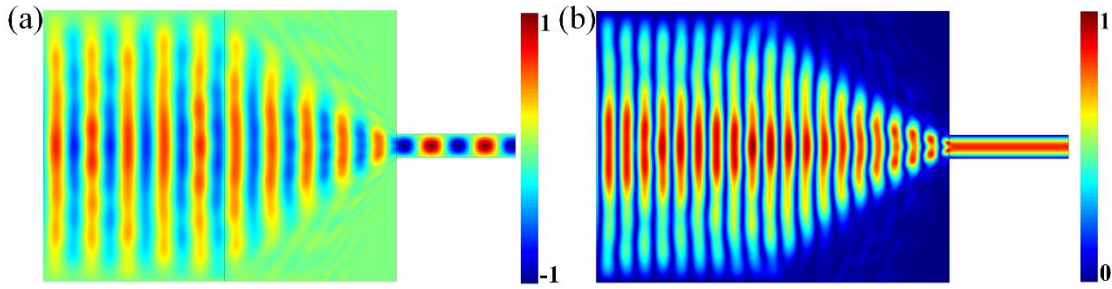


Figure 3-10: (a) Real part of electric field and (b) norm of electric field distribution for the logarithm transformation.

3.2.4 Reciprocal transformation

Finally a reciprocal transformation is introduced. The formulation of the transformation approach is presented in the Equation (3-4):

$$\begin{cases} x' = x \\ y' = y \frac{2m}{a(x+n)} \\ z' = z \end{cases} \quad (3-4)$$

Where $m = \frac{abl}{2(a-b)}$ and $n = \frac{bl}{a-b}$.

The permittivity and permeability distributions of the reciprocal transformation is presented in Figure 3-11. For ψ_{xx} , ψ_{zz} and ψ_{xy} , the range of the value is achievable. But the positive value 69 for ψ_{yy} is impossible to realize.

Figure 3-12 shows the electric field amplitude and norm distributions. In the output waveguide, the field in this transformation configuration is the strongest among the four proposed types of transformations.

Even though the transmission from the reciprocal transformation is much better than any other transformations we have introduced, there is still a parameter that we cannot realize for the moment. So we have to explore another method which can taper the cross section of two waveguides of width ratio 11.4 by achievable material properties.

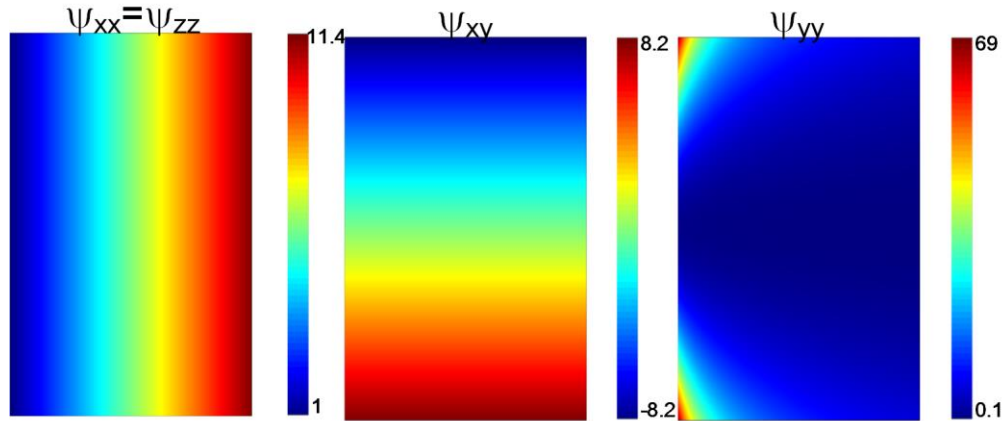


Figure 3-11: Representation of components of the permittivity and permeability tensors θ for the reciprocal transformation.

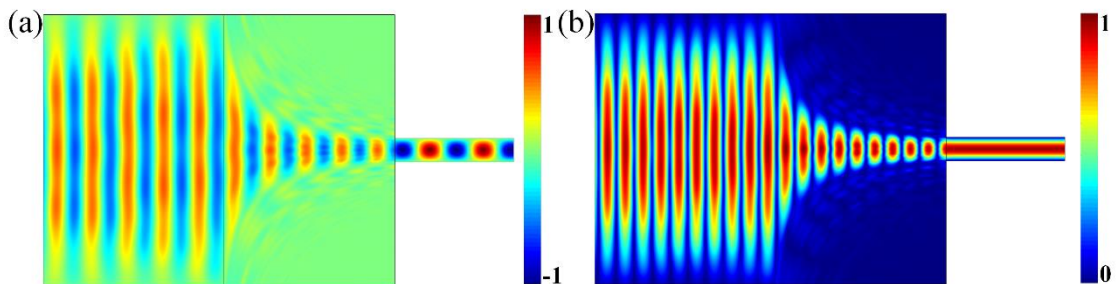


Figure 3-12: (a) Real part of electric field and (b) norm of electric field distribution for the reciprocal transformation.

3.3 Two tapers and two adapters system

In this section, we introduce a two tapers and two adapters system in order to be able to propose a realistic solution for prototyping. The top view of the structure of the system is presented in Figure 3-13. The input and output waveguides are shown as the dark red zones in free space with isotropic permittivity and permeability tensors $\epsilon^{ij} = \mu^{ij} = \delta^{ij}$. Two different formulations, corresponding to two taper parts (the orange zones), are proposed to achieve a low reflection taper between two waveguides of different cross sections. Thus in geometric approximation, each ray of light, presented as blue lines, in the first waveguide is guided into the first adapter by the first taper part. And after passing through the first adapter, the wave propagates into the

second taper. Finally the rays are concentrated into the output waveguide. With another adapter at the entrance of the output waveguide, the transmission can achieve -0.2 dB. For the formulations of both the first and second taper parts, we assume a reciprocal function transformation by connecting the two spaces with straight lines as shown in Figure 3-13. The formulations of the adapter parts use a linear decreasing function of index to achieve the connection. The width of the input and output waveguides is respectively noted a and b_2 , the width of the first adapter part is noted b_1 . And the length of the first taper part, first adapter part, second taper part and second adapter part are taken to be l_1 , l_2 , l_3 , l_4 respectively.

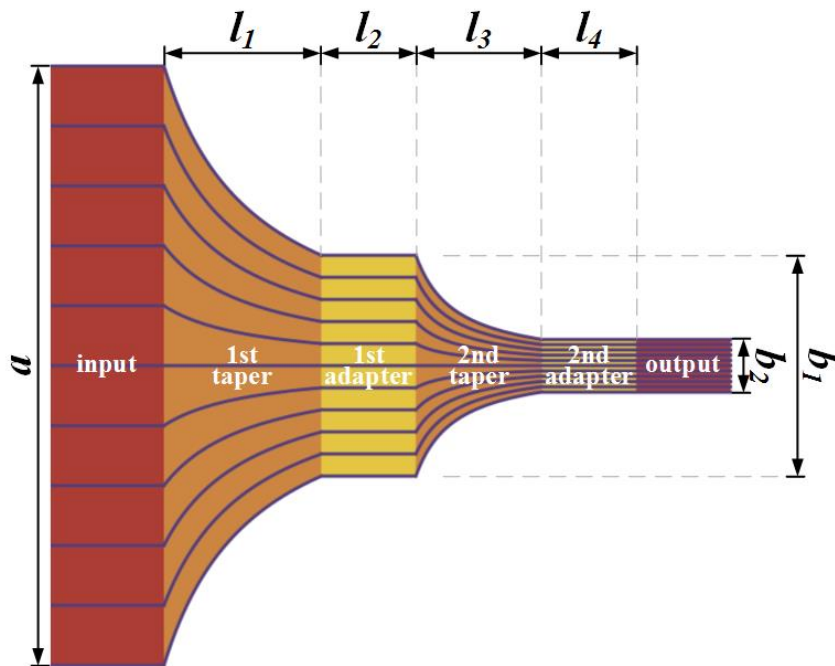


Figure 3-13: Sketch of two transformed tapers (orange zones) and two adapters (yellow zones) device between two waveguides (red zones) with different cross sections.

Mathematical expressions defining each formulation of the transformation approaches are given in Equation (2-5) and (2-6). x' , y' and z' are the coordinates in the transformed (new) space while x , y and z are those in the initial space. As it can be observed from the mathematical expressions, the different formulations depend on the geometric parameters (a , b_1 , l_1) or (b_1 , b_2 , l_3).

Formulation of the transformation in the first taper part:

$$\begin{cases} x' = x \\ y' = y * \frac{b_1 l_1}{(a - b_1)x + b_1 l_1} \\ z' = z \end{cases} \quad (3-5)$$

Formulation of the transformation in the second taper part:

$$\begin{cases} x' = x \\ y' = y * \frac{b_2 l_3}{(b_1 - b_2)(x - l_1 - l_2) + b_2 l_3} \\ z' = z \end{cases} \quad (3-6)$$

The electromagnetic properties of the transformation-optical medium can now be readily obtained by calculation. We then can obtain the permittivity and permeability tensors of the two steps of the waveguide tapers.

$$\bar{\theta} = \begin{bmatrix} \theta_{xx}(x', y') & \theta_{xy}(x', y') & 0 \\ \theta_{xy}(x', y') & \theta_{yy}(x', y') & 0 \\ 0 & 0 & \theta_{zz}(x', y') \end{bmatrix} \quad (3-7)$$

The components values of $\bar{\theta}$ tensor are given in Table 3-I where a non-diagonal term (θ_{xy}) appears. This non-diagonal term is necessary to guide electromagnetic waves in the x - y plane like it is the case for this taper.

Figure 3-14 shows the variation in the permittivity and permeability tensor components distribution in the two transformed taper areas.

Table 3-I: Components values of $\bar{\theta}$ tensor for the transformation of two taper parts.

	$\theta_{xx}(x', y') = \theta_{zz}(x', y')$	$\theta_{xy}(x', y')$	$\theta_{yy}(x', y')$
First taper	$\frac{b l_1 + (a - b)x'}{b l_1}$	$\frac{(b - a)y'}{b l_1}$	$\frac{b^2 l_1^2 + (a - b)^2 y'^2}{b^2 l_1^2 - b l_1 (a - b)x'}$
Second taper	$\frac{b_1 l_3 + (b - b_1)(x' - l_1 - l_2)}{b_1 l_3}$	$\frac{(b_1 - b)y'}{b_1 l_3}$	$\frac{(b - b_1)^2 y'^2 + b_1^2 l_3^2}{b_1^2 l_3^2 - b_1 l_3 (b - b_1)(x' - l_1 - l_2)}$

The components for the two taper parts have different expressions. But the principle of the two taper parts are the same, it is just the variables and locations in the coordinate system that are different. As we can see in the table, there exist four parameters for both of the two taper parts. In order to realize this design, a further parameter reduction needs to be performed.

The different geometrical dimensions of the initial and transformed spaces are, $a = 28.5$ cm, $b_1 = 10.5$ cm, $b_2 = 2.5$ cm, $l_1 = 7.5$ cm, $l_2 = l_4 = 4.5$ cm and $l_3 = 6$ cm respectively. For the first taper part, the maximum value is 2.74 and the minimum value is -1.32. And for the second taper part, the maximum value is 7.25 and the minimum value is -2.5. These values can be obtained from electric LC resonators or split rings resonators.

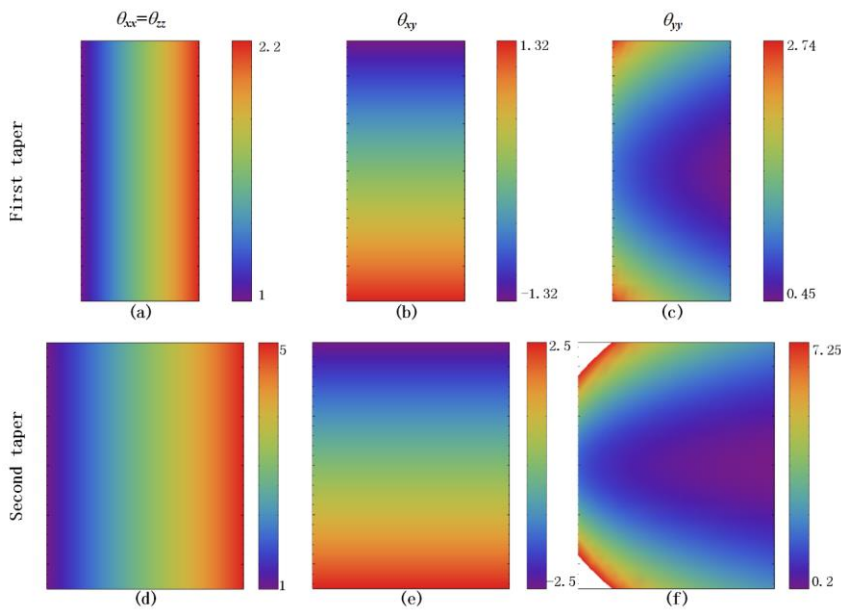


Figure 3-14: Variation of the material parameter tensor components ψ_{xx} , ψ_{xy} , ψ_{yy} and ψ_{zz} of two different taper parts. The dimension variables are $a = 28.5$ cm, $b_1 = 10.5$ cm, $b_2 = 2.5$ cm, $l_1 = 7.5$ cm, $l_2 = l_4 = 4.5$ cm and $l_3 = 6$ cm.

But at this stage, we have another problem. For further realization and validation, the resonators can only provide a permittivity or permeability value in the direction of the electric field or magnetic field. So a further parameter reduction should keep only two components.

Before the parameter reduction, we need to verify the functionality of this tapering system. The

electric field and norm of electric field distribution of this two tapers and two adapters system is presented in Figure 3-15.

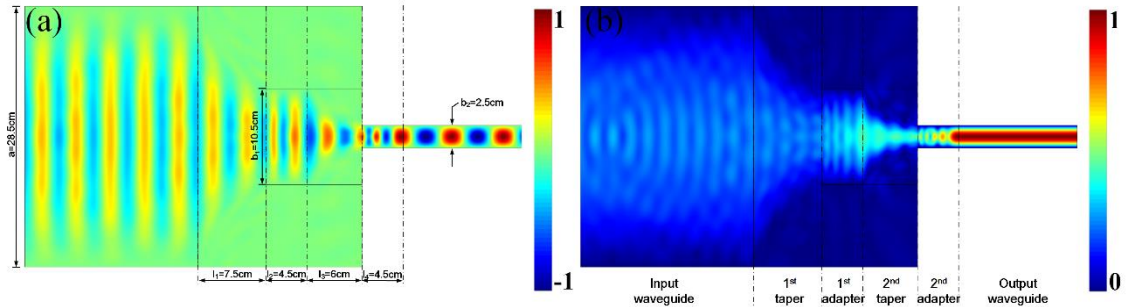


Figure 3-15: (a) Real part of electric field and (b) norm of electric field distribution for the two tapers and two adapters system.

An input wave port is placed on the left boundary while an output wave port is placed on the right boundary of the output waveguide. The electric field is compressed two times in the two taper parts respectively. And the field is adapted by the two adapter parts to minimize the reflection on the boundaries between each two parts. In Figure 3-15(b), the field intensity is light before the tapering, and it becomes extremely high which means highly concentrated after the compression. The transmission of this system can go up to -0.2 dB, i.e. 98%.

3.3.1 Parametric study on the two adapters

The material in the two adapters are isotropic. So the material properties in the adapters are variations of index. In the first adapter, the index starts from n_1 on the left boundary and decreases to 1 on the right boundary. In the second adapter, the index starts from n_2 on the left boundary and decreases to 1 on the right boundary.

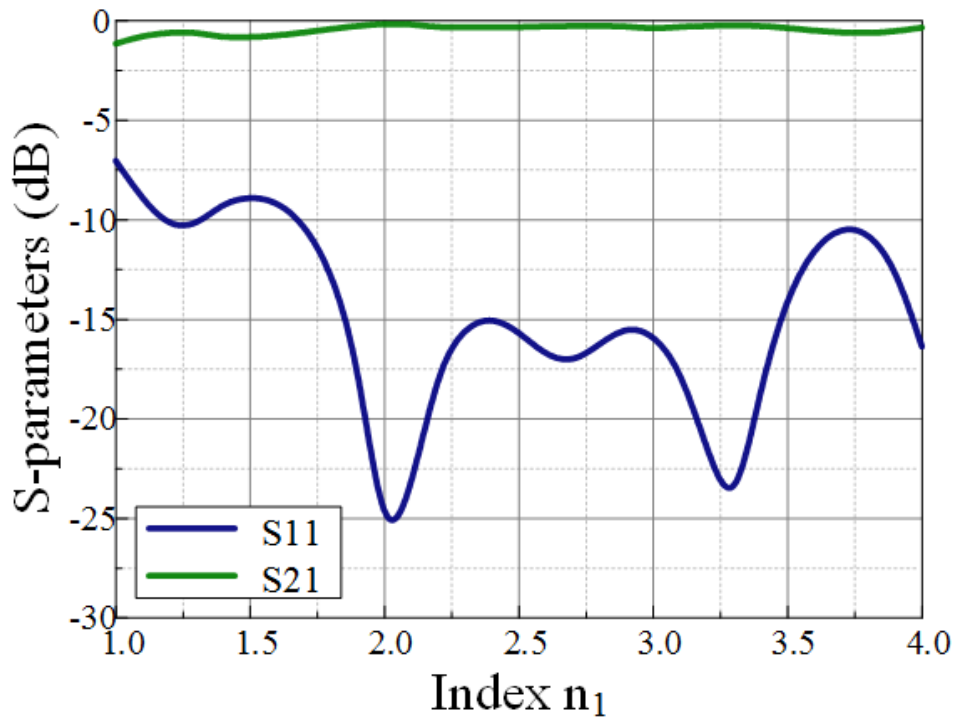


Figure 3-16: Parametric study on the starting index of the first adapter n_1 .

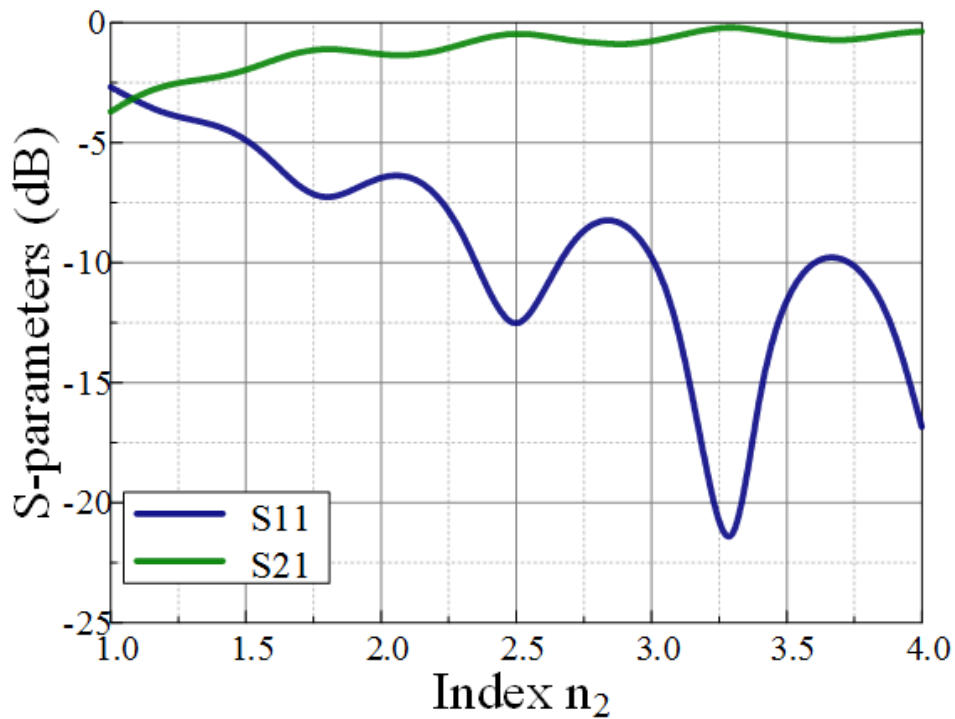


Figure 3-17: Parametric study on the starting index of the second adapter n_2 .

At first, we set $n_2 = 3.3$, and make a parametric study on n_1 from 1 to 4. The total transmission of the system is presented in Figure 3-16. As shown in the figure, when $n_1 = 2.1$, the transmission is closest to 0 dB and the reflection is about -25 dB which is the minimum value throughout the whole study. So we select this value as the starting index value of the first adapter.

For the second adapter. We set $n_1 = 2.1$, and the same parameter study for n_2 is performed from 1 to 4. The result is presented in Figure 3-17. In the curve, we can see that, when $n_2 = 3.3$, the transmission is the highest and the reflection is the lowest. From both of the two parametric studies on the index, we find out the starting index for the two adapters which can ensure the best transmission for the system.

3.3.2 2D discrete model

We discretized the continuous model in Figure 3-15 and full wave simulations have been done to verify the discrete model. We choose the size of the unit cells to be $15 \text{ mm} \times 15 \text{ mm}$ for the two taper parts. The discrete permittivity or permeability of each cell is constant and equals to the permittivity or permeability value at the center of each cell. In this case, the first taper is composed of 95 (19×5) unit cells, while the second taper is composed of 28 (7×4) unit cells.

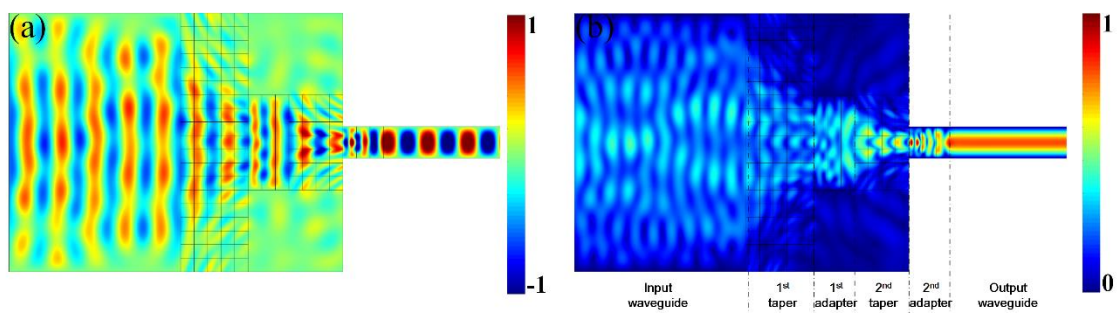


Figure 3-18: (a) Real part of electric field and (b) norm of electric field distribution for 2D discrete two tapers and two adapters system.

For the two adapters, since the index decreases along the direction of the wave propagation, we

only discretize them by 15 mm each step along this direction. The electric field and norm of the electric field distribution for the discrete model is a little bit different than the distribution for the continuous model. The discretization causes some reflections at the interfaces where the index changes. But the transmission can achieve -1.2 dB.

3.3.3 Parameter reduction

Since there are four parameters to realize for the moment, we have to find a way to simplify them by keeping only two of them. In order to do this, we separate the simplification into two steps as shown in Figure 3-19(a).

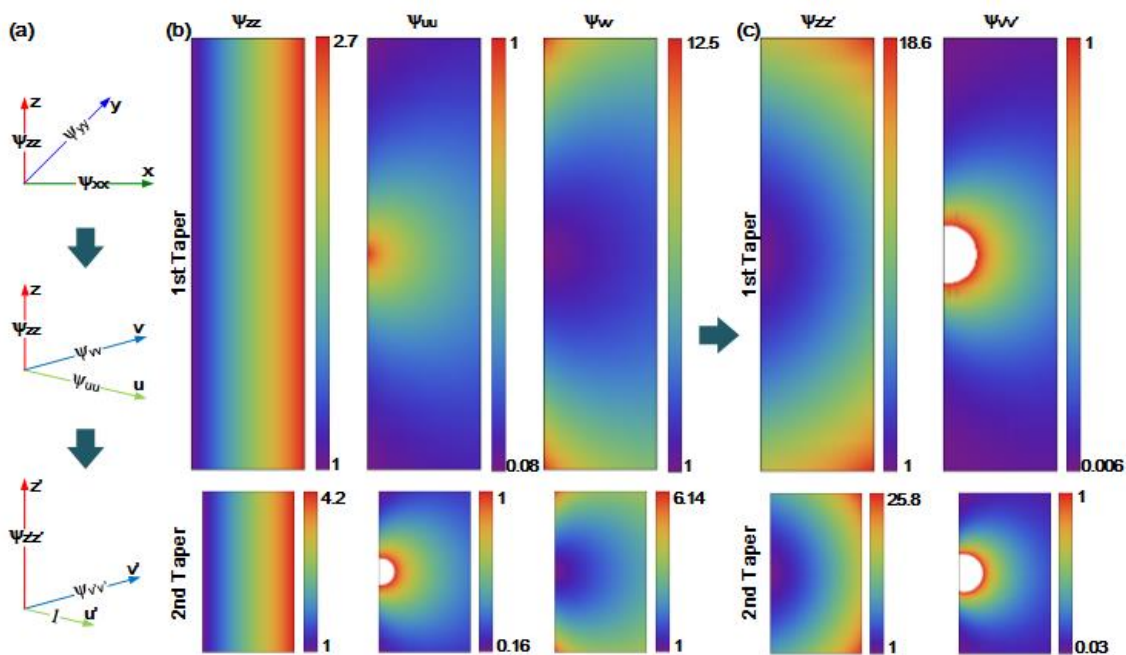


Figure 3-19: (a) Sketch of the principle of the parameter reduction. (b) Permittivity and permeability distribution in the eigenvector coordinate system. (c) Permittivity and permeability distribution after parameter reduction in the eigenvector coordinate system. The source is sometimes saturated and the white region in the figure corresponds to parameters outside the color scale.

The first step is to calculate the eigenvalues and eigenvectors of each unit cell. For each unit cell,

the eigenvectors are different from others. One of the eigenvectors is the same as z -axis. The vector \vec{v} is along the direction of the magnetic field and the other vector \vec{u} is orthogonal to the direction of magnetic field. The permittivity and permeability distributions after the first step are presented in Figure 3-19(b). As we can see, four parameters are reduced to three. And the maximum value is 12.5, which is achievable with metamaterial resonators. Choosing a polarization along z for the electric field, and adjusting the dispersion equation in polar coordinates in each unit cell, a further parameter reduction can be achieved. At last only two parameters are kept. The final parameter distribution after parameter reduction is then presented in Figure 3-19(c). Only two parameters are needed and the maximum value of the permittivity is 25.8.

3.4 Experimental validation using ELC and split rings resonator

We consider here a source that has a z -polarization of electric field. The parameter $\Psi_{z'z'}$ stands for a permittivity component. While the parameter $\Psi_{y'y'}$ stands for a permeability component. The structure of the ELC resonator used to engineer the permittivity parameters of the transformed tapering system is presented in Figure 3-20(a). The 35 μm thick copper resonator is printed on a low loss RT/Duroid[®] 5880 substrate having a dielectric permittivity 2.2, a low loss tangent 0.001 and a thickness $t = 0.51$ mm. The properties of the resonator are characterized numerically using Finite Element Method (FEM) simulations done with ANSYS commercial code HFSS [122]. Using reflection and transmission responses from the sample, effective parameters can be extracted using the retrieval procedure described in Chapter 1 “General Definition”. This is possible since the structure period along the propagation direction is very small compared to the working wavelength.

In performing the retrieval, we assume along propagation direction a z -direction size $p_z = 5$ mm corresponding to a cubic unit cell. Extracted permittivity and permeability are also shown in

Figure 3-20(a). As shown in the figure, the ELC resonator has a resonance at about 8.5 GHz. And At 8 GHz, it can provide a positive permittivity between 5 and 10. With possible variation on the dimension of the structure (a , d , w and t), all the permittivity values that are needed for this tapering system can be achieved.

Figure 3-20(b) represents the structure of the split ring resonator used to engineer the magnetic parameters of the transformed tapering system. The same size of cubic cells is assumed and the same substrate is used for the split rings. The extracted permittivity and permeability are presented in Figure 3-20(b). The split ring resonator gives a magnetic resonance at about 8.5 GHz, so that it will provide the permeability we need for the tapering system by verifying the dimension variables: b , b_1 , g_1 , g_2 .

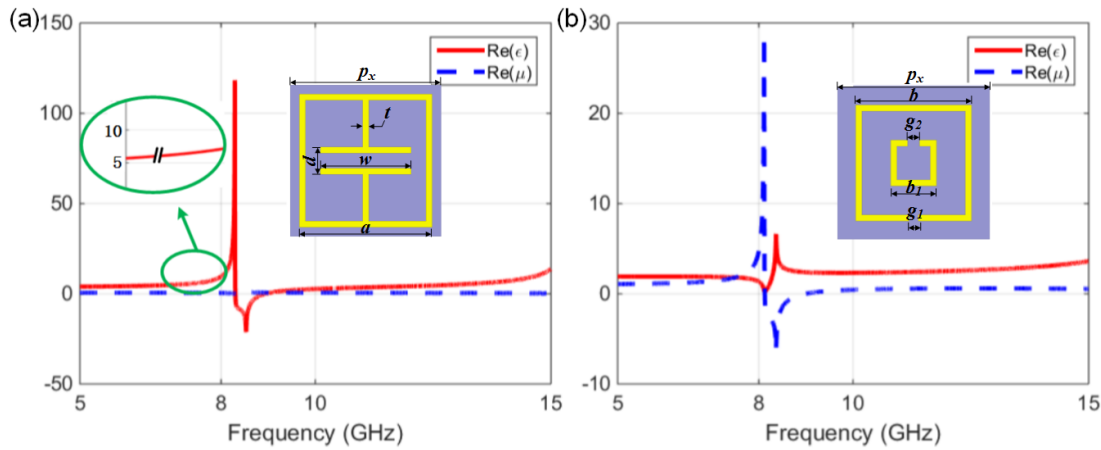


Figure 3-20: (a) Typical ELC unit cell structure and the extracted permittivity and permeability characteristics of such ELC resonator ($p_x = 5$ mm, $a = 4.5$ mm, $t = 0.2$ mm, $d = 0.5$ mm, $w = 3$ mm). (b) Typical split rings unit cell structure and the extracted permittivity and permeability characteristics of such split rings resonator ($p_x = 5$ mm, $b = 4$ mm, $b_1 = 1.8$ mm, $g_1 = 0.4$ mm, $g_2 = 0.3$ mm).

The resonators are assumed to be $5 \text{ mm} \times 5 \text{ mm} \times 5 \text{ mm}$ cubic cells in the simulation. While in the discrete model, the size of unit cells is $15 \text{ mm} \times 15 \text{ mm}$. So to build up the 3D model of the system. Each discretized cell consists of 9 (3×3) ELC resonators for ϵ and 9 (3×3) split ring

resonators for μ in x - y plane. Then we consider a system of 2 cm high along z -axis, which means four identical resonators along z -direction. So a 3D model for this two tapers - two adapters system is first build up (Figure 3-21(a)) and then fabricated by printed circuit board technology. A photography of the prototype is presented in Figure 3-21(b).

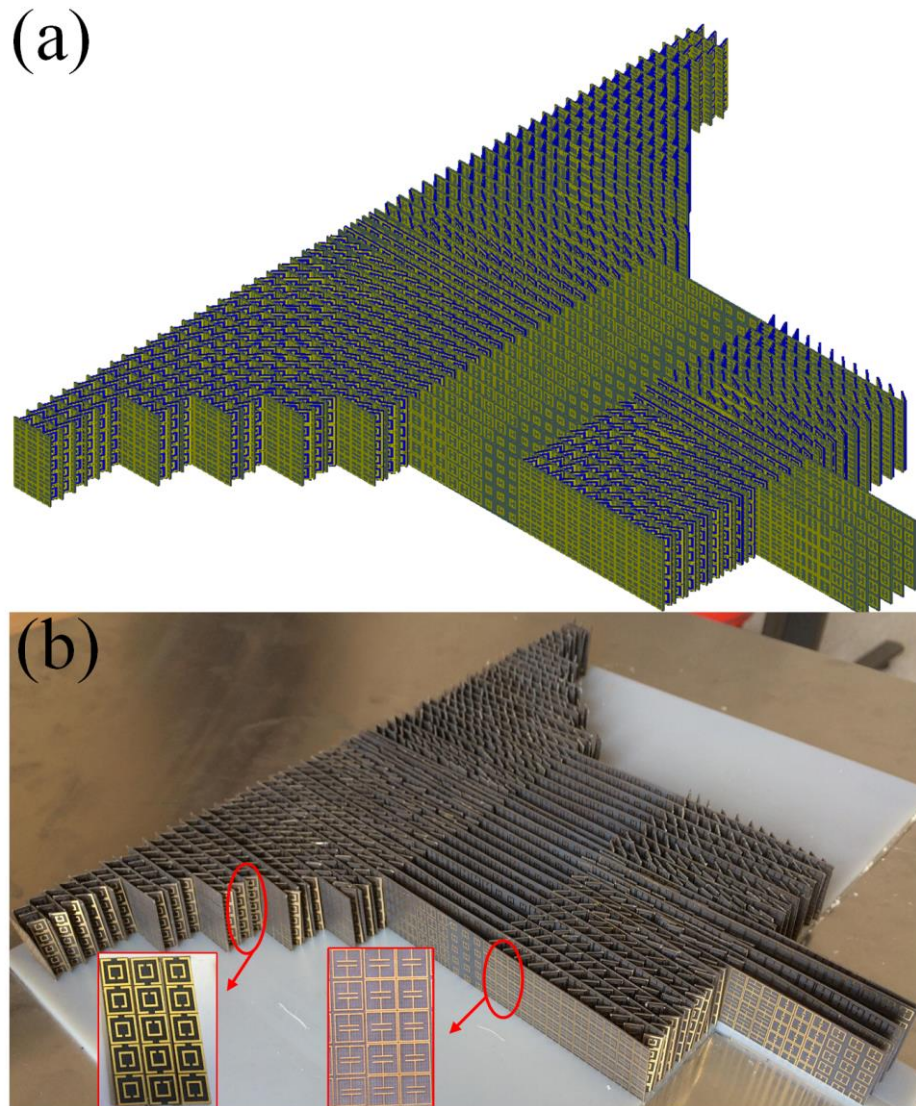


Figure 3-21: (a) 3D discrete model design and (b) the fabricated prototype.

This tapering system requires a directive planar wave input, which is 28.5 cm long. The wave vector has to be orthogonal to the input boundary of the system. But unfortunately in our lab, we cannot provide such a long and directive source at 8 GHz. We have to use the source which is

2.5 cm long. We put this source 25 cm far from the taper in order to have an input that close to plane wave. We simulated this source and the electric field distribution of the source is presented in Figure 3-22(a). As shown in the figure, the wavefronts are not quite planar. And the electric field of the tapering system with this source as input is also numerically calculated and presented in Figure 3-22(b). The field is distorted compared to the simulations with a long wave port as input in Figure 3-18. But we can still observe some compression of the fields inside the taper.

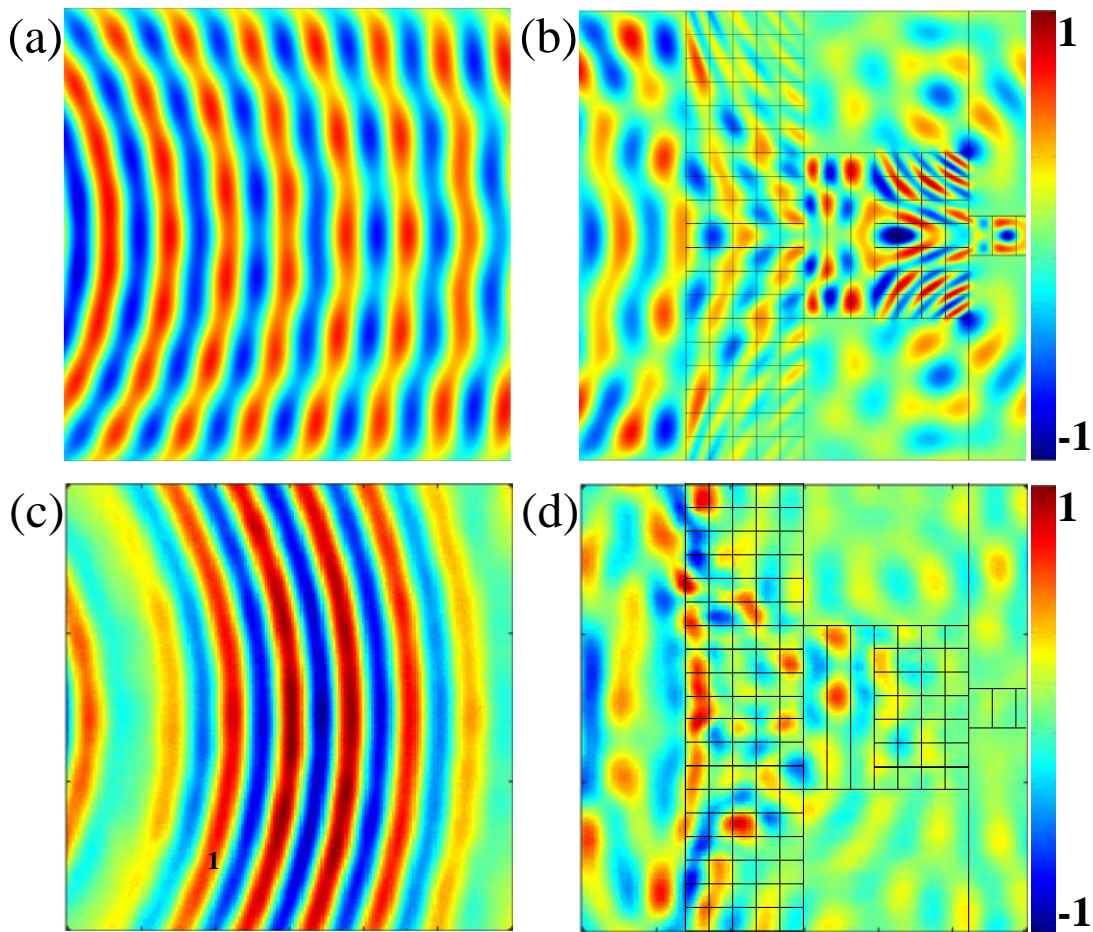


Figure 3-22: Numerically calculated real part of electric field distribution of (a) 2.5 cm source and (b) tapering system. Measured electric field distribution of (c) 2.5 cm source and (d) tapering system. The wavelength is 3.75 cm and the size length of the unit cells is 5 mm.

The electric field is scanned by our near-field measurement system described previously between two parallel metallic plates (TEM waveguide). The electric field of the source and the tapering system are presented in Figure 3-22(c) and (d) respectively. As shown in the figure, a quite overall good qualitative agreement is noted between the simulated and measured characteristics.

3.5 Conclusion

In this chapter, firstly we have firstly presented a review on the former works about the waveguide taper by our group and other research teams. Then four new kinds of coordinate transformations have been introduced with the main goal to fabricate a prototype of this tapering system. These four transformations are compared and discussed both on the provided material properties and the field distributions. Then we considered a tapering system which consists two tapers and two adapters. Such solution allows to work with material parameters that can be obtained from resonant metamaterials. Parametric study are done for the starting index of the two adapters to optimize the transmission. Then the 2D model we designed is discretized and the electric field distribution is calculated for this discrete model. A parameter reduction has been performed to allow working with only two material parameters. One is permittivity and the other one is permeability. ELC and Split Ring Resonators are used to provide permittivity and permeability values respectively at 8 GHz. Finally a 3D model is designed and fabricated. Numerical simulations and measurements of the electric field for both the source and the tapering system are presented and compared. A quite overall good qualitative agreement is noted between the simulated and measured characteristics.

PART II

LENS DESIGNS BY TRANSFORMATION

OPTICS CONCEPT BASED ON LAPLACE'S

EQUATION

Transformation Optics (TO) has enabled to control EM fields in unprecedented and unbelievable ways through the use of judiciously engineered materials with parameters that vary spatially. The designs we introduced based on coordinate transformation have been discussed in Part I.

These structures designed using coordinate transformation concept technique generally exhibit anisotropy and spatial inhomogeneity and sometimes present a challenge for practical implementations, leaving lots of devices unrealized experimentally. Metamaterial structures like split ring resonators (SRR)[30] and electric LC (ELC)[31] resonators, to name the most common, have widely participated in the implementation of TO based devices. However, their resonant nature limits the frequency bandwidth and performances of the devices. To overcome such limitations, quasi-conformal transformation optics (QCTO) has been proposed. QCTO helps to minimize the anisotropy of the constitutive materials, allowing the possibility of all-dielectric implementations. As a result, nearly-isotropic gradient index (GRIN) materials with broad bandwidth and low losses can be employed, opening the way to broadband antennas and devices.

In this part, two lenses that perform different functionalities are presented. Both of these two lenses are designed by the method of transformation optics based on Laplace's equation. This part is composed of three chapters; Chapter 4 to Chapter 5. In Chapter 4, a functional lens, which is capable of restoring in-phase emissions over a broad frequency range, is designed, fabricated and validated experimentally. In Chapter 5, we introduce a lens capable of changing the direction of propagation of an electromagnetic radiated beam. This beam steering lens is also designed using transformation optics based on Laplace's equation. Two different prototypes are proposed for this design. One makes use of electric LC resonators and is fabricated by Printed Circuit Board (PCB) technology, and the other uses an all-dielectric material and is fabricated through 3D printing technology.

4 RESTORING IN-PHASE EMISSIONS FROM NON-PLANAR RADIATING ELEMENTS USING WAVE-MATTER INTERACTION

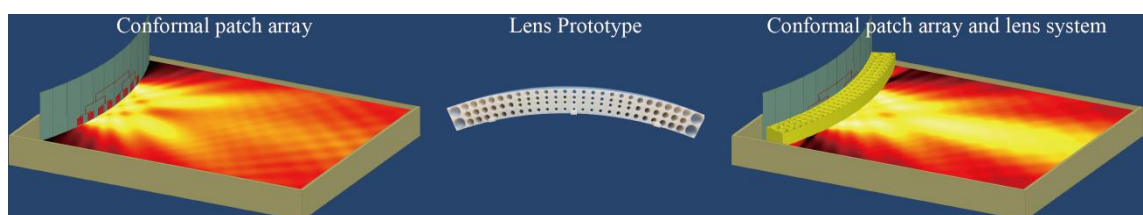


Figure 4-1 : Diagrammatic sketch of the function of the conformal lens and the photograph of the fabricated prototype.

Microwave antennas conformed on non-planar surfaces are of great interest to the scientific community and to the large public because they can potentially provide communication in any direction and more importantly, they can be easily mounted on masts or embedded in the skin of vehicles and therefore be down in the landscape such that they become less visually intrusive.

However, when several radiating elements are conformed on a non-planar surface, a radiation presenting multiple beams and defocusing effect, is emitted if no phase shifters are used to compensate for the different phase shifts introduced due to the location of the individual radiators. The broadband directive in-phase emission from an array of sources conformed cylindrically is numerically and experimentally reported in this chapter. By using the space transformation theory, a functional lens, which is capable of restoring in-phase emissions over a broad frequency range, is proposed and realized. The operating principle is presented of Figure 4-1. An all-dielectric, compact and very low-cost lens prototype presenting a graded refractive index is realized through three-dimensional (3D) polyjet printing. An array consisting of eight planar microstrip antenna elements, fabricated using standard lithography technique, is used as Transverse Electric (TE) polarized wave launcher to feed the lens. To validate the proposed lens, we experimentally demonstrate the broadband focusing properties and in-phase directive emissions. Both the far-field radiation patterns and the near-field distributions are measured and reported. It is observed that measurements agree quantitatively and qualitatively with numerical full-wave simulations and confirm the corresponding physical characteristics.

4.1 Introduction

Conformal antennas have received a lot of attention. Modern communication systems, aerospace application, high-speed vehicles and missiles require antennas conformed to their surfaces, with the main goal to reduce aerodynamic drag. Such conformal antennas are able to offer various advantages such as a potential of 360° coverage so as to secure continuous communications, a minimal level of unwanted radiations, low weight, and the possibility of obtaining significant gains. When the curved surface has a large radius compared to the operating wavelength, the influence of curvature on the performances is low. However, when the curvature radius is small compared to wavelength, the antenna's radiation patterns are

distorted due to the different phase shifts caused by the varying path lengths of the electromagnetic (EM) waves due to the location of the individual antennas on the curved surface. Therefore to avoid the degraded antenna performances, complex systems such as phase shifters are essential to compensate for the introduced phase shifts. But today, with the advent of metamaterials and space transformation concept, novel low cost devices can be proposed to replace the complex phase shifting systems.

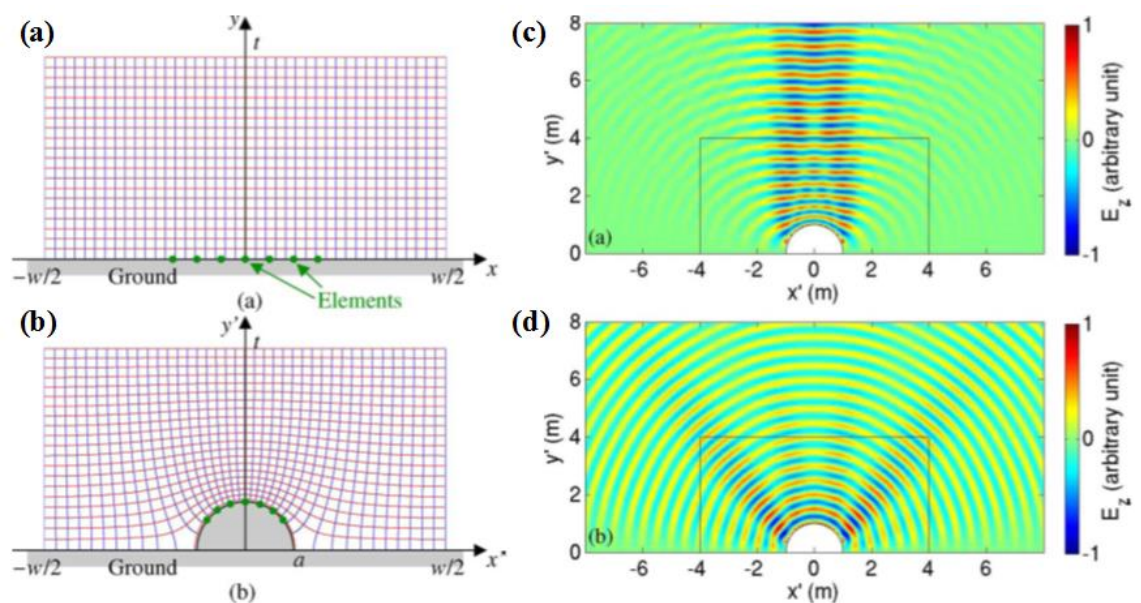


Figure 4-2: Coordinate systems for lens designs for 2-D dipole arrays on a conducting ground plane [121]. (a) (x, y, z) system for a linear array of sources. (b) (x', y', z') system for a cylindrical array of sources. (c) Real part of electric field of cylindrical array with a carpet-cloak lens. (d) The same array without lens.

Recently, theoretical studies have shown the possibility of enhancing the directivity through the use of a QCTO-based lens conformed on a non-linear array of radiating elements that follow a cylindrical or other arbitrary shape [123, 124]. The lens is capable of restoring in-phase emissions from a conformal array of antennas so as to obtain performances similar to that of a linear one, as presented in Figure 4-2. Figure 4-2(a) and (b) represents the conformal mapping of this principle. The planar antenna array is conformed into a cylindrical one. The electric field

distribution of this lens is shown in Figure 4-2(c) and compared to the antenna array alone presented in Figure 4-2(d). The lens totally changes the emission of the cylindrical antenna array and transforms a diffused emission into a directive one. However, the lens in these works is quite large compared to the antenna array and has been evaluated only theoretically.

In this chapter, we present the theoretical formulation to transform the radiation emitted by a cylindrical array into that of a planar one. We then synthesize the material to fabricate the conformal lens and we perform the experimental demonstration of in-phase restoration of the emission by the proposed lens over a wide frequency range spanning from 8 to 12 GHz. Laplace's equation is used to determine the constitutive electromagnetic parameters of the transformation medium. The conformed cylindrical antenna array used as excitation source radiates through the conformal lens corresponding to the transformed medium, which restores radiation patterns similar to those of a planar antenna array. Full wave simulations based on finite element method is used to validate the design method. An all-dielectric prototype is fabricated through easily available inexpensive 3D printing technology. Measurements are performed and reported experimental near-field distributions and far-field radiation patterns demonstrate clearly broadband focusing properties of the lens and in-phase directive emissions.

4.2 Design of the directivity enhancement lens

4.2.1 Concept and analytical design

The design of the conformal lens is presented in Figure 4-3. Figure 4-3(a) represents the virtual space which a sector of a cylindrical surface. The physical space presented in Figure 4-3(b) is formed by a 54° angular sector of the annular region between the circles of radius R and r .

Segments AB and $\widehat{A'B'}$ are perfect electric conductor boundaries, corresponding to the ground plane of the antenna array represented by the black line elements are the patches. The segments DA and CB have the same length and are equal to $R-r$. The transformation established between

the physical and virtual spaces aims to transform the conformed patch array into a linear planar one.

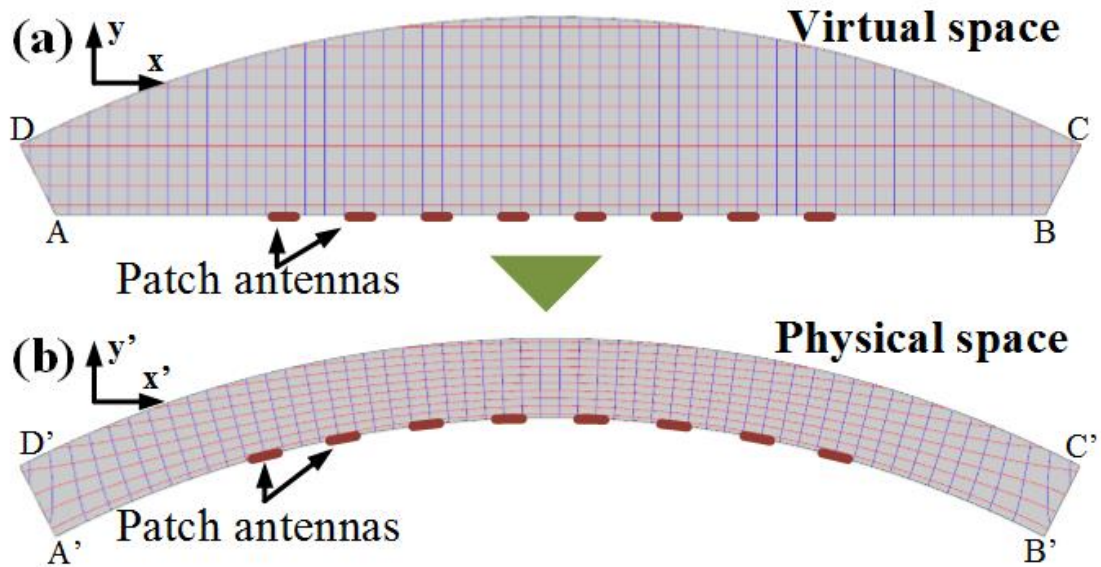


Figure 4-3: Illustration showing the space mapping from the virtual space to the physical space.

In the x - y plane, we suppose that the coordinate transformation between the physical space (x', y') and the virtual space (x, y) is $x = f(x', y')$ and $y = g(x', y')$. The mathematical equivalence of this mapping is expressed by a Jacobian matrix J whose elements are defined by $J = \partial(x, y)/\partial(x', y')$. By solving Laplace's equations in the virtual space with respect to specific boundary conditions, J can be obtained:

$$\frac{\partial^2 x}{\partial x'^2} + \frac{\partial^2 x}{\partial y'^2} = 0, \quad \frac{\partial^2 y}{\partial x'^2} + \frac{\partial^2 y}{\partial y'^2} = 0 \quad (4-1)$$

The physical space performs an inverse function of the virtual space. Thus the Jacobian matrix of this inverse transformation from (x, y) to (x', y') can be represented by J^{-1} . Here we assume that the conformal module of the virtual space is 1 while the conformal module of the physical space is M . Once J^{-1} is known, the properties of the intermediate medium can be calculated. In

terms of fields' equivalence with the virtual space upon the outer boundaries, Neumann and Dirichlet boundary conditions are set at the edges of the lens. The boundary conditions for the conformal lens are:

$$\begin{aligned} x \Big|_{\widehat{B'C', C'D', D'A'}} = x, \quad \hat{n} \cdot \nabla x \Big|_{\widehat{A'B'}} = 0 \\ y \Big|_{\widehat{A'B'}} = 0, \quad y \Big|_{\widehat{C'D'}} = y, \quad \hat{n} \cdot \nabla y \Big|_{\widehat{B'C', D'A'}} = 0 \end{aligned} \quad (4-2)$$

where \hat{n} is the outward normal to the surface boundaries.

It can be observed that the effective property tensors obtained from Laplace's equation are not isotropic in the x - y plane anymore. But if the conformal module M of the physical space is not quite different with the conformal module of the virtual space, which is 1 in this case, Li and Pendry suggested that the small anisotropy can be ignored in this case [79]. The near-isotropy resulting from the quasi-conformal mapping leads to the approximation. For simplicity, the transformation deals with a two-dimensional (2D) model with incident TE-polarized wave having only a z -directed component. Considering the polarization of the excitation, the properties of the intermediate medium can be further simplified as:

$$\varepsilon = \frac{\varepsilon_r}{\det(J^{-1})}, \quad \mu = 1 \quad (4-3)$$

where ε_r is the permittivity of free space. The determination of the mapping is introduced by solving Laplace's equations subject to predefined boundary conditions by Comsol Multiphysics Partial Differential Equation (PDE) solver [117].

Finite element method based 2D numerical simulations with COMSOL Multiphysics are firstly used to numerically validate the calculated transformed conformal lens. Scattering boundary conditions are set around the computational domain and an array of eight dipole antennas is used as source. The different dipoles are excited with equal amplitude and phase so as to obtain a directive beam at boresight direction. The electric field of the exciting sources is polarized along the z direction. The lens is considered to be 2 cm thick and is parameterized with $R = 29$

cm and $r = 27$ cm.

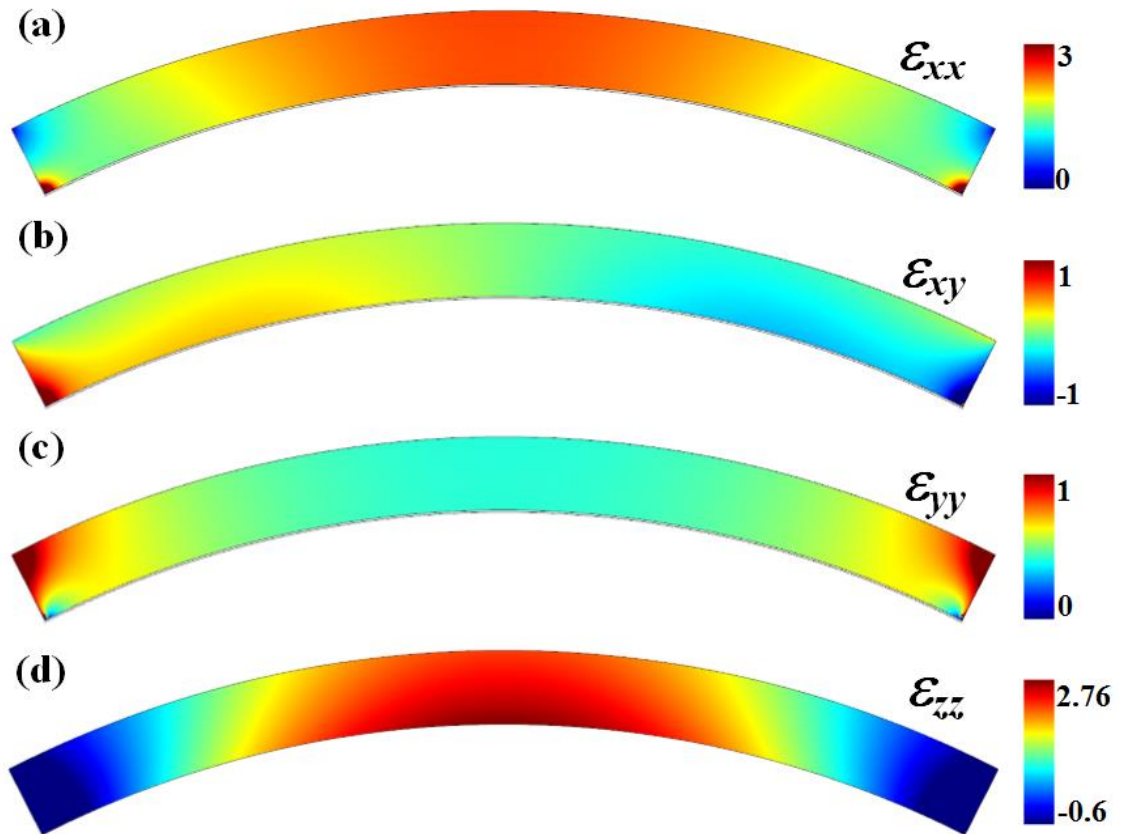


Figure 4-4: Permittivity distribution (a) ϵ_{xx} , (b) ϵ_{xy} , (c) ϵ_{yy} , (d) ϵ_{zz} .

As shown in Figure 4-4, the permittivity (ϵ_{zz}) distribution ranges from -0.6 to 2.76 for the calculated theoretical continuous lens. Low and high permittivity values are located at the outer borders and at the centre of the lens, respectively. The other three parameters are either close to 1 or close to 0. According to the concept of QCTO, we decide to ignore this anisotropy.

In Figure 4-5, the electric field distribution of three different structures, planar array, conformal array with the lens assigned by all the four parameters and conformal array with the lens assigned by isotropic material, are presented. As presented in Figure 4-5(b), the full parameter assigning lens restores the in phase emission almost identical as the planar array does. While after ignoring the anisotropy, in Figure 4-5(c), the lens can still perform the focusing functionality, but with two higher side lobes.

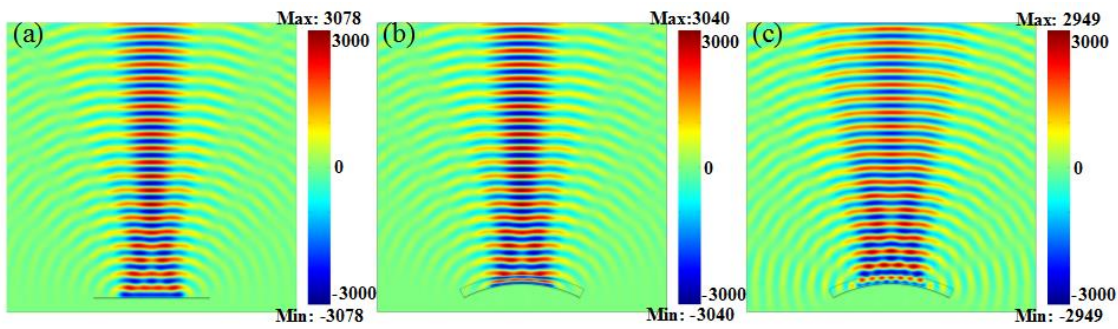


Figure 4-5: Real part of electric field distribution for three different configuration of the dipole array at 10 GHz. (a) Ideal rectilinear array showing planar wavefronts and a directive emission. (b) Conformal array with the lens assigned by all the four parameters restoring the emission almost identical with the planar array. (c) Conformal array with the lens assigned by isotropic material restoring the emission with higher side lobes.

The phenomenon of high side lobes can also be observed clearly in the 2D far field radiation pattern as shown in Figure 4-6.

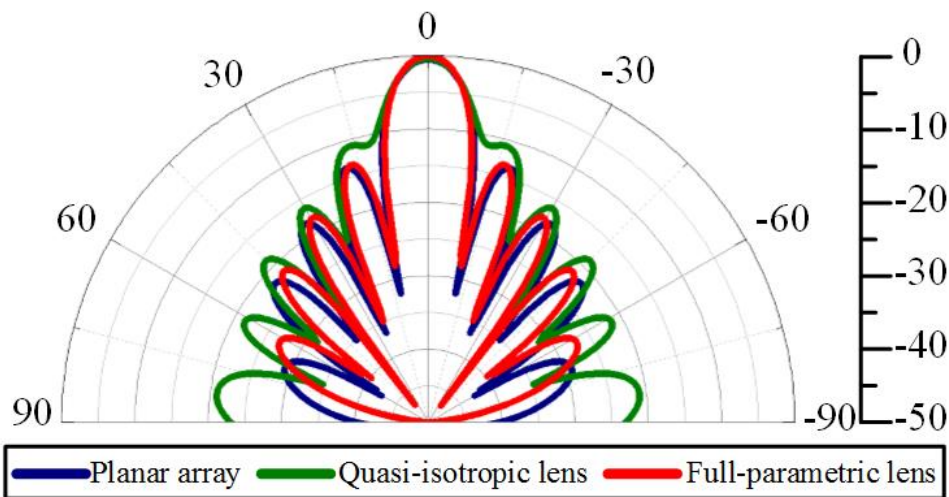


Figure 4-6: 2D far field radiation pattern at 10 GHz for three different configurations.

Our main aim in this chapter is to recover a directive beam in the main lobe of a conformal array of radiators, similar to that of a planar one. For this, we consider the simplified lens with only isotropic permittivity which can be fabricated from all dielectric materials. Moreover such materials provide wide-band operation compared to the use of resonant metamaterials. However,

such simplified dielectric lens shows radiation leakage on its lateral sides.

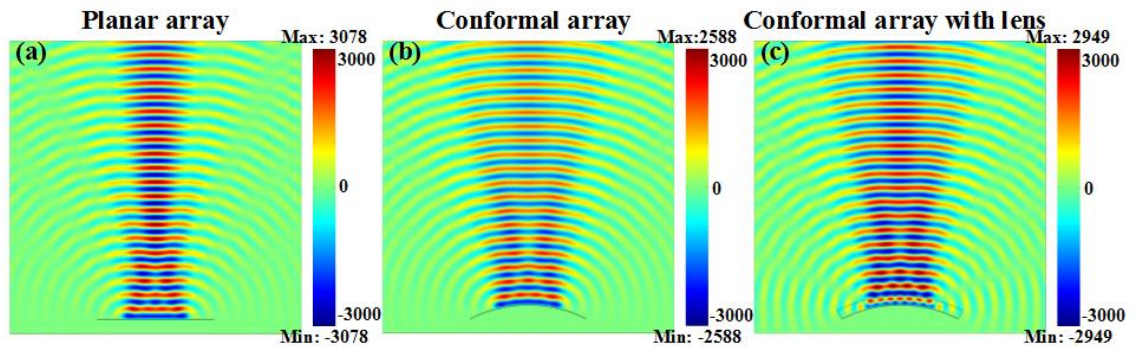


Figure 4-7: Real part of electric field distribution for three different configuration of the dipole array at 10 GHz. (a) Ideal rectilinear array showing planar wavefronts and a directive emission. (b) Conformal array showing cylindrical wavefronts and diffusion. (c) Conformal array in presence of the calculated lens (with continuous parameter profile) restoring the in-phase emissions.

Simulation results of the electric field distribution for different configurations are shown in Figure 4-7 at 10 GHz. Three configurations are considered: an ideal rectilinear (planar) dipole array, a conformal dipole array and a dipole array-lens system. As it can be clearly observed in Figure 4-7(a), the outgoing waves of the planar array present planar wavefronts and therefore a directive emission, at 10 GHz. However, in the case of the conformal array alone, the wavefronts are not planar anymore but rather cylindrical, as illustrated in Figure 4-7(b). A defocusing phenomenon is produced, with an electromagnetic radiation producing several beams. This phenomenon is due to the fact that the different dipoles, though excited with equal amplitude and phase, do not emit in phase with each other to create a constructive interference that produces a clear focused radiated beam at boresight. The defocusing is corrected when the calculated continuous parameter profile lens is placed above the conformal array (Figure 4-7(c)). The wavefronts of the conformal array in presence of the lens are quasi-planar and are consistent with those of the planar array. The performances obtained from the conformal antenna array show clearly the usefulness of the lens in restoring in-phase emissions. In Figure

4-7(a) and (c), the maximum value of intensity is about 3000, which shows a clear concentration of the emitted beam. While in Figure 4-7(b), since the conformal array disperses the beam, the intensity is lower.

4.3 Dimension study of the lens

For the dimension of the lens, we intend to find a smaller one in size which is easy for possible fabrication. This small lens also should provide achievable parameter distribution. Of course, the quality of the functionality is also supposed to be guaranteed. For these reasons, we launch a parametric study on the dimension of the lens.

4.3.1 Parametric study of the thickness of the lens

In this study, we set $r = 27$ cm and $d = R-r$. We vary d in the following discussion and evaluate the permittivity distribution inside the lens region.

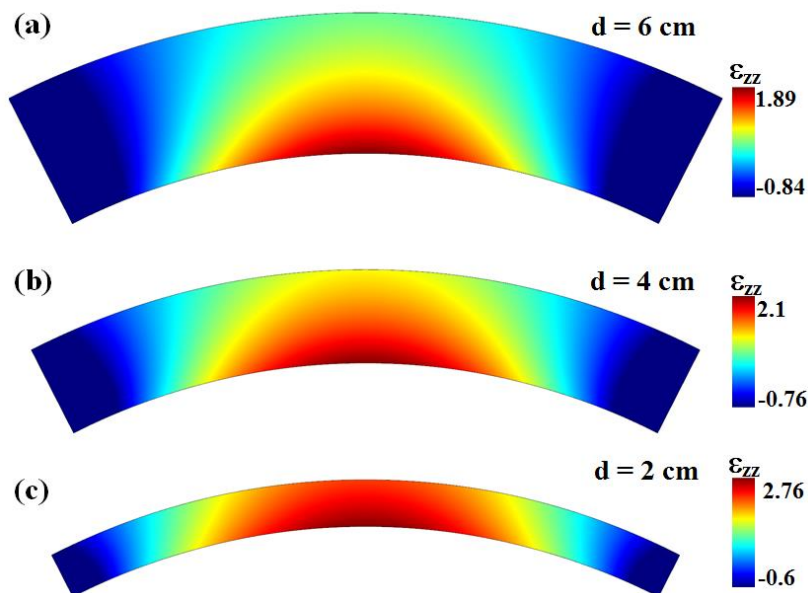


Figure 4-8: Permittivity (ϵ_{zz}) distribution of different thickness of the lens, (a) $d = 6$ cm. (b) $d = 4$ cm. (c) $d = 2$ cm.

As shown in Figure 4-8, d is set to 2 cm, 4 cm and 6 cm respectively. In Figure 4-8(a), when $d = 6$ cm, the range of the permittivity starts from -0.84 to 1.89. The highest value is located at the bottom center of lens. And the lowest value mostly distributes on the two sides of the lens. In Figure 4-8(b), when $d = 4$ cm, the maximum value of the permittivity has increased from 1.89 to 2.1, while the minimum value of the permittivity remains practically the same. We continue reducing the thickness of the lens to 2 cm. The maximum value of the permittivity keeps increasing to 2.76. When the thickness of the lens increases, the range of the distribution of the permittivity increases. They share the same form of distribution but the ranges differ.

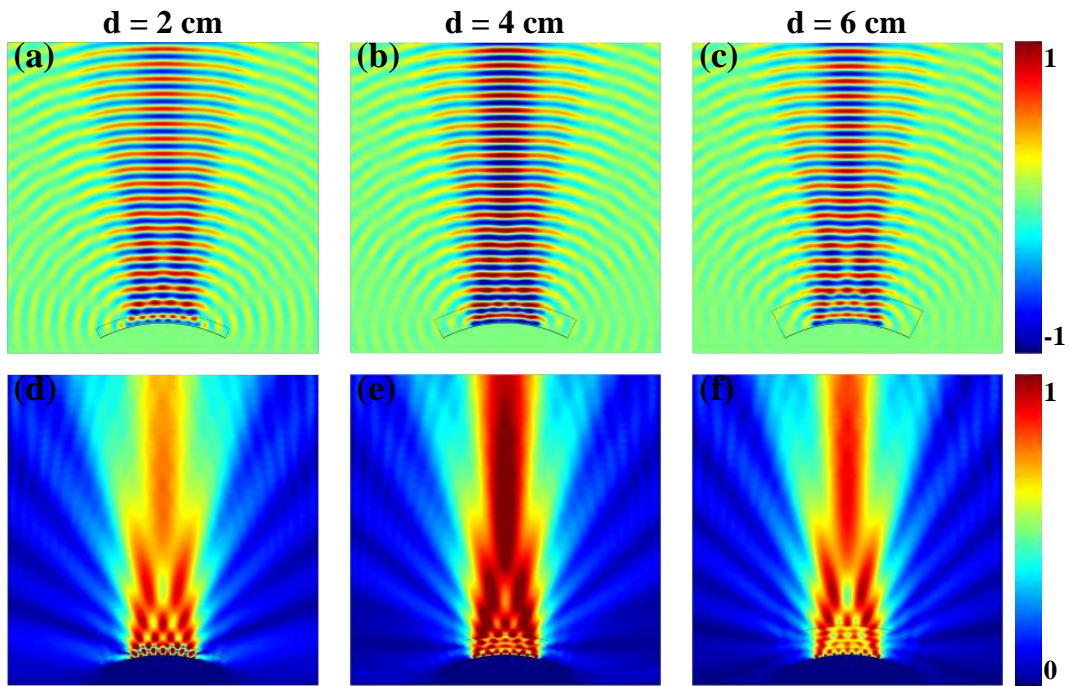


Figure 4-9: Real part of electric field distribution emitted from the continuous lens. (a) $d = 2$ cm. (b) $d = 4$ cm. (c) $d = 6$ cm. Electric field norm distribution emitted from the lens. (d) $d = 2$ cm. (e) $d = 4$ cm. (f) $d = 6$ cm.

The electric field and electric field norm radiated from the conformal dipole array and transmitted through the lenses are presented in Figure 4-9. For all the three lenses with different thickness, a clear focused beam is observed. All these three lenses perform the transformation functionality well to produce the overall in-phase emission.

4.3.2 Parametric study of the radius of the sector:

Normally you study a conformal lens for a given curvature radius. This radius does not change in the study. Then this parametric study seems inappropriate? But you could make a parametric study concerning the lens length.

In order to study the grade of the conformation (how much the lens is conformed), we continue the study of the lens by evaluating the radius of the inner factor of the lens. In this study, we keep the straight-line distance AB in Figure 4-3(a) the same. Moreover, the thickness of the lens $d = R - r = 2$ cm. The inner radius r is chosen to be 22.5 cm, 27.5 cm and 32.5 cm respectively. As we can see in Figure 4-10, the range of the permittivity distribution decreases as r increases. The maximum value of ϵ_{zz} reduces from 3.26 to 2.45. And the minimum value of ϵ_{zz} increases from -1 to -0.31. Of course, if r is large, the bottom boundary is more close to the planar ground plane. In another word, the conformal grade is quite small.

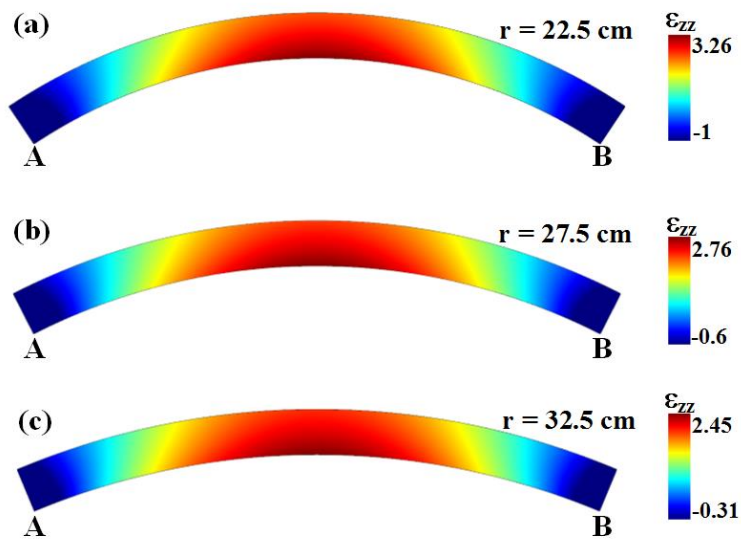


Figure 4-10: Permittivity distribution of different radius. (a) $r = 22.5$ cm. (b) $r = 27.5$ cm. (c) $r = 32.5$ cm.

The radiated E-field is presented in Figure 4-11. The first observation we can make is that in Figure 4-11(a) and (d), is the fact that despite the lens is able to focus the radiated beam, there is

a leakage on both sides of the lens. In this case $r = 22.5$ cm, and the thickness of the lens is 2 cm, the lens region is too small compared to the region that we conform. We can also state here that the conformal module is too large for such case. In this situation, when we ignore the anisotropy and keep only ε_{zz} , the lens doesn't perform well any more. On the other side for the other two lenses, the focusing phenomenon is very clear and no parasitic lobes are observed.

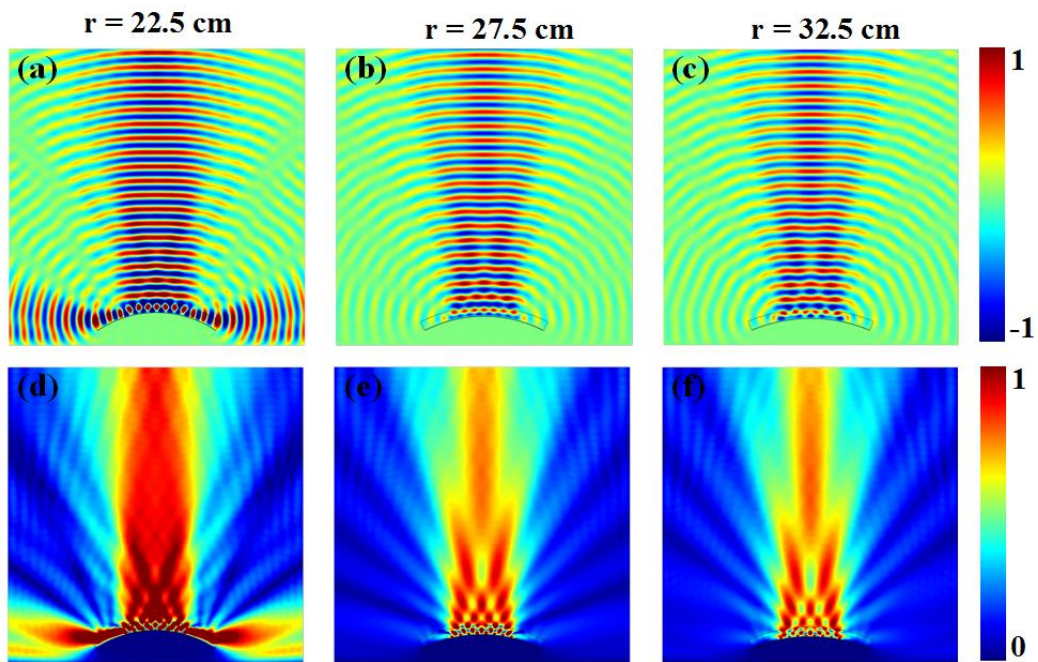


Figure 4-11: Real part of electric field distribution emitted from the continuous lens. (a) $r = 22.5$ cm. (b) $r = 27.5$ cm. (c) $r = 32.5$ cm. Electric field norm distribution emitted from the lens. (d) $r = 22.5$ cm. (e) $r = 27.5$ cm. (f) $r = 32.5$ cm.

4.4 2D discretization and full-wave simulations

A 2D discrete lens is designed for further realistic full-wave numerical simulations. The dimensions of the lens are set as $r = 27$ cm, $d = 2$ cm. The permittivity profile of the designed lens is shown in Figure 4-12(a). According to effective medium theory, if the operating wavelength is large enough with respect to the size, the composite material can be considered isotropic and homogenous. We therefore propose a discrete lens model, as presented in Figure

4-12(b), which is composed of 92 unit cells (13 of the row that consists 4 cells, 12 of the row that consists 3 cells and 2 of the row that consists 2 cells). The respective permittivity of each cell is considered to be constant and equals to the permittivity value at the center of each cell. In the discrete approximation, the two edges with permittivity values close to 1 are deleted from the continuous lens such that permittivity ranges from 1.5 and 2.6 in the discrete lens.

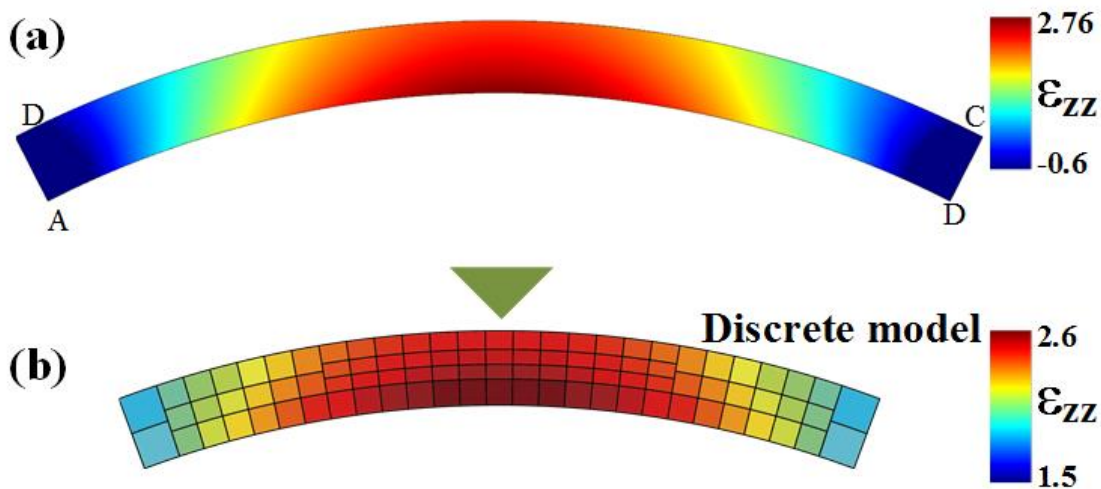


Figure 4-12: Design of 2D discrete model composed of 92 cubic cells.

Based on this discrete model, full wave simulations are performed using Comsol. Numerical results of the electric field distribution and the electric field norm for the discrete lens model are shown in Figure 4-13 at 10 GHz. The cylindrical dipole array is conformed under the discrete lens. As it can be clearly observed in Figure 4-13, the outgoing waves present a directive emission at 10 GHz, compared to the case of the conformal array alone, where wavefronts are not planar anymore but rather cylindrical, as illustrated in Figure 4-7(b). The defocusing is corrected when the calculated continuous parameter profile lens is placed above the conformal array. The wavefronts of the conformal array in presence of the lens are quasi-planar and are consistent with those of the planar array alone in Figure 4-7(a). The performances obtained from the conformal antenna array show clearly the usefulness of the lens in restoring in-phase emissions.

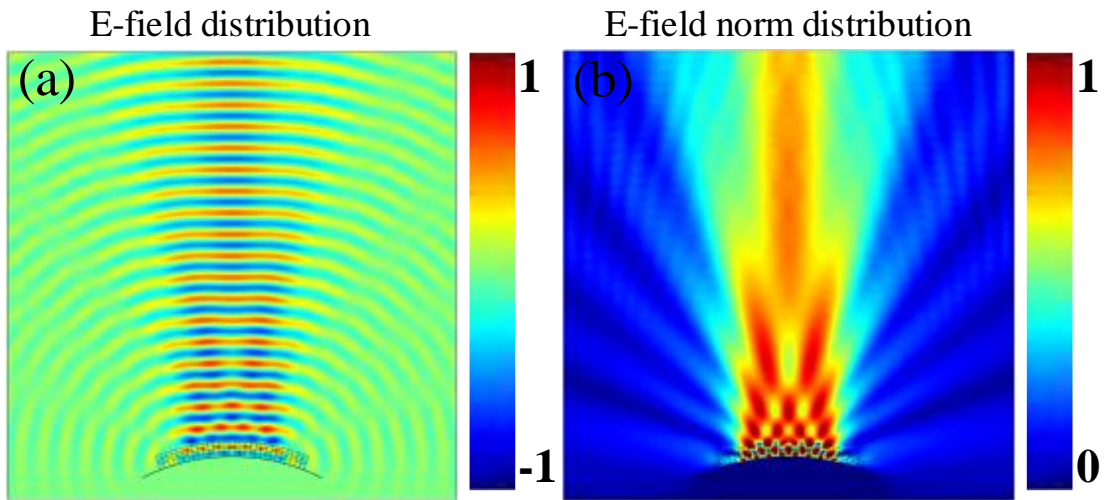


Figure 4-13 Real part of electric field and electric field norm distribution emitted from the lens.

To give a better insight on the radiated beam, we present the antenna far field radiation pattern from 2D simulations in Comsol at 10 GHz in Figure 4-14. The three configurations are considered: planar dipole array alone, conformal dipole array alone and dipole array-lens system. As previously observed from the electric field distribution, the planar array shows a clear highly directive radiation lobe.

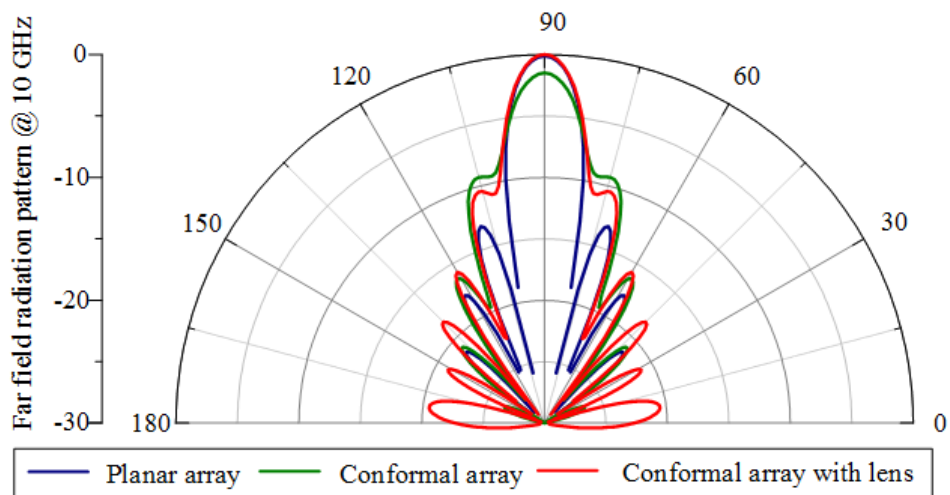


Figure 4-14: 2D far field radiation pattern at 10 GHz for three different configurations.

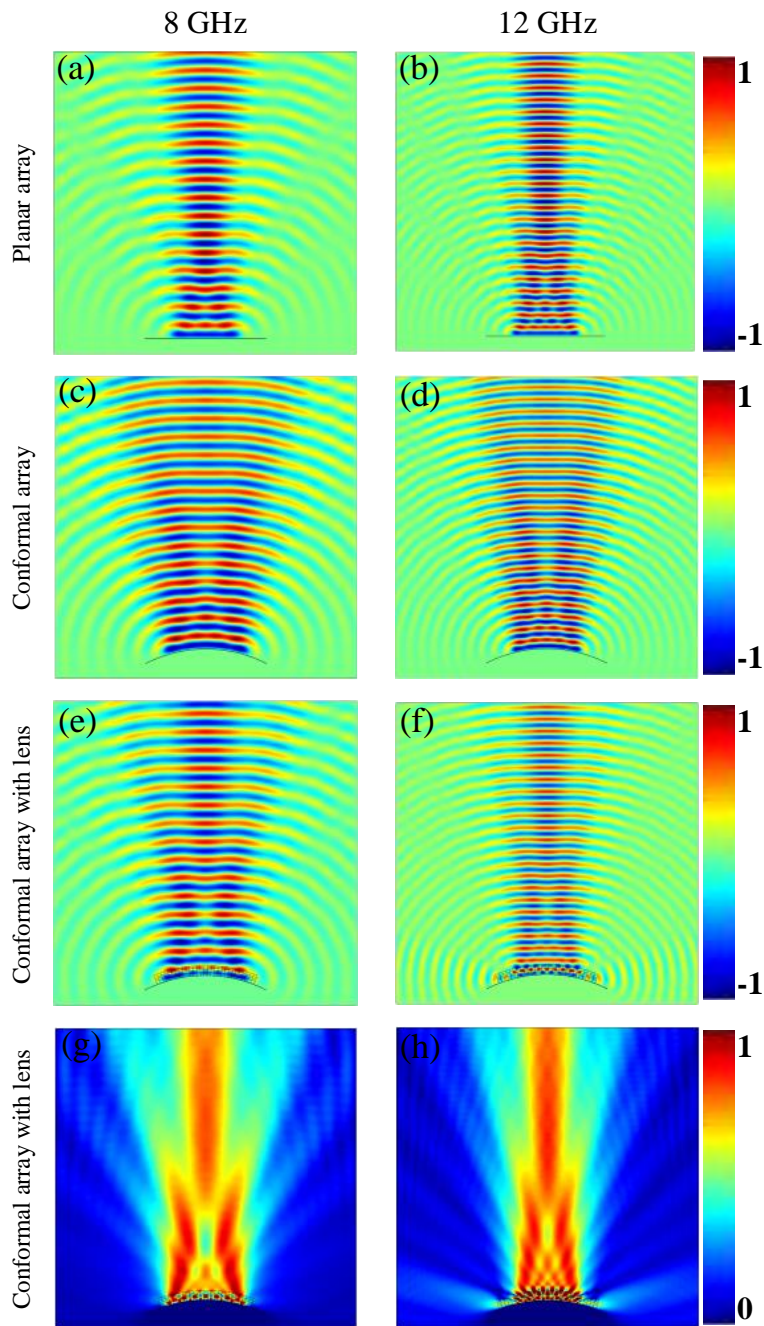


Figure 4-15: Real part of electric field distribution for three different configuration of the dipole array at 8 GHz and 12 GHz. (a) and (b) Ideal rectilinear array showing planar wavefronts and a directive emission. (c) and (d) Conformal array showing cylindrical wavefronts and defocusing phenomenon. (e) and (f) Real part of electric field, (g) and (h) electric field norm of conformal array in presence of the calculated lens (with discrete parameter profile) restoring the in-phase emissions.

The conformal array presents a distorted diagram with a lower radiation level than the planar array. The use of the lens above the conformal array allows restoring the in-phase emission to create a radiation pattern with a clear directive main beam. The transformed lens is capable of retaining similar performances to the planar microstrip patch array. Although the second lobe is still a little bit high, the difference between the first lobe and second lobe is about 12 dB.

We further continue to study this lens at several other frequencies. The same simulation as in Figure 4-13 is performed at 8 GHz and 12 GHz. The field distributions, shown in Figure 4-15, at 8 GHz and 12 GHz show very good agreement with the distribution at 10 GHz.

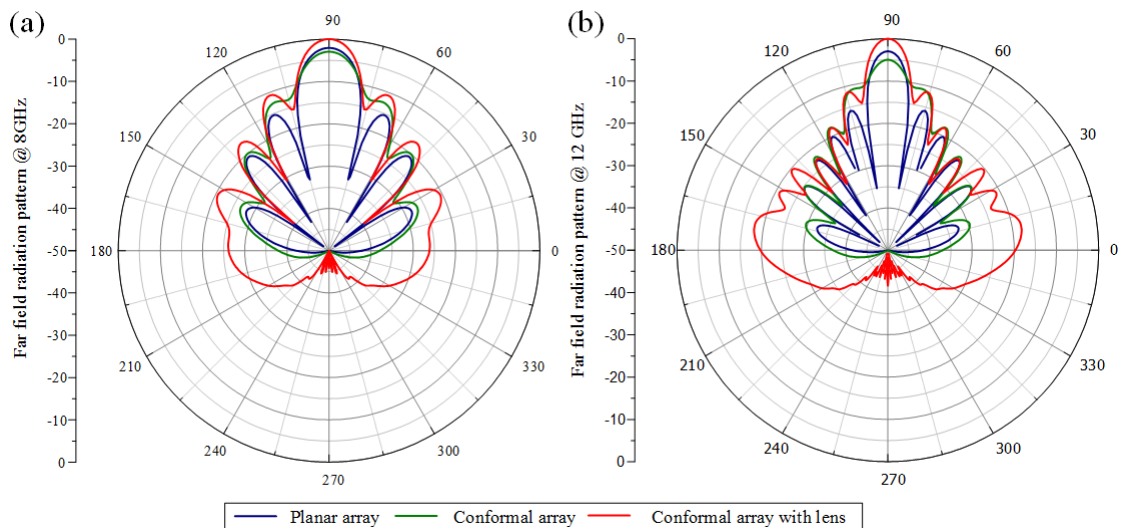


Figure 4-16: 2D far field radiation pattern for three different configurations. (a) 8GHz. (b) 12GHz.

The far field patterns at 8 GHz and 12 GHz are presented in Figure 4-16. The results here at both of the two frequencies present similarities in the sense that the lens is able to increase the level of the first lobe of the conformal patch array. Although the pattern of the conformal patch and lens system is not identical to the pattern of the planar array, the lens can still enhance the level between of the main beam (how much?). Now we take a closer look at the red curves in Figure 4-14 and Figure 4-16. At 0° and 180° , the level of the pattern is much higher than the other two curves. This means there is leakage on the sides of the lens. This leakage could be

reduced with a much thicker and larger lens. This is because that when we ignore the anisotropy of the material parameters, the index on the two sides of the lens is changed.

4.5 Dielectric material analyse and 3D prototype proposal

Since only ϵ_{zz} varies from 1.5 to 2.6 in the lens design, we are able to consider using it over a broad frequency range. The lens is thus realized from non-resonant cells. Air holes in a dielectric host medium of relative permittivity $\epsilon_h = 2.8$ is therefore considered. Suppose that two materials are mixed together, the effective parameter can be calculated by:

$$\epsilon_e = \epsilon_a f_a + \epsilon_h f_h \quad (4-4)$$

where $\epsilon_a = 1$ and f_a and $f_h = 1 - f_a$ are respectively the volume fraction of the air holes and the host material, respectively.

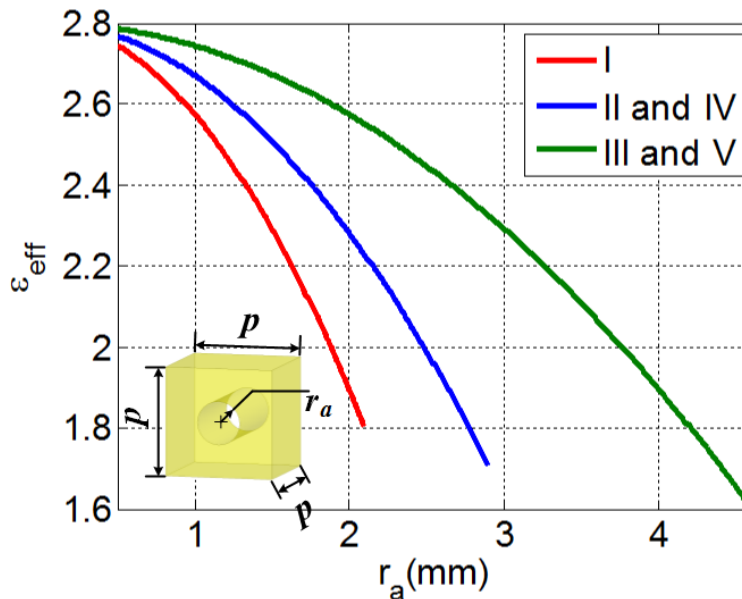


Figure 4-17: Effective permittivity of the cell composed of air hole in a dielectric host medium. A parametric analysis is performed to extract the effective permittivity value according to the radius r_a of the air hole with respect to a cubic cell of period p (p changes according to the regions of the discrete lens).

By adjusting the volume fraction of the air holes in the dielectric host medium, the effective permittivity of the cell can then be adjusted. Figure 4-17 shows the typical values of effective permittivity that can be obtained for a cubic cell in the different regions of the discrete lens.

A 3D discrete lens is designed for further realistic full-wave numerical simulations. The permittivity profile of the designed lens is shown in Figure 4-12. The profile is divided into five different regions composed of 92 cubic cells.

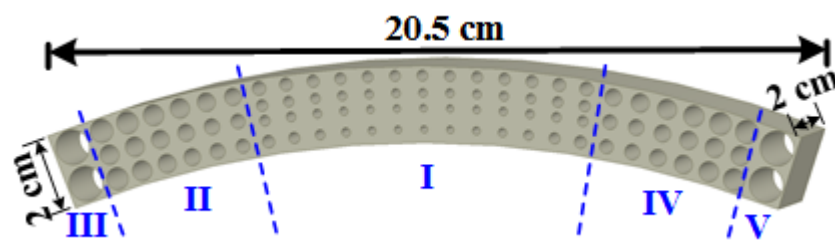


Figure 4-18: Design of the 3D discrete lens composed of five regions.

Region II and region III share similar characteristics with respectively region IV and region V, as illustrated in Figure 4-18. Region I is discretized into 13 rows of 4 cells where $p = 5$ mm, regions II and IV are each discretized into 6 rows of 3 cells where $p = 6.7$ mm and regions III and V are decomposed each into 1 row of 2 cells where $p = 10$ mm. The discrete permittivity of each cell is constant and is equal to the average permittivity within the cell.

4.6 Full-wave simulations on 3D discrete model

Full-wave simulations using Ansys HFSS [122] are performed to numerically verify the functionality of the lens.

A microstrip patch antenna array composed of eight linear radiating elements is used as primary source and the simulation results from 6 GHz to 14 GHz are presented in Figure 4-19. It must be noted that for each tested frequency, a different microstrip patch array is used. Indeed such patch radiators present a narrow band frequency response. Therefore to cover the 8 GHz to 12 GHz frequency band, three different arrays have been used. However, it is supposed that in real

applications, a primary source presenting a wideband frequency response will be used. The structures of the patch arrays are presented in Figure 4-19(a)-(c). And the return loss is plotted in Figure 4-19(d).

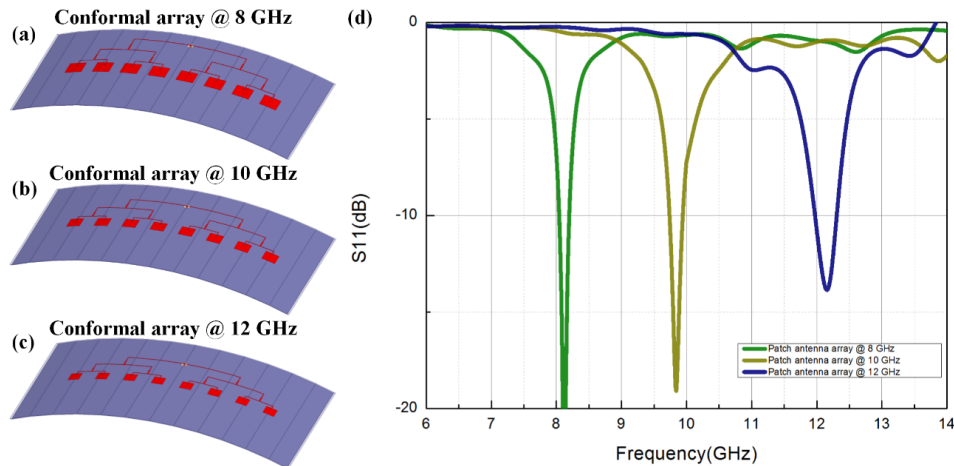


Figure 4-19: The conformal microstrip patch array. (a) Resonance at 8 GHz. (b) Resonance at 10 GHz. (c) Resonance at 12 GHz. (d) The return loss of the three microstrip patch arrays.

The simulation setup in HFSS of this conformal lens model has been taken as an example in Chapter 1 when we introduce the simulation tools.

In Figure 4-20, for the planar array, a main lobe with a directivity reaching 15.3 dB is observed. It should be noted that here a sectorial beam, *i.e.* a wide beam in one plane and a narrow beam in the other plane is obtained since we are using a linear array of radiating elements. For the conformal array, a lower directivity is obtained for the primary radiated lobe (12.3 dB) and a slight distortion can also be observed in the main beam. However in presence of the designed dielectric lens, the distortion disappears and a directivity of 15.7 is obtained, which agrees quantitatively with the planar array. A slightly higher directivity is even observed, confirming the fact that the lens is able to create a constructive interference between the emissions of the radiating elements of the conformal array and hence produce an overall in-phase emission. The color scale in Figure 4-20 is in decibels on the right.

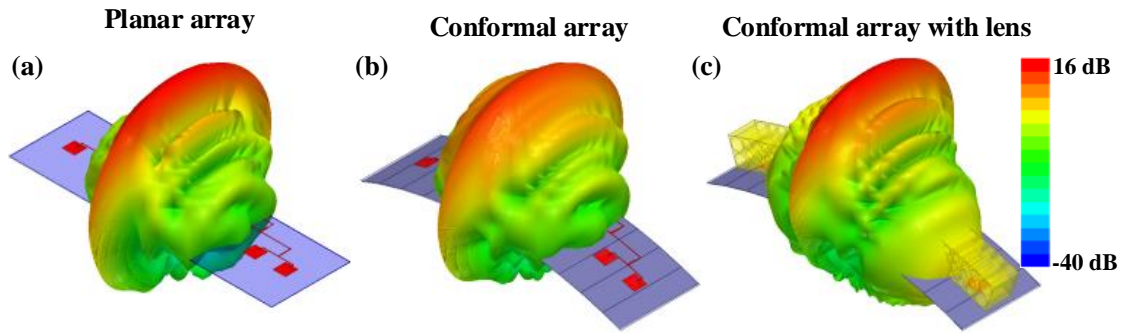


Figure 4-20: 3D simulated radiation patterns at 10 GHz. (a) Planar array with a directivity of 15.3 dB. (b) Conformal array without lens with a directivity of 12.3 dB. (c) Conformal array in presence of lens with a directivity of 15.7 dB. The color scale is in dB.

The simulated far field radiation pattern of the 3D model is shown in Figure 4-21.

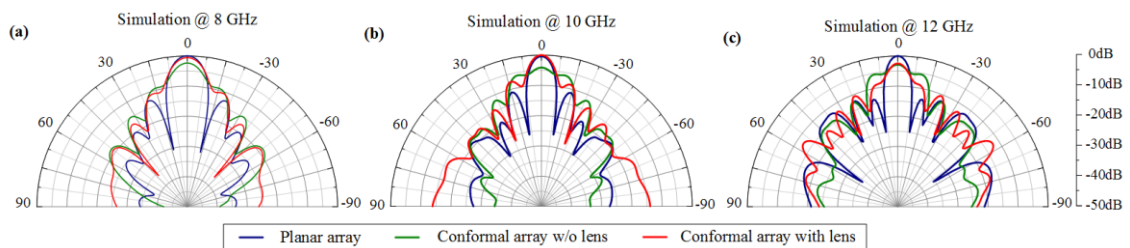


Figure 4-21: Simulated radiation patterns in the focusing plane (x-y plane). (a) 8 GHz. (b) 10 GHz. (c) 12 GHz. The conformal array presents a distorted diagram with a lower radiation level than the planar array. The lens above the conformal array allows restoring the in-phase emission to create a radiation pattern with a clear directive main beam, similar to a planar array.

The far field radiation patterns simulated from the 3D model show good agreement with the patterns simulated from the 2D model in Figure 4-14 and Figure 4-16. The planar arrays present a directive radiation with a clear narrow main lobe, while the conformal arrays presents a wider main beam of lower magnitude. The patch and lens system is able to increase the magnitude of the first lobe and decreases the level of the second lobe. The conformal array without lens has a directivity of 12.3 dB. The conformal array in presence of lens has a directivity of 15.7 dB, which is better than the directivity of the planar array alone (15.3 dB). In another word, the

patch and lens system can recover the distorted field into a directive one.

4.7 Conformal lens fabrication and experimental characterization

The lens is fabricated at AIRBUS Group Innovations using the 3D dielectric printing technology using the Objet Eden260VS 3D printer [100]. The 3D printing is based on the polyjet technology consisting in jetting layers of curable liquid photopolymer onto a build tray.

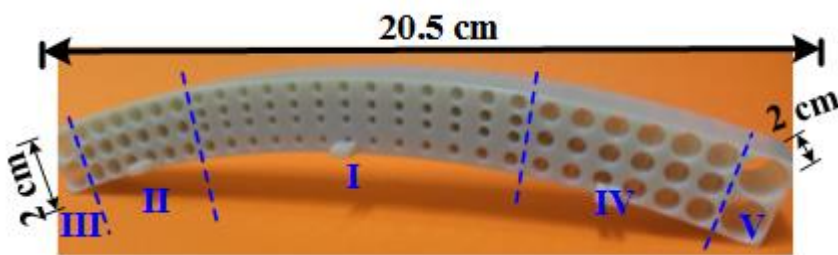


Figure 4-22: Photograph of the fabricated prototype.

The final prototype model then consists of an accumulation of fine layers on the build tray. During the printing process, the air holes are filled with a gel-like material that is easily removed with water after the printing process. The dielectric photopolymer is the one considered in simulations and has a relative permittivity of 2.8. A photograph of the fabricated prototype is presented in Figure 4-22.

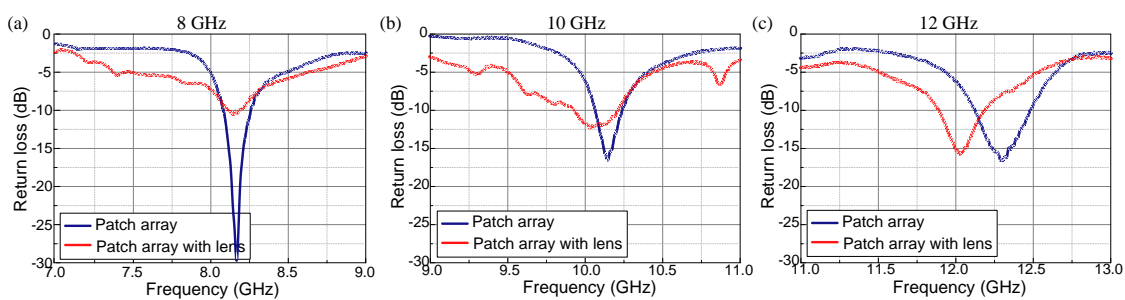


Figure 4-23: Measured S11 distribution at (a) 8 GHz, (b) 10 GHz and (c) 12 GHz, where the blue curves represent the S11 of the patch array and the red curves represent the S11 of the patch and lens system.

In Figure 4-23, the S11 of the patch array antenna and the dielectric lens antenna system are presented. The measurement is carried out at 8 GHz, 10 GHz and 12 GHz respectively in order to cover the whole X-band. The blue curves represent the S11 of the patch array and the red curves represent the S11 of the patch and lens system. It's clear that the dielectric lens keeps the same bandwidth as the patch array antenna alone. But the center operation frequency is shifted down a little.

A first experimental setup is set to scan the near-field microwave radiation. The electric field is scanned by a field-sensing monopole probe connected to one port of an Agilent 8722ES vector network analyzer by a coaxial cable.

The probe is mounted on two orthogonal linear translation stages (computer-controlled Newport MM4006), so that the probe can be translated with respect to the radiation region of the system under test. By stepping the field sensor in small increments and recording the field amplitude and phase at every step, a full 2D spatial field map of the microwave near-field pattern is acquired in free-space. The total scanning area covers $400 \times 400 \text{ mm}^2$ with a step resolution of 2 mm. Microwave absorbers are applied around the measurement stage in order to suppress undesired scattered radiations at the boundaries.

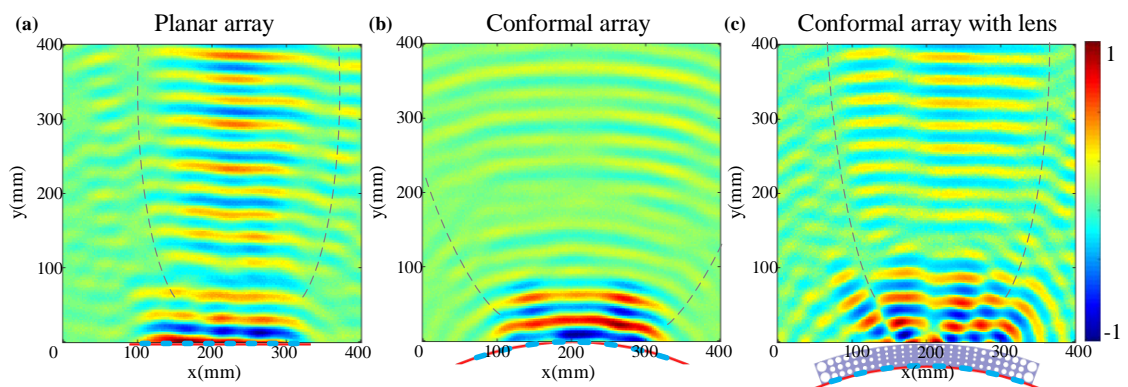


Figure 4-24: Real part of electric field distribution at 10 GHz. (a) Planar array. (b) Conformal array. (c) Conformal array in presence of lens. The defocusing introduced by the conformal array is corrected through the use of the lens.

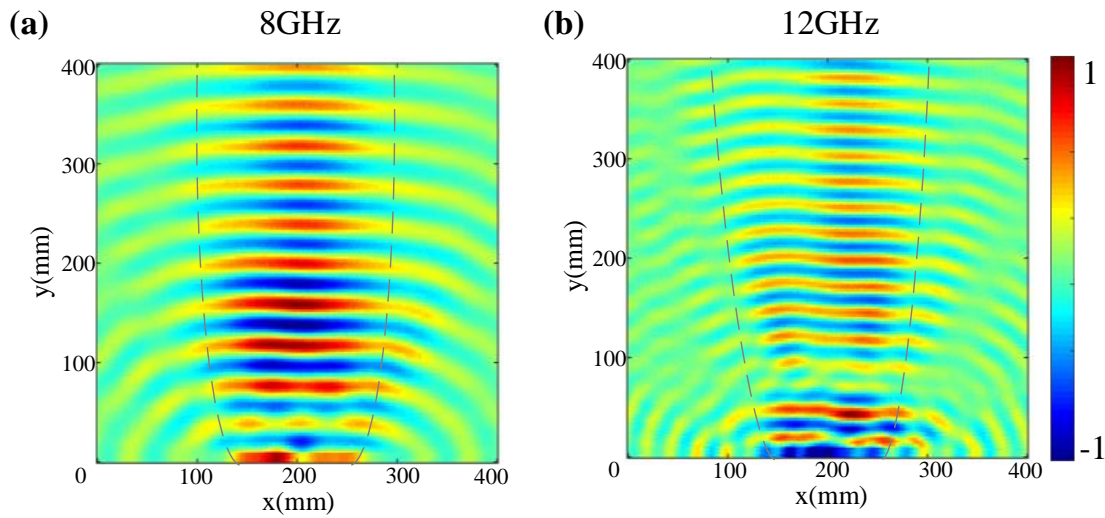


Figure 4-25: Measured real part of electric field distribution for the conformal array in presence of lens. (a) At 8 GHz. (b) At 12 GHz.

The electric field mapping of the antenna system is depicted in Figure 4-24 for the different configurations at 10 GHz. Planar wavefronts are observed for the linear array of patch antennas, indicating a directive radiated beam. As in numerical simulations, the conformal array presents cylindrical wavefronts and defocusing. When placed in contact with the lens, the cylindrical wavefronts are flattened and transformed into planar wavefronts and the measured data show similar characteristics to those of the planar array. Similar field mappings are measured at 8 GHz and 12 GHz (Figure 4-25), demonstrating the broadband behavior of the lens and verifying the 2D perfect simulation results in Figure 4-13 and Figure 4-15 obtained with the theoretical discrete lens.

To further investigate the directive behavior of the lens-antenna system, far-field radiation patterns have been measured in a full anechoic chamber. The measured radiations patterns in the x - y plane are presented in Figure 4-26.

A quite overall good qualitative agreement is noted between the simulated and measured characteristics. From the different plots, a clear highly directive radiation lobe is observed at all tested frequencies for the planar array. As predicted in the 3D simulations and confirmed in the

electric field cartographies, the conformal array presents a distorted diagram with a lower radiation level than the planar array. The use of the lens above the conformal array allows restoring the in-phase emission to create a radiation pattern with a clear directive main beam. The transformed lens is capable of retaining similar performances to the planar microstrip patch array. However, some imperfections exist due to the assumption of the isotropy of the material property.

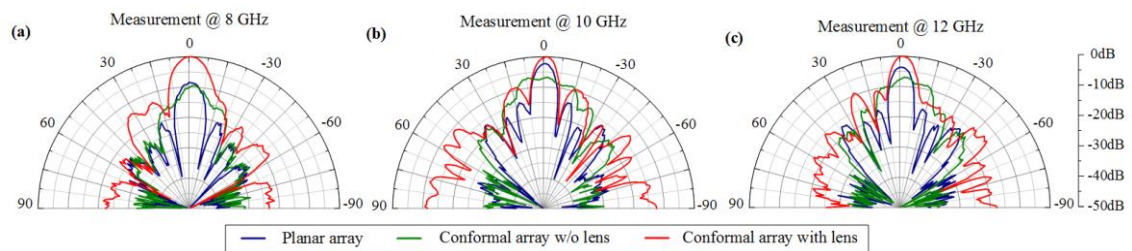


Figure 4-26: Measured radiation patterns in the focusing plane (x-y plane). (a) 8 GHz. (b) 10 GHz. (c) 12 GHz. The conformal array presents a distorted diagram with a lower radiation level than the planar array. The lens above the conformal array allows restoring the in-phase emission to create a radiation pattern with a clear directive main beam, similar to a planar array.

4.8 Conclusions

In summary, we have presented the experimental validation of a compact all-dielectric conformal lens operating on a wide frequency range and capable of restoring in-phase emissions from a conformal array of radiators. The lens has been designed by making use of Laplace's equations and has been tested over a wide frequency band ranging from 8 GHz to 12 GHz. Such a lens is able to compensate the out of phase distribution occurring on a conformal array of radiating elements and to allow a control of the emission in order to produce a main radiated lobe boresight direction. Furthermore, calculated and measured near-field distributions and far-field antenna patterns show directive emissions from the conformal array. The proposed method is low-cost and presents potential airborne and trainborne applications in communication

systems and environments where antennas are conformed on non-planar surfaces. The method is general and can be freely applied to any 2D and 3D shapes.

5 COHERENT BEAM CONTROL WITH A TRANSFORMATION OPTICS BASED LENS

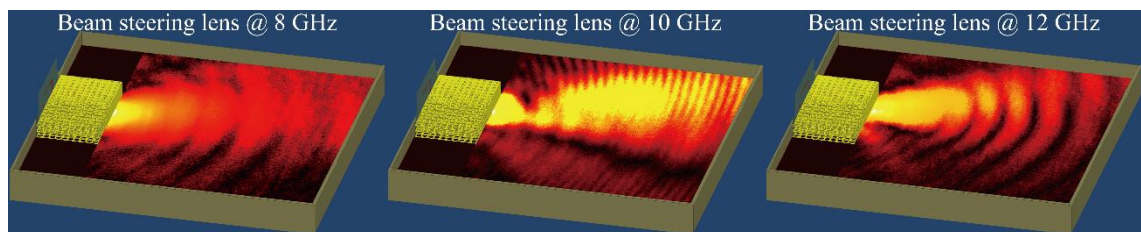


Figure 5-1: Diagrammatic sketch of the function of the beam steering lens.

In this chapter, based on transformation electromagnetics, the design procedure of a lens antenna, which steers the radiated beam of a patch array, is presented. The demonstrated metamaterial lens placed above a linear array of similarly excited radiating elements deflects the radiated beam to an off-normal direction, as presented in Figure 5-1. The space transformation modifies the space above the array of radiators and thereby alters its radiating pattern. Laplace's equation is adopted to construct the mapping between the virtual space and the physical space. To validate the design methodology, two prototypes have been fabricated and tested. The first one is a metamaterial-based lens prototype, designed using electric LC resonators. The second

one is a broadband all-dielectric compact low-cost lens prototype, fabricated through three-dimensional (3D) polyjet printing technology. An array of radiators composed of four planar microstrip antennas realized using standard lithography techniques is used as excitation source for the lens. Both the far-field radiation patterns and the near-field distributions are measured and reported. Measurements agree quantitatively and qualitatively with numerical full-wave simulations and confirm the corresponding steering properties. It is observed that by placing the lens on a feeding source instead of phase shifters, we are able to steer the radiation emitted by the latter source with a lens that can operate over a large frequency band.

The experimental validation of the lens paves the way to a wide range of potential applications in electromagnetics and daily communications employing lenses and antennas. This concept of wave control can be applied in other scientific engineering domains such as energy harvesting or radiation illusion. More generally, the ability to modify the space around an object so as to transform its radiating behavior or its electromagnetic response can lead to other unprecedented applications in the fields of wave propagation.

5.1 Designs of the beam steering lens and 2D analysis

The scalar two-dimensional Helmholtz equation is form invariant with respect to coordinate transformations which are equivalent to a conformal mapping. Thus QCTO is an approximate solution of minimizing the anisotropy for general boundary conditions. Here, we use QCTO to propose the design of a lens capable of deflecting electromagnetic waves. To transform the angle between the wave vector k and y -axis from 0° to 45° , we first study two different designs based on Laplace's equation in this section.

5.1.1 Beam steering lens design 1

In this first example we want design a lens which steers the beam of a directive antenna at 45° .

5.1.1.1 Concept of the lens design 1

For this first design, the virtual space which is free space filled with air and the physical space which is the transformed medium lens are respectively presented in Figure 5-2(a) and (b). The points B' , C' and D' in the physical space share the same location as B , C and D in the virtual space. We consider the length of the segment CD to be equal to W and that of BC to be H . Therefore the segment $A'B'$ has a length $W/\cos(\pi/4)$ and $D'A'$ has a length $W+H$. The determination of the mapping is introduced by solving Laplace's equations subject to predefined boundary conditions by Comsol Multiphysics Partial Differential Equation (PDE) solver [115].

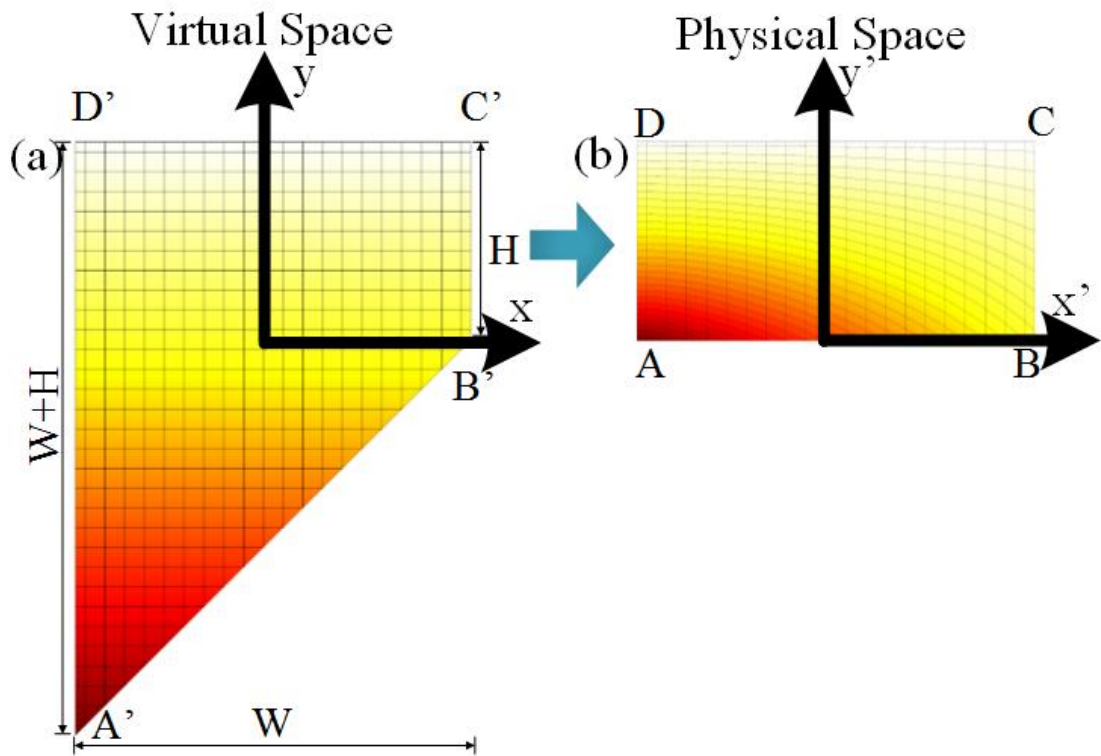


Figure 5-2: Illustration of conformal mapping from the virtual space to the physical space for Design 1 of the beam steering lens.

In Figure 5-2, a color plot of the contour of the design is shown. For simplicity, the transformation deals with a 2D model with incident Transverse Electric (TE) polarized wave. In this case, the electric field only has the z -directed component. Suppose that the coordinate

transformation between the physical space (x', y') and the virtual space (x, y) is $x = f(x', y')$, $y = g(x', y')$. The mathematical equivalence of this mapping can be expressed by a Jacobian matrix J whose elements are defined by $J = \partial(x, y)/\partial(x', y')$. By solving Laplace's equations in the virtual space with respect to specific boundary conditions, the Jacobian matrix J of the mapping can be obtained:

$$\frac{\partial^2 x}{\partial x'^2} + \frac{\partial^2 x}{\partial y'^2} = 0, \quad \frac{\partial^2 y}{\partial x'^2} + \frac{\partial^2 y}{\partial y'^2} = 0 \quad (5-1)$$

The physical space performs an inverse function of the virtual space. Thus the Jacobian matrix of this inverse transformation from (x', y') to (x, y) can be represented by J^{-1} . Here we assume that the conformal module of the virtual space (vacuum) is 1 while the conformal module of the physical space is M . Once J^{-1} is known, the properties of the intermediate medium can be calculated. In terms of fields' equivalence with the virtual space upon the outer boundaries, Neumann and Dirichlet boundary conditions are set at the edges of the lens. For the lens design 1, the boundary conditions are:

$$\begin{aligned} x' \Big|_{B'C', C'D', D'A'} = x, \quad \hat{n} \cdot \nabla x' \Big|_{A'B'} = 0 \\ y' \Big|_{B'C', C'D'} = y, \quad y' \Big|_{A'B'} = \tan\left(\frac{\pi}{4}\right) \left(x - \frac{W}{2}\right), \quad \hat{n} \cdot \nabla y' \Big|_{D'A'} = 0 \end{aligned} \quad (5-2)$$

where \hat{n} is the outward normal to the surface boundaries. The designed lens is fully parameterized with $W = 1$ m and $H = 0.5$ m too have a super directive source at 10 GHz. The properties of lens design 1 are shown in Figure 5-3.

It can be observed that the effective property tensors obtained from Laplace's equation are not isotropic in the x - y plane. But if the conformal module M of the physical space is not quite different with the conformal module of the virtual space, which is 1 in this case, Li and Pendry suggested that the small anisotropy can be ignored in this case [79]. Considering the polarization of the excitation, the properties of the intermediate medium can be further simplified as:

$$\varepsilon = \frac{\varepsilon_r}{\det(J^{-1})}, \quad \mu = 1 \quad (5-3)$$

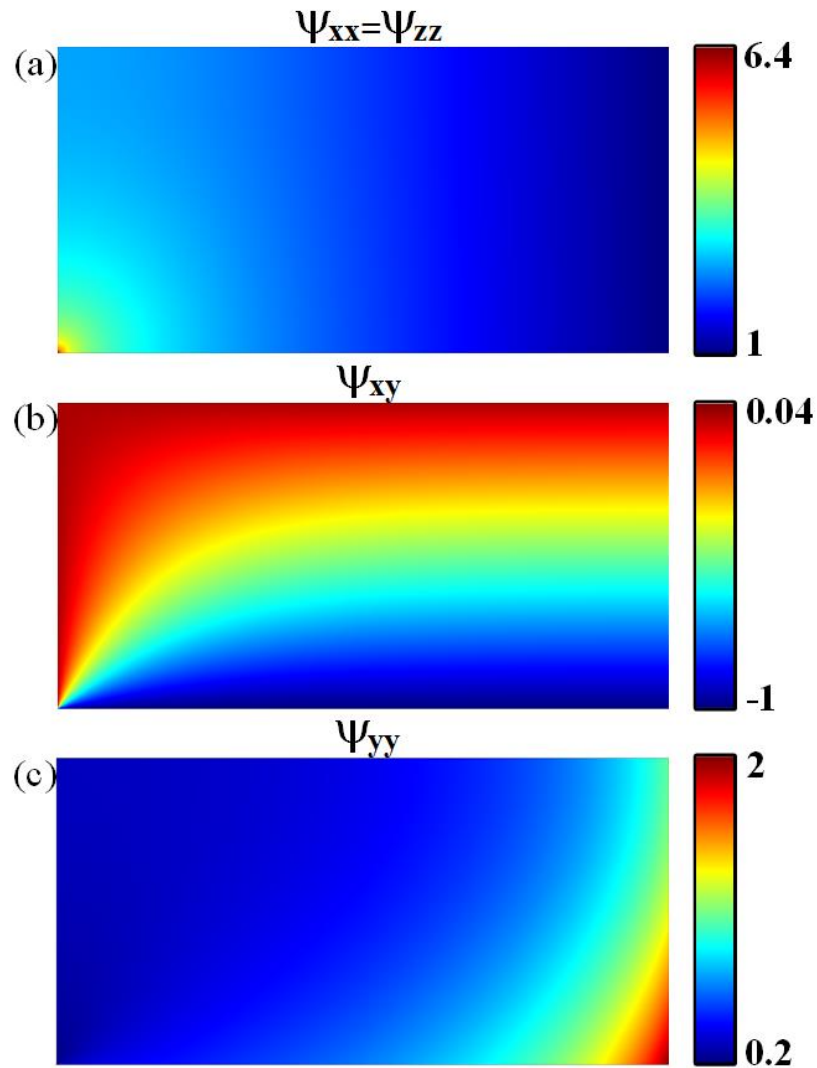


Figure 5-3: Anisotropic material parameter values for design 1 of the beam steering lens, (a) ψ_{xx} and ψ_{zz} , (b) ψ_{xy} , (c) ψ_{yy} .

5.1.1.2 Numerical validation of full parametric lens (design 1)

In this section, finite element method based numerical simulations are used to design and characterize the proposed transformed beam steering lens. In the simulation model using Comsol Multiphysics, scattering boundary conditions are set around the computational domain.

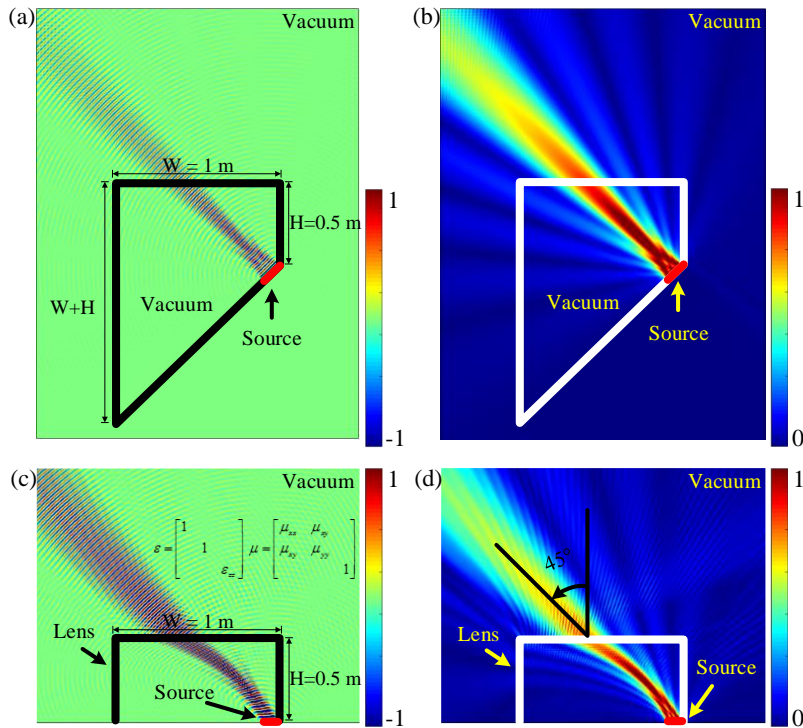


Figure 5-4: (a) Electric field and (b) norm of the electric field distribution at 10 GHz illustrating the propagation of the radiated beam of a linear source in air-filled initial virtual space. (c) Electric field amplitude and (d) norm at 10 GHz illustrating the propagation of the radiated beam of a linear source through and out of the lens when $H = 0.5\text{ m}$. A 45° beam deflection is observed in the design.

5.1.1.3 Study on the height dimension of full parametric lens

For the proposed dimension, lens design 1 has shown consistent behavior as in the virtual space. Then we begin to wonder what will happen if we change the dimension of the lens. So we perform a parametric study on the height of the lens H . In the original design, H was set to 0.5 m. In the following study, we will test one model whose height is reduced to 0.2 m and another model whose height is increased to 0.8 m. The length of the source L_s remains the same as before.

The material properties of lens design 1 analysed from COMSOL Multiphysics are shown in Figure 5-5. Figure 5-5(a) represents the properties when $H = 0.2\text{ m}$. Although this lens area is

smaller, the parameters share similar distribution with the design where $H = 0.5$ m. But the maximum value of the components ψ_{xx} and ψ_{zz} has increased to 8.85. When $H = 0.8$ m, this maximum value decreases to 5.98. The smaller H is, the more compressed the field is. Of course, the material parameter will be higher.

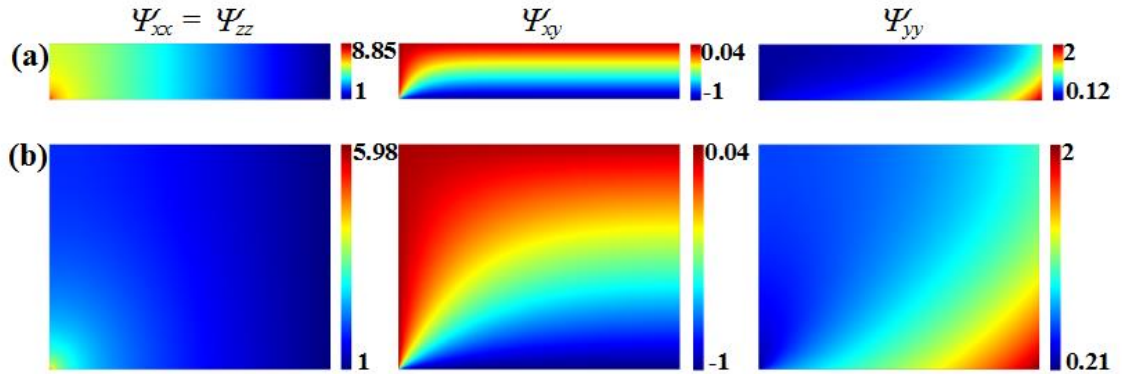


Figure 5-5 Material parameter values for design 1 of the beam steering lens. (a) $H = 0.2$ m. (b) $H = 0.8$ m.

The electric field distribution and the norm of the electric field of the two models in virtual space and transformed space are presented in Figure 5-6.

In Figure 5-6(a), (b), (e) and (f), a line source which is $\sqrt{2} * L_s / 2$ long is placed on the boundary $A'B'$. The whole virtual space is filled with nothing but air. When $H = 0.2$ m, shown in Figure 5-6(c)-(d), the designed lens is still able to steer the beam by 45° . However when $H = 0.8$ m, in the virtual space shown in Figure 5-6(e) and (f), the beam propagates through both the boundaries $C'D'$ and $D'A'$. So in the transformed space, shown in Figure 5-6(g) and (h), the beam tends to transmit through the boundary DA . But due to the compression on the boundary DA , the index on this boundary has changed. A reflection on this boundary can therefore be observed in Figure 5-6(h). This indicates that the width of the lens must be increased in this case. Generally speaking the height, the width and the desired beam steering angle are correlated.

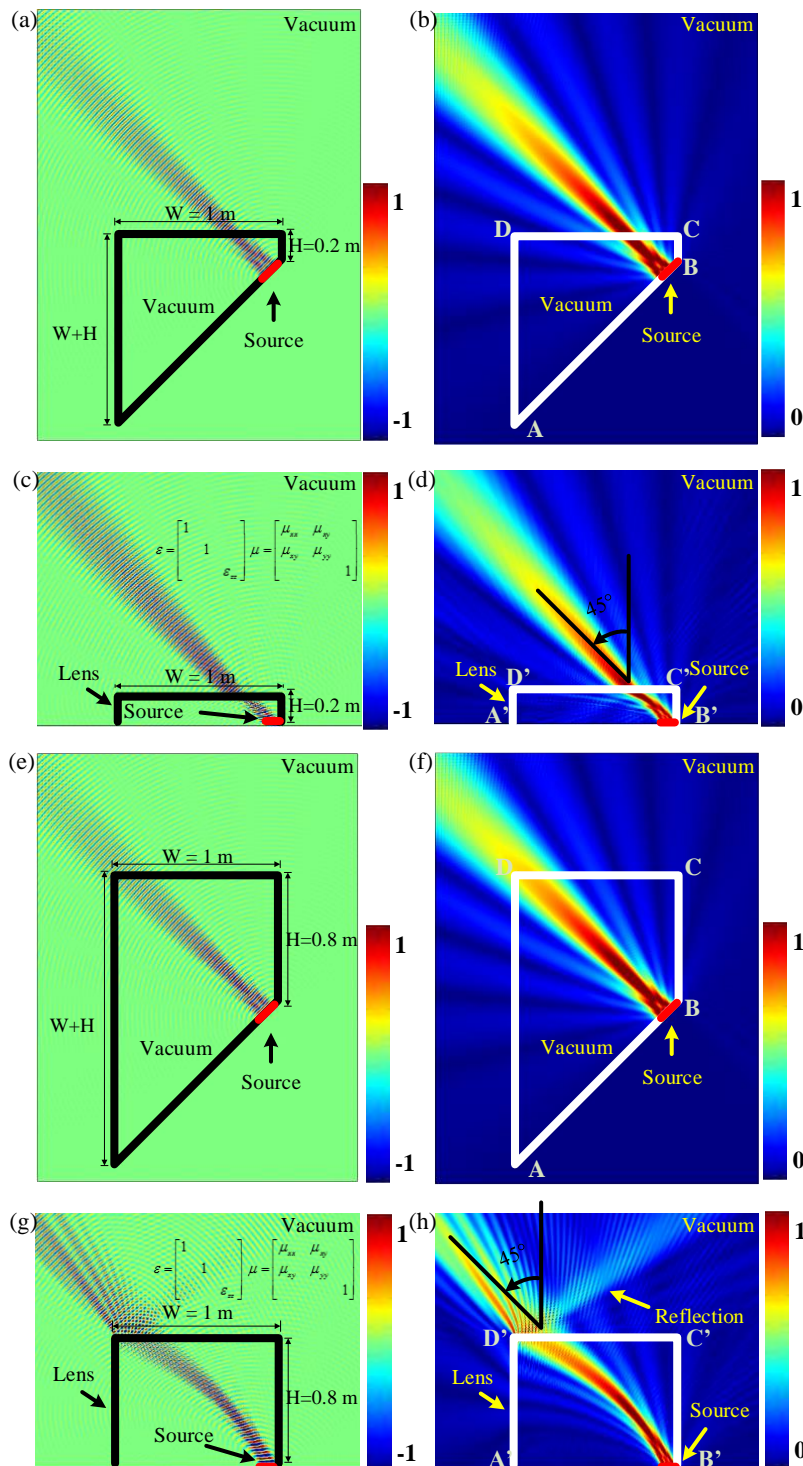


Figure 5-6: Real part of electric field and norm of the electric field distribution at 10 GHz illustrating the propagation of the radiated beam of a linear source in air-filled initial virtual space [(a), (b), (e) and (f)] and of source-lens system [(c), (d), (g) and (h)]. (a) – (d) $H = 0.2$ m. (e) – (h) $H = 0.8$ m.

5.1.1.4 Parameter reduction of lens design 1.

For further fabrication, we intend to have a designed lens that is small in size. When $H = 0.2$ m, the maximum permittivity value is 8.85, which is a big challenge for all dielectric fabrication. In this study, we fix the dimension of the lens as $W = 1$ m and $H = 0.5$ m. In the lens area, we assign an isotropic material property after the reduction from the design we introduced before.

This reduction is done by ignoring the anisotropy and keeping only the component ϵ_{zz} . Both the electric field amplitude and norm are presented in Figure 5-7.

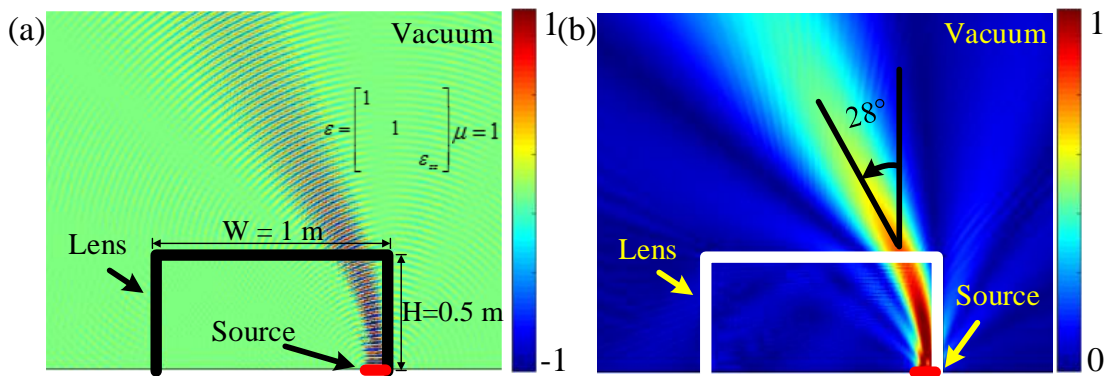


Figure 5-7: (a) Real part of electric field amplitude and (b) norm at 10 GHz illustrating the propagation of the radiated beam of a linear source through and out of the lens assigned by simplified parameters.

As shown in Figure 5-7, the lenses are now assigned only a permittivity parameter along z -direction, while the permeability is isotropic. It is clear that, since the physical space of lens design 1 is distorted and the conformal module is far from 1, the lens still steers the beam but by an angle of 28° , smaller than the expected 45° . This is due to the fact that the conformal module is much larger than 1. So the anisotropy cannot be ignored if a deflection of 45° is still desired. Therefore, the beam steering functionality is weakened when the anisotropy is ignored. If we consider the ϵ_{zz} distribution for lens design 1, it can be noted that ϵ_{zz} value ranges from 1 to 6.4. Such values can be achieved using for example, nano- and micro-sized titanates dispersed in a

polymeric host material [125] or by drilling holes in a high constant dielectric [126, 127].

5.1.1.5 Study on the height dimension of lens design 1 after parameter reduction.

The same dimension study is performed on this model after parameter reduction. H is set to be 0.2 m and 0.8 m respectively. The electric field distribution and the norm of the electric field are presented in Figure 5-8.

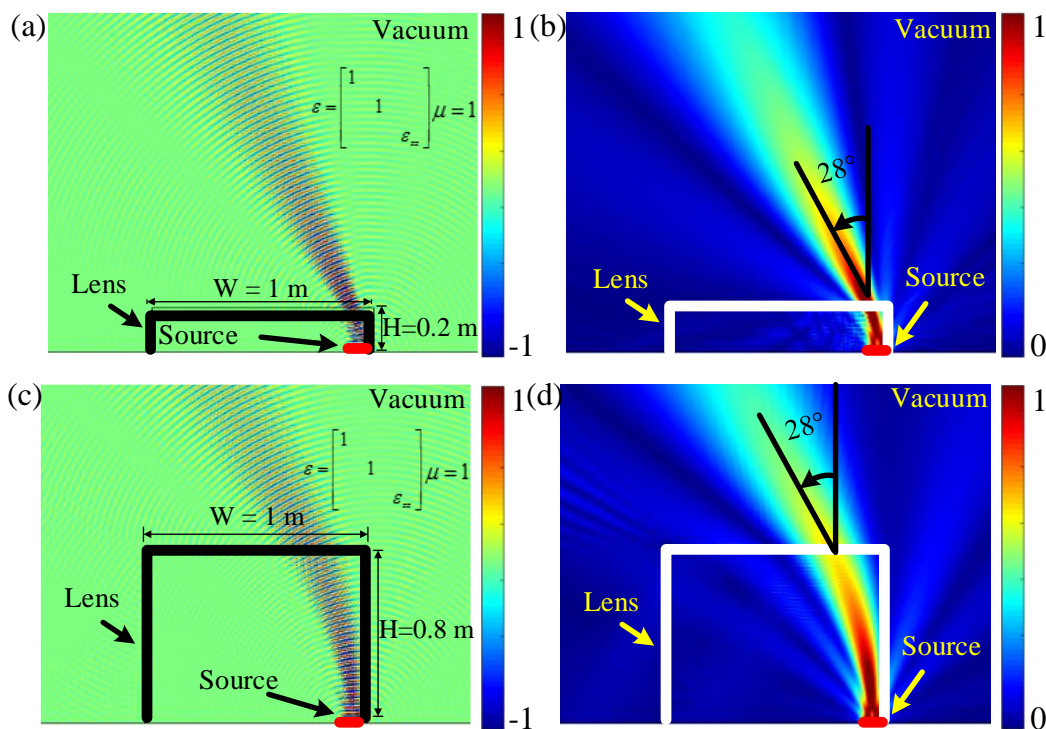


Figure 5-8: (a) and (c) Real part of electric field and (b) and (d) norm of the electric field distribution at 10 GHz illustrating the propagation of the radiated beam of a linear source through and out of the lens assigned by simplified parameters. (a) and (b) $H = 0.2$ m. (c) and (d) $H = 0.8$ m.

From the field distribution in Figure 5-8, we can see that no matter the height of the lens is 0.2 m or 0.8 m, the lens is always capable to deflect the beam by 28° when only isotropic material is assigned. The beam steering performances are also clearly shown by the antenna radiation patterns calculated from Comsol Multiphysics in Figure 5-9.

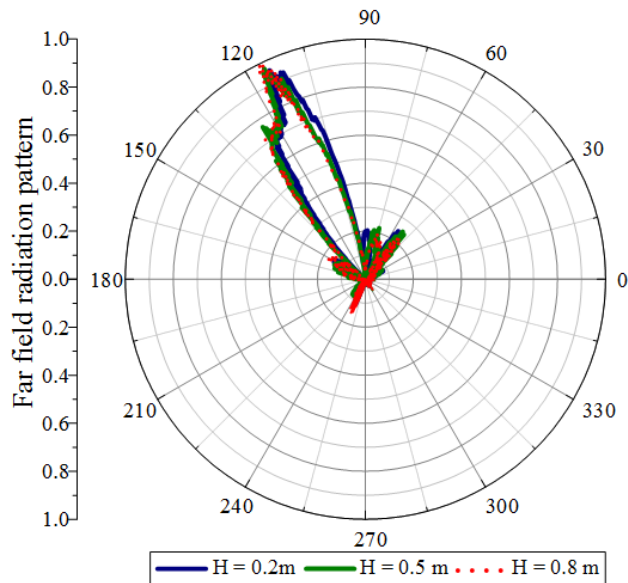


Figure 5-9: Normalized antenna radiation patterns showing the beam steering performances of the lens designs with different height H .

5.1.1.6 Beam splitter

Furthermore, we have designed a beam splitter by using four adjacent lenses based on the design 1. The line source is enlarged to $L_s = 0.2$ m and is placed in the middle of the four lenses as illustrated in Figure 5-10.

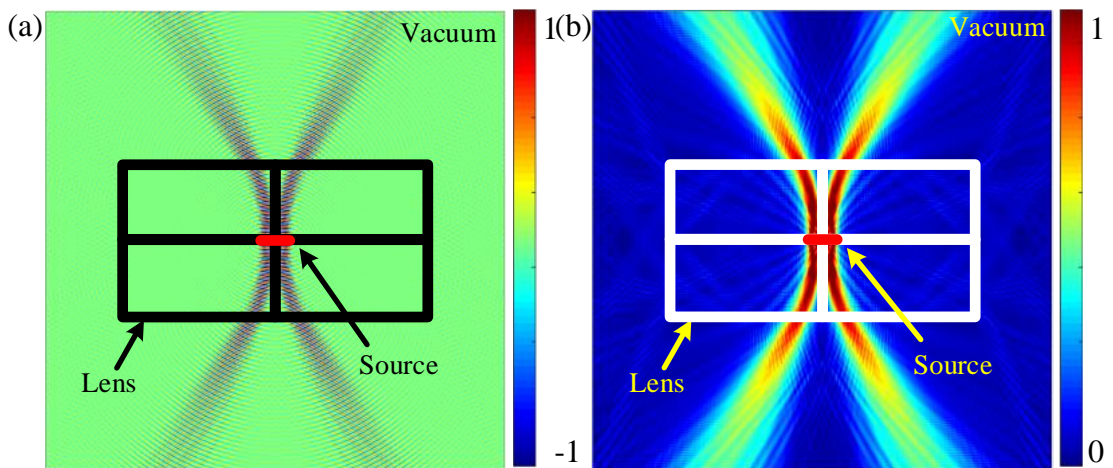


Figure 5-10: Beam splitting device. (a) Real part of electric field distribution at 10 GHz illustrating the transmission of four splitted beams. (b) Norm of the electric field.

The electric field distribution and the norm of the electric field show clearly the transmission of four splitted beams through the lenses. The angle of deflection of the beams with respect to the normal is 28° as for the lens design 1.

5.1.1.7 Dimension study on both height and width of the lens after parameter reduction.

A parametric study on the size of the isotropic lens allows showing that a reduction in the size of the lens does not alter the deflection angle, as presented in the different parts of Figure 5-11. In this study, we keep the ratio $W/H = 2$. We first try the check the field distribution by reducing the size of the lens from 1m to 30 cm, then two other dimensions are studied (20 cm and 10 cm).

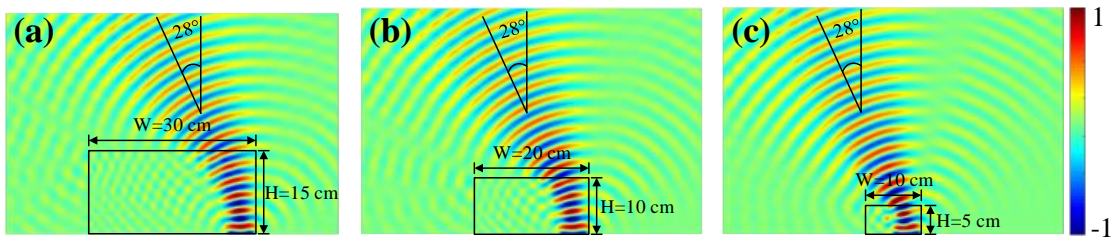


Figure 5-11: Parametric study performed on the size of the lens. When reducing the dimensions of the lens, the beam deflection is not modified.

It is clear that even though the sizes of the lens we present in Figure 5-11 are different, the field distributions are the same. It is important at this stage to note that the deflection angle depends mostly on the material parameters of the lens and very little on the size of the lens.

5.1.1.8 Frequency study on the lens design 1 after parameter reduction

Lens design 1 is supposed to be a wideband lens which is not limited by frequency. So we tested this design model at several different frequencies.

As we have shown in the dimension study, the size of the lens can be shrunk. In this study, the dimension of the lens is $W = 10\text{ cm}$ and $H = 5\text{ cm}$. The length of the source $L_s = 5\text{ cm}$, presented as the red segment in Figure 5-12. As shown in Figure 5-12 below, the field distributions at 8

GHz, 10 GHz and 12 GHz are basically the same except for the difference of the wavelength.

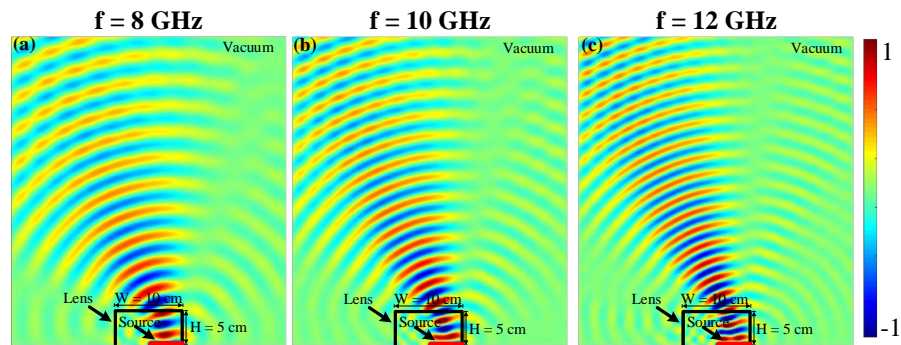


Figure 5-12: Frequency study performed on the lens. When changing the operating frequency, the beam deflection is not modified.

5.1.2 Beam steering lens design 2

5.1.2.1 Concept of the lens design 2

The second design is illustrated by the virtual and physical spaces shown in Figure 5-13.

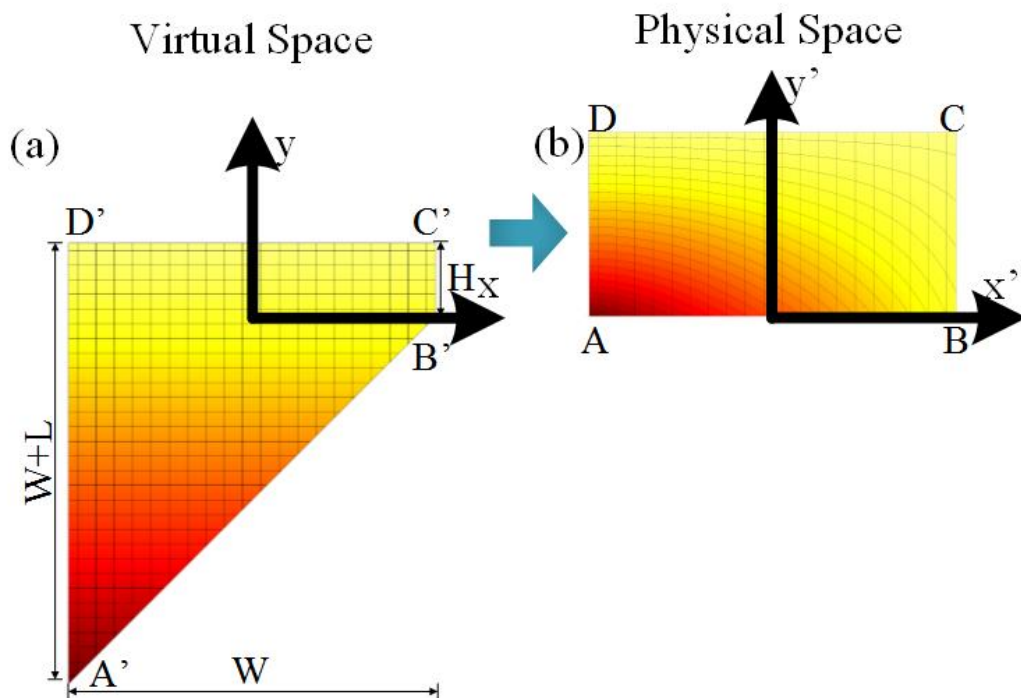


Figure 5-13: Illustration of conformal mapping from the virtual space to the physical space for Design 2 of the beam steering lens.

The rectangle $EFGH$ is mapped from the quadrilateral $E'F'G'H'$, where $EF = W$, $FG = H$. In the quadrilateral $E'F'G'H'$, the different dimensions are: $E'F' = W/\cos(\pi/4)$, $F'G' = \frac{2}{5}L$, $G'H' = W$ and $E'H' = W + \frac{2}{5}H$. The determination of the mapping is introduced by solving Laplace's equations subject to predefined boundary conditions by Comsol Multiphysics Partial Differential Equation (PDE) solver.

For the lens design 2, the boundary conditions are:

$$\begin{aligned} x' \Big|_{F'G', G'H', H'E'} &= x, & \hat{n} \cdot \nabla x' \Big|_{E'F'} &= 0 \\ y' \Big|_{G'H'} &= \frac{2}{5}y, & y' \Big|_{E'F'} &= \tan\left(\frac{\pi}{4}\right) * \left(x - \frac{W}{2}\right), & \hat{n} \cdot \nabla y' \Big|_{F'G', H'E'} &= 0 \end{aligned} \quad (5-4)$$

It is clear that for the design 2 the conformal module difference between the virtual space and physical space is smaller than in design 1. In summary, the anisotropy in design 2 is smaller than in design 1.

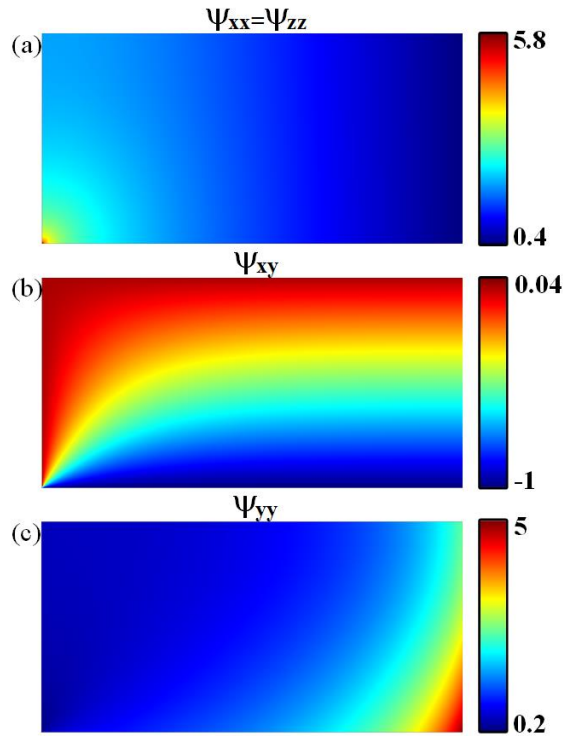


Figure 5-14: Material parameter values for Design 2 of the beam steering lens.

The designed lenses is fully parameterized with $W = 1$ m and $L = 0.5$ m. The properties of the lens design 2 shown in Figure 5-14 share similar parameter variation as lens design 1, but with different range of values. For the component ϵ_{zz} , the range was from 1 to 6.4 in design 1, while in design 2, the range is from 0.4 to 5.8.

5.1.2.2 Numerical validation of lens design 2

In this section, finite element method based numerical simulations are used to design and characterize the proposed transformed beam steering lens design 2. As before in the simulation model using Comsol Multiphysics, scattering boundary conditions are set around the computational domain. The same configuration as for the simulation of the lens design 1 is used. A current line source of length $L_s = 0.1$ cm is used and the electric field of the source is polarized along the z -direction. The operation frequency is set to 10 GHz.

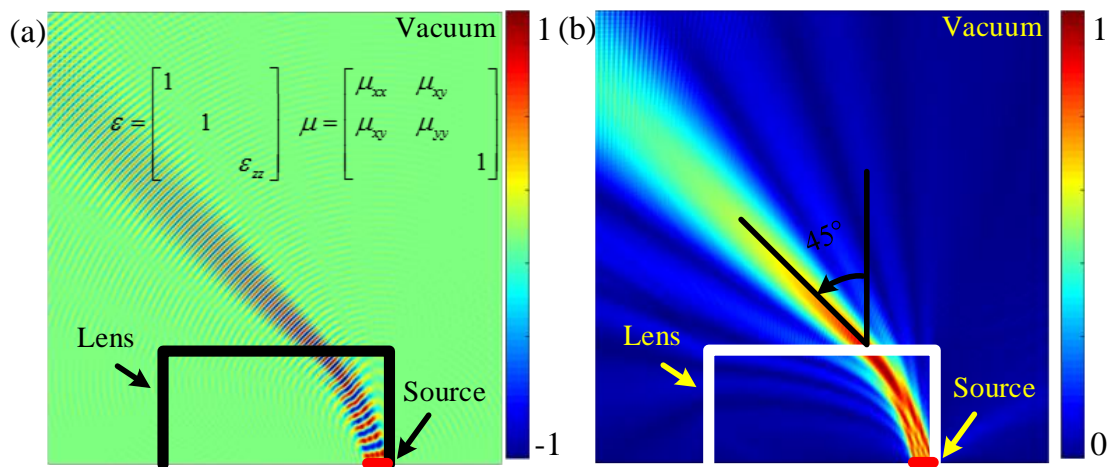


Figure 5-15: (a) Real part of electric field and (b) norm of the electric field distribution at 10 GHz illustrating the propagation of the radiated beam of a linear source through and out of the lens design 2 assigned by anisotropic parameters.

In Figure 5-15(a) and (b), a beam is emitted at 0° by the source. An area filled with vacuum should give the same field distribution after the beam emits out of the lens. We apply the material properties obtained from calculations for lens design 2 to the transformed lens area.

These parameters are anisotropic before the parameter reduction. The radiated beam is deflected by 45° after propagating through the lens. From this simulation, we can note that the functionality of the lens design 2 is capable of the beam steering functionality.

5.1.2.3 Parameter reduction

The parameter we assign to the lens in Figure 5-15 is anisotropic. Here we continue to test the functionality of the lens design 2 by ignoring the anisotropy by keep only ϵ_{zz} . The electric field distribution and the norm of the electric field are presented in Figure 5-16. Different from the simulation result for lens design 1, the isotropic lens design 2 can still deflect the beam by 45° . The conformal module of the lens design 2 is much smaller than the conformal module of lens design 1. In another word, the anisotropy of this design is small enough to be neglected. So when we keep only on permittivity component, the lens does not lose the steering functionality.

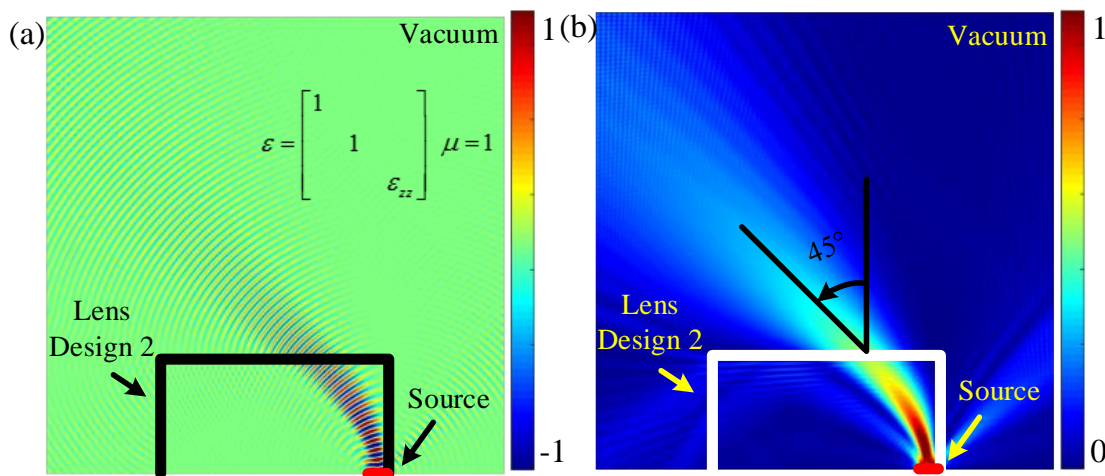


Figure 5-16: (a) Real part of electric field and (b) norm of the electric field distribution at 10 GHz illustrating the propagation of the radiated beam of a linear source through and out of the lens design 2 assigned by simplified parameters.

The far field radiation patterns of both anisotropic and isotropic lens are presented in Figure 5-17. The beam steering angles of these two models are both 45° . Although the beam steering angles are the same, there are still some drawbacks in neglecting the anisotropy. The main lobe

of the pattern becomes wider and the two side lobes are higher.

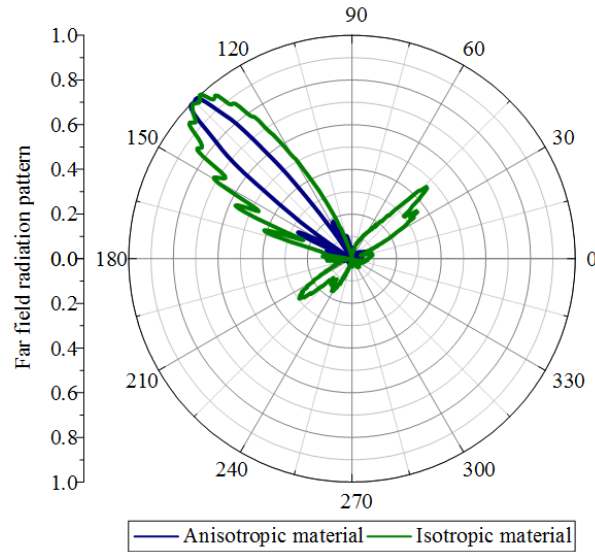


Figure 5-17: Normalized antenna radiation patterns showing the beam steering performances of lens design 2 assigned by anisotropic material and isotropic material.

5.2 Discretization of the lens design 1

In the distribution of ε_{zz} for design 2, the value between 0.4 and 1 distributes in most part of the lens area. This is impossible to realize by the 3D all dielectric printing. In this section, we select the lenses based on design 1 with parameter reduction when $H = 5$ cm for discretization and further implementation. The properties of the transformed medium are shown in Figure 5-18. According to the effective medium theory, if the operating wavelength is large enough (relative to the actual size of unit cell size), the composite material can be considered isotropic and homogenous. We choose the size of the unit cells to be $5 \text{ mm} \times 5 \text{ mm}$. In this case, the whole lens is composed of 200 (20×10) unit cells. The discrete permittivity of each cell is constant and equals to the permittivity value at the centre of each cell.

The discrete model of the proposed lens design is presented. After the discretization, the range of the permittivity has decreased, which is shown in Figure 5-18. As illustrated by the color plot in Figure 5-18(b), the permittivity ε_{zz} values range from 1 to 4 in the discrete approximation.

Since the electric field of the source is polarized along z direction, we further simplify the design by keeping only the properties along z direction, which is ϵ_{zz} in this case.

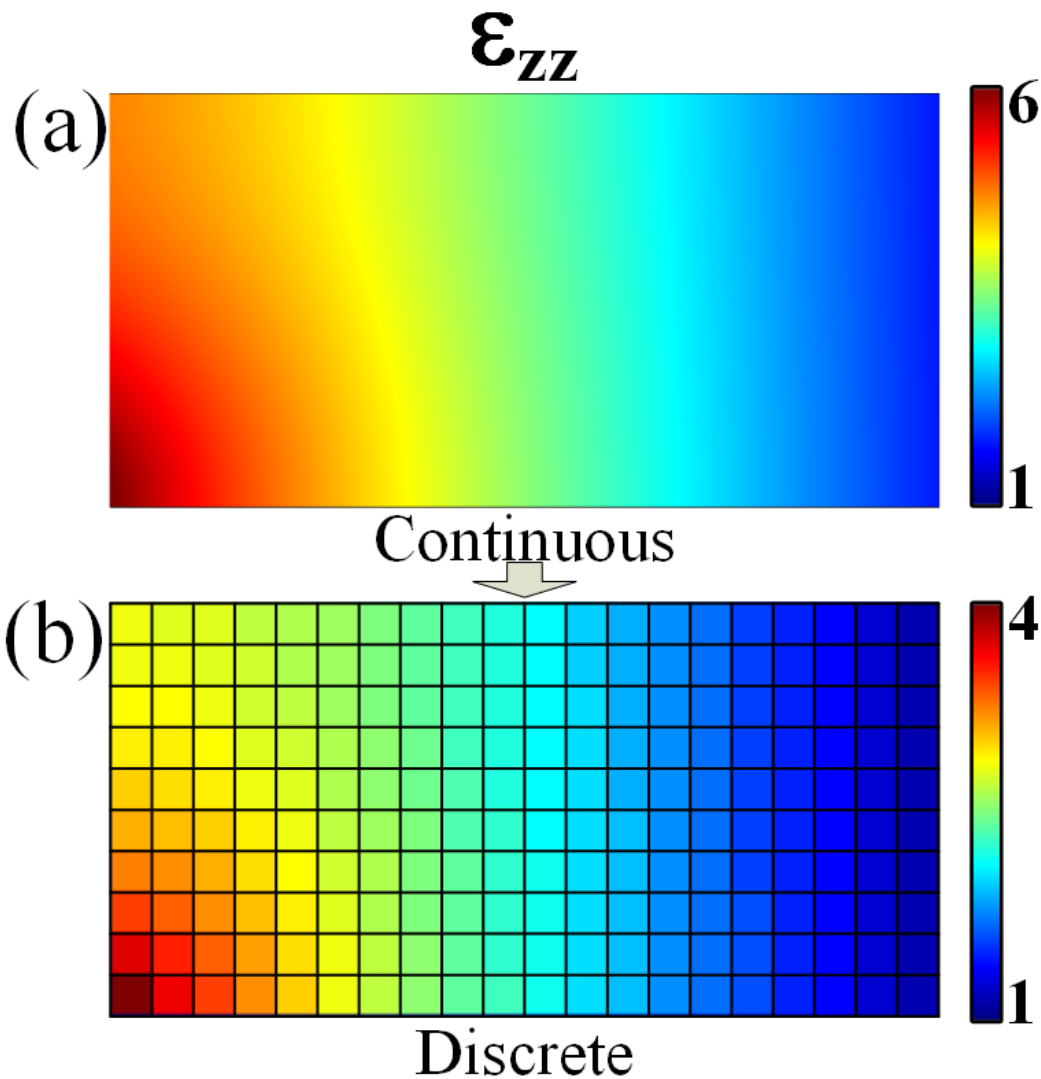


Figure 5-18: Discretization of the proposed lens design 1. The permittivity (ϵ_{zz}) distribution varies from 1 to 4.

Full wave simulations are performed on this 2-D discrete model. And the E-field and E-field norm distributions are shown in Figure 5-19. The simulation results of the discrete model are consistent with the results of the continuous model shown previously in Figure 5-4(c) and (d).

The discretization has caused reflection between the unit cells and on the boundary of the lens.

Therefore, instead of 28° , the discrete lens is able to steer the beam by 22.5° .

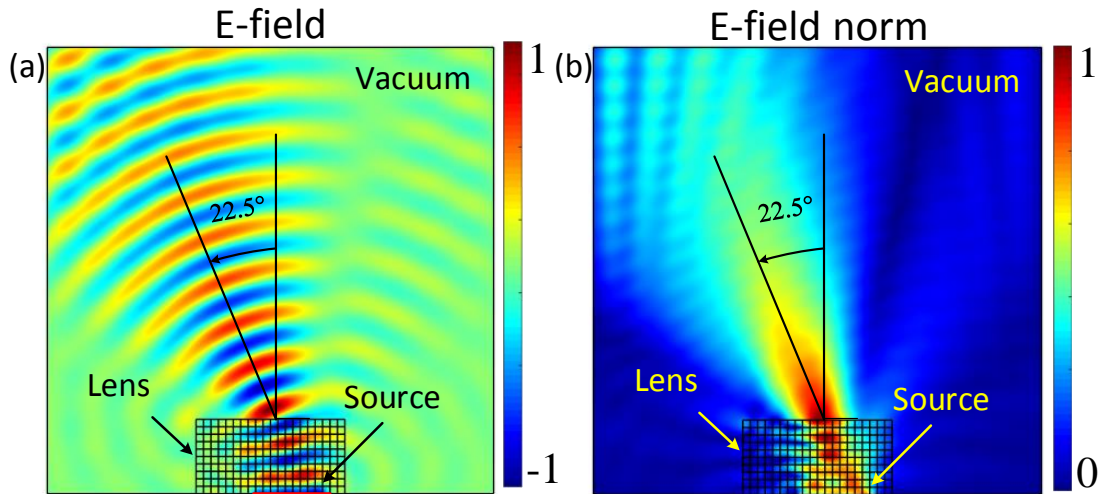
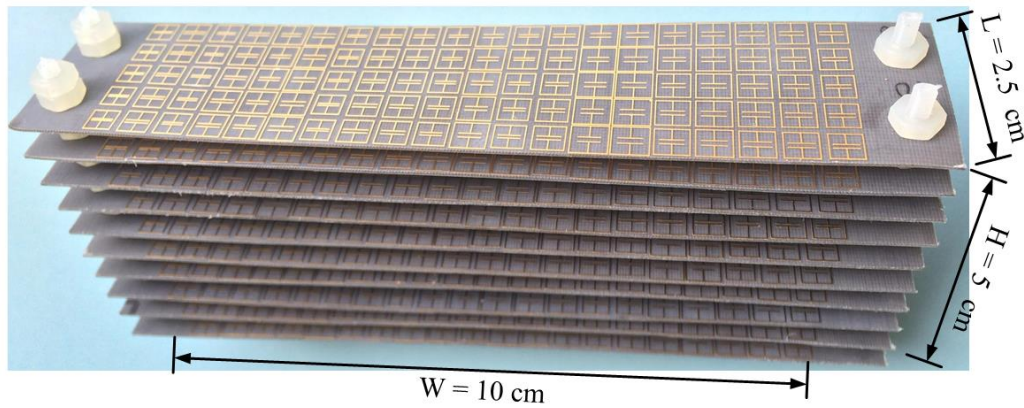


Figure 5-19: (a) Real part of electric field and (b) norm of the electric field distribution at 10 GHz illustrating the propagation of the radiated beam of a linear source through and out of the discrete lens assigned by simplified parameters.

5.3 Experimental validation using electric LC resonators

We fabricate the transformed lens by using electric *LC* (ELC) resonators and we experimentally validate the proposed lens in the microwave domain around 10 GHz. As known to all, the metamaterial suffers the narrow bandwidth limitation. But due to our fabrication resources, where it is impossible to realize permittivity values above 2.8 from all-dielectric material as in the previous chapter, the only way to achieve such values is by using metamaterials. Here, we make use of ELC resonators. However, such solution can be quite complex due to the large number of different needed values. Therefore, to demonstrate experimentally the mechanism of beam deflection, a prototype is fabricated using low cost printed circuit board (PCB) technology, as shown by the photography in Figure 5-20.

(a) Realistic prototype



(b) Top view

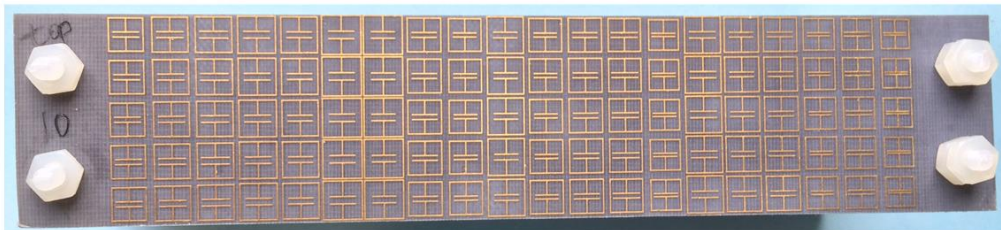


Figure 5-20: (a) Photography of the metamaterial based fabricated prototype. (b) Top view of one metamaterial layer composed of ELC resonators.

The model is composed of 10 different metamaterial layers stacked with a periodicity of 5 mm. Each layer contains 20 rows of ELC resonators and each row consists of 5 identical ELC cells [Figure 5-20(b)]. Hence, the whole metamaterial lens structure is composed of 200 rows, synthesizing the 200 different ϵ_{zz} values of the lens. The designed lens has geometrical dimensions 10 cm x 2.5 cm x 5 cm. Such solution using the resonant ELC structures then implies a narrow frequency bandwidth operation, meanwhile sufficient enough to experimentally validate the proposed lens.

A planar microstrip patch antenna array used as excitation source transmits through the metamaterial lens, which modifies the direction of the radiation. As shown in Figure 5-21(a), the antenna array consists 4 patches. The length of the side of the patch $l = 9.6$ mm. This patch

array has a resonance at 10 GHz. The simulated return losses of this patch antenna array are presented in Figure 5-21(b).

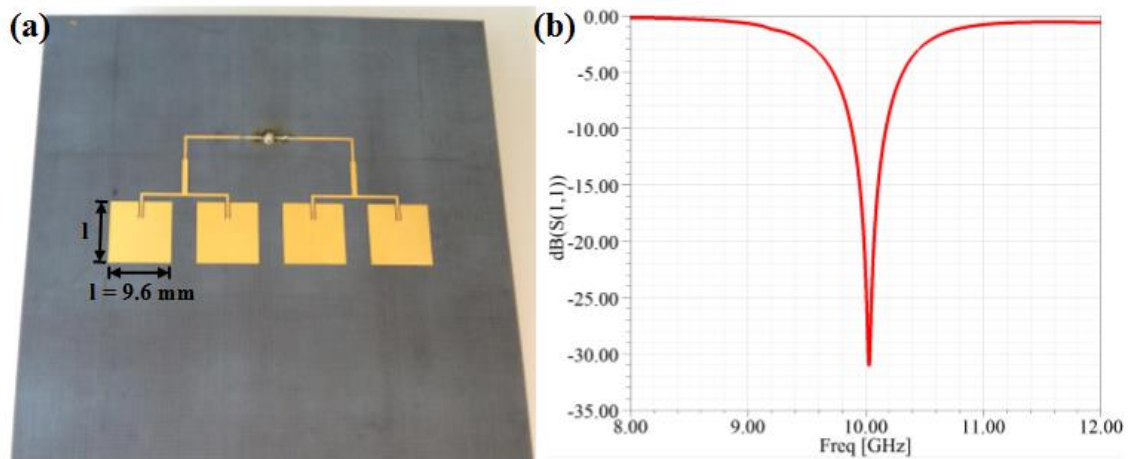


Figure 5-21: (a) Array of equally fed microstrip patch antenna used as wave launcher for the lens at 10 GHz. (b) return loss of the patch array antenna.

The structure of the ELC resonator used to engineer the material parameters of the transformed lens is presented in Figure 5-22(a). The 35 μm thick copper resonator is printed on a low loss substrate having dielectric permittivity 2.2, loss tangent 0.001 and thickness $t = 0.51$ mm. The properties of the resonator are characterized numerically using Finite Element Method (FEM) simulations done with ANSYS commercial code HFSS.⁴⁰ For an electromagnetic wave incident with a wave vector and field polarization of Fig. 2(a), the ELC resonator will exhibit an electric resonance. Figure 5-22(b) shows the reflection and transmission characteristics of such ELC resonator with geometrical dimensions: $p_x = p_y = 5$ mm, $b = 4.4$ mm, $c = 2$ mm $d = 0.2$ mm, and $g = 1$ mm. A resonance around 10 GHz is observed.

Using reflection and transmission responses from the sample, effective parameters can be extracted using the retrieval procedure reported in chapter 1. This is possible since the structure period along the propagation direction is very small compared to the operating wavelength. In performing the retrieval, we assume along propagation direction a cell size $p_z = 5$ mm corresponding to a cubic unit cell. Extracted permittivity and permeability are shown in Figure

5-22(c). Parametric studies have been performed on geometrical parameters b , c , and g to change the effective capacitance and inductance of the resonators, so that the resonance frequency will shift. In this way, the different desired material parameters of the lens are engineered. The influence of these three geometrical parameters on the extracted permittivity is shown at 10 GHz in Figure 5-22(d).

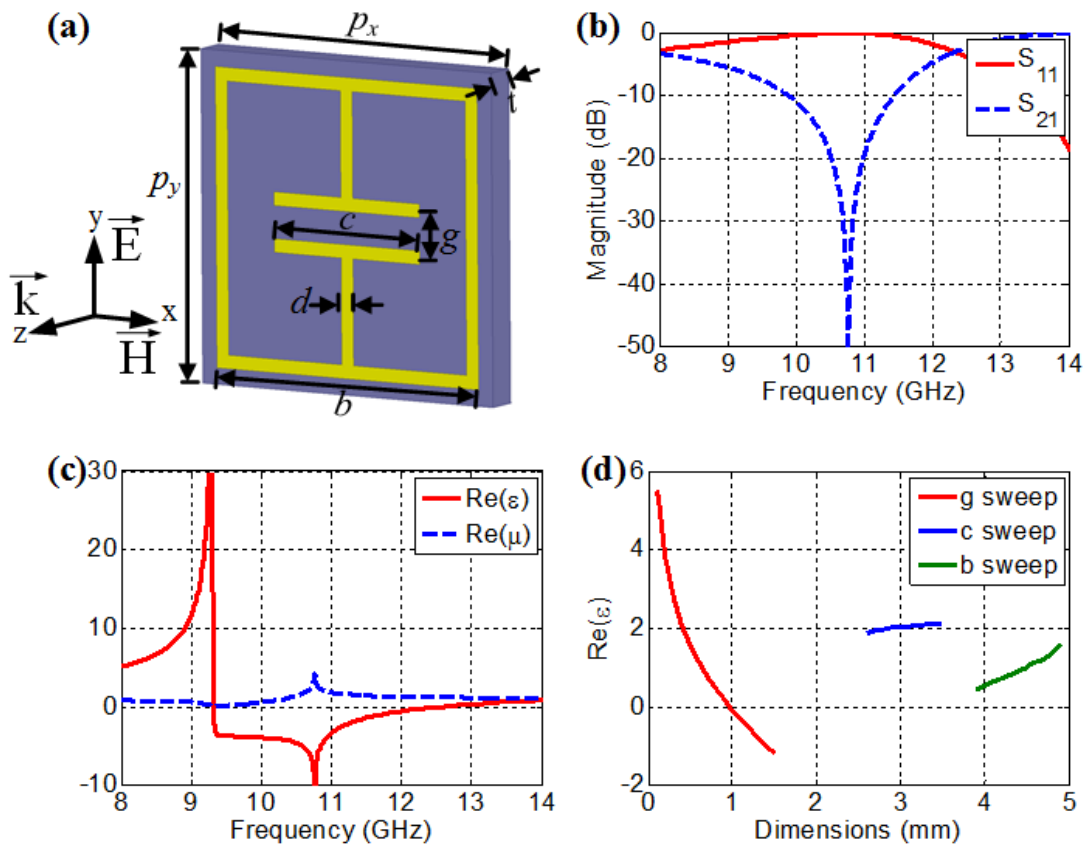


Figure 5-22: (a) Typical ELC unit cell structure. (b) Resonance of a parameterized unit cell with $p_x = p_y = 5$ mm, $b = 4.4$ mm, $c = 2$ mm, $d = 0.2$ mm, and $g = 1$ mm. (c) The extracted permittivity and permeability characteristics of such ELC resonator. (d) Influence of different geometrical parameters on the extracted permittivity. The fixed parameters for all sweeps are: $p_x = p_y = 5$ mm and $d = 0.2$ mm. When g is made variable, $b = 4.8$ mm and $c = 3$ mm, when c is made variable, $b = 4.8$ mm and $g = 0.5$ mm and when b is made variable, $c = 3$ mm and $g = 0.3$ mm.

A 3D discrete lens is designed for further realistic numerical simulations. The permittivity profile of the designed lens is shown in Figure 5-18. Full-wave simulations using Ansys HFSS³³ have been performed on the 3D discrete lens to verify the beam steering functionality. The microstrip patch antenna array, which operates at 10 GHz as we introduced just before, is used as primary source and the corresponding radiated emissions at 10 GHz are presented in Figure 5-23(a). Indeed such patch radiators present a narrow band frequency response. Here a sectorial beam, *i.e.* a wide beam in one plane and a narrow beam in the other plane is obtained since we are using a linear array of radiating elements. As it can be observed, in presence of the designed 3D ELC-based lens, the radiated wavefronts undergo a deflection of 13° . The color scale is in dB.

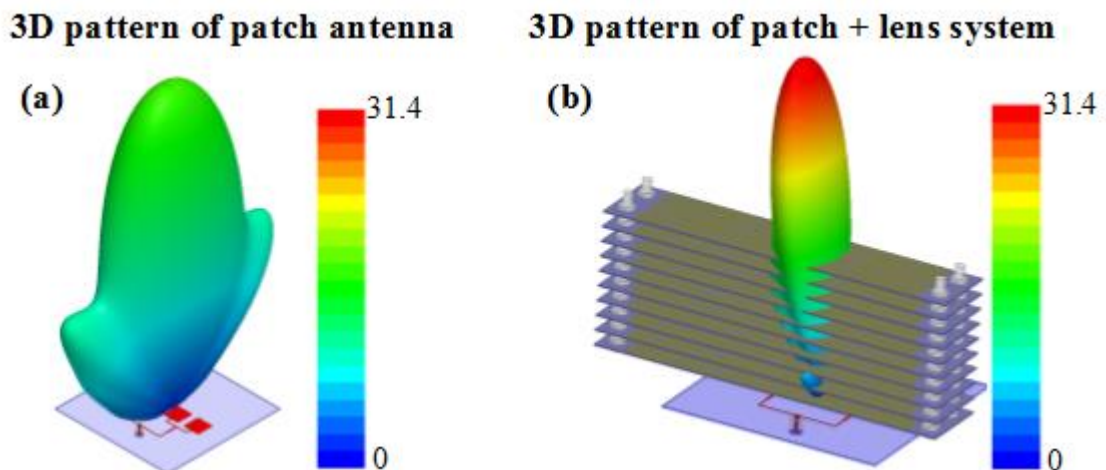


Figure 5-23: Simulated 3D radiation patterns in linear scale. (a) Linear array of patch elements at 10 GHz. (b) Lens antenna system at 10 GHz. The influence of the lens is twofold; firstly to enhance the directivity of the patch array source and secondly, to steer the radiated beam.

The reflection of this metamaterial lens and patch array system is measured at 10 GHz, and presented in **Figure 5-24**. The blue curve represents the S11 of the patch array antenna. The frequency band is from 9.9 GHz to 10.5 GHz, and the center frequency is at about 10.2 GHz. With the metamaterial lens above the patch array, the center operating frequency has shifted to

10.4 GHz. And the bandwidth is from 10 GHz to 10.7 GHz. The metamaterial lens operates at almost the same frequency and keeps almost the same bandwidth as the patch array alone. The center frequency is shifted high by just 0.2 GHz.

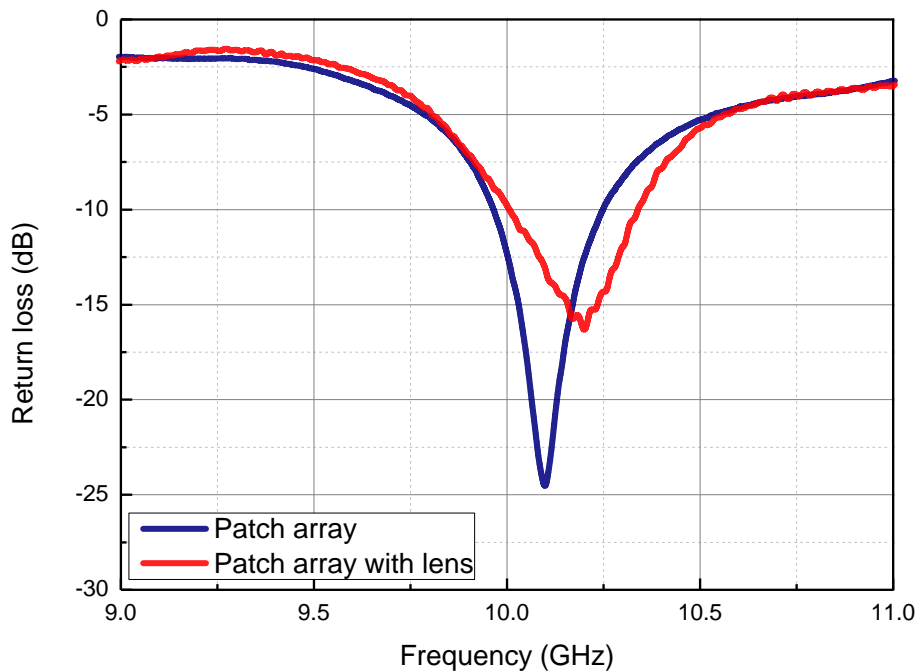


Figure 5-24: Measured S11 distribution at 10 GHz, where the blue curve represents the S11 of the patch array and the red curve represents the S11 of the patch and metamaterial lens system.

Full-wave simulations in far field are performed to numerically verify the functionality of the transformed beam steering lens. The excitation source is placed just below the lens parallel to the plane of the resonators (x - y plane) and produces a narrow radiated beam in the x - y plane. For experimental validation, far-field radiation patterns have also been measured in a full anechoic chamber. The measured radiations patterns in the x - y plane are compared to the simulated ones and are presented in Figure 5-25.

A quite overall good qualitative agreement is noted between the numerical and experimental performances. The characteristics obtained from the lens are further compared to the excitation source alone so as to show the influence of the lens. As it can be clearly observed from the

dotted blue and continuous green traces on the different plots, representing the simulated and measured radiation patterns respectively, the primary source alone produces a radiated beam at boresight direction ($\theta = 0^\circ$). The designed lens allows to steer the radiated beam by 13° at 10 GHz, as depicted by the dashed violet and continuous red traces in Figure 5-25(b), corresponding to respectively simulations and measurements on the lens-antenna system.

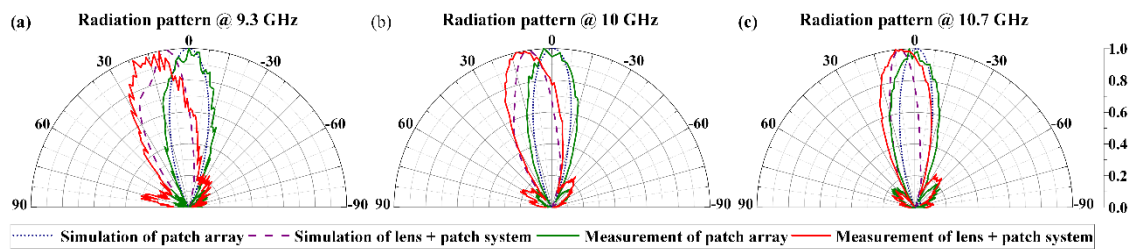


Figure 5-25: Simulated and measured far-field radiation patterns in the deflection lane (x-y plane) at (a) 9.3 GHz, (b) 10 GHz and (c) 10.7 GHz.

Although the individual resonators constituting the lens present narrow-band resonances, the metamaterial lens operates on a non-narrow frequency band. The far field patterns at 9.3 GHz and 10.7 GHz are also shown in Figure 5-25(a) and (c), where the beam is deflected by 15° and 8° respectively. The deflection angle changes with frequency since the permittivity gradient is also frequency dependent. The reason for the non-narrow frequency band phenomenon is that although the individual resonators constituting the lens present narrow-band resonances, the metamaterial lens operates on a non-narrow frequency band. In fact, in the [9.3 GHz - 10.7 GHz] frequency band, the metamaterial lens exhibits a gradient in ϵ_{zz} which is slightly different at each frequency point and which allows producing the beam steering.

To further investigate the steering behavior of the lens-antenna system, near electric field distributions have been measured. The electric field mapping of the lens-antenna system is depicted in Figure 5-26 at different frequencies. As predicted by the simulated and measured far-field radiation patterns, the beam steering behavior is confirmed by the near-field distributions. The wavefronts emanating from the lens are deflected from the normal direction.

Moreover, similar non-narrow frequency band operation of the lens is observed, confirming the far field simulation and measurement results in Figure 5-25.

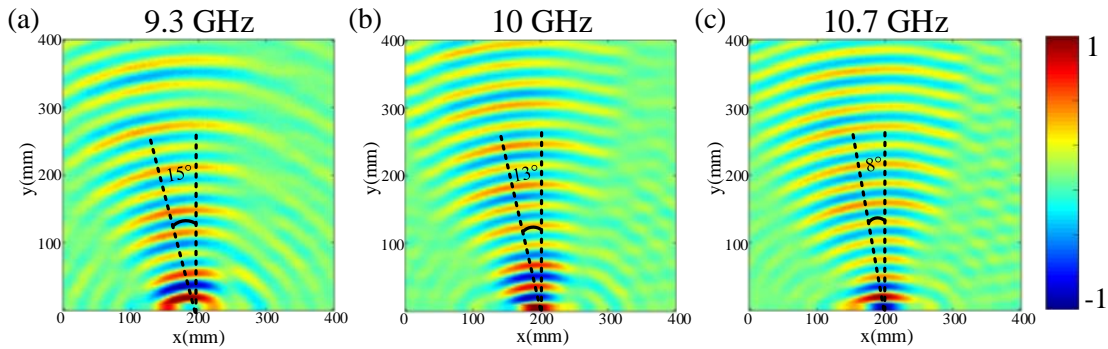


Figure 5-26: Measured real part of electric near-field distributions at (a) 9.3 GHz, (b) 10 GHz and (c) 10.7 GHz. A deflection of the beam from the normal direction is observed.

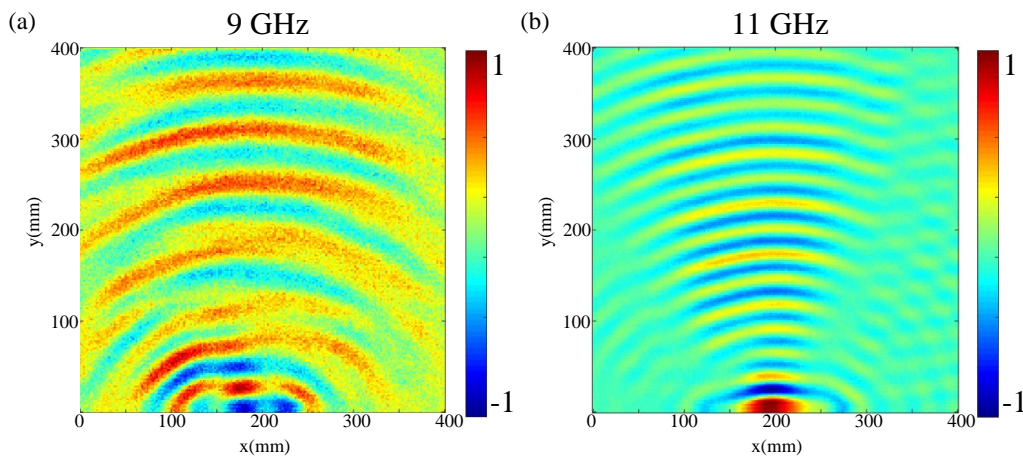


Figure 5-27: Measured real part of electric near-field distributions at (a) 9 GHz, (b) 11 GHz. No deflection is observed.

We further enlarge the testing frequency band. However the lens does not show any beam steering at 9 GHz or 11 GHz. By analysing the near field distribution of this patch lens system within the frequency band from 9 GHz to 11 GHz, we are able to plot a curve of the beam steering angle variation with frequency. The curve is presented in Figure 5-28. It is clear that the lens starts to operate from 9.3 GHz, and stops performing the functionality at 10.7 GHz, which confirms the results we stated before. Maximum beam steering can be clearly observed around

9.5 GHz.

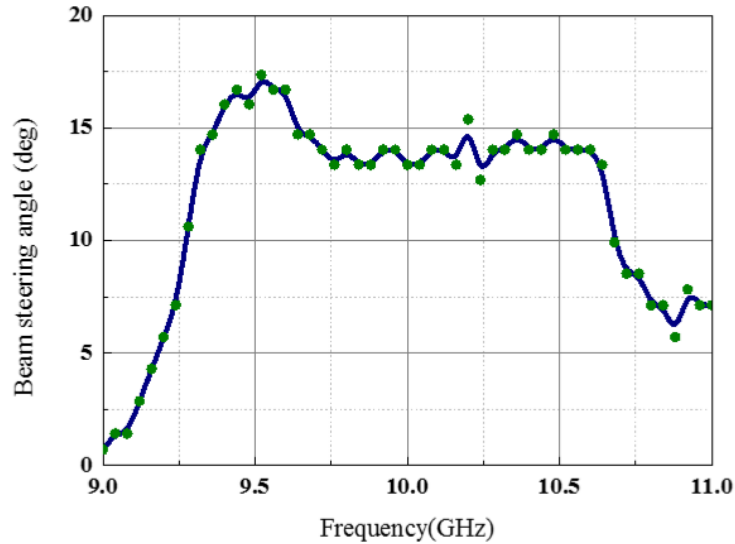


Figure 5-28: Frequency study on beam steering angle variation.

5.4 Experimental validation using all-dielectric material

Besides the ELC metamaterial lens, an all-dielectric lens prototype presenting a graded permittivity profile is also fabricated for potential wide frequency band through three-dimensional (3D) polyjet printing technology. The dielectric material used for this fabrication is the same as the one we have mentioned in Chapter 4 for the in-phase emissions restoring lens. As known, the permittivity of this material in our polyjet printing fabrication facilities is 2.8. We decide to fabricate the part of the beam steering lens that has the permittivity value below 2.8. Therefore the part between 2.8 to 4 is discarded.

We therefore propose a discrete lens model, as presented in Figure 5-29(a), which is composed of only 170 unit cells. The respective permittivity of each cell is considered to be constant across the cell and is equal to the average permittivity within the cell. As illustrated by the colour plot in Figure 5-29(a), the permittivity ϵ_{zz} values range from 1 to 2.8 in the discrete approximation.

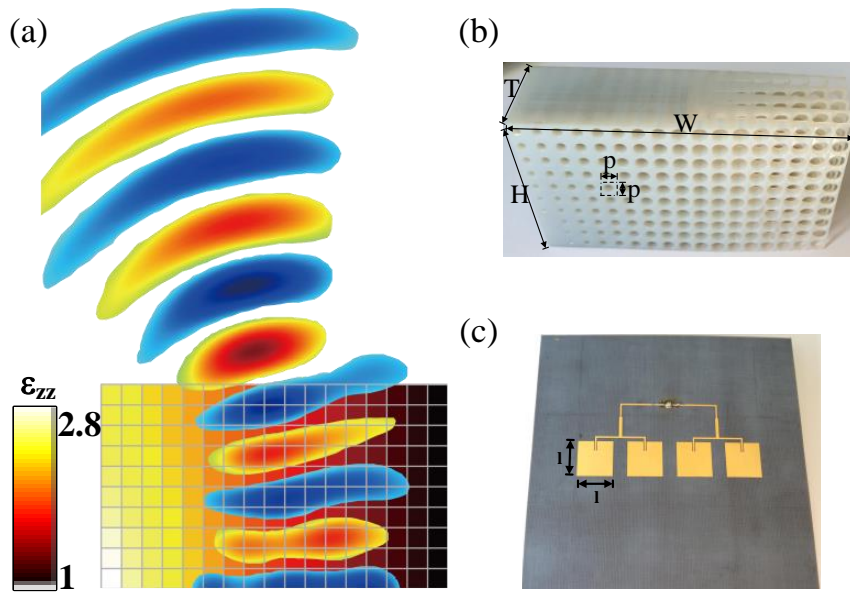


Figure 5-29: Beam steering lens realization. (a) Calculated discrete lens with 170 values of ϵ_{zz} varying from 1 to 2.8. (b) Photography of the fabricated all-dielectric lens prototype, where $W = 8.5$ cm, $H = 5$ cm, $T = 2.5$ cm and $p = 5$ mm. (c) Array of equally fed microstrip patch antennas used as wave launcher for the lens.

Finite element method based 2D numerical simulations with COMSOL Multiphysics are firstly used to numerically validate the calculated transformed isotropic beam steering lens. Scattering boundary conditions are set around the computational domain and an array of four dipoles, convenient for 2D simulations, is used as source. The different dipoles are excited with equal amplitude and phase so as to produce a directive beam at boresight (normal) direction. The beam steering functionality will then be achieved by the influence of the designed lens. The electric field of the feeding sources is polarized along the z direction. The final dimensions of the discrete lens are: $W = 8.5$ cm, $H = 5$ cm and $T = 2.5$ cm. as shown in Figure 5-29(b).

Other than the patch array operating at 10 GHz that we introduced in the last section for the ECL-based beam steering lens, two other arrays are fabricated with $l = 12$ mm and $l = 8$ mm for the wide frequency band test at 8 GHz and 12 GHz respectively. The return losses of these three sources are presented in Figure 5-30.

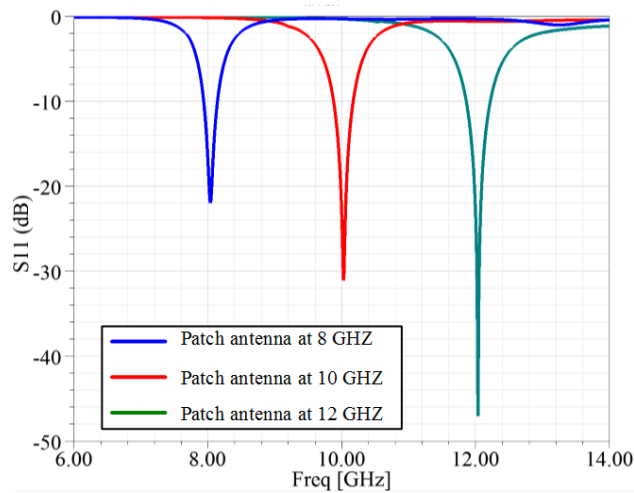


Figure 5-30: Return loss of the array of equally fed microstrip patch antenna used as wave launcher for the lens at 8 GHz, 10 GHz and 12 GHz.

Simulation results of the electric field distribution are shown in Figure 5-31(a), (b) and (c) at 8 GHz, 10 GHz and 12 GHz respectively. As it can be clearly observed, the outgoing waves of the planar array present planar wavefronts and therefore a directive emission, at the three tested frequencies. The electromagnetic radiated beam undergoes a deflection inside the lens and transmits out of the lens in an off-normal direction. The obtained performances show clearly the usefulness of the lens in controlling the beam direction. Moreover, the norm of the electric field presented in Figure 5-31(d), (e) and (f) shows a very good impedance matching between the lens and free space.

As we can see here, although we have neglected part of the lens that contained high permittivity value, the lens performs almost the same functionality with the original one. The emitted beam is steered by an angle around 22.5° at all these three frequencies.

A 3D discrete lens is designed for further realistic numerical simulations. The permittivity profile of the designed lens is shown in Figure 5-29(a). The profile is divided into 170 cubic cells. In order to be able to use the lens over a broad frequency range, the lens is realized from non-resonant cells. Air holes in a dielectric host medium of relative permittivity $\epsilon_h = 2.8$ is therefore considered.

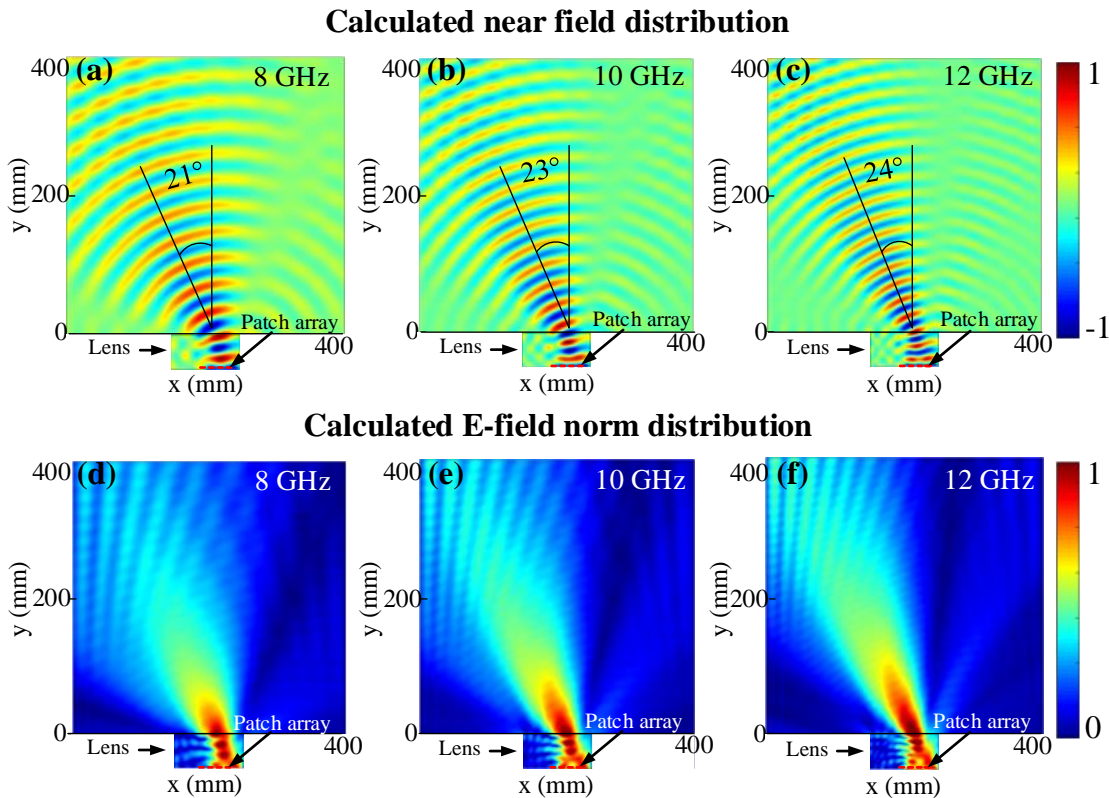


Figure 5-31: (a)-(c) 2D simulated electric field distribution at 8 GHz, 10 GHz and 12 GHz, where an array of dipoles is used as excitation feed for the lens with discrete parameter profile. A directive beam showing planar wavefronts oriented in an off-normal direction is observed. (d)-(f) Norm of the electric field showing very good impedance matching between the array-lens system and free space.

Full-wave simulations using Ansys HFSS have been performed on the 3D discrete lens to verify the beam steering functionality. The microstrip patch antenna array composed of four equally fed linear radiating elements is used as primary source and the corresponding radiated emissions at 8 GHz, 10 GHz and 12 GHz are presented in Figure 5-32. Therefore to cover the 8 GHz to 12 GHz frequency band, three different arrays have been used. However, it is supposed that in real applications, a primary source presenting a wideband frequency response will be used. Here a sectorial beam, i.e. a wide beam in one plane and a narrow beam in the other plane is obtained since we are using a linear array of radiating elements.

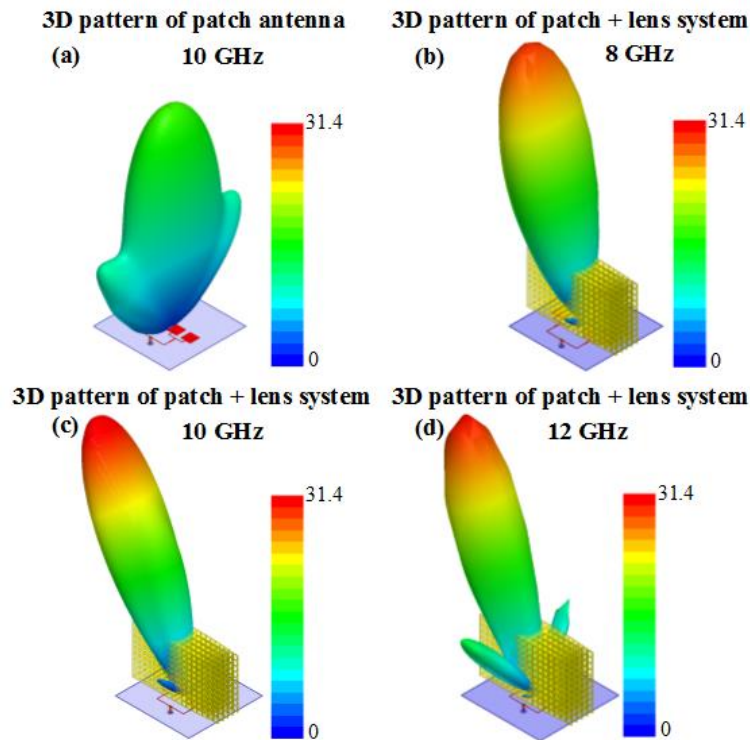


Figure 5-32: Simulated 3D radiation patterns in linear scale. (a) Linear array of patch elements at 10 GHz. (b) Lens antenna system at 8 GHz. (c) Lens antenna system at 10 GHz. (d) Lens antenna system at 12 GHz. The influence of the lens is twofold; firstly to enhance the directivity of the patch array source and secondly, to steer the radiated beam.

As it can be observed in Figure 5-32(c), in presence of the designed 3D dielectric lens, the radiated wavefronts undergo a deflection of 28° , confirming the 2D simulation results and the fact that the lens is able to modify the direction of wave propagation. Moreover, the lens is able to enhance the directivity of the radiated beam from 16 to more than 31.

In Figure 5-33, the S11 of the patch array antenna and the dielectric lens antenna system are presented. The measurement is carried out at 8 GHz, 10 GHz and 12 GHz respectively in order to cover the whole X-band. The blue curves represent the S11 of the patch array and the red curves represent the S11 of the patch and lens system. It's clear that the dielectric lens keeps the same bandwidth as the patch array antenna alone. But the center operation frequency is shifted down a little.

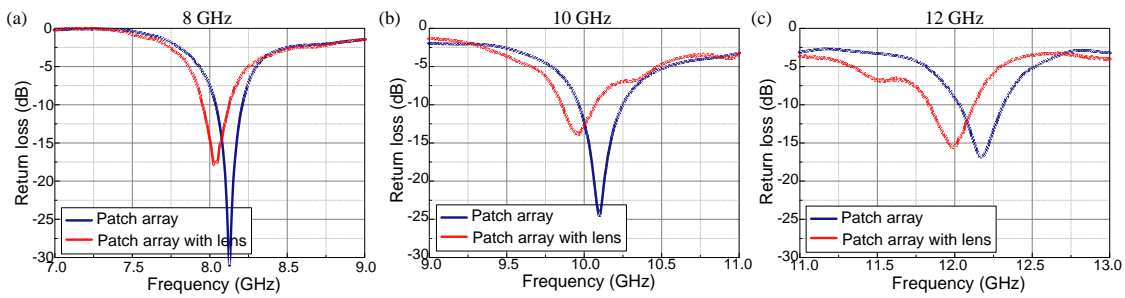


Figure 5-33: Measured S11 distribution at (a) 8 GHz, (b) 10 GHz and (c) 12 GHz, where the blue curves represent the S11 of the patch array and the red curves represent the S11 of the patch and lens system.

A photography of the fabricated lens prototype is presented in Figure 5-29(b). The lens is excited by a microstrip patch linear array consisting of four elements fed with equal magnitude and phase (Figure 5-29(c)). A first experimental system aiming to scan the electric near-field microwave radiation is set up. The electric field mapping of the antenna system is depicted in Figure 5-34 for the three tested frequencies. As in numerical simulations, quasi-planar wavefronts emanating from the lens-antenna in an off-normal direction are observed at each tested frequency.

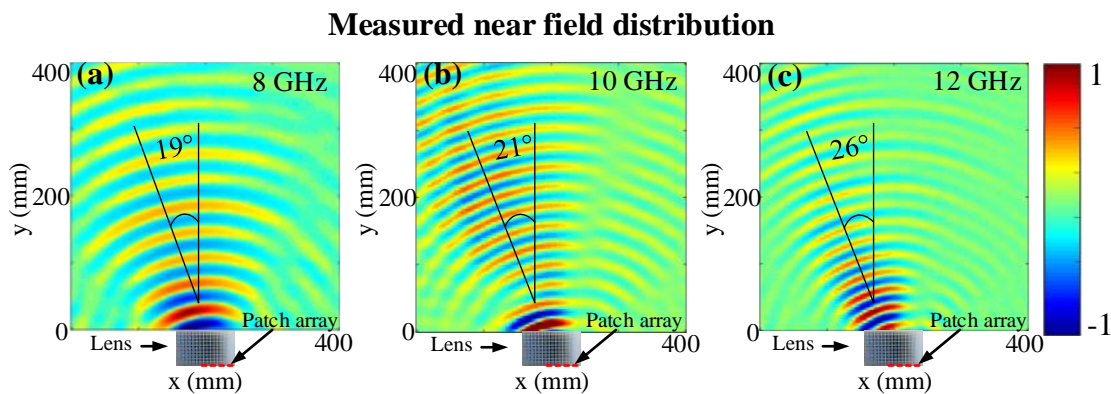


Figure 5-34: Measured real part of electric near-field distribution at (a) 8 GHz, (b) 10 GHz and (c) 12 GHz, where an array of patch radiators is used as excitation feed for the lens. A directive beam showing planar wavefronts oriented in an off-normal direction is observed.

We further investigate the beam steering functionality of the lens-antenna system by measuring the far-field antenna diagrams in a full anechoic chamber. The normalized measured radiation patterns in the x-y plane are compared to the simulated ones and are presented in Figure 5-35. A quite overall good qualitative agreement is noted between the simulated and measured characteristics. From the different plots, a clear directive radiation lobe is observed at all tested frequencies for the lens-antenna system. As predicted in 3D simulations (Figure 5-32(a)), the patch antenna array used as feeding source presents a radiation diagram with a maximum directivity at boresight. However, when associated to the transformed lens, a beam deflection from the normal is obtained as illustrated in Figure 5-35. Thus, the use of the transformed lens above the patch array allows steering the radiated beam to an off-normal direction. Moreover, the use of the dielectric lens allows achieving a broad bandwidth due to the non-resonant nature of the air hole cells. The far-field antenna's radiation patterns confirm the performances obtained from the near-field measurements, that are shown by the wavefronts in Figure 5-34.

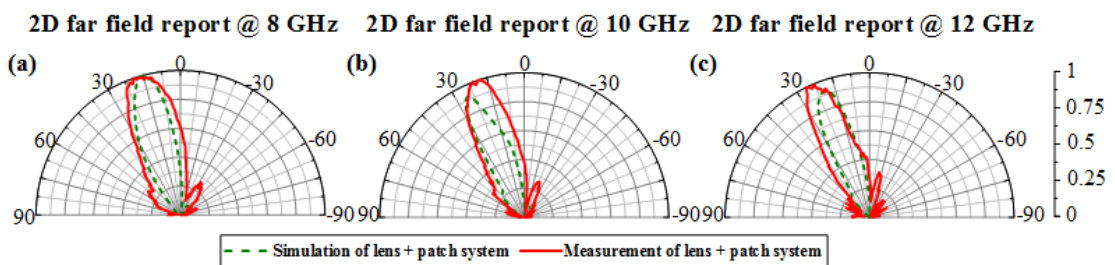


Figure 5-35: Comparison of the normalized simulated and measured radiation patterns in the focusing plane (x-y plane). (a) 8 GHz. (b) 10 GHz. (c) 12 GHz.

5.5 Conclusion

To conclude, in this chapter, we have proposed a concept to manipulate electromagnetic waves and design a beam steering lens. The latter manipulation is enabled by using quasi-conformal transformation and Laplace's equation is utilized to construct the mapping between the virtual space and the physical space. Numerical verifications have been performed on two different

designs; one where the conformal module of the mapping is close to 1 and another one where the conformal module is far from 1. The radiation of a current line source has been steered off the normal in both designs. It has also been observed that when ignoring material anisotropy in the design where the conformal module is far from 1, the beam steering functionality is weakened and hence, beam steering angle is less compared to the case where anisotropic parameters are used. However, when the conformal module is close to 1, material anisotropy can be ignored without deterioration of the steering performances.

We have also presented the experimental validation of a metamaterial based beam steering lens when the conformal module is far from 1. ELC resonators have first been used to tailor the material parameters of the lens by a judicious engineering of the geometrical dimensions. The lens has been tested experimentally on a frequency band spanning from 9.3 GHz to 10.7 GHz.

Another experimental realization of a compact all-dielectric beam steering lens operating on a wider frequency range has then been presented. The lens has been tested over a broad frequency band spanning from 8 GHz to 12 GHz. Such lenses are able to both enhance the directivity and modify the direction of propagation, allowing a control of the emission. The concept has been validated through calculated and measured near-field distributions and far-field antenna patterns. The proposed method is easy of fabrication, low-cost and presents potential airborne and trainborne applications in communication systems and environments where radiation direction needs to be controlled in a passive way. The proposed designs open the way to a wide range of potential applications in electromagnetics and daily communications employing lenses and antennas.

CONCLUSION

Transformation optics is an efficient tool to manipulate the electromagnetic field distributions. The form-invariance of Maxwell's equations is exploited to design complex electromagnetic media with desired and particular properties. The device that is assigned by the designed electromagnetic media can perform a certain functionality that have never been demonstrated before or that are very difficult to realize with naturally common materials.

Coordinate transformation is able to compress, rotate or fold the space at will. It is a useful and powerful concept that can really control the field at one's will. It has been demonstrated in this thesis that, by applying a two-step linear transformation, an illusion device can be designed based on coordinate transformation. This illusion device is able to change the radiation pattern and to make the radiation location appear outside the latter space. In addition, a tapering device can be designed by several kinds of transformations. However, the material properties designed from coordinate transformation are always complex or singular. In most case, the parameter tensor consists of non-diagonal components whose value are either negative or too high to be achieved. Therefore, although the designs based on coordinate transformation are usually fascinating, very few of them can be realized. Even they can be realized, normally resonant metamaterials are required, which is limited by narrow frequency band.

Transformation optics based on Laplace's equation is another method to reshape the electromagnetic field. Other than mapping the virtual and physical space from point to point as in coordinate transformation, the mapping can also be established by solving Laplace's equation with specified boundary conditions. A beam focusing lens and a beam steering lens are designed by this concept and validated experimentally. Transformation based on Laplace's equation provides a much easier way for the device designing. Indeed for quasi-conformal transformation optics, an in-plane isotropic material can be applied to the designs which can further be realized by non-resonant all-dielectric materials, allowing a broad band operations. However, this concept requires the transformed virtual and physical space to be quite similar with each other, where no subversive mapping can be established.

Transformation optics therefore requires the use of engineered values of permittivity and permeability. Metamaterials which are complex artificial materials can be used to fabricate structures which mimic a material response that has no natural equivalent. This capability has led to an explosion of interests in the physical properties of these materials and the ways in which they can be used. Two structures of resonant metamaterial resonators are implemented in this thesis to realize near zero permeability values and high permittivity values. But these resonators present the drawback of having narrow-band resonances. Thus, frequency independent designs from transformation optics are limited by the resonators. All-dielectric materials are generally utilized for QCTO designs. Such materials can be for example engineered by dielectric 3D printing as it has been done in this thesis. These prototypes operate on a wide frequency to fabricate the isotropic designs.

BIBLIOGRAPHY

- [1] D. Schurig, J. J. Mock, B. J. Justice, S. A. Cummer, J. B. Pendry, A. F. Starr, D. R. Smith, *Science* 314,5801(2006).
- [2] P. Tassin, T. Koschny, M. Kafesaki, C. M. Soukoulis. *Nature Photonics*, 2012; 6 (4): 259
DOI: 10.1038/nphoton.2012.27
- [3] S. Linden, C. Enkrich, M. Wegener, J. Zhou, T. Koschny, and C. M. Soukoulis, *Science* 306, 1351–1353 (2004).
- [4] N. Liu and H. Giessen, *Angewandte Chemie International Edition* 49, 9838–9852 (2010).
- [5] M. Kafesaki, T. Koschny, R. S. Penciu, T. F. Gundogdu, E. N. Economou, and C. M. Soukoulis, *Journal of Optics A* 7, S12–S22 (2005).
- [6] V. M. Shalaev, *Nature Photonics* 1, 41–48 (2007).
- [7] G. Dolling, M. Wegener, S. Linden and C. Hormann, *Optics Express*, Vol. 14, No. 5 (2006).
- [8] R. A. Shelby, D. R. Smith, and S. Schultz, *Science*, 292(5514):77{79, 2001.

- [9] S. Enoch, G. Tayeb, P. Sabouroux, N. Guérin, and P. Vincent, *Physics Review Letters* 89, 213902
- [10] E. Lier, D. H. Werner, C. P. Scarborough, Q. Wu & J. A. Bossard, *Nature Materials* 10, 216–222 (2011)
- [11] Z. H. Jiang, M. D. Gregory and D. H. Werner, *IEEE Antennas and Wireless Propagation Letters*, VOL. 10, 2011.
- [12] T. Driscoll, D. N. Basov, A. F. Starr, P. M. Rye, S. Nemat-Nasser et al., *Applied Physics Letters* 88, 081101 (2006).
- [13] A. Ourir, S. N. Burokur, R. Yahiaoui, A. de Lustrac, *Comptes Rendus Physique*, vol. 10, no. 5, pp. 414-422, June 2009.
- [14] S. N. Burokur, J.-P. Daniel, P. Ratajczak, A. de Lustrac, *Microwave and Optical Technology Letters*, vol. 53, no. 10, pp. 2291-2295, October 2011.
- [15] A. Dhouibi, S. N. Burokur, A. de Lustrac, A. Priou, *IEEE Antennas and Wireless Propagation Letters*, vol. 11, pp. 1504-1507, 2012.
- [16] D. Germain, D. Seetharamdoo, S. N. Burokur, A. de Lustrac, *Applied Physics Letters*, vol. 103, no. 12 (124102), Septembre 2013.
- [17] A. Ghasemi, S. N. Burokur, A. Dhouibi, A. de Lustrac, *IEEE Antennas and Wireless Propagation Letters*, vol. 12, pp. 261-264, 2013.
- [18] A. Dhouibi, S. N. Burokur, A. de Lustrac, A. Priou, *Applied Physics Letters*, vol. 102, no. 2 (024102), January 2013.
- [19] A. J. Ward and J. B. Pendry. *Journal of Modern Optics*, 43:773–793, 1996.

- [20] V. M. Shalaev. Transforming light. *Science*, 322:384–386, 2008.
- [21] J. B. Pendry, D. Schurig, and D. R. Smith, *Science* 312 (5781), 1780-1782 (2006).
- [22] J. Valentine, J. Li, T. Zentgraf, G. Bartal, and X. Zhang, *Nature Materials* 8 (7), 568-571 (2009).
- [23] T. Ergin, N. Stenger, P. Brenner, J. B. Pendry, and M. Wegener, *Science* 328 (5976), 337-339 (2010).
- [24] U. Leonhardt, and T. Tyc, *Science* 323 (5910), 110-112 (2009).
- [25] P. Zhang, Y. Jin, and S. L. He, *Applied Physics Letters* 93 (24), 243502 (2008).
- [26] A. V. Kildishev, W. Cai, U. K. Chettiar, and V. M. Shalaev, *New Journal of Physics* 10 (11), 115029 (2008).
- [27] Y. Lai, J. Ng, H. Chen, D. Han, J. Xiao, Z. Q. Zhang, and C. T. Chan, *Physical Review Letters* 102 (25), 253902 (2009).
- [28] C. Li, X. Meng, X. Liu, F. Li, G. Fang, H. Chen, and C. T. Chan, *Physical Review Letters* 105 (23), 233906 (2010).
- [29] Y. Xu, S. Du, L. Gao, and H. Chen, *New Journal of Physics* 13 (2), 023010, (2011).
- [30] C. Li, X. Liu, G. Liu, F. Li, and G. Fang, *Applied Physics Letters* 99 (8), 084104 (2011).
- [31] Y. Lai, J. Ng, H. Y. Chen, Z. Q. Zhang, and C. T. Chan, *Frontiers of Physics China* 5, 308-318 (2010).
- [32] D. H. Kwon, and D. H. Werner, *Optics Express* 17 (10), 7807-7817 (2009).
- [33] D. A. Roberts, N. Kundtz, and D. R. Smith, *Optics Express* 17 (19), 16535-16542.

- [34] N. Kundtz, and D. R. Smith, *Nature Materials* 9 (2), 129-132 (2010).
- [35] R. Yang, W. Tang, and Y. Hao, *Optics Express* 19 (13), 12348-12355 (2011).
- [36] O. Quevedo-Teruel, and Y. Hao, *Optics Letters* 38 (4), 392-394 (2013).
- [37] Q. Wu, Z. H. Jiang, O. Quevedo-Teruel, J. P. Turpin, W. Tang, Y. Hao, and D. H. Werner, *IEEE Antennas and Propagation* 61 (12), 5910-5922 (2013).
- [38] D. A. Genov, S. Zhang, and X. Zhang, *Nature Physics* 5 (9), 687-692 (2009).
- [39] H. Chen, R. X. Miao, and M. Li, *Optics Express* 18 (14), 15183-15188 (2010).
- [40] A. Greenleaf, Y. Kurylev, M. Lassas, and G. Uhlmann, *Physical Review Letters* 99 (18), 183901 (2007).
- [41] A. Greenleaf, Y. Kurylev, M. Lassas, and G. Uhlmann, *SIAM Review* 51 (1), 3-33 (2009).
- [42] M. Kadic, G. Dupont, S. Enoch, and S. Guenneau, *Physical Review A* 90, 043812 (2014)
- [43] M. Rahm, D. Schurig, D. A. Roberts, S. A. Cummer, D. R. Smith, and J. B. Pendry, *Photonics and Nanostructures* 6, 87-95 (2008).
- [44] K. Zhang, Q. Wu, J. H. Fu, and L. W. Li, *Journal of Optics Soc. Am. B* 28 (6), 1573-1577 (2011).
- [45] T. Li, M. Huang, J. Yang, S. Mu, and Y. Lan, *Progress in Electromagnetic Research M* 18, 119-130 (2011).
- [46] H. Chen, B. Hou, S. Chen, X. Ao, W. Wen, and C. T. Chan, *Physical Review Letters* 102 (18), 183903 (2009).

- [47] H. Chen, and C. T. Chan, *Applied Physics Letters* 90 (24), 241105 (2007).
- [48] J. B. Pendry, *Physical Review Letters* 85 (18), 3966 (2000).
- [49] M. Tsang, and D. Psaltis, *Physical Review B* 77 (3), 035122 (2008).
- [50] M. Yan, W. Yan, and M. Qiu, *Physical Review B* 78 (12), 125113 (2008).
- [51] S. Guenneau, and S. A. Ramakrishna, *Comptes Rendus Physique* 10 (5), 352-378 (2009).
- [52] D. P. Gaillot, C. Croënne, F. Zhang, and D. Lippens, *New Journal of Physics* 10 (11), 115039 (2008).
- [53] W. H. Wee, and J. B. Pendry, *New Journal of Physics* 11 (7), 073033 (2009).
- [54] J. Ng, H. Chen, and C. T. Chan, *Optics Letters* 34 (5), 644-646 (2009).
- [55] T. Yang, H. Chen, X. Luo, and H. Ma, *Optics Express* 16 (22), 18545-18550 (2008).
- [56] X. Zang, and C. Jiang, *Optics Express* 18 (7), 6891-6899 (2010).
- [57] C. Yang, J. Yang, M. Huang, J. Peng, and G. Cai, *Comp. Mater, Science* 49 (4), 820-825 (2010).
- [58] J. Ng, H. Chen, and C. T. Chan, *Optics Letters* 34 (5), 644-646 (2009).
- [59] M. Rahm, S. A. Cummer, D. Schurig, J. B. Pendry, and D. R. Smith, *Physical Review Letters* 100 (6), 063903 (2008).
- [60] D. H. Kwon, and D. H. Werner, *Optics Express* 16 (23), 18731-18738 (2008).
- [61] T. Zhai, Y. Zhou, J. Zhou, and D. Liu, *Optics Express* 17 (20), 17206-17213 (2009).
- [62] V. Giniis, P. Tassin, J. Danckaert, C. M. Soukoulis, and I. Veretennicoff, *New Journal of Physics* 14 (3), 033007 (2012).

- [63] G. X. Yu, L. Cao, and M. Zhou, *Cent. Eur. Journal of Physics* 10 (1), 140-144 (2012).
- [64] V. Giniis, P. Tassin, C. M. Soukoulis, and I. Veretennicoff, *Physical Review B* 82 (11), 113102 (2010).
- [65] Z. Wang, Y. Luo, W. Cui, W. Ma, L. Peng, J. Huangfu, and L. Ran, *Applied Physics Letters* 94 (23), 234101 (2009).
- [66] P. H. Tichit, S. N. Burokur, and A. de Lustrac, *Optics Express* 18 (2), 767-772 (2010).
- [67] N. I. Landy, and W. J. Padilla, *Optics Express* 17 (17), 14872-14879 (2009).
- [68] Y. G. Ma, N. Wang, and C. K. Ong, *Journal of the Optical Society of America A* 27 (5), 968-972 (2010).
- [69] J. Zhang, Y. Luo, H. Chen, J. Huangfu, B. I. Wu, L. Ran, and J. A. Kong, *Optics Express* 17 (8), 6203-6208 (2009).
- [70] P. H. Tichit, S. N. Burokur, and A. de Lustrac, *Optics Express* 21 (4), 5053-5062 (2013).
- [71] Y. Luo, J. Zhang, L. Ran, H. Chen, and J. A. Kong, *Progress in Electromagnetic Research* 4 (7), 795-800 (2008).
- [72] J. Allen, N. Kundtz, D. A. Roberts, S. A. Cummer, and D. R. Smith, *Applied Physics Letters* 94, 194101 (2009).
- [73] B. Popa, I., J. Allen, and S. A. Cummer, *Applied Physics Letters* 94, 244102 (2009).
- [74] P. H. Tichit, S. N. Burokur, and A. de Lustrac, *Journal of Applied Physics* 115 (2), 024901 (2014).
- [75] P. Zhang, Y. Jin, and S. He, *Optics Express* 16 (5), 3161-3166 (2008).

- [76] B. Zhang, Y. Luo, X. Liu, and G. Barbastathis *Physical Review Letters* 106 (3), 033901 (2011).
- [77] M. Gharghi, C. Gladden, T. Zentgraf, Y. Liu, X. Yin, J. Valentine, and X. Zhang, *Nano Letters* 11 (7), 2825-2828 (2011).
- [78] J. Li, and J. B. Pendry, *Physical Review Letters* 101 (20), 203901 (2008).
- [79] P. Zhang, M. Lobet, and S. He, *Optics Express* 18 (17), 18158-18163 (2010).
- [80] E.J. Post. *Formal Structure of Electromagnetics*. Dover Publications, Inc., New York, 1962.
- [81] M. Rahm, D. A. Roberts, J. B. Pendry, and D. R. Smith, *Optics Express* Vol. 16, Issue 15, pp. 11555-11567 (2008).
- [82] Jin Hu, Xiaoming Zhou and Gengkai Hu, *Optics Express* Vol. 17, Issue 3, pp. 1308-1320 (2009).
- [83] Ulf Leonhardt, *New Journal of Physics* 8 (2006).
- [84] H. Ma, S. B. Qu, Z. Xu, J. Q. Zhang, B. W. Chen, and J. F. Wang, *Physical Review A* 77, 013825 (2008).
- [85] Y. You, G. W. Kattawar, P. W. Zhai, and P. Yang, *Optics Express* 16, 6134-6145 (2008).
- [86] D. Kwon and D. H. Werner, *Applied Physics Letters* 92, 013505 (2008).
- [87] W. X. Jiang, T. J. Cui, G. X. Yu, X. Q. Lin, Q. Cheng and J. Y. Chin, *Journal of Physics D: Applied Physics* 41, 085504 (2008).
- [88] W. X. Jiang, J. Y. Chin, Z. Li, Q. Cheng, R. Liu, and T. J. Cui, *Physical Review E* 77, 066607 (2008).

- [89] A. Nicolet, F. Zolla, and S. Guenneau, *Optics Letters* 33, 1584-1586 (2008).
- [90] H. Ma, S. Qu, Z. Xu, and J. Wang, *Physical Review E* 78, 036608(2008).
- [91] R. Courant, D. Hilbert, *Methods of Mathematical Physics, Vol.2*, 1 edition. (Wiley-Interscience, New York, 1989).
- [92] Tang, W., Argyropoulos, C., and Kallos, E., *IEEE Transactions on Antennas and Propagation* 58 (2010) 3795.
- [93] Kong, F. et al., *Applied Physics Letters* 91 (2007) 253509.
- [94] Mei, Z. L., Bai, J., and Cui, T. J., *New Journal of Physics* 13 (2011) 063028.
- [95] A. Nicolson and G. F. Ross, *Instrumentation and Measurement, IEEE Transactions on*, vol. 19, pp. 377–382, 1970.
- [96] D. R. Smith, S. Schultz, P. Markoš, and C. M. Soukoulis, *Physical Review B*, vol. 65, p. 195104, 2002.
- [97] D. Schurig, J. J. Mock, and D. R. Smith, *Applied Physics Letters* 88, 041109 (2006).
- [98] J. B. Pendry, A. J. Holden, D. J. Robbins, and W. J. Stewart, *IEEE Transactions on Microwave Theory and Techniques*, VOL. 47, NO. 11, 1999.
- [99] R. Marqués, F. Medina, and R. Rafii-El-Idrissi, *Physical Review B, Condens. Matter*, vol. 65, pp. 144 441(1)–144 441(6), 2002.
- [100] <http://www.stratasys.com/3d-printers/design-series/objet-eden260vs>
- [101] U. Leonhardt, *Science* 312, 1777 (2006).

- [102] D. Schurig, J. J. Mock, B. J. Justice, S. A. Cummer, J. B. Pendry, A. F. Starr, and D. R. Smith, *Science* 314, 403 (2006).
- [103] M. Rahm, D. A. Roberts, J. B. Pendry, and D. R. Smith, *Optics Express* 16, 11555 (2008).
- [104] J. Huangfu, S. Xi, F. Kong, J. Zhang, H. Chen, D. Wang, B.-I. Wu, L. Ran, and J. A. Kong, *Journal of Applied Physics* 104, 014502 (2008).
- [105] W. X. Jiang, T. J. Cui, H. F. Ma, X. M. Yang, and Q. Cheng, *Applied Physics Letters* 93, 221906 (2008).
- [106] Z. L. Mei, J. Bai, T. M. Niu, and T. J. Cui, *PIER M* 13, 261 (2010).
- [107] Y. G. Ma, C. K. Ong, T. Tyc and U. Leonhardt, *Nature Materials* 8, 639 (2009).
- [108] Y. Luo, J. Zhang, L. Ran, H. Chen, and J. A. Kong, *PIERS Online* 4, 795 (2008).
- [109] P.-H. Tichit, S. N. Burokur, D. Germain, and A. de Lustrac, *Physical Review B* 83, 155108 (2011).
- [110] Z. H. Jiang, M. D. Gregory, and D. H. Werner, *Physical Review B* 84, 165111 (2011).
- [111] P.-H. Tichit, S. N. Burokur, C.-W. Qiu, and A. de Lustrac, *Physical Review Letters* 111, 133901 (2013).
- [112] W. X. Jiang, H. F. Ma, Q. Cheng, and T. J. Cui, *Physical Review Letters* 96, 121910 (2010).
- [113] W. X. Jiang and T. J. Cui, *Physical Review E* 83, 026601 (2011).
- [114] W. X. Jiang, T. J. Cui, H. F. Ma, X. M. Yang, and Q. Cheng, *Applied Physics Letters* 98, 204101 (2011).

- [115] W. Jiang, C.-W. Qiu, T. C. Han, S. Zhang, and T. J. Cui, *Advanced Functional Material* 23, 4028 (2013).
- [116] J. B. Pendry, *Optics Express* 11, 755 (2003).
- [117] P.-H. Tichit, S. N. Burokur, J. Yi, A. de Lustrac, *IEEE Antennas and Wireless Propagation Letters*, vol. 13, pp. 1796-1799, 2014.
- [118] Comsol Multiphysics Modeling (<http://www.comsol.com>).
- [119] H. Chen, C. T. Chan, and P. Sheng, *Nature Materials* 9, 387 (2010).
- [120] J. B. Pendry, A. J. Holden, D. J. Robbins, and W. J. Stewart, *IEEE Microwave Theory and Techniques* 47, 2075 (1999).
- [121] S. N. Burokur, A. Sellier, B. Kanté, and A. de Lustrac, *Applied Physics Letters* 94, 201111 (2009).
- [122] High Frequency Structure Simulator v. 15, Ansys Ltd.
- [123] G. Oliveri, E. T. Bekele, D. H. Werner, J. P. Turpin and A. Massa, *IEEE Transactions on Antennas and Propagation*, VOL. 62, NO. 8, AUGUST 2014
- [124] Do-Hoon Kwon, *IEEE Antennas and Wireless Propagation Letters*, VOL. 11, 2012
- [125] O. Quevedo-Teruel, W. Tang, R. C. Mitchell-Thomas, A. Dyke, H. Dyke, L. Zhang, S. Haq, and Y. Hao, *Scientific Reports* 3, 1903 (2013).
- [126] H. F. Ma and T. J. Cui, *Nature Communication* 1(8), 124 (2010).
- [127] S. Li, Z. Zhang, J. Wang, and X. He, *Optics Express* 22(21), 25455–25465 (2014).

Bibliography

[128] F. Zolla, S. Guenneau, A. Nicolet, and J. B. Pendry, *Optics Letters* Vol. 32, (2007).

[129] J. Yi, P.-ichit, S. N. Burokur, A. de Lustrac, *Journal of Applied Physics*, vol. 117, no. 8 (084903), 2015.

LIST OF PUBLICATIONS

Journal papers

1. J. Yi, S. N. Burokur, G.-P. Piau, A. de Lustrac, “3D printed broadband transformation optics based all-dielectric microwave lenses,” submitted to Journal of Optics.
2. J. Yi, S. N. Burokur, A. de Lustrac, “Coherent beam control with an all-dielectric transformation optics based lens,” submitted to Scientific Reports.
3. J. Yi, S. N. Burokur, A. de Lustrac, “Experimental validation of a transformation optics based lens for beam steering,” submitted to Applied Physics Letters.
4. J. Yi, S. N. Burokur, G.-P. Piau, A. de Lustrac, “Restoring in-phase emissions from non-planar radiating elements using a transformation optics based lens,” Applied Physics Letters, vol. 107, 024101, 2015.
5. J. Yi, S. N. Burokur, A. de Lustrac, “Conceptual design of a beam steering lens through transformation electromagnetics,” Optics Express, vol. 23, no. 10 (12942), 2015.
6. J. Yi, P.-ichit, S. N. Burokur, A. de Lustrac, “Illusion optics: Optically transforming the

nature and the location of electromagnetic emissions,” *Journal of Applied Physics*, vol. 117, no. 8 (084903), 2015.

7. P.-H. Tichit, S. N. Burokur, J. Yi, A. de Lustrac, “Transformation electromagnetics for antennas with an illusion on the radiation pattern,” *IEEE Antennas and Wireless Propagation Letters*, vol. 13, pp. 1796-1799, 2014 (Special Cluster on Transformation Electromagnetics - Invitée).

International confereneeces

1. J. Yi, S. N. Burokur, A. de Lustrac, “Beam Steering Lens Based On Transformation Electromagnetics Concept,” *Metamaterials’*, Oxford (UK), September 2015.
2. J. Yi, S. N. Burokur, A. de Lustrac, “Direction Enhancing Lens Design Through Quasi-Conformal Transformation Optics,” *Metamaterials’*, Oxford (UK), September 2015.
3. S. N. Burokur, P.-H. Tichit, J. Yi, A. de Lustrac, “Engineering of electromagnetic emissions through Transformation Electromagnetics,” 6th International Conference on Metamaterials, Photonic Crystals and Plasmonics (META'15), New York (USA), August 2015. (Invited)
4. P.-H. Tichit, J. Yi, S. N. Burokur, A. de Lustrac, “Application of Transformation Electromagnetics concept to delocalize emissions,” 9th European Conference on Antennas and Propagation (EuCAP 2015), Lisbon (Portugal), April 2015.
5. J. Yi, P.-H. Tichit, S. N. Burokur, A. de Lustrac, “Design of a waveguide tapering device via coordinate transformation,” XXXIst General Assembly of International Union of Radio Science (URSI), Beijing (China), August 2014.

Reports

List of publications

1. J. Yi, S. N. Burokur, A. de Lustrac, G.-P. Piau, "VHF metamaterial antenna," unpublished.

Titre : Optique de transformation : Application aux antennes et aux dispositifs micro-ondes

Mots clés : optique de transformation, métamatériau, lentille, antenne, gradient d'indice et impression 3D

Résumé : Le concept de l'optique de transformation qui permet de contrôler le trajet des ondes électromagnétiques à volonté en appliquant une variation spatiale judicieusement définie dans les paramètres constitutifs, est exploré pour concevoir des nouveaux types d'antennes et de dispositifs micro-ondes. Dans une première partie, basée sur la transformation de coordonnées, un dispositif d'illusion capable de modifier l'apparence d'une émission électromagnétique et de la délocaliser, est validé par le biais de simulations numériques. Un dispositif de transition de guide d'ondes, permettant d'assurer une transmission quasi totale entre deux guides d'ondes de sections transversales différentes est également conçu et validé expérimentalement par l'utilisation des résonateurs à métamatériau.

Dans une seconde partie, la transformation de l'espace basée sur l'équation de Laplace est étudiée pour concevoir des lentilles pour les applications antennaires. Une lentille de focalisation capable de restaurer les émissions en phase d'un réseau conforme d'éléments rayonnants et une lentille à dépointage qui permet de dévier la direction du faisceau rayonné d'une antenne sont conçues. Des prototypes fabriqués à partir d'un matériau isotrope tout-diélectrique grâce à la technologie d'impression en trois dimensions (3D) permettent de valider expérimentalement la fonctionnalité des lentilles sur une large bande de fréquence.

Title : Transformation optics: Application for antennas and microwave devices

Keywords : transformation optics, metamaterials, lens, antenna, gradient index and 3D printing

Abstract : The concept of transformation optics which can control electromagnetic waves at will by applying a judiciously defined spatial variation in the constitutive parameters is explored to design novel type antennas and microwave devices. In a first part, based on coordinate transformation, an illusion device able to modify the appearance of an electromagnetic emission and then delocalize it is validated through numerical simulations. A waveguide tapering device allowing to assure quasi-total transmission between two waveguides of different cross-sections is also designed and validated experimentally through the use of metamaterial resonators.

In a second part, space transformation based on Laplace's equation is studied to design lenses for antenna applications. A beam focusing lens able to restore in-phase emissions from a conformal array of radiators and a beam steering lens that allows deflecting the radiated beam of an antenna are designed. Prototypes fabricated by an all-dielectric isotropic material through three-dimensional (3D) polyjet printing technology allow to experimentally validate the functionality of the lenses on a wide frequency range.

